Gas Sensors on Plastic Foil with Reduced Power Consumption for Wireless Applications

THÈSE N^{O} 4710 (2010)

PRÉSENTÉE LE 10 JUIN 2010

À LA FACULTÉ SCIENCES ET TECHNIQUES DE L'INGÉNIEUR
LABORATOIRE DE CAPTEURS, ACTUATEURS ET MICROSYSTÈMES
SECTION DE MICROTECHNIQUE

ÉCOLE POLYTECHNIQUE FÉDÉRALE DE LAUSANNE

POUR L'OBTENTION DU GRADE DE DOCTEUR ÈS SCIENCES

PAR

Jérôme COURBAT

acceptée sur proposition du jury:

Prof. C. Enz, président du jury
Prof. N. de Rooij, Dr D. Briand, directeurs de thèse
Prof. J. Brugger, rapporteur
Prof. C. Pijolat, rapporteur
Prof. J. Wöllenstein, rapporteur

ÉCOLE POLYTECHNIQUE
FÉDÉRALE DE LAUSANNE
Suisse
2010

Abstract

Recently, there is a growing interest in developing so-called “smart” RFID tags for logistic applications. These smart tags incorporate sensing devices to monitor environmental parameters such as humidity and temperature throughout the supply chain. To fulfill these requirements cost-effectively, RFID tags were produced on plastic foil through large scale manufacturing techniques. To benefit from sensing capabilities on these systems, the integration of gas sensors directly produced on plastic foil was explored. Their gas sensing performances were investigated when fabricated on same polymeric substrates than the labels. To be compatible with wireless applications, all sensors were designed to operate in the sub-milliwatt power range.

The integration of three different transducers on plastic foil for the detection of different gaseous species was investigated. First, the direct use of the PET or PEN foil as an optical waveguide for the fabrication of a selective colorimetric ammonia gas sensor was carried out. It led to a simplified processing based on additive fabrication techniques compatible with large scale manufacturing. Second, the impact of miniaturization on drop-coated metal-oxide gas sensors when fabricated on polyimide foil on their sensing performances was investigated. They took advantage from the low thermal conductivity of the substrate to reduce the power consumption with a simplified processing. The detection of oxidizing and reducing gases was achieved at low power consumption when pulsing the sensors. Lastly, the benefits brought by the gas absorption in a polyimide foil were exploited with the design of a simple capacitive structure. By operating it in a differential mode with a second functionalized capacitor, the discrimination between low-concentrations of volatile organic compounds and humidity was achieved. The design and fabrication of these sensors were developed with a vision of their future production performed by large scale manufacturing techniques.

The gas sensing performances of all three transducers were assessed and revealed sensitivities comparable to standard devices made on silicon. Each sensor was associated with low-power electronics targeting an integration on wireless systems. The concept of a smart gas sensing system was demonstrated with the interfacing of a capacitive humidity sensor on a passive RFID label.

Keywords: Gas sensor, Plastic foil, Colorimetric, Metal-oxide, Capacitive, Low-power, Smart sensing system, RFID.

Résumé

Un intérêt croissant se porte sur le développement d'étiquettes RFID "intelligentes" pour des applications en logistique. Ces étiquettes incorporent des capteurs pour mesurer les paramètres environnementaux durant la chaîne d'approvisionnement tels que l'humidité et la température. Afin de minimiser leur coût, ces étiquettes RFID sont produites sur des feuilles plastiques par des méthodes de fabrication à grande échelle. Dans ce travail de thèse, l'intégration de capteurs de gaz sur substrats plastiques a été examinée afin d'assurer une compatibilité entre étiquette et capteur. La performance de ces capteurs a été étudiée en termes de détection de gaz. Et finalement, afin d'être associables aux applications sans fil, tous ces capteurs ont été conçus pour une consommation inférieure au milliwatt.

Trois transducteurs différents ont été intégrés sur substrat plastique pour la détection d'espèces gazeuses différentes. Premièrement, un guide d'onde optique a été développé sur feuilles plastiques (en PET ou en PEN) pour la l'implémentation d'un capteur colorimétrique d'ammoniaque. Ceci nous a permis de simplifier la fabrication en nous basant sur des techniques additives compatibles avec la production à grande échelle. Deuxièmement, des capteurs de gaz de type oxyde-métallique déposés sous forme de goutte ont été fabriqués sur une feuille de polyimide. Après examen de l'impact de leur miniaturisation sur leurs performances, nous avons pu bénéficier de la basse conductivité thermique du substrat afin de réduire leur consommation et de simplifier leur fabrication. Des gaz oxydants et réducteurs ont été détectés à basse consommation en pulsant la température de ces capteurs. Finalement, il a été possible d'exploiter les atouts apportés par l'absorption de gaz dans une feuille de polyimide en concevant une structure capacitive. En l'opérant dans un mode différentiel avec un second condensateur fonctionnalisé, la discrimination de basses concentrations de composés organiques volatiles de l'humidité a été réalisée. La conception et la fabrication de ces capteurs ont suivi notre vision de production à grande échelle.

Les performances en termes de détection de gaz des trois capteurs ont prouvé et révélé des sensibilités comparables à celles obtenues sur des dispositifs en silicium. Une électronique basse consommation visant une intégration sur des systèmes sans fil a été associée à chaque capteur. Le concept de système intelligent de détection de gaz a été démontré en interfaçant un capteur d'humidité capacitif sur une étiquette RFID passive.

Mots-clés: Capteur de gaz, feuille plastique, colorimétrique, oxyde métallique, capacitif, basse consommation, système de détection intelligent, RFID.

Contents

Chapter 1

Introduction

The use of printed electronics for the fabrication of goods has seen a growing interest these last years. This field is mainly driven by the flat display industry with the deposition of color dyes on glass substrates [1]. Other applications have seen the potential of printing technologies for the realization of solar cells [2–4] or organic light emitting diodes (OLED) [5, 6].

Beside these domains, the development of plastic electronics for low-cost and disposable devices fabricated on plastic foil has arisen with the fabrication of displays for instance [7]. Organic thin film transistors (OTFT) [8–10] foresee the production at large scale of low-cost circuitry for widely spread devices such as e-papers. In addition, new applications can emerge from the use of plastic foils. Their possible bending and conformality have found interest for wearable and smart textiles for the potential human care [11–16]. Heart beat, temperature, acceleration can be monitored to prevent or delay diseases. The life quality can be improved with cost-effective technologies that decrease health care costs.

Another field where the use of low-cost plastic foil predicts a strong potential is the logistics with the replacement of barcodes by RFID (Radio Frequency Identification) tags, for which no direct optical contact is required to identify an item. It leads to higher efficiency in goods handling [17]. The quality of the supply chain can be enhanced with the development and manufacturing at large scale of low-cost RFID labels, which has been identified as one of the cornerstone for the logistic chain management. Their complete fabrication by roll-to-roll manufacturing has been seen as a potential solution to allow their diffusion at a larger scale. An FP6 European Project "PolyApply" [18] led to the fabrication of a passive tag with roll-to-roll compatible techniques. It led to the commercialization of the first entirely printed RFID tag by *PolyIC*, Germany [19]. Further possible developments to reduce the cost would consist in directly printing the tag in the package.

The focus is now moving towards the generation of networked and interconnected systems to report not only the identity of objects or their location, but also their environmental conditions over wireless communications [20] with the development of "intelligent" tags. Monitoring environmental parameters in a distributed manner can contribute to improve the energy consumption and efficiency.

Logistics is an important field of interest where these developments can encounter a significant impact. Since 1950, the international trade has increased twenty folds [21]. Nowadays, 90% of trade occurs by sea for which a large part of the goods shipped are in containers. In the 2000s, 500 millions of containers have been shipped by sea every year, among which a significant part concerns foodstuffs. According to the March-April 2007 edition of the RFID Journal:

- 90% of perishable goods are transported in containers worldwide;
- In the area of perishable food, one faces an average loss of 56% in the USA and 50% in the UK;
- 20% of the vegetables distributed in China are lost during or because of transportation.

The early detection of pertinent gases during the transportation of perishable goods foresees a high potential to reduce waste. Volatile organic compounds (VOCs) and ammonia are generated with the deterioration of respectively carbohydrates and proteins [22, 23]. Ethylene acts physiologically as a hormone in plants throughout their life cycle by stimulating or regulating the ripening of fruits and is known as a risk factor during transportation [24]. With the integration of sensors on RFID tags, the supply chain efficiency can be improved [25–28].

Several issues have to be addressed to implement *smart* RFID tags for environmental monitoring. The embedded gas sensors and their interface need to function at very low power to ensure the operation of the system with a battery during the whole shipping time. To make them cost effective, they should be fabricated with methods compatible with RFID tag manufacturing on plastic foil for their directly integration on the label during its production. Finally, a very high sensitivity is expected to detect traces of the targeted analytes.

1.1 Radio frequency identification (RFID) systems

Among wireless devices, RFID (Radio Frequency Identification) systems have shown a fast growing development during the last years. They combine wireless transmission of a small amount of data without power supply on the transponder, unlike for Wifi- and Bluetooth-based systems. Such device can thus operate for years, which make them particularly attractive for logistic applications.

1.1.1 Description of an RFID system

An RFID system consists in a transceiver and a transponder as illustrated in figure 1.1. The transceiver (or reader) sends data and energy to the transponder (or tag) and recovers the modulated backscattered signal emitted by the tag.

Three types of transponders are found, active, semi-active and passive. An active tag is supplied by a battery, while the passive one is only powered by the RF field from the transceiver.

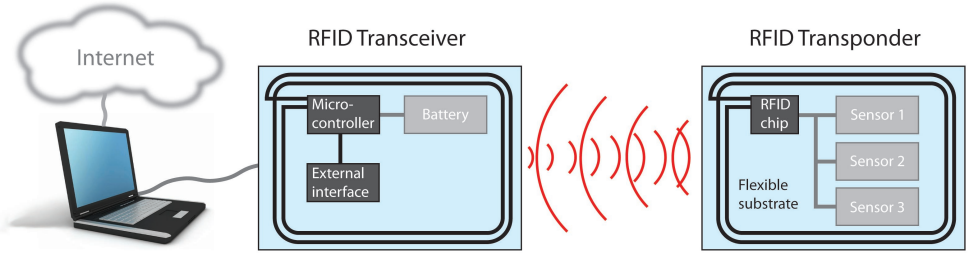

Figure 1.1: Schematic of an RFID system. A transceiver sends data and energy to a transponder, which send back information through a backscattered signal.

A semi-active tag relates to a device where the communication part is activated by the RF field, while additional components – sensors, microcontroller, etc. – on the tag are supplied by a battery. Active and semi-active transponders can thus operate when no RF field is present, i.e. when no reader is in close vicinity.

The simplest transponder embeds a silicon chip with an identification number and an antenna for the communication. When the tag is supplied by the RF field the identification number is sent back to the reader. Such a configuration is limited to the identification of items. Additional functions can be implemented among which the integration of sensors and their electronic interface for the transmission of environmental parameters. They can be integrated on a passive tag, in which case the sensors are only activated when the tag is read. To continuously operate the sensors when no RF field is present, semi-active or active are used.

Different frequencies are available for RFID. They are selected according to the application requirements. They are given in table 1.1 with their coupling principle and their reading distances. At low frequencies, the transmission of energy and information rely on an inductive coupling. It involves large antennas and a small distance between the tag and the reader, typically below one meter. Longer reading distances are achieved at higher frequencies through a electromagnetic coupling and thus smaller antennas. Each configuration however presents some advantages and drawbacks. They are summarized in table 1.2.

Table 1.1: Frequencies for RFID communication and the reading range of the tag.

Designation	Frequency	Coupling type	Reading range
Low frequency (LF)	135 kHz	Inductive	< 1 m
High frequency (HF)	13.56 MHz	Inductive	< 1 m
Ultra high frequency (UHF)	868 or 915 MHz	Electromagnetic	> 1 m
Microwave frequency (MWF)	2.45 GHz	Electromagnetic	> 1 m

For item tracking, these frequencies do not work particularly well due to the presence of metal (e.g. cans,...) or water (e.g. drinks, vegetables, meat,...), which absorb some of them. Even if there is a push for the development of high frequency devices, so far, operation at

Table 1.2: Properties of each frequency for RFID communication.

Frequency	Advantages	Disadvantages
Low frequency (LF)	Standard CMOS chips	Slow data rate
	Good penetration in materials	Large antennas
High frequency (HF)	Standard CMOS chips	Large antennas
	Good penetration of water	Bad penetration of metals
Ultra high frequency (UHF)	Reading distance 2 to 20 m	Worldwide regulatory issues
	Small antenna	No penetration of water or metal
Microwave frequency (MWF)	Tags of small size	Sensitive to electronic noise
	Long reading range	No penetration of water or metal
	High data rate	Chip highly technical

13.56 MHz or lower have shown to be attractive for these applications since the substantial RF absorption can be reduced. Tags at 135 kHz are generally too large with a very low data rate and the use of the highest frequencies is problematic in the presence of metal or water. A long reading distance may however find assets for logistic applications. For instance all items on a pallet can be rapidly identified without pointing each individual package if the penetration of the RF field is sufficient.

1.1.2 Applications of RFID tags and integration of sensing capabilities

The main applications of RFID systems are the access control, pet identification, payment application and the logistic field, which is of first interest here. These devices have become a standard for the identification and traceability of commodities in the retail industry where RFID tags are widely used as smart management in yards and distribution centers: the retailer knows the position and the amount of items in the different stages of the logistic chain, from the warehouse to the final shop.

Unlike barcodes and besides improving the traceability of items, the RFID technology allows the implementation of sensing features for the monitoring of parameters during the supply chain. Recently, the logistic industry has been investigating the possibility of using passive and active RFID tags to gather information about the environmental conditions of goods during shipment. A few companies have developed temperature, humidity or shock sensors on RFID tags [29–33]. They remain too expensive for a general use, which reduces their application to high value and sensitive goods such as drugs, explosives or dangerous chemicals.

An initiative in Finland was launched by *VTT* on implementing sensors in RFID modules [34, 35]. It is mainly focused on the development of the electronics allowing users to connect their own sensors. The integration of sensors on the tag is therefore not directly addressed. A

more specific focus on the actual developments of gas sensors for RFID tags will be given in section 1.2.2.

1.2 Gas sensor operation and technologies

1.2.1 Characteristics of a gas sensor response

A gas sensor aims at converting a chemical signal into an electrical one for further data processing. A typical response of a gas sensing device is depicted in figure 1.2. The output signal changes when the sensor is exposed to a specific analyte to which it is sensitive. Several parameters can be extracted from this curve for its characterization [36].

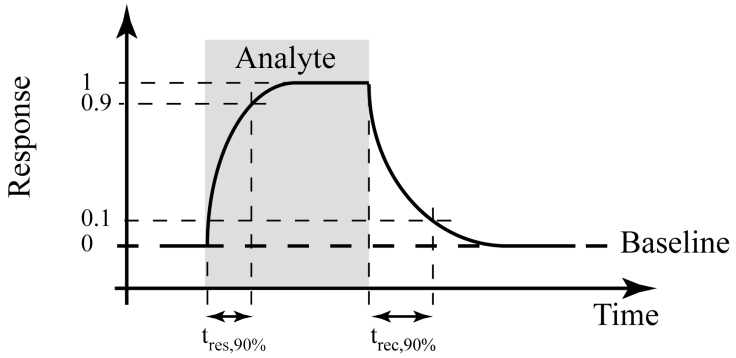

Figure 1.2: Typical gas sensor response when exposed to a targeted analyte.

The *response* of the sensor is given by the variation of the output signal. It can be described as:

$$x = f_{gas}(c_{gas}) \tag{1.1}$$

where f_{gas} is a function (usually non-linear) and c_{gas} the gas concentration. In most cases, the response corresponds to the difference or ratio between the baseline and the steady-state output value when the analyte is present. Its unit depends on the output signal delivered by the device. Most commonly, voltage, resistance or capacitance shifts or ratio are obtained. The type of response – shift or ratio – will always be clearly indicated throughout this document.

When exposing the sensor to different concentrations of an analyte, the *sensitivity* is determined as the relation response-concentration defined as:

$$\gamma_{gas} = \frac{\partial x}{\partial c_{gas}} \tag{1.2}$$

A typical unit is mV/ppm. Another parameter that can be extracted is the *theoretical limit of detection* (LOD) of the sensor. Values in the ppm (parts per million) or ppb (parts per billion) are typically reached. The LOD can be expressed by the 3σ rule given by:

$$3 \cdot \sigma = 3 \cdot RSD \cdot \gamma_{gas} \tag{1.3}$$

where *RSD* is the relative standard deviation of the baseline of the sensor due to noise.

The *response* and *recovery times* of the sensor can also be derived from such a curve. They correspond to the time required by the device to reach a new steady-state when exposed to a different gaseous atmosphere. In this thesis, those values relate to the time to reach the 90% of the steady-state response.

In general, the *selectivity*, Ξ, of a gas sensor is a non-linear function of the concentration. It is usually defined as the ratio of the sensitivity related to the gas concentration to be detected in its linear region to the maximal sensitivity to all other interfering agents:

$$\Xi = \frac{\gamma_{gas}}{max_{all\ other\ gas}(\gamma)} \tag{1.4}$$

The aforementioned parameters characterize a gas sensor when exposed to known concentrations of known gases. If the identification of a gaseous mixture is expected, an array of sensors with a certain sensitivity overlap is generally used. Several factors (baseline, response, recovery, etc.) of the response of each sensor are extracted and processed to obtain a reduced number of parameters, which are typical features of a mixture. A pattern recognition is performed generally through a multivariate analysis to determine the different gases in presence and their concentrations [37, 38].

1.2.2 Gas sensors on plastic foil and for RFID applications

The monitoring of the gaseous atmosphere during the transportation of perishable goods can bring some benefits to reduce waste of food and energy. So far, perished food is still shipped to its final destination since no systematic control can be performed during the supply chain.

Low-cost polymeric sensors have been developed to be compatible with plastic electronics. The fabrication of organic thin film transistors (OTFT) is based on additive processes with a potential compatibility with roll-to-roll manufacturing. Their use as gas sensor was investigated but revealed a low sensitivity towards VOCs [39]. In addition, issues remain with their stability and reproducibility [40, 41]. This technology is therefore not yet mature for its reliable integration and sensing performances for RFID applications.

To simplify the fabrication and reduce its cost, Potyrailo et al. [42] developed a gas sensing tag by coating a standard RFID label with a polymeric material. By measuring the amplitude and phase shift of the backscattered signal, information on the gaseous atmosphere can be extracted. Such a configuration is however limited by the passive nature of the system since no information can be obtained during transportation. Moreover, the gas response depends on the distance between the reader and the tag as well as its orientation [43].

The integration of silicon-based gas sensors on RFID tag was also demonstrated through the FP6 Integrated Project “Goodfood” for ethylene detection. They consisted in combining metal-oxide gas sensors to a flexible RFID tag. These sensors rely on very well established technologies and are commonly used by the automotive industry. They are dedicated to the monitoring of the gas combustion efficiency in the engines [44, 45] or are present in HVAC

(Heating, Ventilating and Air Conditioning) systems to enhance the passengers' comfort and safety [46]. For RFID applications, the main challenge is to reduce their power consumption. It was achieved by decreasing their size [47] to make them power efficient for an RFID tag [48]. Due to the silicon substrate used, these sensors needed an assembly step for their integration on the flexible tag, which involves a certain cost.

Based on the situation with silicon-based devices for RFID applications, one can easily imagine that only little has been done so far for the development of smart gas sensing systems on plastic foil. Due to their potential low-cost processing, new applications can be generated with sensors on plastic film. The simplified fabrication processes on plastic and the flexibility of such devices can generate new perspectives. Common substrates found in large scale processing are polyethylene terephthalate (PET), polyethylene naphthalate (PEN) and polyimide (PI) foils.

The fabrication of transducers on polyimide has received the first attention because of its thermal stability, good chemical resistance and excellent mechanical properties, which make it compatible with standard microfabrication processes. Oprea et al. [49] implemented a capacitive humidity sensor aiming at RFID applications. Its simple architecture with only one metallization layer made it particularly interesting for its integration on smart labels. Briand et al. [50] demonstrated the principle of a metal-oxide gas sensor on polyimide foil. The device however consumed a too high power to make it attractive for wireless systems.

Polyimide may remain too expensive compared to PET foil, which was preferred when less demanding specifications were required (low temperature during fabrication or operation, no contact with aggressive chemical). The first chemical sensing devices on PET were dedicated to the measurement of humidity [51, 52]. Further developments led to the detection of NO_2 [53] or warfare agents [54]. They rely on carbon nanotubes for the detection, which has not yet been validate for reliable and reproducible gas measurements.

1.3 Objectives and motivations of the thesis

This thesis aims at investigating the gas sensing capabilities of devices fabricated on plastic foil for wireless applications. The main objectives consist in:

- Developing gas sensors on plastic foil;
- Operating them at a very low power consumption;
- Investigating their gas sensing capabilities.

The implications and benefits of designing sensors on polymeric substrates were explored. By envisioning their fabrication at large scale by roll-to-roll manufacturing to make them potentially cost-effective, simple sensor architectures with a minimum of processing steps were addressed. Existing fabrication techniques used for silicon-based devices were adapted and new ones were developed for the processing on foil. The choice of the substrate was driven by the benefits it can bring for the operation of the sensor.

In this thesis, the adaptation of well-known transducers developed for years on standard substrates were transposed on plastic foil. The selected devices were metal-oxide, capacitive and colorimetric gas sensors. By characterizing their environmental sensing performances, a first achievement was performed towards the use of polymeric substrates for the effective and reliable detection of gaseous species. The vision is to develop sensors with a perspective of production by printed electronics processes for their potential use as gas sensor for RFID tags.

The detection of oxidizing and reducing gases (e.g. ethylene and ammonia) was performed with a metal-oxide gas sensor. A cross-sectional view of this device is schematized in figure 1.3. To allow the chemical reactions to occur, these sensors need to operate at temperatures between 200 and 300°C. The consequences of using a plastic substrate on their functioning and gas sensing properties were evaluated. To reduce the power consumption, the impact of their down-scaling was investigated for both the transducer and the gas sensitive layer deposited by drop-coating. The influence of the integration of a membrane on the power consumption was also considered to reduce the thermal losses.

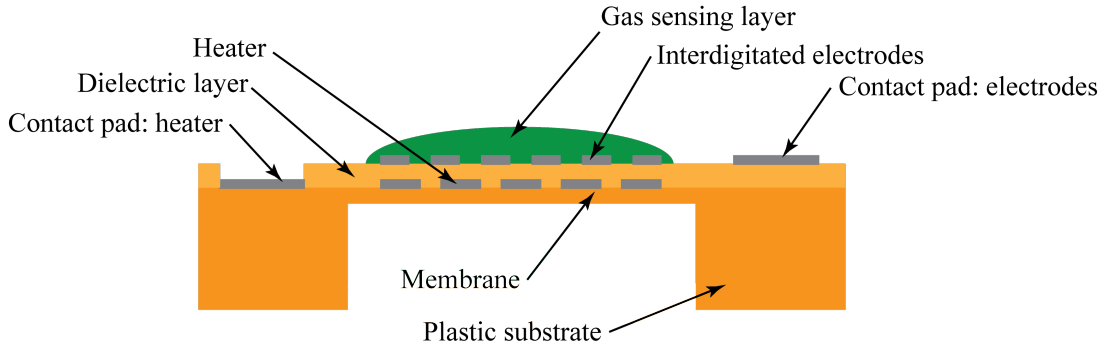

Figure 1.3: Cross-sectional schematic of a metal-oxide gas sensor. The resistor is used as a heating element and its thermal insulation is improved by a thin membrane.

To explore the possibilities offered by the absorption of gaseous compounds by the plastic substrate, capacitive structures were designed as illustrated in figure 1.4. They rely on a very simple architecture with only one fabrication step to pattern conductive lines. The benefits of combining it with a second functionalized capacitor for the discrimination of VOCs and humidity were investigated by operating them in a differential mode.

The design of a sensor with method compatible with large scale fabrication was carried out with the fabrication of a colorimetric sensor on standard foils used in plastic electronics. A cross-sectional view of the device is given in figure 1.5. The principle of operation of this sensor relies on the light absorption in the evanescent field penetrating the colorimetric film. This evanescent field has a typical depth of a few tens to hundreds of nanometers [55, 56]. Due to the optical transparency of the foil used as substrate, its direct application as a waveguide was evaluated. The fabrication in a planar configuration was addressed for a possible fabrication by roll-to-roll methods. Its configuration implicated the realization of light coupling elements on the foil. The use of an additive technique – inkjet printing – for the deposition of the gas sensitive film was investigated.

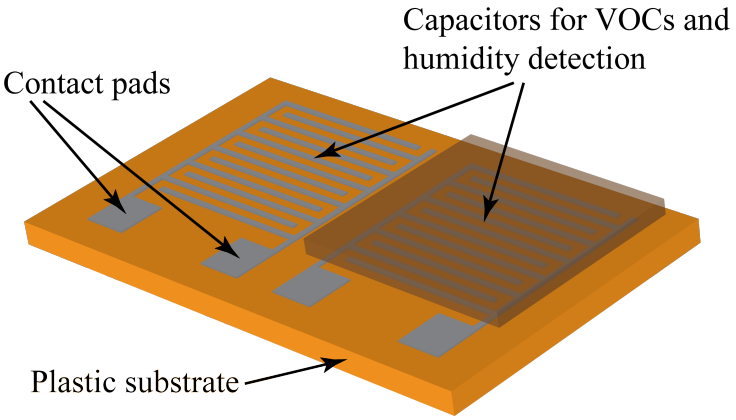

Figure 1.4: Schematic view of two capacitors (one uncoated on the left, one coated with a functional material on the right) patterned on a plastic substrate.

Due to the nature of the substrate involved in the fabrication of the sensors, a technique of encapsulation to protect their active area from external aggressions was developed. It was performed at the foil level to be compatible with roll-to-roll processing. For the packaging of gas sensors on polymeric substrates, several issues had to be considered. The technique implemented had to be based on low-temperature fabrication. Moreover, a dry process was preferred to avoid damaging the gas sensitive layer. A schematic view of the suggested concept for the packaging of sensor on plastic foil is depicted in figure 1.6.

Once the sensors were fabricated on plastic foil, their electronic interfaces were addressed. To meet the requirements of the targeted application, simple circuitries with low-cost components were developed. Their performances were evaluated in terms of power consumption and sensing capabilities. To assess the concept of a smart sensing system, the integration of gas sensors on a passive RFID label was considered. The power consumption of the tag was determined to define its limitations. With the proof of its proper operation, it will lead to future developments for the direct integration of all printed sensors on RFID tag produced by roll-to-roll processing.

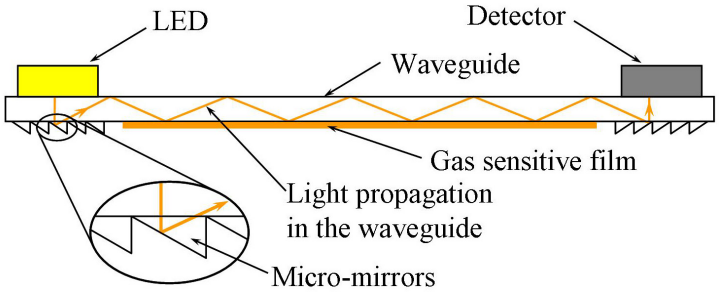

Figure 1.5: Cross-sectional schematic of the colorimetric gas sensor.

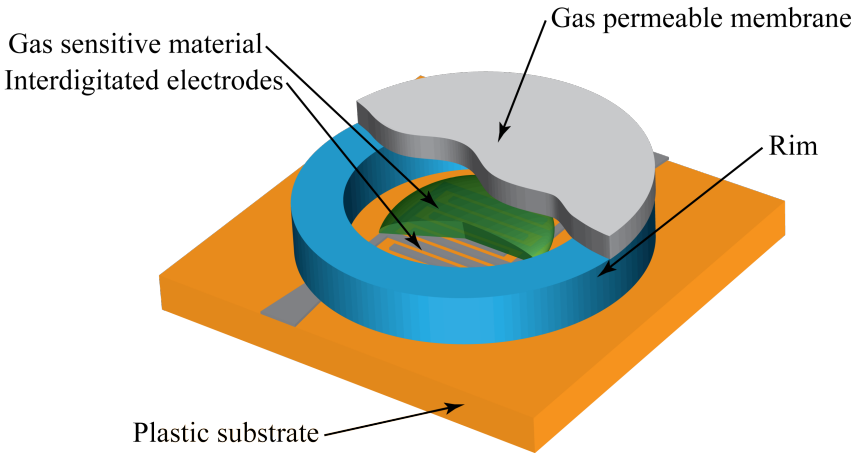

Figure 1.6: Schematic view of a packaged gas sensor. The gas sensitive material is deposited on interdigitated electrodes. The active area of the device is protected by a rim surmounted by a gas permeable membrane.

1.4 Thesis structure

Due to the polymeric nature of the substrates used in this thesis, fabrication techniques standardly used for the processing of silicon substrates were adapted to be compatible with plastic foils. They are presented in chapter 2. More specifically, the deposition and the adhesion of Pt layers on polyimide foil were investigated for the fabrication of the capacitive and metal-oxide gas sensors. The bulk micromachining of polyimide foil was employed for the design of thin membranes to thermally insulate the MOX sensors. Besides, the inkjet printing of dissolved polymers for the fabrication of the colorimetric gas sensor was addressed and a technique of foil level packaging for chemical sensors was developed.

In the next chapters, the design of the gas sensors based on different transducing principles is presented. The development of a colorimetric ammonia gas sensor fabricated with regular and inexpensive PET and PEN substrates combined with additive deposition techniques found in printed electronics manufacturing is depicted in chapter 3. In chapter 4, the operation and the gas sensing capabilities of ultra low-power drop-coated metal-oxide gas sensors fabricated on polyimide foil are investigated for the detection of oxidizing and reducing gases. The sensing potential of a capacitive sensor exploiting the plastic substrate absorptivity of gaseous compounds in the substrate is explored in chapter 5. It was combined with a second capacitor coated with a functional material for the detection and discrimination of VOCs and humidity. In chapter 6, the development of a smart sensing system is addressed. Firstly, through the development of a gas sensing platform that combined two types of devices, capacitive and metal-oxide gas sensors, for the detection of VOCs, oxidizing and reducing gases as well as the humidity and the temperature. Secondly, the low-power sensor interface with a very simple electronics is demonstrated with a metal-oxide gas sensor through a time-to-digital conversion for the readout of the device. Finally, a complete prototype of a smart sensing system is presented. It consists

in interfacing capacitive humidity and resistive temperature sensors made on plastic foil on a passive RFID tag. The perspectives on the investigated sensors fabricated on plastic foil for wireless applications is given in chapter 7 and a conclusion in chapter 8.

Chapter 2

Processing on foil

2.1 Introduction

Processing devices on plastic foil is not straightforward due to their chemical nature and their flexibility. For instance, materials deposited on plastic do not exhibit the same adhesion than on silicon or glass. An investigation – and adaptation – of the fabrication techniques standardly used for Si [57] is thus required to design sensors on plastic foils. The combination of polymeric substrates with appropriate fabrication methods can lead to important manufacturing cost reductions.

This chapter presents generic fabrication techniques that were investigated and developed in the frame of this thesis. They are of particular interest to offer a wide range of possibilities for the production of sensors on plastic substrates. They were combined with standard processing methods to obtain the desired structures that will be characterized in terms of gas sensing abilities in the next chapters.

Our attention was focused on a few technological steps for the fabrication of transducers on plastic foil. Platinum lines on polyimide were required for the design of the heater and electrodes of the metal-oxide sensor, the electrodes of capacitive gas sensors and for the resistance of the temperature sensor. Bulk micromachining of polyimide was necessary for the fabrication of very thin membranes to improve the thermal insulation of the heating element of the MOX sensor. Inkjet printing of dissolved polymers was needed for the localized deposition of the gas sensing film on the waveguide of the colorimetric sensor. By processing these sensors on foil, an encapsulation technique compatible with these polymeric substrates was developed. Its application will be demonstrated with the metal-oxide gas sensors. To summarize, the following methods were adapted or developed for the fabrication of transducers on plastic foil:

- Metal deposition on polyimide foil (section 2.2);
- Dry etching of polyimide (section 2.3);
- Lamination of pre-patterned dry photoresist (section 2.4);
- Inkjet printing of dissolved polymers (section 2.5).

2.2 Metalization on plastic foil

2.2.1 Introduction

An essential part in the fabrication of sensors is the deposition and patterning of electrical conductive pathways. The reliability of the sensor will be deeply dependent on the quality of these electrical lines since they will drive the electrical signal that will be further interpreted as physical or chemical information. A slight variation of the resistivity of a conductor in a resistive sensor can lead to significant errors.

The patterning of conductive lines on silicon substrates has been mastered for years. Their mechanical and electrical properties were deeply investigated. However, on plastic substrates, only little has been published so far [58]. The driving market for the plastic electronics field is the development of flexible displays [59–63] and solar cells [64] that usually uses TCO (Transparent Conductive Oxide) as conductors such as ITO (Indium Tin Oxide). This material suffers from several drawbacks. When bent, it tends to crack [65] and has a high resistivity [66, 67]. For the network of conductive lines on solar panels, silver is preferred [3]. However, this material tarnishes and is thus not suitable for the chemical sensors presented in this thesis. Sidler et al. [68] investigated the resistance of evaporated gold films on polymeric substrates and Lichtenwalner et al. [69] the sputtering of Pt layer on polyimide sheets for the design of a strain sensor.

In this thesis, the attention was focused on the deposition of platinum due to its temperature stability, chemical inertness (does not oxidize) and good electrical properties. Briand et al. [70] has already deposited Pt with an adhesion layer of chromium on polyimide for the development of a metal-oxide gas sensor. Despite its good adhesion properties, chromium oxidizes and diffuses easily in Pt, modifying its electrical properties. Moreover, Pt has shown better performances than any other noble metal when used as electrodes for gas sensors [71].

This section is focused on the deposition and patterning of platinum on polyimide foil. Pt has been extensively used for microsystems fabricated on polymeric substrates. Among other, anemometers [72], bolometers [73], temperature [15, 69, 74], humidity [49, 51] or strain [75] sensors were developed. This material also find applications in the growing field of plastic and textile electronics [15]. In this thesis, it will be used as heater and electrodes for the metal-oxide gas sensors presented in chapter 4 and electrodes for the capacitive sensors depicted in chapter 5.

2.2.2 Experimental

Platinum was deposited on polyimide foil (*Upilex-50S* from *UBE Industries, Ltd.*). This substrate was selected because of its better performances at high temperatures than the well-known *Kapton* foil from *DuPont* [70]. The adhesion of Pt to the substrate was investigated with different adhesion layers: Cr, Ti, Ta. The thicknesses of the adhesion layer and of the Pt were

respectively of 20 and 130 nm. Two deposition techniques were used. Metal evaporation was carried out with a *Leybold* evaporator in the clean room of the CSEM, Neuchâtel, Switzerland, while the sputtering of metals was performed with a *SPIDER 600* in the clean room of the EPFL (CMI), Lausanne, Switzerland. Table 2.1 gives the adhesion layers deposited under Pt as a function of the machine and its capabilities. The adhesion of the films deposited was qualitatively determined through a scotch tape test (*3M Green*).

Table 2.1: Adhesion layers for Pt deposited depending the machine capabilities.

Leybold (CSEM) E-beam evaporation	SPIDER 600 (EPFL-CMI) DC sputtering
Cr	-
Ti	Ti
Ta	-

Patterning of metallic lines

The patterning of the metallic structures on the polymeric substrate was performed using a bi-layer lift-off technique based on a *LOR* resist developed by *MicroChem* [76]. The compatibility of the process with polyimide instead of silicon was first verified to ensure the suitability of the chemicals used (resists, developer, remover) with the polymeric materials. The process flow is illustrated in figure 2.1. Two successive resists were spun one on the other on the plastic foil previously dehydrated at 120°C. The first resist (*LOR*) was not photosensitive, unlike the second layer. The stacked resists were exposed to UV light through a photolithographic mask. During the development, the top layer behaves as a standard positive-tone photoresist, while the underlying film had an isotropic dissolution in the developer, creating an undercut of few hundreds of nanometers (fig. 2.1a). The metal was then deposited by evaporation or sputtering (fig. 2.1b). Finally, the resists were striped, leaving the patterned metallic layer on the polymeric substrate (fig. 2.1c). Such a lift-off technique allows the fine patterning of very narrow structures. Due to the undercut, it is particularly useful for deposition processes with machines with a poor directionality, such as sputters.

2.2.3 Results

The results of the adhesion of the Pt layer on PI with different adhesion layers are presented in table 2.2. A *good* adhesion means none of the metallic film could be removed from the plastic substrate. A *satisfactory* adhesion was for films where only small spots of metal detached during the test, while a *poor* adhesion related to films that could completely be removed from the plastic foil.

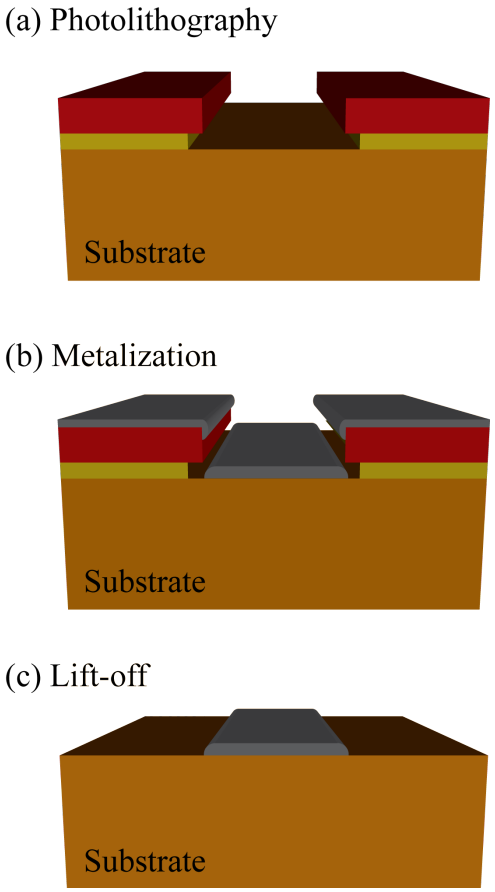

Figure 2.1: Schematic view of a lift-off process developed by *MicroChem*. (a) Photolithography of the photoresist on top of the *LOR* layer; (b) Metalization (c) Lift-off of the metal layer.

The sputtering of Ti/Pt in the *SPIDER 600* machine provided the best adhesion properties because of both the plasma activation of the surface before the deposition and the higher energy of the sputtered metallic atoms. The use of Cr led generally to satisfactory adhesion results by evaporation. However, despite its good adhesive properties for Pt, this metal suffers from oxidation when exposed to air and diffuses easily in platinum. They are significant disadvantages for heating elements or chemical sensors where a high stability over time is required. To counteract these drawbacks, Ta should ideally be used. It however showed a poor adhesion when evaporated. Its deposition by sputtering should be envisaged. Unfortunately, no activation of the surface immediately before its sputtering was possible with the machine used.

2.2.4 Conclusion on the metalization on polyimide foil

Different adhesion layers were evaluated to ensure the adhesion of Pt film to polyimide substrates. Its choice and the type of deposition – sputtering or evaporation – revealed to be of prime importance. The poorest adhesion was obtained with the evaporation of Ta. Cr showed satisfactory performances, but that material oxidizes and diffuses within the platinum, modifying its electrical properties. It makes it not suitable for chemical sensors, especially when

Table 2.2: Adhesion results of the metallic layer to polyimide performed with a scotch tape test.

	Leybold (CSEM Div-C)	SPIDER 600 (EPFL-CMI)
Adhesion layer	E-beam evaporation	DC sputtering
Cr	Satisfactory	-
Ti	Satisfactory	Good
Ta	Poor	-

operating at high temperature like the metal-oxide gas sensors. Hence, the best solution in terms of adhesion and chemical inertness was Ti. Satisfactory results were achieved with its evaporation but deposition by sputtering provided a good adhesion. These results shows the suitability of sputtered Ti/Pt layers as conductive lines deposited on a flexible polyimide foil for the development of sensors and actuators.

2.3 Dry etching of polyimide

2.3.1 Introduction

This section presents the bulk structuring by dry etching of a plastic substrate made of polyimide foil, *Upilex-50S* from *UBE Industries, Ltd*. This material can withstand very high temperatures, up to 450°C, and was used for the fabrication of membranes for chemoresistive metal-oxide gas sensors presented in chapter 4. Since MOX gas sensitive layers operate at temperature between 200 and 300°C, their power consumption can be reduced by improving the thermal insulation of the heater by designing it on a thin membrane. Dry etching was used here to locally make the substrate thinner under the active area of the MOX sensor.

In the literature, only little has been published on the dry etching of polyimide. This material and its patterning is often found for the design of humidity sensors, where it is used as humidity sensitive layer [77–81]. To structure it, the thin polyimide layer is dry etched in an oxygen plasma. Turban et al. [82] studied the influence of the addition of CF_4 or SF_6 to oxygen in the plasma on the etch rate achievable. More recently, Buder et al. [83] fully investigated the impact of the concentration of SF_6 in an O_2 plasma and the total gas flow, on the etch rate, roughness of the etched film and the mask underetch. This concluded a small concentration of SF_6 – between 10 and 20% – in the gas mixture with a flow relatively low – below 100 sccm – led to an etch rate between 1 and 1.4 µm/min and relative low roughness of 0.4 to 2 µm.

In this study, two different gas mixtures – Only O_2 or SF_6 in O_2 – were evaluated in terms of roughness of the etched film, which is the most important parameter to achieve the fabrication of a very thin membrane.

2.3.2 Experimental

For the dry etching of polyimide foil, a 1 μm thick aluminum mask was first patterned onto the substrate by means of standard photolithography technique combined with wet etching. The pattern consisted in 200 μm wide squares.

The dry etching of the polyimide foil was performed in an *STS Multiplex ICP* DRIE (Deep Reactive Ion Etching) plasma etcher. A power of 1000 W and 150 W were respectively applied to the coil and to the platten. The influence of two different gas mixtures on the etching of the PI were investigated: 100% of O_2 (60 sccm) and a mixture of SF_6 (16.7%, 10 sccm) in O_2 (50 sccm). These gas flows were selected according to the capabilities of the system and to the results found in [83].

2.3.3 Results

Adding SF_6 (16.7%) in O_2 showed a reduction of the roughness at the bottom of the membrane to the sub-micrometer range compared to the results achieved with only O_2. In the case when only O_2 was used, a roughness of several micrometers was observed. Additionally, the etching was not optimum since grass was obtained at the bottom of the etched holes. SEM pictures of the results achieved with both gas mixtures are presented in figure 2.2.

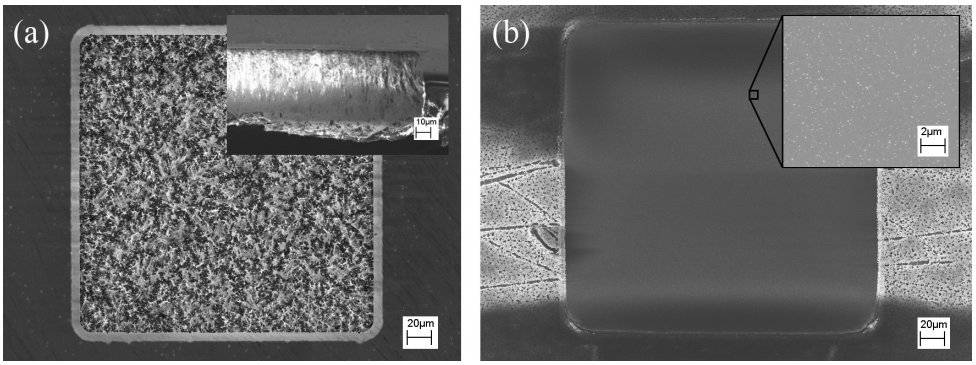

Figure 2.2: SEM pictures of etched polyimide foils (a) in an O_2 plasma, where the mask-underetch is visible (Insert: cross-sectional view where grass is observable); (b) in a mixture of and SF_6 in O_2, which reduced both the roughness and the mask underetch.

The mixture of SF_6 (16.7%) in O_2 showed a bottom part of the etched hole much smoother than with the use of only O_2 as observed in [83]. Figure 2.3 displays the cross-sectional views of the obtained membranes with the two gas mixtures. With the addition of SF_6, the roughness was reduced from a few micrometers to the sub-micrometer range. Due to the presence of grass when etched with a plasma of only O_2 a precise roughness measurement was not possible. When etching with SF_6 and O_2, such measurement could not be conducted either because of the sharpness of the remaining tips and the transparent nature of the material. With a reduced roughness, thinner membranes were obtained. A reasonable and reproducible thickness that can be fabricated was of 3 μm. Moreover, the use of SF_6 reduced the mask underetch and led

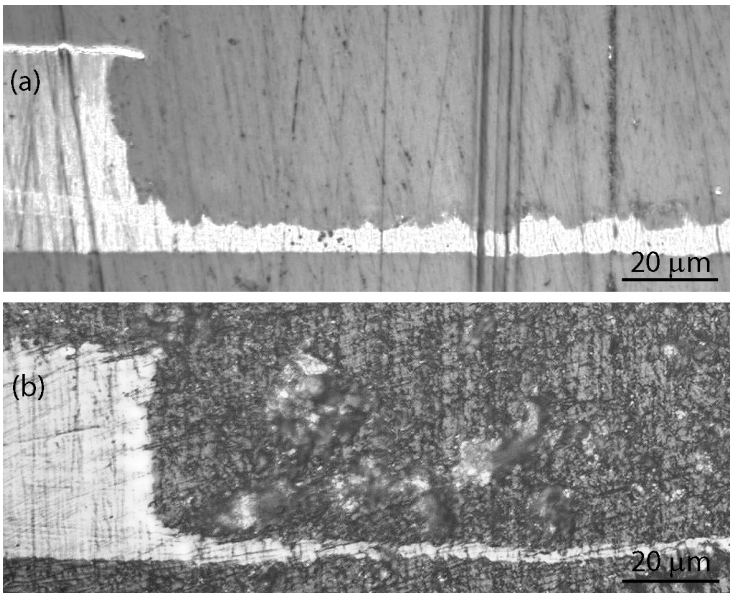

Figure 2.3: Optical picture of a cross-sectional view of a membrane etched in (a) only O_2 and in (b) a mixture of and SF_6 in O_2, which reduced the roughness and the mask underetch.

to structures better defined. Finally, an etch rate of 1.2 µm/min was reached, similar to values found in the literature [83].

2.3.4 Conclusion on the dry etching of polyimide foil

With the dry etching of a polymeric foil – here polyimide – the possibility of fabricating small suspended structures becomes possible. Addition of SF_6 showed a reduction of the roughness at the bottom of the etched hole as well as reducing the under-mask etching. It led to a more reliable process with well defined structures compared to the use of only O_2. This dry process allowed the fabrication of very thin membranes of 3 µm in thickness and 200 µm in width with a sub-micrometric roughness. It will be used to improve the thermal insulation of the micro-heater of the MOX sensors. Other applications could be envisaged in microfluidics for the fabrication of microchannels or for the release of heating structures for wind or flow sensors for instance.

2.4 Reverse processing of dry photoresist

2.4.1 Introduction

A technique based on the reverse processing of dry photoresist was developed for the encapsulation of chemical sensors. The method depicted in this section was proven with the foil level packaging of the metal-oxide gas sensors presented in chapter 4. It was based on a dry process since solvents have to be prohibited in some particular applications to avoid damaging pre-existing structures, such as functional layers. For that purpose, a fabrication method

based on the lamination of pre-patterned parts made from dry photoresist (PR) films was developed, leading to a dry fabrication step. These dry PR films present a combination of several advantages over conventional liquid photoresists:

- Excellent adhesion to a wide range of substrates (silicon, glass, PET, polyimide,...);
- Unlimited shapes;
- Good conformability;
- Less solvent involved;
- Uniform thickness (e.g. no edge bead);
- Low price;
- Short processing time.

Such films were first developed by *DuPont* for the fabrication of printed circuit board (PCB) in the 1960s [84]. Nowadays, several products are commercially available and widely used such as *Riston* from *DuPont* [85], *Ordyl* from *Elga* [86], *Etertec* from *Eternal* [87] or *DFR* from *Asahi Kasei* [88]. Since the 1990s, the use of these materials has arisen in the fabrication of microsystems. The first applications were the development of molds for the fabrication of metallic parts by electroplating [89, 90]. More recently, the fabrication of microchannels for microfluidics was presented [91–94]. By stacking several layers, three dimensional fluidic structures were achieved [95]. Since those materials are provided as non-permanent films, they can be used to cover deep trenches during photolithography steps [96] where the use of standard photoresists would lead to poor results or can be conformed to non-flat substrates, such as the patterning of rolls [97].

Dry photoresist: standard process flow

The dry film *PerMX3000* from *DuPont* is a permanent negative-tone photosensitive epoxy film, especially designed for packaging applications. It can be cured at relatively low temperature (150°C), which make it attractive for its combination with polymeric substrates. The structure of the material before its processing is illustrated in figure 2.4. Several thicknesses are available, ranging from 10 to 50 μm.

A main advantage of dry resist results in the possibility of laminating several layers one on the other to obtain thicker films. The successive lamination can occur either before the exposure – if only one mask is used – or after the development – if three-dimensional structures are desired [91, 95]. The main properties of the *PerMX3000* film are given in table 2.3 and compared to *SU-8*, a standard thick photoresist.

The standard processing of *PerMX3000* is depicted in figure 2.5. The polyethylene (PE) foil is first peeled off while the dry photoresist (PR) is laminated onto a substrate, which was previously cleaned in diluted sulfuric acid. This photosensitive film exhibits good adhesion to silicon, glass and some polymers, such as polyimide and PET. According to the material process sheet, typical temperatures for the lamination are in the range of 65 to 85°C, with a pressure of the roll between 30 and 40 N/cm^2 and a speed from 0.3 to 1.2 m/min. The film can be then baked

Table 2.3: Comparison between *PerMX3000* and *SU-8*.

Properties	PerMX3000	SU-8 2000	SU-8 3000
Aspect ratio	4:1	10:1	5:1
Glass transition temperature (°C)	220		
5% weight loss temperature (°C)	346	279	
Coefficient of thermal expansion (ppm/°C)	72	52	52
Young's modulus (GPa)	2.0	2.0	2.0
Tensile strength (MPa)	50	60	73
Elongation (%)	11	6.5	4.8
Dielectric constant (1 GHz, 50% r.h.)	3.2	4.1	3.2
Dielectric strength (V/µm)	220	112	115
Volume resistivity (Ω·cm)	$2.8{\cdot}10^{16}$	$2.8{\cdot}10^{16}$	$1.8{\cdot}10^{16}$
Surface resistivity (Ω/□)	7.5×10^{16}	$1.8{\cdot}10^{17}$	$5.1{\cdot}10^{16}$
Shelf life (yr)	1	1	1

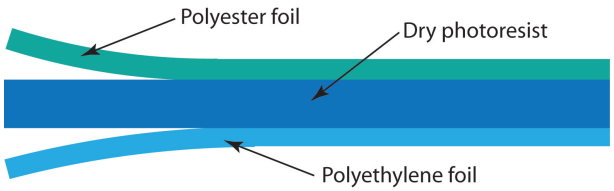

Figure 2.4: Cross-sectional schematic of the *PerMX3000* series. The dry film photoresist is embedded in two polymeric layers.

at 95-115°C for 2 to 10 min to improve its adhesion to the substrate. To enhance the sidewall geometry, the polyester film is removed prior to the exposure with standard photolithographic techniques. Depending on the thickness of the laminated film, an exposure dose between 250 and 500 mJ/cm^2 is required. A subsequent post-exposure bake for 10 min at 60°C is performed. The film is then developed in PGMEA for 3 to 4 min, rinsed in isopropanol and immediately dried. A hard-bake of 1 h at 150°C followed by 1 h at 200°C in an oven is finally carried out.

Application of dry photoresist for packaging

For the encapsulation of sensors, the fabrication process was reversed. The dry PR film was first exposed and developed to obtain pre-patterned structures lying on a polymeric handling film. The dry PR film is thus patterned *before* its lamination. They could be then laminated through a dry process on another plastic foil embedding the transducers. The lamination step occurred at low temperature without the need of an intermediate binding layer. By being compatible with roll-to-roll processing, this technique preserves the advantage of the cost reduction conferred by the fabrication of devices at the foil level.

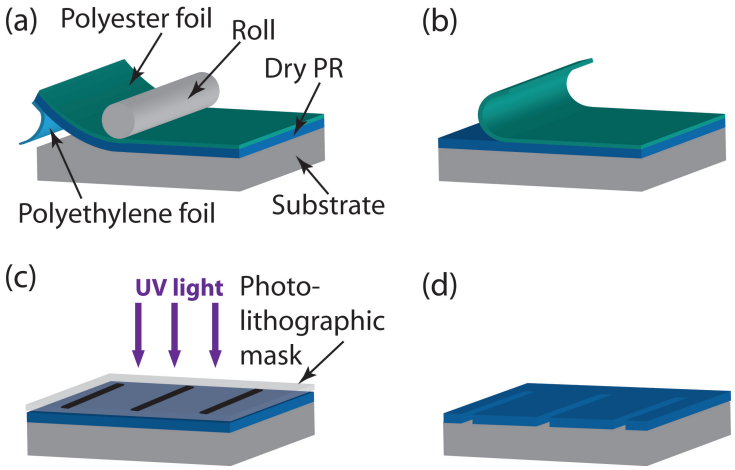

Figure 2.5: Standard processing of the *PerMX3000*. (a) The dry PR is laminated onto a substrate; (b) The protective layer is removed before (c) its patterning by standard photolithography; (d) The exposed film is developed to reveal the structures.

2.4.2 Experimental

The reversed processing of *PerMX3000* permanent film consists in first patterning the structures in the dry photoresist prior to their lamination. Such technique may find applications for devices where only dry processing and low temperature are acceptable to avoid damaging sensitive structures or materials, a situation that often occurs when dealing with chemical sensors for instance.

The layout of the pre-patterned structures consisted in rings with internal and external diameters of 700 and 1200 µm, respectively. They were designed according to the packaging requirements of the metal-oxide gas sensors fabricated on polyimide foil (chapter 4), where they will act as a spacer surrounding their active area.

The reversed processing of *PerMX* is illustrated in figure 2.6. After peeling off the polyester film, the negative-tone dry PR – still laying on its PE handling film – was patterned by standard photolithography with an exposure dose of 450 mJ/cm^2. A post-exposure bake at 60°C for 10 min was then performed to cross-link the exposed zones. To reveal the rims lying on the PE foil, the structures were then developed in PGMEA for 3 min, rinsed in IPA for 30 s before their drying with N_2.

2.4.3 Results

As an example, 50 µm thick pre-patterned structures made of dry photoresist on their PE handling film are exhibited in figure 2.7. These structures will be then laminated on their final substrate, such as a plastic foil.

For a polyimide substrate, they were laminated at 75°C in a press for 3 min. Prior to the lamination, an activation of the surface of the polyimide layer was performed with an O_2 plasma to enhance the adhesion. The PE handling film was next removed. Finally, an optional hard-

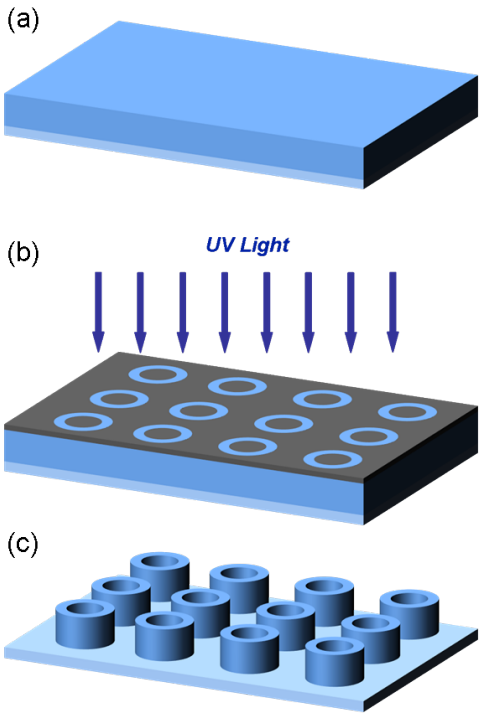

Figure 2.6: Processing of the rims made of dry photoresist. (a) Dry photoresist on its handling PE film; (b) Exposure of the film through a Cr mask by standard photolithography; (c) Rims on the handling film after development.

bake can be undertaken to improve the adhesion to the substrate. The structures were baked in for 1 h at 150°C. The resulting bonded structures are presented in figure 2.8a. An adhesion test with the standard *3M Green* scotch tape was performed and revealed a good adhesion of the rims to the polyimide substrate, even prior to the hard-bake. The latter was thus not mandatory.

As a comparison, the results obtained with the standard processing is illustrated in figure 2.8b with the rims patterned on a silicon substrate. A better uniformity of the structure is observed in this second case.

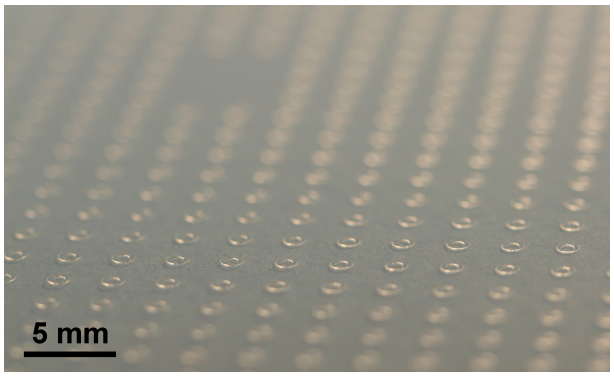

Figure 2.7: 50 µm thick pre-patterned rims on their PE handling film.

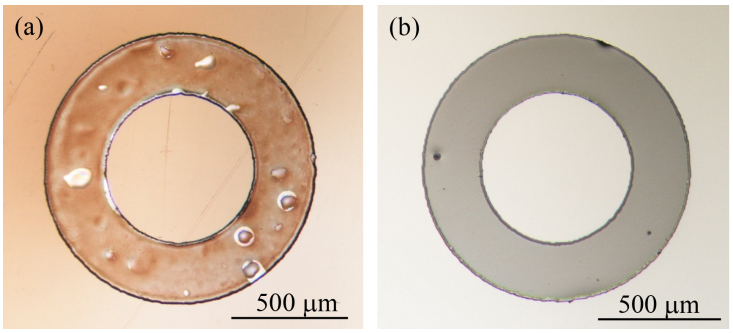

Figure 2.8: Rings patterned in *PerMX3050* dry film photoresist. (a) Reversed process on polyimide; (b) Standard process on silicon.

2.4.4 Conclusion on the reverse processing of dry photoresist

The generic technique presented for the fabrication of polymer-based microsystems was established on the lamination of pre-patterned dry film photoresist. This technique is compatible with low-cost and large scale manufacturing techniques such as roll-to-roll processing. Being based on dry processing, no contamination or damage of the sensor can occur. Due to its low-temperature processing – a maximum 75°C for the lamination – and its good adhesion on various substrates, it is thus compatible with polymeric devices as well as standard microsystems based on conventional materials such as silicon or glass. Beside packaging of gas sensors, other applications are foreseen using this fabrication technique. The design of complex systems – e.g. plastic or textile electronics, microfluidics, high aspect ratio devices – by laminating several pre-patterned layer to obtain 3D structures could also be envisaged.

2.5 Inkjet printing of polymers

2.5.1 Introduction

The last technological development presented in this chapter was the deposition of a polymer by means of inkjet printing. It will be used for the localized deposition of the gas sensing film on the waveguide of the colorimetric gas sensor in chapter 3. A thickness corresponding to the depth of the evanescent field is targeted [55, 56].

Inkjet printing has gained a lot of attention these last years for the deposition of a wide range of materials on different substrates. It offers many advantages over conventional manufacturing techniques used in the field of microsystems such as photolithography-based processes. It is a versatile tool for the accurate deposition of very small amount (tens of picoliters) of a fluid. It combines pattern capability, high speed of deposition on very large area on – but not limited to – flexible substrates, low-cost fabrication, room temperature processing with reduction of waste due to the additive nature of the deposition.

The development of inkjet printing is mainly driven by the flat panel industry with the depo-

sition of dyes for color displays [98–100]. It has also found interests for the fabrication of polymeric light emitting diodes (OLED) [5, 6]. A wide variety of material can be deposited with this technique, among other: polymers [1, 101–104], nanoparticles such as silver [105–108], gold [109–112], aluminum [113], copper [113] or ITO (indium tin oxide) [114]. These materials led to the fabrication of fully or partially printed devices. For instance, a lot of effort has been dedicated to the design of thin film transistors [115–120] for organic electronics. The design of resistors [121] or capacitors [110, 122] were published as well and aimed at fabricating complete organic electronic circuitry. In parallel, the development of sensors has arisen. In the specific field of gas sensors, Mabrook et al. [123] presented a humidity sensor based on the deposition of conductive polypyrrole films on PET foil and O'Toole et al. [124] an inkjet printed gas sensing film on an LED for the colorimetric detection of acetic acid.

Inkjet printing foresees a high potential for the fabrication at large scale and low cost of complete systems. Recent developments have led to the use of inkjet printing in the fabrication of systems-in-package [125] such as smart labels [113, 126].

2.5.2 Printing with a *DMP* printer from *Dimatix*

Several parameters come into account for the inkjet printing of a fluid. On one hand, there are the composition of the solution to be deposited and the type of substrate. These two factors will significantly influence the resolution that can be achieved, due to the wettability of the fluid. On the other hand, some constrains arise with the inkjet printer itself as it will be discussed in the next sections. The model used in this study was the *DMP-2831* from *Fujifilm Dimatix, Inc*. Some limitations of the printer include the volume of the ejected drop, the surface tension and the viscosity of the fluid that can be ejected from the nozzle. These factors will also have an important effect on the resolution of the printed film.

Ink requirements

To allow the ejection of the fluid from the nozzle of the printhead, some parameters of the ink have to be taken into account. The fluid requirements suggested in the user guide of the *DMP-2831* inkjet printer are the following:

- Viscosity: 10-12 cP at the jetting temperature;
- Surface tension: 28-33 dynes at the jetting temperature;
- Low volatility: Boiling points higher than 100°C are preferred;
- Density: Specific gravity greater than 1 is beneficial.

Moreover, solvents with high boiling points are favored to reduce the coffee ring effect, which is due to a too fast evaporation and leave the solute on the outer part of the dried drop [127–129]. De Gans [1] reported the solvent was responsible for the shape of the dried drop rather than

the dissolved material. Among other, adequate solvents for the *Dimatix* printer are butanol or longer chains and propylene glycol. Solvents with a high polarity like water are not compatible with the printhead. Solutions containing xylene or dichlorobenzene should be avoided since they may dissolve some plastic parts, mainly the o-rings, within the ink cartridge.

Drop ejection

To jet the ink out of the nozzle of the printhead, a voltage is applied to a piezo-element. Its cross-sectional schematic is illustrated in figure 2.9. To eject a drop, the fluid is first sunk in the chamber before a deformation of the piezo-element jet it out of the nozzle. The voltage pulse applied to the piezo-element will vary depending on the nature of the ink. Figure 2.10 shows a typical pulse – or waveform – used with the *Dimatix DMP-2831* inkjet printer for the ejection of the dissolved polymers used in this study. The waveform is a scaling factor for the voltage applied. The optimum voltage required to obtain the proper ejection of a drop depends on each nozzle. Therefore, a same value cannot be used for the sixteen nozzles available on the *Dimatix* printer.

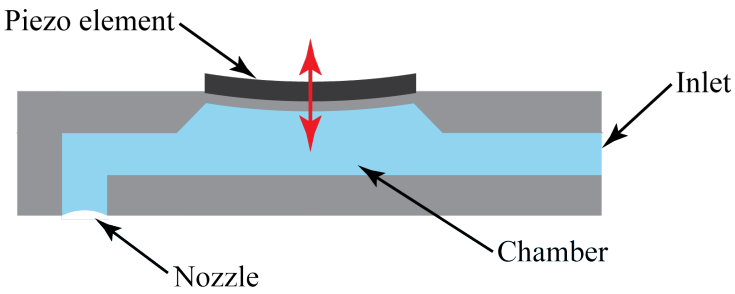

Figure 2.9: Cross-sectional schematic of an inkjet printhead. A drop is ejected from the nozzle by the pumping of the fluid by a piezoelectric element.

A typical waveform can be divided in four steps as illustrated in figure 2.10. During the first step, the voltage applied to the piezo-element decreases to 0 V to bring it in its neutral position with the pumping chamber at its maximal volume. The fluid is sunk through the inlet. The higher the amplitude of the signal applied to the piezo, the higher the volume of ink is pulled in the chamber. The second step of the pulse aims at ejecting the drop from the nozzle. The chamber is compressed by the piezo-element and the pressure generated ejects the drop of fluid. A decrease of the slew rate of this step will reduce the velocity of the ejected drop. Typically, low slew rate are used with low viscosity liquids. Moreover, by making this second step shorter, the volume of the ejected fluid can be reduced. The recovery phase of the piezo-element occurs with the third and fourth steps. The piezo is brought back up, the chamber decompress to be partially refilled with the fluid as a preparation for the next pulse. A pull back of the ejected drop and the nozzle meniscus arise at that moment. The tuning of the amplitude of the third step allows the reduction of the tail of the ejected drop, while its slew rate has almost no influence on it. This step also acts as a dampening segment to avoid that air is sucked into the nozzle,

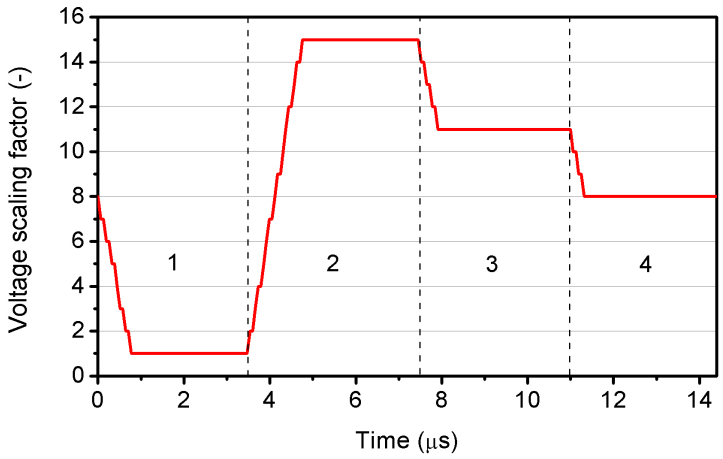

Figure 2.10: Waveform applied to the piezoelectric elements of the printhead of the *Dimatix* printer for jetting dissolved polymers (PMMA mixed with tributyl phosphate).

which would clog the system. The fourth step just brings back the voltage at its initial value to start a new pulse.

Once the waveform was finely tuned as a function of the fluid to be jetted to reach a drop as round as possible and without any tail, the maximum voltage applied to each piezo-element of each nozzle has to be adapted separately. The fluid can thus reach the same jetting velocity and improve the resolution of the printed layer.

2.5.3 Experimental

Polymeric-based ink formulation

The fluid was a mixture of dissolved polymethyl methacrylate (PMMA) (*Aldrich*) and tributyl phosphate (*Fluka*) as plasticizer to improve the flexibility of the film when deposited on a plastic foil. Their concentrations were respectively of 6 mg/ml and 6 µl/ml. They were dissolved in toluene (low boiling point solvent) or dimethylformamide, DMF, (high boiling point solvent).

A cartridge ejecting 10 pl drops was filled with the fluid. The minimum and maximum voltages applied to the piezo-elements were of 15.0 and 19.4 V. The total pulse duration was of 14.4 µs at a jetting frequency of 2 kHz. The printhead was kept at room temperature and the meniscus vacuum was set to a pretty high value of 4 in. H_2O to avoid the solution came out of the nozzles by capillary forces. The sixteen nozzles available were all used, which tremendously decreases the printing time. It is even more important when the area to print is fairly wide as it is the case for the colorimetric gas sensor presented in chapter 3. To ensure a proper coverage, the optimum drop spacing was of 35 µm with a distance between the printhead and the substrate of 800 µm. The platen was heated to 40°C to slightly increase the evaporation rate of the solvent.

The fluid was inkjet printed on PET foils (*Melinex 506*, *DuPont Teijin Films*), which will be used as substrate for the colorimetric gas sensor. Prior to the deposition, the polymeric

substrates were cleaned in acetone, isopropanol and rinsed in DI water. No surface pretreatment was carried out.

2.5.4 Results

After finely tuning the jetting parameters, the dissolved polymers were ejected from the sixteen nozzles of the *Dimatix* printhead as shown in figure 2.11. By independently tuning the applied voltage to each piezo-element, the velocity reached by the drops was of about 7 m/s. During the ejection, no tail or separation of the drop occurred, showing the adequate composition of the solution jetted in terms of surface tension and viscosity. These parameters could however not be precisely determined because of the absence of the measurement equipments in the laboratory.

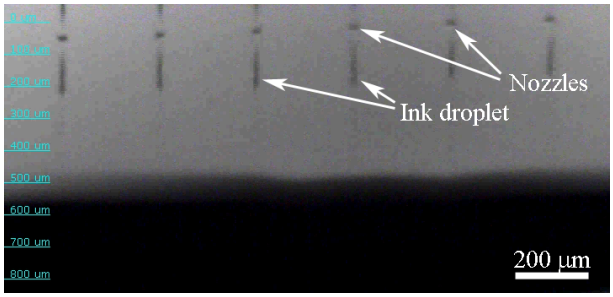

Figure 2.11: Optical picture of the jetting nozzles. The ink was based on dissolved polymers (PMMA and tributyl phosphate).

The nature of the solvents considerably influenced the coffee ring effect as explained in [1]. The results obtained with the same polymeric composition dissolved in low and high boiling point solvents are presented in figure 2.12. Since the thickness achieved in the center of the drop with the solution based on the low boiling point solvent was too thin for a proper measurement, a stack of ten printed layers were deposited for both films. Even with a high boiling point solvent, the coffee ring could not be avoided. The thicknesses in the center of the drop were of 0.14 and 0.04 µm, and their diameters of 500 and 300 µm by respectively using DMF and toluene. Their ratio between the highest point of the ring and the lowest one were of 10 and 31. The coffee ring effect could be decreased with the use of high boiling point solvent, which was therefore preferred. Further experiments however need to be conducted to reduce it and obtain a smoother layer. It can be performed by choosing solvents with higher boiling points, but also with the printing parameters. It involves mainly the temperature of the substrate, the drop spacing and the waiting time between the printing of two successive layers. Surface treatments of the substrate could also improve the wettability of the fluid and lead to a more uniform layer.

The thickness of the deposited polymeric film dissolved in a high boiling point solvent was measured as a function of the number of printed layers. It was averaged over a distance of at least 100 µm at the center of the drop, where the thickness is minimum. The results are given in table 2.4. These values should be more seen as estimations since the flexibility of PET foil

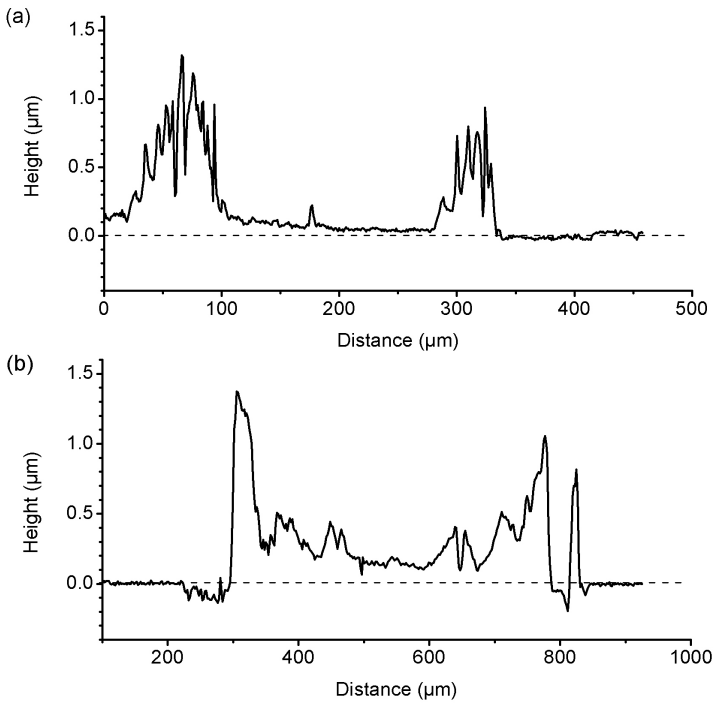

Figure 2.12: Profile of ten printed layers of the colorimetric film dissolved in a solvent with (a) low and (b) high boiling point, which gave a higher film thickness and decreased the coffee ring effect.

used and the very thin deposited layers caused significant difficulties for these measurements. The presence of coffee rings once the film was dried further complicated their estimation. The thickness of one layer was measured to be of about 0.02 µm. By printing ten overlapping layers, a thickness of 0.14 µm was reached, which made suitable for the targeted application.

Table 2.4: Thickness of the polymeric film as a function of the printed layer.

Layer	Thickness (µm)
1	0.02
3	0.03
5	0.09
10	0.14

2.5.5 Conclusion on the inkjet printing of dissolved polymers

The successful additive deposition of dissolved polymers was achieved using a *DMP-2831* inkjet printer from *Fujifilm Dimatix, Inc*. The solution was composed of a polymer, PMMA, and a plasticizer, tributyl phosphate. They were dissolved in a low or a high boiling point solvent

to investigate their influence on the printed layer. The fluid was deposited on PET foil used for their characterization.

Better results were achieved with the high boiling point solvent since it reduced the coffee ring effect. A thickness of about 140 nm was obtained in the center of the drop when printing ten layers. It corresponds to the depth of the evanescent field in a colorimetric sensor.

Further development should be performed to reduce the coffee ring effect. It could be achieved by using solvents with higher boiling points. Additional investigations with the printing parameters – temperature of the platen, drop spacing, waiting time between two printed layers, etc. – should be more deeply investigated to obtain a smoother film. The surface pretreatment of the foil could also be envisaged to improve the wettability of the fluid.

2.5.6 Conclusion

The fabrication techniques presented in this chapter, their combinations and the order they are used during the processing allows developing numerous devices on plastic substrates. They are not limited to a specific type but should be seen as generic techniques for the development and manufacturing of sensors on polymeric foils. Despite their potential use for a wide range of transducers, they will be limited to the development of gas sensors in the frame of this thesis.

Chapter 3

Colorimetric gas sensor on plastic foil

3.1 Introduction

The first gas sensing device presented in this thesis is based on the colorimetric detection of ammonia (NH_3). This gas is produced during the putrefaction of foodstuffs, for example seafood [22, 23], which makes its detection of high interest for the monitoring of perishable goods during shipment. It is also present in chemical compounds such as refrigerant, explosives or fertilizers [130].

The goal here was to implement a polymeric optical transducer with a simple architecture combined with a high selectivity and sensitivity film to NH_3 on ordinary and inexpensive polymeric foils. Its design was based on minimum additive processing steps to meet the cost requirements of logistic applications. It was combined with a very-low power electronic circuitry to be compatible with wireless systems.

A cross-sectional view of the colorimetric gas sensor is depicted in figure 3.1. The original concept presented in this chapter took the advantage of the good optical transparency of the substrate in the visible spectrum to directly use it as an optical waveguide. The transducer was designed in a planar configuration and realized in polymeric materials to make it compatible with large scale fabrication techniques and thus more cost-effective. An LED was used as light source at one extremity. Micro-mirrors coupled the light into the waveguide for its propagation by total internal reflection. The resulting evanescent field penetrates the colorimetric film [131], which changes color when exposed to the target gas. A variation of light absorption occurs depending on its concentration, changing the light intensity reaching the detector.

3.1.1 State of the art

Colorimetric detection of gases has been used for years. It is based on the change in color of a chemochromic reagent incorporated in a porous matrix. Several products are available on the market, such as the well established *Dräger* [132] gas detection tubes (fig. 3.2). When the gas is sucked in the tube, a color change occurs and its concentration can be evaluated with a graduation. Many scientific contributions have been published on colorimetric gas detection,

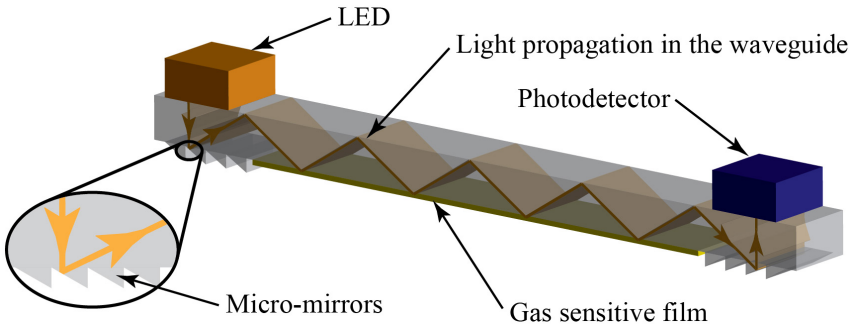

Figure 3.1: Three-dimensional schematic of the principle of operation of the colorimetric gas sensor.

either on the chemical reagent used or the optical transducer designed to measure the light absorption and thus the gas concentration. We focus in the following state of the art only on systems developed for ammonia gas detection.

Colorimetric films sensitive to NH_3

Colorimetric detection of ammonia might be performed by different types of chemochromic reagents such as porphyrin-based [133–135] or pH indicator-based films [131, 136–139]. The former method has shown to be of poor selectivity and is therefore usually used in a matrix where a specific color pattern allows determining the gases in presence and their concentrations [140, 141]. The latter has however demonstrated to be very selective towards a specific gas such as ammonia [142], but also revealed temperature [131, 136, 142] and humidity dependence [143, 144]. To improve its optical quality, the dye is usually embedded in a polymeric film, which is permeable to the analyte to be detected [145]. A plasticizer can be added as well. Besides ensuring a good elasticity of the film and avoiding cracks, it can improve the analyte diffusion, thus the sensitivity, and decrease the response time [146].

Transducers for colorimetric detection

An optical system measures the color change of the dye, which depends on the gas to be detected and on its concentration. Several of them have been developed for colorimetric am-

Figure 3.2: *Dräger* tube for colorimetric gas detection.

monia sensors. They are usually based on lasers [142, 147] or spectrometers combined with a white light source [131, 143, 148, 149]. The combination of gas tubes with mobile phones was suggested as well [150]. The complete realization of the detection system is complex and the final system too expensive to allow a large scale deployment. Shepherd et al. [133] fabricated a system composed of a LED and a photodetector covered with the color changing film. The intensity of the light that was transmitted through the film was monitored to derive the concentration of ammonia. Despite its simplicity, low-cost and the possible integration on different kind of substrates, this system suffers from a lack of sensitivity since the light is only absorbed when it passes through the polymer. It exhibited a limit of detection (LOD) of 5 ppm. A thicker layer of chemochromic film might improve the sensitivity at the cost of a longer response time. Monitoring the intensity of the reflected light on a colorimetric gas sensitive layer for amino-based molecules detection was presented as well [151, 152]. The major drawbacks of such systems when used at large scale are their size, difficulty of integration on planar substrates and low-cost production for disposable use. To improve the sensitivity, optical waveguides have been used, such as fiber optics [131, 143, 148]. The detection principle is based on the light absorption in the evanescent field in the colorimetric film deposited on the waveguide [153]. A cost issue with fiber optics is their integration and alignment with a light source and a detector. To simplify the system, a planar waveguide configuration with prisms to couple the light was also developed [147]. Despite its high sensitivity, such an optical transducer is bulky and power consuming and for these reasons not suitable for the development of cost effective and low-power devices. Planar plastic-based sensor operating with a secondary emitter dye used to propagate light in the optical waveguide was design as well [154]. This device however suffered from a complicated geometry. Several layers of polymeric materials with different refractive indices to properly guide the light were stacked.

3.1.2 Progress beyond the state of the art

An all polymeric colorimetric gas sensor was developed on plastic foil to benefit from its compatibility with printed electronics. The impact of designing these sensors on plastic foils with only polymeric materials on their performances was explored.

For the detection of NH_3, the composition of the colorimetric film was investigated. The influence of the color dye and the choice of polymeric matrix were addressed to optimize their properties for ammonia detection. They revealed to be of high importance to obtain a high sensitivity, a reduced response time and reject parasitic effects such as the influence of humidity. The selected film was then integrated on the optical waveguide to achieve the complete gas sensor and to demonstrate the proper operation of the optical transducer on plastic foil.

Compared to the optical transducers found in the literature, a more simplified architecture was considered. The plastic foil used as substrate was directly exploited as an optical waveguide. Air was used as the surrounding media with a lower refractive index to ensure a propagation of light by total internal reflection in the waveguide coated with the chemochromic

film. Moreover, to couple the light between the light source, the waveguide and the detector, polymeric mirrors were patterned with a simple method.

The colorimetric gas sensor envisions its fabrication by only additive processes to reduce waste and make it more cost-effective. It was achieved here by depositing the colorimetric sensing film by inkjet printing, which permits its very precise localization on the substrate.

3.2 Evaluation of colorimetric films

In this section, the optimization of pH indicator-doped polymeric matrices is presented and the evaluation of ten different colorimetric films to detect ammonia traces in the sub-ppm range is discussed. Their optical gas responses to NH_3 exposure were evaluated. The dilution of the chemicals was adjusted to reach sub-micrometric films. For their evaluation, they were spin-coated on planar glass waveguides, while inkjet printing was used for their deposition on the plastic foils.

3.2.1 Chemistry for the colorimetric detection on ammonia

The operation of such a sensor rely on the change in color of chemochromic reagent that occurs when exposed to a specific gas, such as ammonia. The chemical reaction sequence between NH_3 and a color dye is based on a reversible deprotonization of the latter. The reaction takes place in three steps. First, ammonia reacts with water to produce ammoniumhydroxide:

$$NH_3(gas) + H_2O \longleftrightarrow NH_4^+OH^- \tag{3.1}$$

The ammoniumhydroxide then deprotonizes the color dye to give it another form – with a change in color – and water:

$$NH_4^+OH^- + H^+Dye^- \longleftrightarrow NH_4^+Dye^- + H_2O \tag{3.2}$$

Depending on the dye, the reaction is fully reversible. Thus, the final step is the return of the dye to its original state and color:

$$NH_4^+Dye^- \longleftrightarrow H^+Dye^- + NH_3(gas) \tag{3.3}$$

3.2.2 Colorimetric film preparation

Each investigated film was composed of three components:

- a pH indicator that changes color when exposed to ammonia;
- an optically clear polymer that acts as a matrix to embed the pH indicator ;
- and a plasticizer to avoid cracks in the matrix.

The chosen pH indicators for NH_3 detection were bromophenol blue (BPB) (*Riedel-de-Haën*), bromocresol green (BCG) (*Merck*) and bromocresol purple (BCP) (*Merck*) with pKa values

respectively of 4.1, 4.9 and 6.3. A lower pKa results in a lower detection limit as mentioned in [137] and observed in the current study. The polymers selected for the matrix were poly(vinyl butyral) (PVB) (*Polyscience, Inc.*), ethyl cellulose (EC) (*Aldrich*) and poly(methyl methacrylate) (PMMA) (*Aldrich*), all known as hydrophobic to reduce as much as possible the influence of humidity. In addition, those polymers were also chosen because of their high solubility in standard solvent, commercial availability at low price and easy deposition on glass and plastic substrates. Finally, a hydrophobic plasticizer, tributyl phosphate (TBP) (*Fluka*) or dioctyl phthalate (DOP) (*Fluka*), was added into the mixture to enhance its elasticity, to avoid cracks in the film when bent, and improve the diffusion of NH_3 [146]. In total, ten compositions of films were investigated (table 3.1) with the same proportion of pH indicator, polymer and plasticizer to allow their comparisons. Their reference amounts were respectively of 5 mg, 150 mg and 0.15 ml. Such a composition showed to be adequate for NH_3 detection [136]. To evaluate the influence of the quantity of pH indicator and plasticizer on the film sensitivity and response time, their proportions in the film were modified. The mass of color dye was divided by 2 and 4 referred to its initial concentration, i.e. 2.50 and 1.25 mg, while the amount of polymer and plasticizer were left unchanged. To investigate the effect of the plasticizer, its amount was multiplied by 2 and 3, i.e. 0.30 and 0.45 ml, and mixed with the initial amount of color dye and polymer. They were then dissolved in adequate solvents for each type of solution. When spin-coated, films with different thicknesses, ranging from 5 μm down to 130 nm, were obtained by tuning their viscosity with a modification of the amount of solvents. Their thicknesses were measured by stylus profilometry.

Table 3.1: Wavelengths at which the maximum of light absorption in the films occurred.

	Maximum absoption (nm)		
Polymer + plasticizer	BPB	BCG	BCP
PVB + TBP	598	622	598
EC + TBP	577	592	601
PMMA + TBP	577	595	598
PMMA + DOP	604	-	-

3.2.3 Microstructural and optical properties

Experimental

The films were spin-coated on standard silicon wafers leaving their native silicon dioxide layer for optical characterization and observation by scanning electron microscopy (SEM). It was performed with a *Philips ESEM XL 30* microscope. Due to the non conductive nature of the polymers, Environmental SEM (ESEM) inspection of the films were undertaken with

a pressure in the chamber of 2.0 mbar and an acceleration voltage of 20 kV. Optical pictures were taken with a *Reichert Polyvar-MET* microscope. Polarized light was used to investigate the presence of crystallization in the films. Refractive indices of the materials as well as thickness and reflectance of the whole samples were obtained with a phase-modulated spectroscopic ellipsometer *UVISEL* from *Horiba Jobin Yvon*. Ellipsometry is a valuable tool to characterize polymeric films [155, 156]. The aforementioned optical constants were determined in the range of 420 nm to 1700 nm with steps of 5 nm. Depending on the samples, the spectral range was widened. The ellipsometric angles Δ and Ψ were first measured and are defined as the ratio:

$$\rho = tan(\Psi \cdot e^{i\Delta}) \tag{3.4}$$

$$= \frac{r_p}{r_s} \tag{3.5}$$

where r_p and r_s are the complex Fresnel reflection coefficients respectively for parallel and perpendicular polarized light (to the plane of incidence). The useful pseudodielectric functions, ε_i and ε_r (with $\varepsilon = \varepsilon_r + i\varepsilon_i$) were then automatically calculated from Δ and Ψ. In the spectral range of interest, the dielectric function was outweighed by the contributions of the chemical bonds; the material was hence modeled in this case by a single Lorentzian oscillator.

Results

The thicknesses of the spin-coated films were between 150 and 400 nm depending on their composition. No phase separation between the pH indicator, the polymer and the plasticizer was observed, validating the compatibility of the chemicals used. Optical investigations with polarized light did not show the presence of crystallization in the matrices. The topology of the films was determined by the nature of the polymeric matrix used, independently of the color dye embedded. All films exhibited a good wettability but thin PVB-based films (fig. 3.3a). Particles were observed in all films composed of EC (fig. 3.3b). Due to their very low concentration and despite the use of EDX (Energy Dispersive X-Ray) measurements, their composition could not be determined. Films based on PMMA revealed a smooth and uniform aspect. Similar results were obtained with the other pH indicators in the same polymeric matrices. The influence of a plasticizer in PMMA-based layer is presented in figure 3.3c and figure 3.3d. After a few days, cracks appeared in the film without plasticizer even if deposited on a rigid substrate.

Ellipsometric measurements were performed on all investigated films. Figure 3.4 presents the very good fit between the single Lorentzian oscillator model and the measurement obtained for a film composed of BPB+PMMA+TBP. The thickness, reflectance and refractive index of the films at 590 nm, for which a proper fit of their model was achievable, are presented in table 3.2. Due to the high transparency of the matrices, it was not possible to determine their extinction coefficients. All films based on TBP as plasticizer exhibited reflectance between 0.25 and 0.31, while the use of DOP reduced it to about 0.08. The refractive indices were all in the range of 1.48 to 1.49 as expected from the values of the individual polymer used, except for the film based on PVB (2.05) due to a bad homogeneity of the matrix. A decrease of the

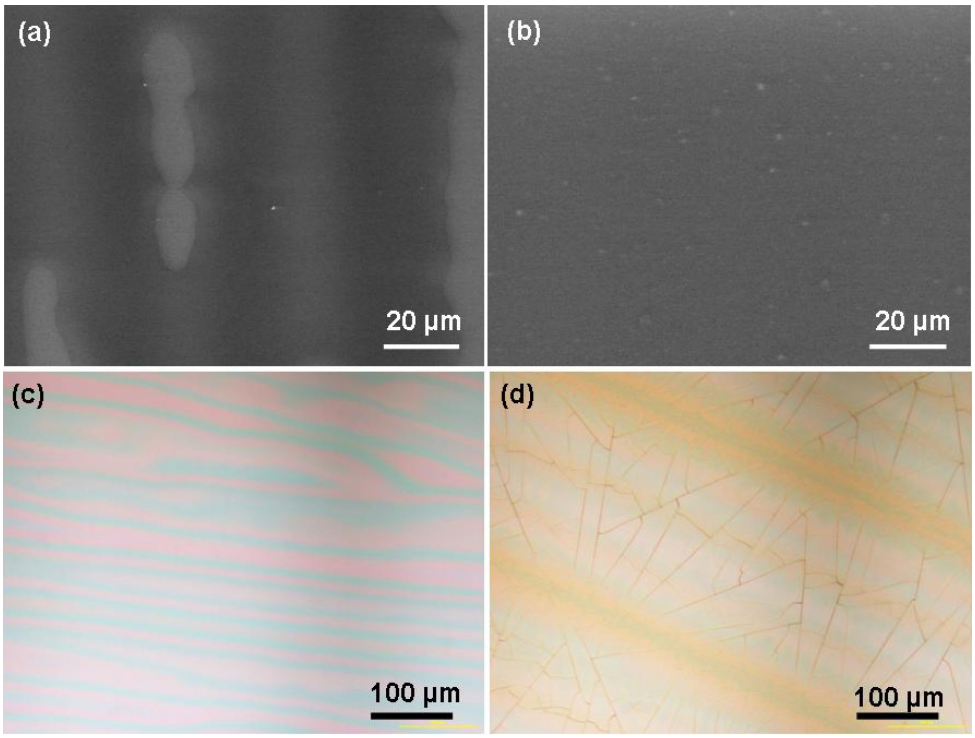

Figure 3.3: Films deposited on silicon wafers, (a) ESEM picture of BPB+PVB+TBP and (b) BPB+EC+TBP; Optical pictures of BCP+PMMA based films (c) with TBP as plasticizer and (d) without plasticizer.

refractive index with an increasing wavelength was observed for all films. The results obtained with PMMA based layers are exhibited in figure 3.5. These measurements also showed the refractive index was slightly increased by adding the pH indicator. However, its influence was

Table 3.2: Thicknesses, refractive indices and reflectance at a wavelength of 590 nm measured by ellipsometry.

Dye	Thickness (nm)	Refractive index at 590 nm (-)	Reflectance at 590 nm (-)
BPB + PVB + TBP	224.2	2.051	0.250
BPB + EC + TBP	363.4	1.486	0.286
BCG + EC + TBP	357.6	1.484	0.275
BCP + EC + TBP	356.6	1.491	0.272
BPB + PMMA + TBP	158.9	1.491	0.284
BCG + PMMA + TBP	159.8	1.491	0.287
BCP + PMMA + TBP	167.9	1.491	0.313
PMMA + TBP	163.2	1.487	0.297
BPB + PMMA + DOP	289.8	1.490	0.078

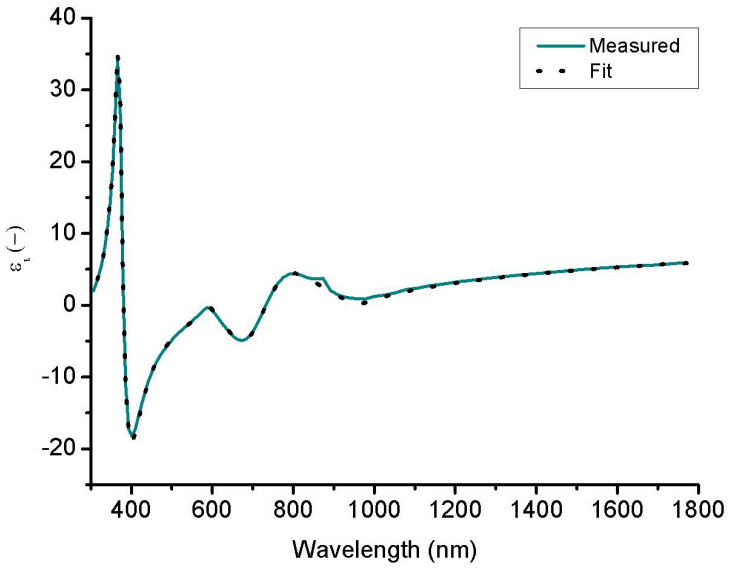

Figure 3.4: Ellipsometric measurement and fit for the BPB+PMMA+TBP film. The result shows the very good accuracy of the single Lorentzian oscillator model used.

limited most likely because of the very low concentrations involved.

Ellipsometry is also capable to provide information on the homogeneity on the whole thickness of the film which is especially relevant for polymeric samples. With ellipsometric measurements in double configuration, two different angles between the modulator and the analyzer, an important inhomogeneity for PVB-based films was measured with a depolarization factor of almost 0.6. More precisely, the top 100 nm of the film were less dense and thus more porous than the underneath layer (values given in table 3.2 for the BPB+PVB+TBP sample are related to the dense material), which could lead to the unexpected refractive index measured. Samples based on PMMA have extremely low depolarization factor and therefore an excellent homogeneity.

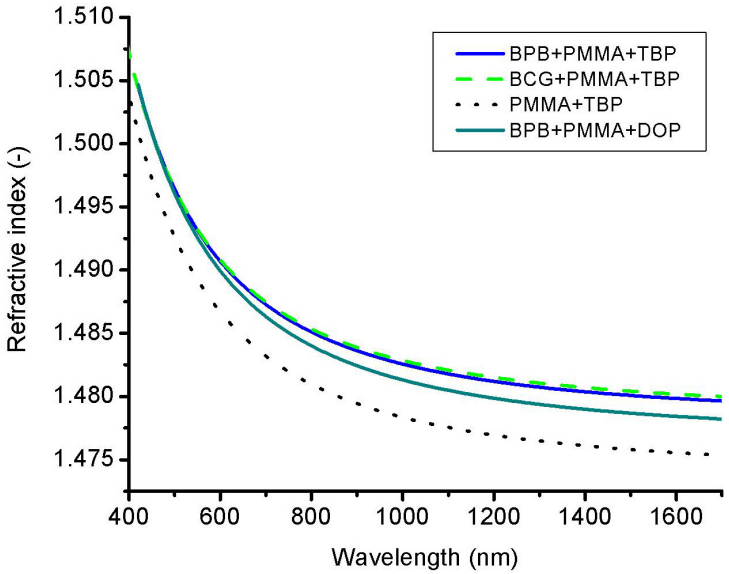

Figure 3.5: Refractive indices as a function of the wavelength for PMMA based films.

The homogeneity of samples based on EC is intermediate between the PMMA and PVB ones.

3.2.4 Optical readout and transducer

Two types of optical characterization of the films were performed to investigate their gas sensing characteristics, throughout spectrometric measurements and in a waveguide configuration. First, thick films, between 2 and 5 µm, were studied using transmission UV-VIS (ultraviolet-visible) spectroscopy to increase the amount of light absorbed. They were spin-coated on glass windows to determine the maximum of absorption of each film in the visible range. The transmission spectra were monitored at wavelengths from 700 nm down to 200 nm with steps of 3 nm with a *Perkin Elmer Lambda 900* UV-VIS spectrophotometer. Knowing the mass of each chemical composing the films, their efficiencies were determined by computing the absorption coefficients from the Beer-Lambert law [157] when they were exposed to 100 ppm of ammonia in dry N_2:

$$\alpha = -\frac{log\left(\frac{I_{out}}{I_{in}}\right)}{l \cdot c} \tag{3.6}$$

where I_{in} and I_{out} are respectively the intensity of the incoming and transmitted light, l the thickness of the film and c the concentration in weight of the color dye in the matrix. This factor will allow defining the most sensitive films by transmission measurements. Based on these results, a first screening of the films to be further investigated was carried out.

Second, these selected films were spin-coated onto a modified microscope slide for a more extensive characterization (fig. 3.6). This 53 mm long slide was used as an optical planar waveguide with both of its extremities cut at 45° to better couple the light. With the aim of increasing the kinetics of reaction between the color dye and NH_3, films with a sub-micrometric thickness, between 130 and 450 nm, were deposited. Using thicker layers would not bring any benefits since the evanescent field only penetrates the polymer at a distance of a few tens to hundreds

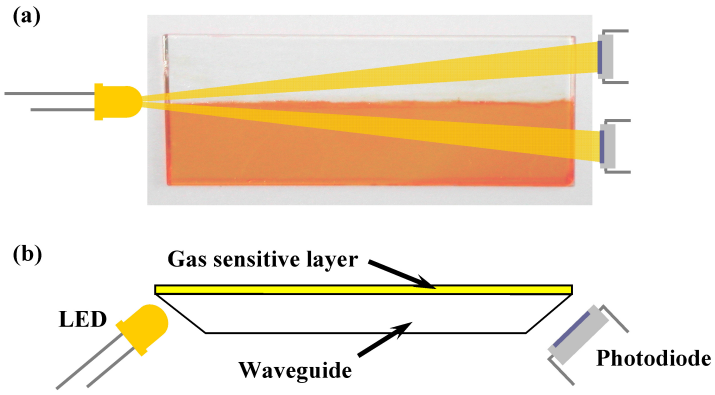

Figure 3.6: (a) Optical picture of the top view of the 53 mm long microscope slide with the lower half covered with the chemochromic film. (b) Schematic cross-sectional view of the measurement system. The planar optical waveguide had its edges cut at 45° for a better light coupling.

of nanometers for this type of configuration [55, 56]. Moreover, due to the very thin layer deposited, total internal reflection in the waveguide occurred, even if the polymer deposited on top has a higher refractive index [142]. A yellow LED (λ_{max} = 590 nm) was chosen as the light source since spectrometric measurements showed that all the films exhibited their highest sensitivity to NH_3 at wavelengths between 577 and 622 nm, as shown in table 3.1. Two photodiodes (BPW34 type) were used as detectors, one acted as reference to keep the light intensity of the LED constant throughout a feedback loop while the second one measured the variation of film absorption under the presence of ammonia. The output of the signal was an analog voltage between 0 and 5 V monitored with an *Agilent 34401A* multimeter.

3.2.5 Gas measurements with films coated on glass slides

A computer-driven gas mixing system was used for the gas measurements. It was composed of ten gas lines controlled by ten mass flow controllers (MFC) that regulated the flow to obtain a gas mixture with the defined concentration. Three lines were dedicated to oxygen, dry nitrogen and wet nitrogen, the latter being obtained by bubbling the gas in water. By mixing these gases, one can obtain N_2 or synthetic air with the desired level of relative humidity (RH), from 0 up to 90%. The other lines were devoted to test gases including ammonia, ethanol, ethylene, hydrogen, carbon dioxide, carbon monoxide and nitrogen dioxide. Besides controlling the MFCs, the computer monitored the temperature and relative humidity of the gas flowing in the gas cell as well as the output signal of the sensor when it was in a waveguide configuration. The flow rate used for all experiments was of 1 l/min. The film was exposed to 100 ppm of NH_3 for 1 h during the spectroscopic measurements and for concentrations ranging from 0.25 to 20 ppm when deposited on a waveguide. Each gas measurement cycle started with a purge with the carrier gas for 1 h before introducing NH_3. When varying the gas concentrations, the gas cell was purged with the carrier gas for 1 to 3 h to bring back the film to its initial state.

First, spectrometric measurements were carried out in dry N_2 with only water adsorbed in the film, which helped the chemical reaction to arise, and under different level of humidity. Indeed, the presence of water is crucial for the reaction between the color dye and ammonia to occur [136]. Then, the influence of humidity under N_2 gaseous atmosphere was investigated to point out its effect on the film response. The latter was chosen as carrier gas because of the wider range of relative humidity level that can be achieved with the gas mixing system at our disposal.

Gas measurements with the film-coated optical waveguide were performed in synthetic air with 50% RH as carrier gas. Those experiments allowed comparing the films in term of sensitivity, response time and limit of detection. Selectivity, cross-selectivity to NH_3 and the influence of humidity were evaluated under 5 ppm of ammonia. In order to clearly see interferences with other gaseous species (C_2H_5OH, C_2H_4, H_2, CO_2, CO, NO_2), the highest gas concentrations available with the gas mixing system were used for these interfering gases.

The gas cell used for spectroscopic measurements had a length and diameter of 10 cm and

2 cm, respectively. No gas cell was used in the reference channel of the spectrometer. When testing the film in a waveguide configuration, the gas cell had a volume of $14\times14\times8$ cm^3. It also included the readout electronics, the light source and the detector with their movable mechanical supports for a better light coupling (fig. 3.7). We verified that the operation of these components was not affected by the gaseous atmosphere in the cell.

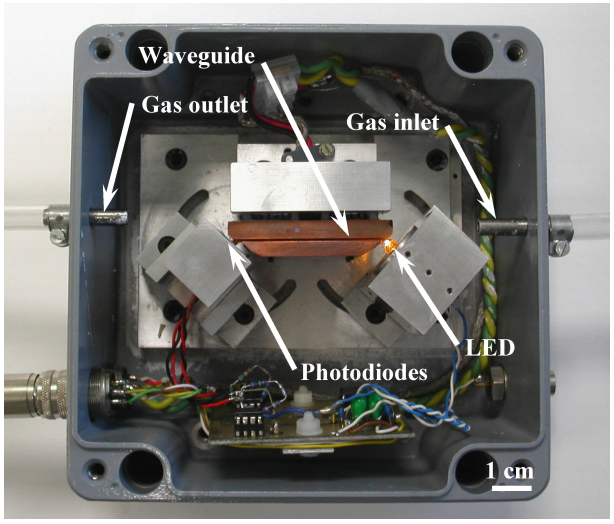

Figure 3.7: Gas cell for the gas measurements in a waveguide configuration.

Response to NH_3

Figure 3.8 presents an example of a spectroscopic light transmission measurement of a film composed of BPB+PMMA+TBP. The highest transmitted light intensity was of about 84% due to losses at the air-glass interface of the two gas cell windows. When not exposed to ammonia, the film exhibited a stable signal with no influence of the carrier gas or humidity. A similar result was obtained when the film was exposed to NH_3 in a dry atmosphere, N_2 or

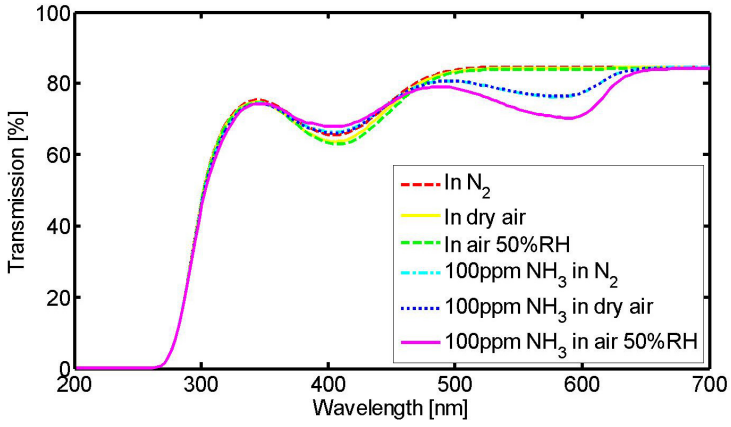

Figure 3.8: Transmission spectra obtained for the BPB+PMMA+TBP when exposed to different atmospheres.

synthetic air. The wavelengths at which the difference in maximum absorption of the light occurred when the film was exposed to only dry N_2 and to NH_3 are presented in table 3.3. The maximum absorption peak of either BPB+PMMA or BPB+EC matrices with TBP as plasticizer rapidly shifted to values between 590 and 600 nm with higher humidity levels, while all the other compositions were subject to insignificant maximum absorption shifts of a few nm. The reactions between the colorimetric films and NH_3 were completely reversible. Typical response and recovery times, $t_{90\%}$, were in the range of a few minutes when exposed to 5 ppm of NH_3 and significantly decreased when exposed to higher concentrations. The efficiency of the films in term of NH_3 response was then deduced by computing their absorption coefficients with the Beer-Lambert law (table 3.3). The reflectivity of the film was not subtracted for this calculation. The film deposited on the glass substrate was considered as a whole, which included their inherent losses found in an optical system such as reflectivity. In transmission mode, the best results were obtained with a mixture of BPB+PVB+TBP with an absorption coefficient (in weight) of 2.55 μm^{-1}. Considering the poor results obtained with the BCP color dye based polymer matrices, those films were not evaluated in a waveguide configuration.

Table 3.3: Light absorption coefficients of the films evaluated by the Beer-Lambert law at the wavelength where their maximum of absorption occurred.

	Absorption coefficient in weight (μm^{-1})		
Polymer + plasticizer	BPB	BCG	BCP
PVB + TBP	2.55	0.50	0.026
EC + TBP	1.41	0.24	0.019
PMMA + TBP	0.72	0.10	0.002
PMMA + DOP	1.10	-	-

Therefore, only the films with BPB and BCG pH indicators were further investigated in a waveguide configuration. As presented in figure 3.9, a concentration of 5 ppm of NH_3 was easily observed. All films exhibited a very long response and recovery times. Since faster reactions were obtained with thicker films with the spectrometer, the origin of these results was ascribed to the size of the gas chamber used for these measurements, which had a volume about 50 times bigger. Measurements should be thus carried out with a more appropriate gas cell, namely with a lower internal volume, to efficiently estimate the response time.

For all the polymers mixed with TBP as plasticizer, films with the BPB color dye gave a higher output signal variation than with BCG, whose gas sensitivities were not high enough to detect NH_3 traces. Only BPB pH indicator based films were further characterized due to their higher sensitivity, S, to NH_3: $S(BPB) > S(BCG) > S(BCP)$. In the contrary to what was observed with spectrometric measurements, PVB-based matrices did not show the best results in this configuration. The highest sensitivity was reached with EC: $S(EC) > S(PMMA) > S(PVB)$.

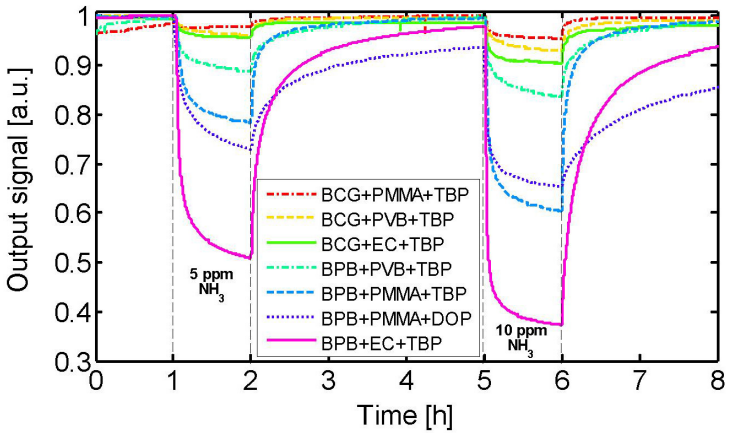

Figure 3.9: Gas measurements with the different films coated on the planar optical waveguide under 5 and 10 ppm of NH_3 in synthetic air with 50% RH.

Actually, the detection principle is completely different between spectrometric and evanescent field measurements. The light intensity after passing through the bulk of the film is monitored in the first case, while in the second case, the output light intensity depends on the depth of the evanescent field in the chemochromic film. A lower depth means an inferior light absorption. Therefore, the evanescent field depth might be lower in the PVB-based matrix than in PMMA-based one due to different refractive indices of the films, reducing thus the light absorption by the color dye embedded. In terms of kinetics of reaction (t: time), the fastest reactions occurring with the BPB+TBP-based films were when using a PMMA matrix: $t(PMMA) < t(PVB) < t(EC)$. Hence, the PVB-based polymer matrix was no longer studied due to its lower sensitivity to NH_3 and EC-based one because of its longer reaction time. At this stage, only BPB+PMMA based films with TBP or DOP were further evaluated to underline the influence of the plasticizer type on the effect of humidity on NH_3 response and on the limit of detection.

Theoretical limit of detection

Measurements under NH_3 in synthetic air (50% RH) were performed at concentrations from 20 ppm down to 0.25 ppm as presented in figure 3.10. Linear responses were observed for both films composed of BPB+PMMA with either TBP or DOP as plasticizer in the lower concentration range ($\leq$ 2 ppm), while a non-linear behavior was obtained for higher concentrations. Gradual saturation of the color dye by reacting with ammonia occurs when increasing the NH_3 concentration, which leads to a decrease in the sensitivity of the film. Similar results were found in the literature for such sensors [131, 143]. By using linear regression for concentration ranging from 0.25 to 2 ppm of NH_3, the coefficient of determination, R^2, of BPB+PMMA+TBP and BPB+PMMA+DOP were respectively of 0.997 and 0.960. An obvious advantage came forward with the former in term of linear response. The LOD was theoretically determined with the 3σ rule given by equation (1.3) for concentrations smaller or equal to 2 ppm (linear region).

Theoretical LOD of about 2 ppb were obtained for both films with different plasticizers.

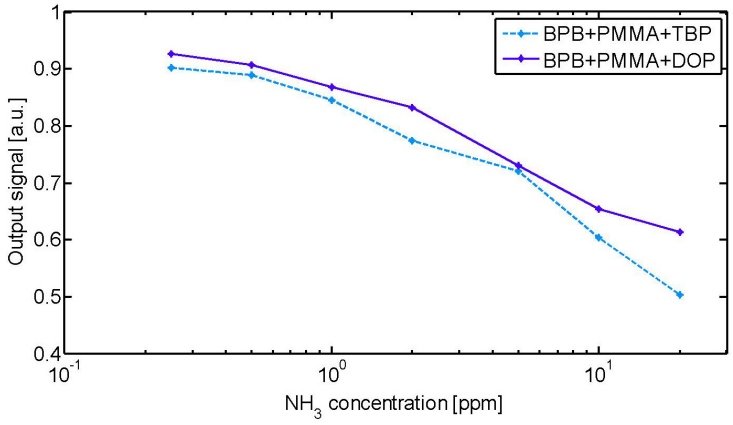

Figure 3.10: Gas responses of the BPB+PMMA films with either TBP or DOP as plasticizer to NH_3 concentrations ranging from 0.25 to 20 ppm in synthetic air with 50% RH.

Humidity dependence

As shown in figure 3.11, an influence of humidity was observed by optical spectrometry when a film was exposed to NH_3. Figure 3.12 presents the results obtained for the BPB+PMMA films were exposed to 5 ppm of NH_3 under different level of humidity in a waveguide configuration. A strong dependence of the sensor signal upon humidity level was exhibited for the TBP plasticizer, while for the DOP one, the response remained pretty unaffected, showing its strong hydrophobic nature, which could also be a reason explaining its slower response time, as observed in figure 3.9.

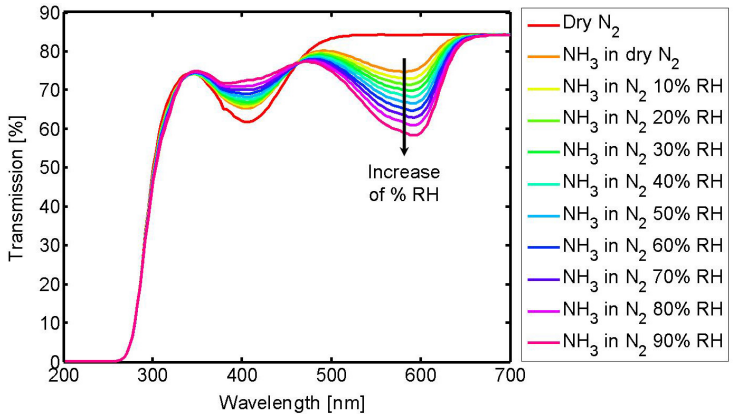

Figure 3.11: Transmission spectra of the BPB+PMMA+TBP film in 100 ppm of NH_3 for different RH levels in N_2.

Selectivity and cross-selectivity

Similar results were obtained in term of limit of detection for both BPB+PMMA when using either TBP or DOP as plasticizer. BPB+PMMA with TBP as plasticizer was further investigated

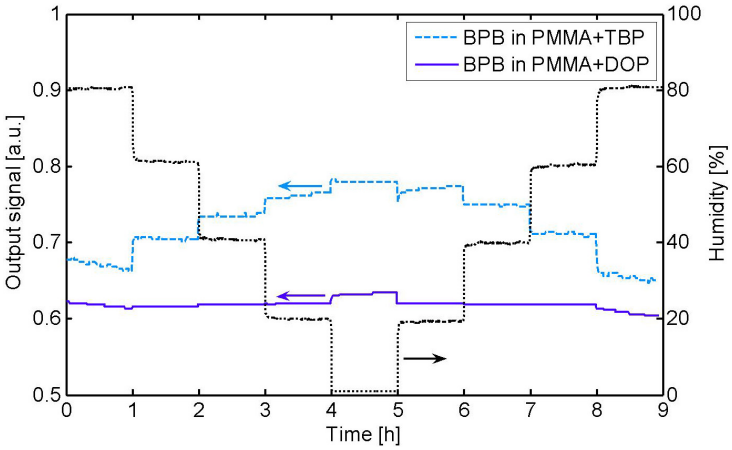

Figure 3.12: Humidity response of the BPB+PMMA films with either TBP or DOP as plasticizer when they were exposed to 5 ppm of NH_3 for different RH levels in synthetic air.

since it showed the highest linearity of response to low NH_3 concentrations and the shortest response/recovery times despite the higher influence of humidity. As presented in figure 3.13, the film exhibited a very high selectivity towards NH_3 during the spectrometer measurements. No transmission variations were noticed when exposed to the carrier gas only or when mixed with some possible interfering gases around the wavelength of interest of 590 nm. When the film was deposited on a waveguide (fig. 3.14), a slight response was observed when the film was exposed to CO_2 (1000 ppm) and NO_2 (5 ppm) only in synthetic air and with 5 ppm of NH_3 in air. Moreover, an almost negligible signal variation to H_2 exposure was also noticed in the latter case. By observing slight variations of the output signal when exposing the film to interfering analytes, it proved a higher sensitivity of the sensing film in a waveguide configuration than

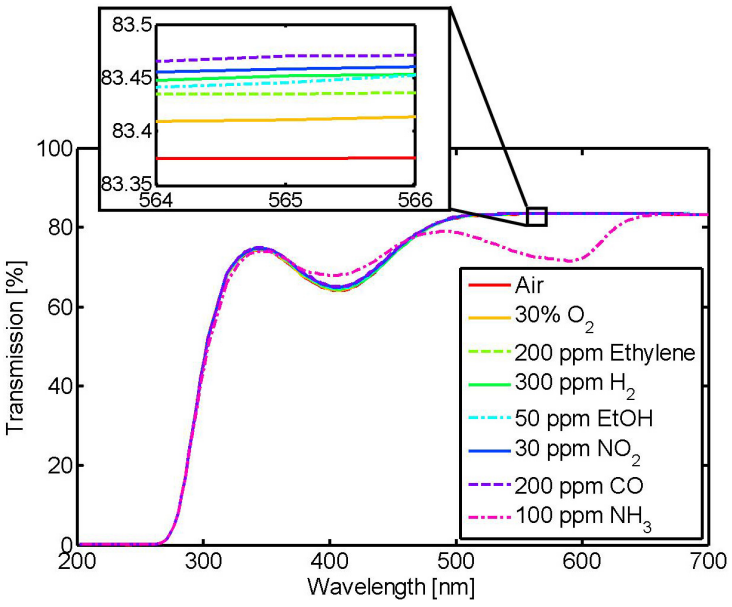

Figure 3.13: Transmission spectra of the BPB+PMMA+TBP composition for NH_3 and other potential interfering gases in air at 50% RH.

in an optical transmission mode of measurements, but at a cost of a slightly lower selectivity. However, these very low responses to pretty high concentrations of interfering gases confirmed the very good selectivity. Additional measurements should be undertaken with other possible interfering gases such as acidic or basic gases. The selectivity towards specifically NH_3 could also be also further investigated with other amino-based analytes.

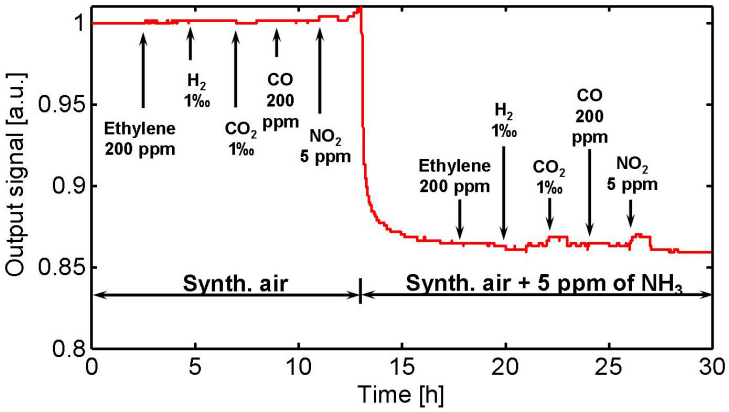

Figure 3.14: Selectivity and cross-selectivity measurements of the BPB+PMMA+TBP film when spin-coated on a glass waveguide.

Influence of the film composition

The pH indicator and plasticizer concentrations were more extensively evaluated for the film composed of BPB, PMMA and TBP. As expected, by decreasing the mass of pH indicator in the film by a factor 2 (2.50 mg) and 4 (1.25 mg), one observed a decrease in sensitivity as shown in figure 3.15. This effect was due to the lower amount of light absorbed in the evanescent field by the pH indicator. The amount of color dye that has to be embedded in the film will depend on the targeted range of NH_3 concentrations that needs to be monitored, namely where a linear response of the film is desired. By decreasing the amount of color dye in the matrix, the sensitivity of the film and the concentration range where a linear response occurs are reduced since less color dye molecules are available to react with NH_3. On the other hand, having a too high concentration of the dye in the film may reduce the light intensity reaching the photodiode due to higher light absorption by the pH indicator.

A second issue to consider is the mechanical stability of the film if the amount of polymer and plasticizer are too low. Moreover, the modification of the composition of the film can also have an influence on its optical properties, such as it absorbance or its refractive index. A variation of the latter may change the depth of the evanescent field and thus the sensitivity of the sensor.

The results obtained with two and three times the original concentration of plasticizer (0.15 ml), tributyl phosphate, is also presented in figure 3.15. With higher plasticizer concentrations, four times higher than the original value, films showed to be unstable and were difficult to deposit on glass waveguides, most likely linked to surface tension issues. No measurements with higher

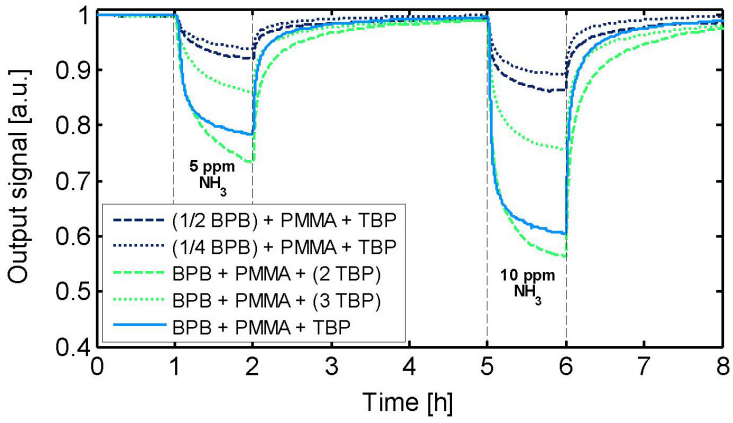

Figure 3.15: Gas responses of BPB+PMMA+TBP films with the quarter, half and initial concentration of color dye, and the initial, two and three times the concentration of plasticizer under 5 and 10 ppm of NH_3.

concentrations than three times the original amount of plasticizer were consequently carried out. By doubling the amount of plasticizer (0.30 ml), these measurements suggested that the sensitivity may significantly be enhanced but the response time was longer. Then, by tripling the amount of plasticizer (0.45 ml), a non-negligible decrease in sensitivity was observed. This behavior has not been fully understood yet, but it might be related of the hydrophobic features of the matrix used. Besides improving diffusion within the film and increasing the response time, plasticizers are also known to cause phase separation in the matrix and leaching [146, 158]. Additional experiments should be undertaken to clarify its effect in the matrix. From these three measurements one can presume the amount of plasticizer has to be minimized for optimum operation of the sensing film since its sensitivity was clearly adequate with the concentration originally used in this work.

3.2.6 Discussion on the composition of the colorimetric film

The deposition of the optimum gas sensitive film on a flexible planar waveguide was targeted for gaseous NH_3 detection. Five main parameters are of prime importance for such an application: the limit of detection, the selectivity, the influence of moisture on the response of the film to NH_3, the kinetics of the reaction, and elasticity of the matrix. Films based on BPB color dye exhibited the highest sensitivity linked to its lower pKa value. The matrices with BCP and BCG as color dyes were therefore rapidly discarded.

Among the films with BPB chemochromic reagent, EC+TBP matrix exhibited the highest sensitivity to NH_3 but a slow kinetics of reaction compared to the other polymers. On the other hand, PMMA with either TBP or DOP as plasticizer offered the best performance for NH_3 trace measurement. A LOD in the low ppb range was reached with a high selectivity and cross-selectivity towards NH_3. Despite its higher sensitivity to humidity, BPB+PMMA+TBP was chosen since it presented the fastest response time and the best linear response to low con-

Table 3.4: Impact of each component of the colorimetric film on the detection of ammonia.

Properties	Material
Sensitivity	BPB > BCG > BCP
	EC > PMMA > PVB
Limit of detection	BPB > BCG > BCP
Selectivity	All similar
Influence of RH	TBP > DOP
Kinetics of the reaction	PMMA > PVB > EC
	TBP > DOP
Elasticity of the matrix	All similar

centrations of NH_3. Table 3.4 summarizes the impact of each components of the colorimetric film on the detection of ammonia.

For an application where the humidity is monitored as well, the influence of moisture can be therefore removed from the NH_3 sensor signal. In the case where there is no need of monitoring the humidity, the possibility of using more hydrophobic matrix components could be also considered but their slow kinetics might be a very significant drawback. Depending on the application, a trade-off will arise between a fast system but consuming more power because of the additional RH sensor and a much slower one which requires less energy to operate.

3.3 Colorimetric gas sensor on plastic foil

3.3.1 Design and fabrication of the colorimetric gas sensor on plastic foil

The optical transducer is based on the combination of SMD photonic devices with a planar optical waveguide as illustrated in figure 3.16. The light coupling between the light source, the waveguide and the light detectors (one reference and one for the measurement) was ensured by light reflection on micro-mirrors formed on the PEN or PET foil directly used as waveguide.

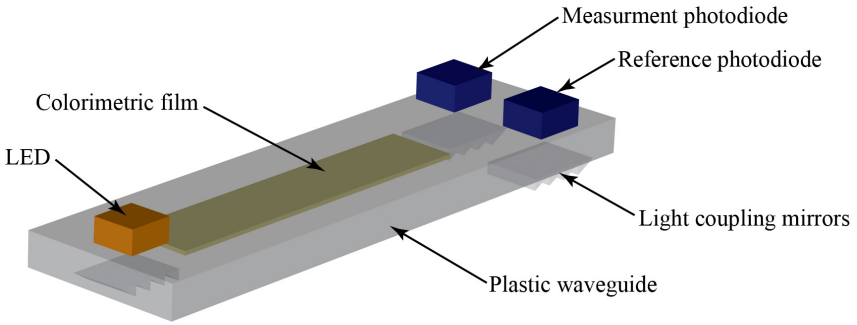

Figure 3.16: Three-dimensional schematic of the colorimetric gas sensor.

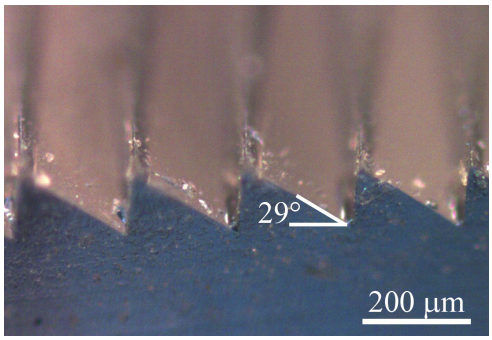

Figure 3.17: Optical picture of the PDMS mold used for the patterning of the UV-curable glue. The angle of the teeth was of about 29°.

Figure 3.17 shows the PDMS mold used for the patterning of the mirrors. It was formed from a Fresnel lens, which led to the desired saw-tooth shape with an angle of about 29°. The perpendicular incident light (i.e. with the highest intensity) will be reflected in the waveguide with an angle of about 32°. In the worst case scenario, the critical angle is of 35° between a PEN foil (n=1.75) and air (n=1). The choice of these mirrors thus ensure a total internal reflection of the light within the optical waveguide. The waveguide was finally coated with the colorimetric film sensitive to ammonia selected in section 3.2.

The optical waveguides were cut out of 125 and 200 µm thick PEN (*Teonex Q65FA* from *DuPont*) or 125 and 250 µm thick PET foils (*Melinex 506* from *DuPont*). Their properties are given in table 3.5. By selecting two different thicknesses, their impact on ammonia detection and optical losses could be addressed. The influence of the length of the waveguide on the light losses and the gas response was investigated as well by designing waveguides with two different lengths, 23 and 46 mm. Due to the nature of the materials involved, their fabrication was based on low temperature processing. For each measurement, two waveguides with the same configuration were fabricated.

Table 3.5: Properties of PEN and PET foils [159].

properties	PEN	PET
Refractive index (-)	1.75	1.58
Young modulus at 20°C (GPa)	5	4
Young modulus at 150°C (GPa)	3	1
Coefficient of thermal expansion (ppm/°C)	18-20	20-25
Glass transition temperature (°C)	120	78
Upper temperature for processing (°C)	180-220	150
Shrinkage in MD at 150°C after 30 min (%)	0.05	0.1
Moisture pickup (20°C, 40%RH) (ppm)	1000	1000
Haze (%)	0.7	0.7

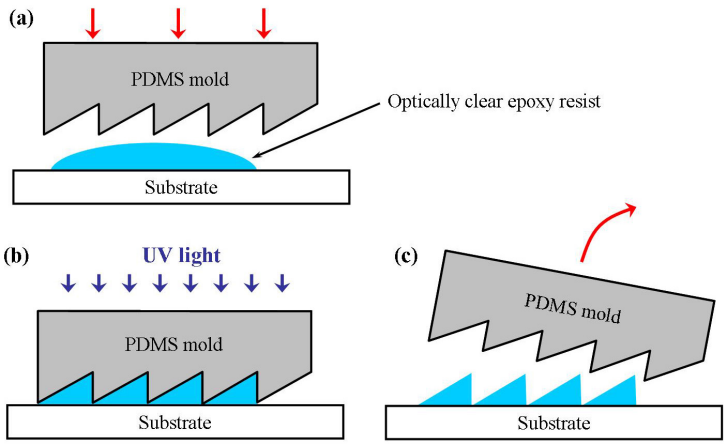

Figure 3.18: Patterning of a UV-curable resist. A droplet of resist was dispensed on the substrate (a) before molding it with a PDMS part (b). The resist was polymerized by UV light before removing the mold (c).

Micro-mirrors were patterned in an UV-curable optically clear epoxy resist (*NOA76* from *Norland Products Inc.*) with the PDMS mold (fig. 3.18). The viscosity of 4500 cP of the glue ensured the complete filling of the available space between the waveguide and the mold. The mirrors covered a wider area than the size of the LED and the photodiodes to avoid alignment issues.

A cross-sectional picture of the micro-mirrors patterned on the waveguides are presented in figure 3.19. Their width and height were respectively of 200 µm and 100 µm. The design was perfectly transferred from the mold to the resist. An opaque aluminum layer, 300 nm thick to ensure a proper step covered edge, could be deposited by e-beam evaporation through a shadow mask on some waveguides to investigate its influence on light reflection on the mirrors and the optical losses.

The chemochromic layer was composed of BPB (bromophenol blue) as sensitive element to NH_3 embedded in polymeric matrix made of PMMA and a hydrophobic plasticizer (tributyl phosphate). The fluid was deposited by inkjet printing. Given the results presented in section 2.5, dimethylformamide was selected as solvent for the dissolution of the polymers due to

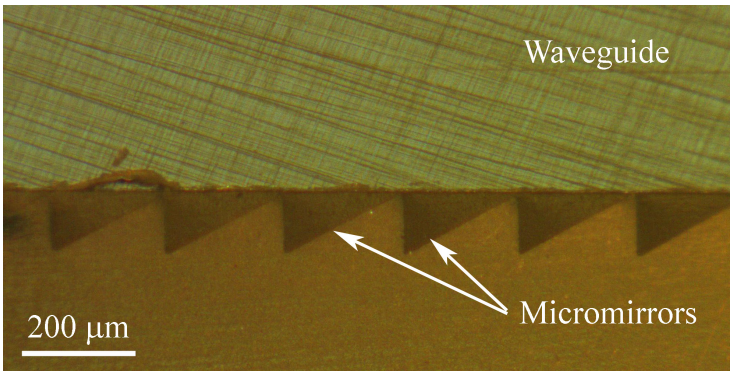

Figure 3.19: Cross-sectional picture of the micro-mirrors patterned on glass slide.

its high boiling point of 155°C and compatibility with the printer.

The colorimetric film covered the area between the LED and the measurement photodiode. To investigate the influence of the film thickness on the sensor's sensitivity to NH_3, between one and ten layers were deposited to reach thicknesses from 20 to 140 nm. Finally, the SMD photonic components, the light source and the detectors, were glued using an *Araldit* epoxy resin. Figure 3.20 shows the technical realization of the waveguide on a PET foil.

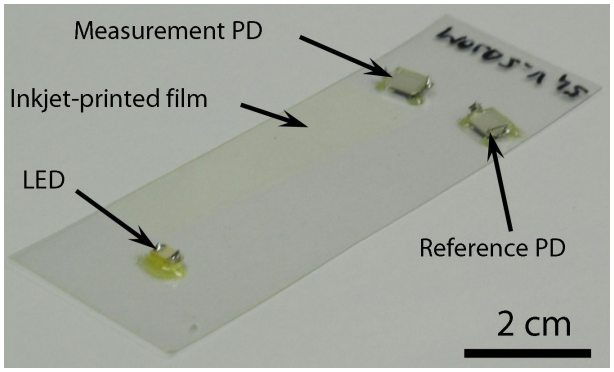

Figure 3.20: Optical picture of the colorimetric ammonia sensor.

3.3.2 Electronic driving and readout circuitry

An electronic driving and readout circuitry designed from ultra-low power components was implemented to operate the sensor. Its schematic is given in figure 3.21. It was based on ultra-low power *MSP430* microcontroller from *Texas Instruments* combined with a yellow LED (*SML-012DTT86AA* from *Rohm*) as light source since the chemochromic film exhibited the highest variation of light absorption at such wavelengths (table 3.1).

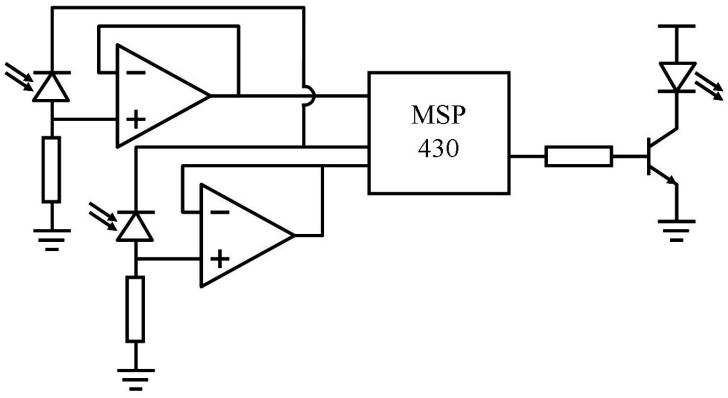

Figure 3.21: Electronic driving and readout circuitry for the colorimetric gas sensor.

The response of the sensor came from the difference of the signal measured by two photodiodes (*BPW34* from *Osram*, $\lambda_{max} = 850$ nm), one reference and one for the gas measurement. They were coupled to two very low power operational amplifiers (*OPA2369* from *Texas Instrument*). A feedback loop allowed keeping the light intensity of the LED constant over time. This

circuitry was used in both constant mode – LED always on – and pulsed mode. In this configuration, the external operational amplifiers were switched off and the microcontroller was set to sleep mode while not computing. In pulsed mode, the LED turned on for 3 and 9 ms every second (duty cycles of 0.3 and 0.9%). These periods showed to be reasonable to regulate the LED.

3.3.3 Experimental

Measurement of the optical losses in the waveguides

First, the light intensity reaching the detector was measured for all the fabricated waveguides to determine the most suitable configuration in term of reduction of the optical losses. The same photonic components than for the electronic circuitry were selected. A full factorial design of experiment – with all the possible waveguide configurations – was designed to evaluated the influence of each parameter on the optical losses [160]. Four measurements (two channels per waveguide) were performed. Once the optical losses were measured, an analysis of variance (ANOVA) with *Matlab* was performed to evaluate the influence of each parameter on the losses. The most significant factor in the waveguide configuration is given by the test statistic value, which is the ratio between the explained and unexplained variances. The higher this value, the more significant is the factor compared to the others.

Evaluation of the sensors through NH_3 gas measurements

The evaluation of the sensors was carried out in three steps with the electronic circuitry operating in continuous mode. First, the influence of the thickness of the inkjet printed gas sensitive film was investigated. One, three, five and ten layers of colorimetric film were deposited on 125 μm thick PEN waveguides.

Once the number of printed layer leading to the highest sensitivity was determined, the parameters of the waveguide on their gas sensing abilities was investigated to achieve the best configuration leading to the highest sensitivity of the sensors towards ammonia. Due to the number of possible combination of waveguide configurations and the time required per gas measurement, a fractional factorial experiment was established [160] to reduce the number of measurements from sixteen to eight (table 3.6). However, only the influence of the main parameters can be evaluated with this method but not their interactions. The gas sensor responses were then analyzed through an analysis of variance to determine the most relevant factor of the waveguide for gas measurement.

Finally, the optimized gas sensor was tested with the electronic circuitry operating in different modes, either continuous mode – with the LED always turned on and continuously regulated – or in pulsed mode. Their power consumptions and noise level were measured and the theoretical limit of detection of NH_3 was evaluated using the 3σ method (equation 1.3).

Table 3.6: Fractional factorial design of experiments to determine the best waveguide configuration for gas sensing applications.

Configuration	Material	Thickness	Length	Coating
1	PET	Thick	Long	Yes
2	PET	Thick	Short	No
3	PET	Thin	Long	No
4	PET	Thin	Short	Yes
5	PEN	Thick	Long	No
6	PEN	Thick	Short	Yes
7	PEN	Thin	Long	Yes
8	PEN	Thin	Short	No

The gas measurements were performed in nitrogen as carrier gas with 50% of relative humidity with a flow of 500 sccm. The sensors were exposed to concentrations of NH_3 ranging from 20 ppm down to 200 ppb, which was the lowest concentration reachable with the gas mixing station at our disposal.

3.4 Results

3.4.1 Optical losses in the waveguides

Figure 3.22 presents the optical losses for all the waveguides investigated. As expected, short and thick waveguides exhibited the lowest attenuation due to a shorter optical path and

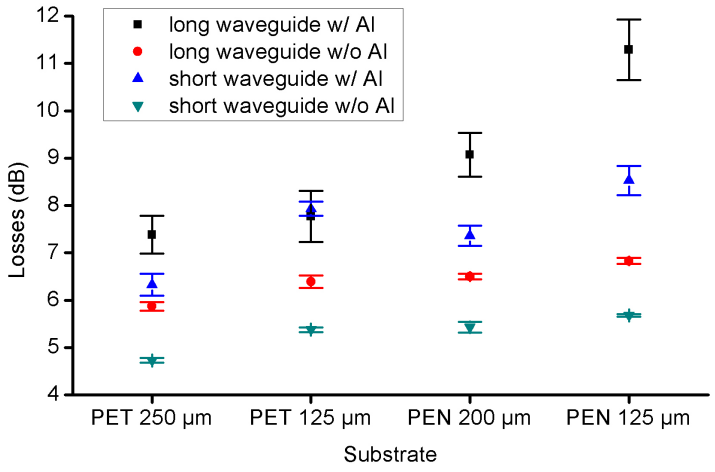

Figure 3.22: Optical losses in the plastic waveguides with a confidence interval of 95%. The lowest optical losses were reached with a short and thick PET waveguide with uncovered mirrors.

less light reflections at the waveguide-air interface. The lowest optical losses were achieved with a PET-based waveguide, which exhibited losses of 4.73 dB.

A summary of the results of the analysis of variance performed on these results are given in table 3.7. The complete table of the ANOVA is given in appendix. It revealed that the coating of the mirror had the highest importance – high significance and highest test statistic value – in terms of optical losses. As confirmed in figure 3.22, it drastically increased the losses, between 1.4 and 4.5 dB depending on the waveguide. Its precise origin is not clear yet, but it might be linked to the light absorption when reflected on a metallic surface. Beside that factor, the length of the waveguide played also a significant role on the optical losses and should be kept in a short configuration to reduce the optical losses. In the case of uncoated mirrors, a lower attenuation of about 1 dB was measured with short waveguides compared to the long configuration. The type of substrate and its thickness had only a smaller impact on the light attenuation. However, the use of PET instead of PEN decreased them by about 0.5 dB. The difference between thick and thin waveguides led to the same variation of about 0.5 dB.

In terms of interactions, some of them exhibited a high significance on the optical losses. However, compared to test statistic values obtained with the individual parameters, their effects are assumed to be negligible on the optical losses.

Table 3.7: Summarized ANOVA table for the optical losses in the waveguide. High significance corresponds to results in a confidence interval of 99%, while significant to an interval 95%. Insignificant means out of these intervals.

Source	Level of effect	Test statistic (F)
Substrate	Highly significant	96.68
Thickness	Highly significant	61.87
Length	Highly significant	115.43
Coating	Highly significant	433.90
Interaction (Substrate, Thickness)	Insignificant	0.76
Interaction (Substrate, Length)	Highly significant	16.13
Interaction (Substrate, Coating)	Highly significant	27.94
Interaction (Thickness, Length)	Significant	0.05
Interaction (Thickness, Coating)	Highly significant	16.13
Interaction (Length, Coating)	Insignificant	1.22

3.4.2 Gas measurements

Impact of the number of inkjet printed layers on the sensor response

The impact of the number of printed layer on the response of the colorimetric film when exposed to 5 ppm of NH_3 is presented in figure 3.23. The precise measurement of their thickness

was difficult to be obtained due to the roughness of the printed film. Given the results presented in section 2.5, they were in the range of 0.02 µm for one layer to 0.14 µm for ten successive depositions.

The thickest film gave the highest sensitivity to NH_3 with a response of 80 mV. The lowest response, 22 mV, was obtained with one printed layer. Therefore, by multiplying by ten the number of layers, the response of the sensors was increased by a factor four. For three and five layers, the responses of the sensors were very close with values respectively of 45 and 48 mV. These very close responses are ascribed to coffee ring effects – as shown in section 2.5 – that drive the solute along the highest peaks of the deposited film by capillary forces, leaving only a very thin layer at the bottom part, where the interaction of light with the chemochromic reagent occurs.

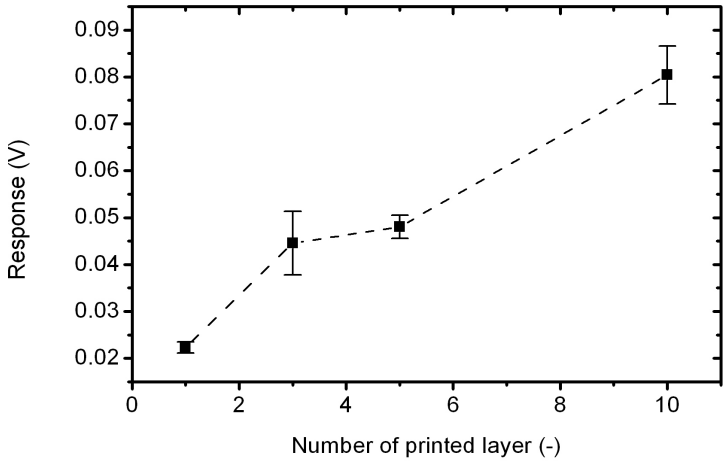

Figure 3.23: Response of the gas sensors to 5 ppm of NH_3 as a function of the number of printed layers of the colorimetric film. Confidence interval: 95%.

Influence of the waveguide configuration

The results of the sensor response according to their configurations defined by a fractional factorial design of experiments are presented in figure 3.24. The sensors were exposed to 5 ppm of NH_3 in synthetic air with a 50% RH background. The highest response, 80 mV, was obtained with a 125 µm thick, short PEN waveguide with uncoated mirrors. All the other response were below 20 mV. In parallel, an ANOVA was carried out on these results with *Matlab* to extract the impact of each parameter of the waveguide on the sensitivity to NH_3. A summary of the ANOVA is given in table 3.8 with the complete table in appendix.

The ANOVA discloses the length of the waveguide had the most important impact on the sensor's response to NH_3, because the highest test statistic value obtained for this factor. It is confirmed by the results displayed in figure 3.24, which clearly shows the shortest devices gave the highest responses. The same results were deduced from the optical losses measurements in section 3.4.1. With a long waveguide, more light is absorbed in the substrate. Moreover, a

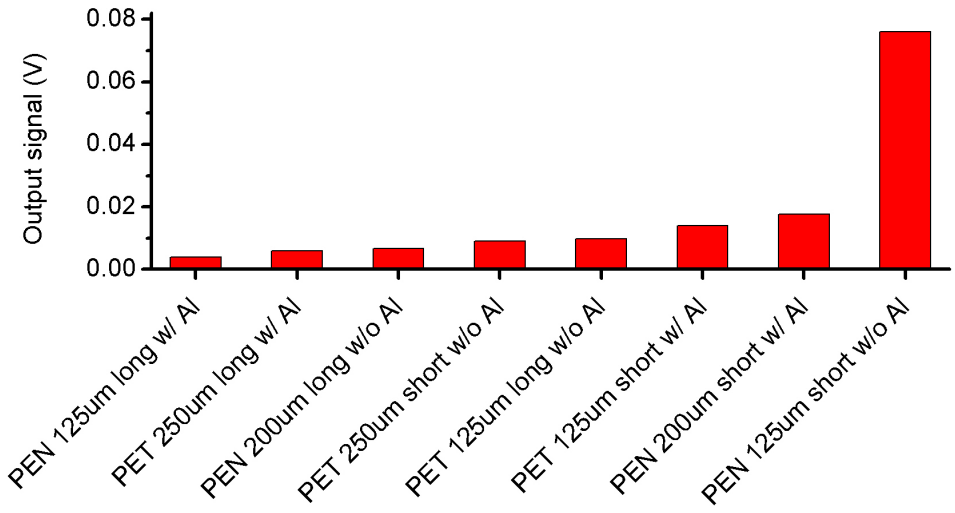

Figure 3.24: Response of the colorimetric sensor in different waveguide configuration when exposed to 5 ppm of NH_3.

longer waveguide implicates more reflection at the waveguide-air and waveguide-sensing film interfaces. It very likely played a role in the light attenuation. The second most significant factor was the substrate's material and showed that PEN should be favored. According to these results, it exhibited a higher optical clarity than PET foils. The two last parameters, the thickness of the waveguide and the presence of a metallic coating on the mirrors, had only a reduced impact on the response to NH_3 compared to the other factors studied. However, for a better sensitivity, the waveguide should be thin with uncoated mirrors.

Consequently, the optimum waveguide for the colorimetric detection of ammonia, should be based on a 125 µm thick, short PEN waveguide with uncoated mirrors and covered with ten layers of sensing film. This configuration was employed for all the next experiments.

Table 3.8: Summarized ANOVA table for the sensor response when exposed to 5 ppm of NH_3 for different waveguide configurations. High significance corresponds to results in a confidence interval of 99%.

Source	Level of effect	Test statistic (F)
Substrate	Highly significant	$19.97 \cdot 10^3$
Thickness	Highly significant	$16.24 \cdot 10^3$
Length	Highly significant	$33.62 \cdot 10^3$
Coating	Highly significant	$16.82 \cdot 10^3$

Gas response of the optimal configuration

Ammonia gas measurements at different concentrations were performed with the optimum transducer. It consisted in a 125 µm thick, short PEN waveguide coated with ten inkjet printed layers of the colorimetric film. The response of the sensor when exposed to concentrations of ammonia ranging from 0.5 to 100 ppm are displayed in figure 3.25. By using a linear regression for concentrations between 0.5 and 2 ppm of NH_3, the coefficient of determination, R^2, was of 0.983. As observed for the film deposited on the glass waveguide (section 3.2.5), a nearly linear behavior occurred at low ammonia concentrations. The sensitivity for NH_3 concentrations of 2 ppm and below was of 12.1 mV/ppm.

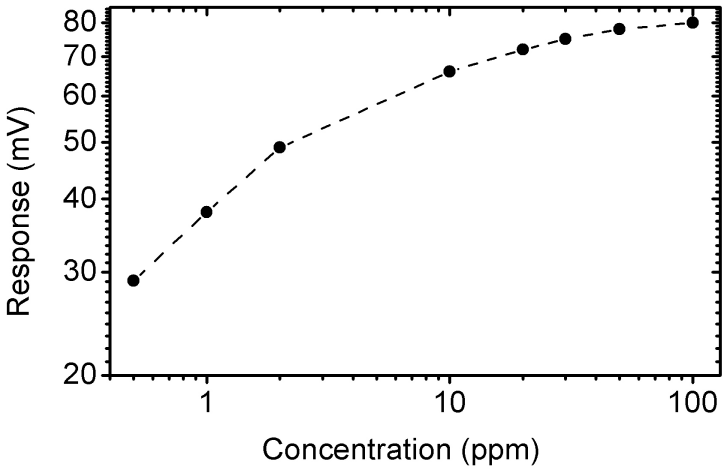

Figure 3.25: Ammonia gas response of the short PEN waveguide coated with ten inkjet printed layers of the colorimetric film.

Response time

A typical response of the colorimetric gas sensor when exposed to NH_3 is presented in figure 3.26. A drawback of such sensors is their low response time at room temperature. However, the kinetics of the chemical reaction was improved by heating up the transducer at 40°C and 60°C during the recovery phase. The recovery times, $t_{90\%}$, was reduced from 43 min at room temperature to 20 and 4 min, respectively.

However, by operating the sensor at higher temperature, one can expect a decrease in sensitivity due to an exponential decay of the partition coefficient with the temperature. The partition coefficient is the ratio of the concentration of an analyte in the gas phase to the concentration in the solid material. The theoretical definition of this coefficient is given in section 5.1.1.

3.4.3 Evaluation of the electronic circuitry

The electronic circuitry was evaluated in terms of power consumption, sensitivity and noise level. The raw signal obtained during the gas measurements for different modes of operation

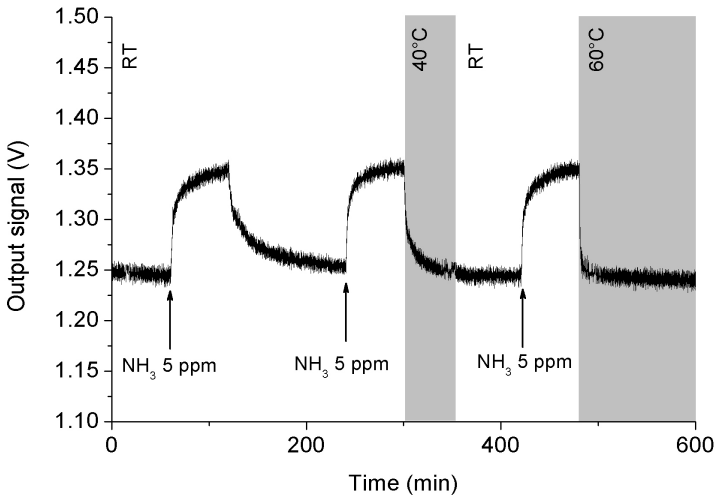

Figure 3.26: Response of a 125 µm thick PEN sensor when expose to 5 ppm of NH_3 in synthetic air with 50% RH and a gas flow of 500 sccm. The desorption rate was increased by heating up the waveguide.

are presented in figure 3.27. The most power consuming device of the circuitry was the yellow LED. Table 3.9 presents the results obtained with the electronic circuitry in different modes of operation. A pulsed mode of 3 ms reduced the power consumption of the system from 8 mW to 868 µW, increased the noise level from 3 to 33 mV and the theoretical limit of detection from 104 ppb to 1.4 ppm. The latter can be reduced by increasing the regulation time of the light source at the cost of a higher power consumption. The best compromise to reach a sub-ppm level of detection was the circuitry operating in pulsed mode with the LED turned on for 9 ms (duty cycle of 0.9%) for a power consumption of 947 µW.

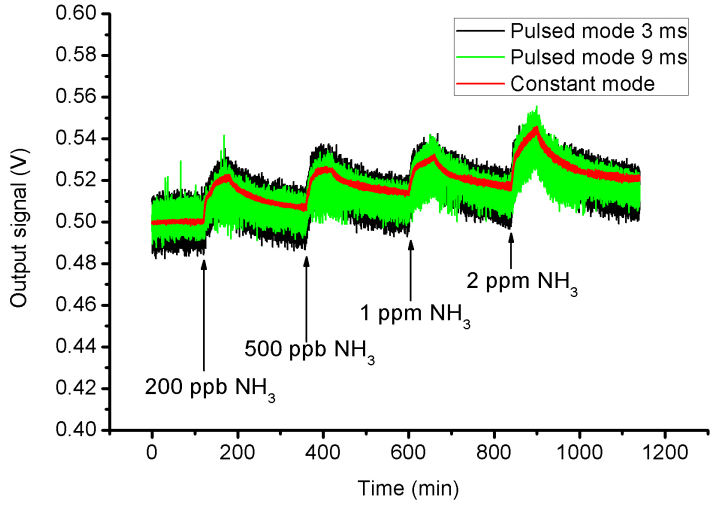

Figure 3.27: Gas response to NH_3 with the electronic circuitry operating in constant and pulsed modes.

Table 3.9: Influence of the operation mode on the sensing abilities of the NH_3 sensor.

Mode of operation	Power cons. (μW)	Noise (mV)	LOD (ppb)
Continuous	7980	3	104
Pulsed 9 ms	947	20	800
Pulsed 3 ms	868	33	1400

3.5 Discussion

3.5.1 Colorimetric ammonia sensor based on plastic foils

The nature of the waveguide – PEN or PET – and its thickness had only a small influence on the optical losses. This was most probably linked to their very close optical properties (table 3.5). For the gas measurements, thick foil-based sensors provided a lower response to ammonia. We suggest that less light reflexions within the waveguide occurred decreasing the light absorption in the evanescent field in the chemochromic film. One can thus foresee that a thinner waveguide might increase the sensitivity until a certain point.

Among the studied factors, the length of the waveguide had a major impact on both the optical losses and the response to NH_3. A long waveguide has very likely a stronger attenuation on the propagating light, reducing thus the sensor response, whereas a very short waveguide will drastically reduce the optical losses. The last factor evaluated was the coating of the mirrors with an aluminum layer. The results obtained with the optical losses measurements revealed its strong influence on the light intensity reaching the detector. A higher signal was measured with uncoated mirrors. It was certainly related to light absorption in the metal, while total internal reflection might occur in the case of uncoated mirrors. To summarize, the optimum waveguide designed here was made of a 23 mm long and 125 μm thick PEN foil with uncovered mirrors.

The waveguide was coated by inkjet printing of the colorimetric film sensitive to NH_3. The impact of the number of printed layers showed the highest response occurred with ten of them, leading to a thickness of about 0.14 μm. We suggest this is due to a better interaction between the evanescent wave than for thinner printed layer, increasing the sensitivity of the sensor. The sensors exhibited a linear response for NH_3 concentrations of 2 ppm or below with a sensitivity of 12.1 mV/ppm. Sub-ppm concentrations of ammonia were measured with a theoretical LOD of about 100 ppb. The latter was higher in this configuration than with the system based on a glass waveguide. A combination of several factors caused this difference. The glass waveguide had a better optical transparency than the plastic foil and a more efficient light coupling.

A main drawback of such sensor is their slow kinetics of reaction. The recovery time was decreased by heating the waveguide during the desorption phase of the gas measurements. However, by constantly heating the device, its sensitivity would be reduced since the partition coef-

ficient strongly decreases with an increase in temperature. It could be envisaged to operate it in pulsed mode to maintain a certain sensitivity and at the same time it could minimize the effect of heating on the power consumption.

3.5.2 Driving and readout circuitry

The electronic circuitry implemented for this sensor could operate in both constant and pulsed mode. The latter allowed saving power, mainly by pulsing the LED that was the most power consuming device of the whole system. The power required by the light source could be reduce by selecting a model of LED with a very high brightness and operate it with a current in the low milliampere range. When pulsing, the microcontroller was in sleep mode most of the time and the external electronic components were turned off. It led to a sub-milliwatt power consumption while keeping the theoretical limit of detection below 1 ppm.

Using a longer period between two successive measurement than 1 s as it was the case here, combined with a longer regulation time of the LED, could lead to a further decrease in power consumption. The LOD could be lowered as well in a pulsed mode by lengthening its regulation time. These improvements could be achieved at the cost of a lower acquisition rate. However, we can expect than for most applications, and more especially in logistics, longer period of time – in the minute or tens of minutes intervals – between two measurements could easily be envisaged.

3.6 Conclusion

An all polymeric optical transducer was implemented for the chemical detection of ammonia. It was based on commercial plastic foils, PEN and PET, directly used as waveguides to simplify the fabrication, which was based only on additive and low-temperature processes. Combined with a planar configuration, it makes it potentially compatible with roll-to-roll processing. The optical transducer was associated with SMD elements as light source and detectors. Light coupling mirrors were patterned in a UV-curable polymer deposited by dispensing and the foil was coated with the colorimetric film by inkjet printing. The sensor was combined with a low-power driving and readout electronics. The system exhibited a power consumption of 947 μW in a pulsed mode of operation for a limit of detection of NH_3 of 800 ppb.

For the detection of ammonia, ten colorimetric films composed of bromophenol blue, bromocresol green or bromocresol purple as color dye, in a matrix made of a polymer – poly(vinyl butyral), ethyl cellulose or poly(methyl methacrylate) – and a plasticizer – tributyl phosphate or dioctyl phthalate – were initially evaluated, first with a spectrometer and then when deposited on a waveguide. During all experiments, BPB color dye based films exhibited the highest sensitivity to NH_3. PMMA was chosen as the polymeric matrix because it offered a good trade-off between response time and sensitivity compared to EC and PVB. Despite its higher influence towards RH, the use of TBP as plasticizer was deeper investigated due to its faster response time.

The BPB+PMMA+TBP film provided thus the best performances among all compositions of the films investigated. The film exhibited a very good selectivity towards ammonia, however additional measurements are required with amine-based gases.

The selected chemochromic film was inkjet printed on polymeric optical waveguides with different configurations. The highest response was obtained with a 23 mm long and 125 µm thick PEN foil. It however showed a relatively long response time at room temperature. Increasing the temperature of a few degrees could be a way of enhancing the kinetics of the chemical reaction for a certainly reduced sensitivity.

Such a detection technique foresees a high potential for the detection of other gases by changing the colorimetric reagent, which further widen the application field of such a system. The combination with hot embossing of the mirrors and the deposition by printing of OLED and PPD would make the sensing device all polymeric and compatible with printed electronics processes.

Chapter 4

Metal-oxide gas sensor on polyimide foil

4.1 Introduction

This chapter deals with the development of drop-coated metal-oxide gas sensors on plastic foil with an ultra-low power consumption. The impact of their extreme miniaturization when fabricated with a polymeric substrate on their sensing performances was investigated. The devices were produced on a polyimide foil to benefit from its low thermal conductivity to reduce the power consumption with a simplified processing. By using such a substrate, the design and the fabrication of the transducer as well as the coating procedure of the gas sensitive material had to be reviewed. The devices were first simulated to optimize their power consumption and temperature uniformity over the active area. After their fabrication, packaging at the foil level was addressed as well. The devices were evaluated in terms of electrical and thermal properties, robustness and gas sensing abilities.

4.1.1 Operating principle of metal-oxide gas sensors

The operation of a metal-oxide gas sensor relies on the change in resistance of a n or p-type semiconducting layer – mainly SnO_2 – when exposed to reducing or oxidizing gases [161]. Other metal-oxides are used for their gas sensing abilities such as WO_3, TiO_2, ZnO or In_2O_3 [45, 162–164]. A schematic typical cross-sectional view of a silicon micromachined MOX sensor is presented in figure 4.1. Their development has evolved towards this substrate to produce devices suitable for commercialization due to their low-cost, low-power consumption and high reliability, which are of prime importance for portable instruments or in the automotive industry.

The gas sensitive layer is deposited on top of electrodes for its electrical resistance measurement. It exhibits a high resistance at room temperature, in the megohm to gigohm range. To lower it as well as to improve the kinetics of the chemical reaction with the gas species and reduce the influence of humidity [161], the metal-oxide layer is heated up to temperature between 150 and 600°C [71] with a micro-heater. The heated area is usually embedded in a thin dielectric membrane to improve the thermal insulation and reduce the power consumption of the device, which is typically of a few tens of milliwatts.

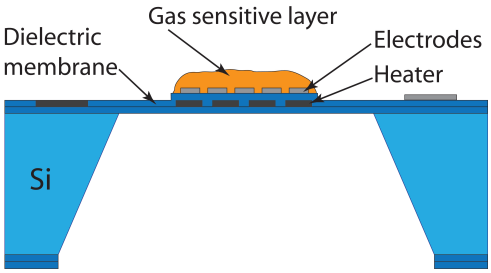

Figure 4.1: Cross-sectional schematic of a micromachined metal-oxide gas sensor [165].

Figure 4.2 illustrates the very basic principle of the chemical reaction of oxidizing and reducing gases at the surface of an SnO_2 layer with oxygen and carbon monoxide, respectively. Tin oxide is an n-type semi-conductor as a result of oxygen vacancies within the lattice of the oxide. Under the exposure of reducing gases (CO, H_2, CH_4, NH_3,...) a decrease in resistivity occurs. This is due to electrons linked to the oxygen species (O^-, O_2^-) and hydroxyl group (OH^-) adsorbed at the surface of the grains [71, 161, 166] that are released back in the conduction band of the semiconductor, while the gas is oxidized at the material surface. On the other hand, when the layer is exposed to an oxidizing gas (O_2, NO_2,...), the MOX resistance increases. This is due to adsorption of electrons from the conduction band by the gas. The kinetics of the chemical reaction and the selectivity towards more specific gaseous species can be enhanced by doping the gas sensitive layer [44, 167]. Noble metals such as Pd, Pt or Au are usually used [161, 168].

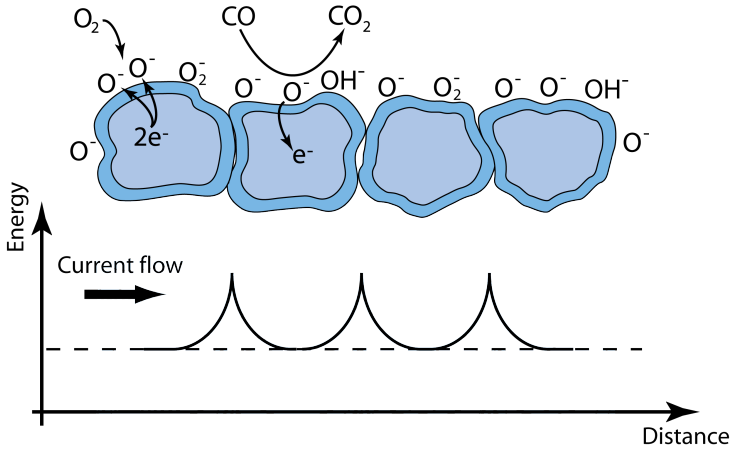

Figure 4.2: Schematic representation of an oxidizing (O_2) and a reducing (CO) chemical reactions that occur at the surface of an SnO_2 porous layer [71]. The thickness of the depleted layer – and the resistance of the film – depends on the gaseous atmosphere.

4.1.2 State of the art

Design and fabrication

Metal-oxide gas sensors were first developed in the 1960s by Seiyama [169]. It consisted of zinc oxide particles squeezed between two plates used as electrodes. When heating the

system at 400°C, changes in the electrical conduction of the metal-oxide particles occurred when exposed to different gaseous atmospheres. It led to the first commercialization of these sensors by *Figaro Engineering Inc.* in 1967. They were fabricated on ceramic substrates and are still on the market. They have a wide selection of sensing materials for different gases [170]. Since then, numerous studies have been published on their mode of operation [166, 171, 172] and to improve their selectivity [173] and stability [174]. More recently, a trend in metal-oxide gas sensor is the use of nanowires, such as SnO_2, In_2O_3 or ZnO to improve the sensor's sensitivity and response time [175–178] or to reduce its operating temperature [179, 180]. The deposition of the sensing material combined with its functionalization directly on the transducer has also been performed [181, 182].

In the 1990s, the progress in microfabrication technologies allowed the development of miniaturized gas sensors for low-cost and low-power applications [165, 183, 184]. The first silicon micromachined thin film metal-oxide gas sensor was developed at *CSEM*, Switzerland and commercialized at the end of the 1980s by *Microsens SA*, Switzerland. Since then, two other companies have entered the fray, *Microchemical Systems (MiCS)*, Switzerland [185], producing thin-film MOX sensors, and *AppliedSensor GmbH*, Germany [186], based on the results of the European project CIA on thick-film MOX gas sensors [165]. These devices were based on a silicon frame, which supported a dielectric membrane made of SiO_2 and/or Si_3N_4. It thermally insulated the heated area and reduced thus the power consumption of the devices when operating at a typical temperature of 300°C [165, 184]. More recently, the first proof of concept of a gas sensor based on a micro-hotplate on plastic foil was demonstrated [70]. However, its power consumption too high to be compatible with low power devices such as wireless systems.

To enhance the chemical reaction between the gaseous environment and the sensing layer, heat is required. It can be provided by Joule effect through MOSFET [187–190] or polysilicon resistor [184, 191, 192] for devices based on CMOS processing. To reduce the drift occurring with polysilicon heaters, Pt [193] or tungsten [194] have been preferred. Different heater layout have been published, mainly meander [184] or spiral [165, 195] shapes. This second option exhibits a better spatial temperature uniformity [191, 196]. Regarding to the electrodes, platinum is also favored since it shows a very good chemical stability and can provide a higher gas response [71].

Two types of metal-oxide films are found for the gas sensitive layer, thin or thick films. The former is usually deposited by evaporation [162] or sputtering [162], while the latter, among other, is deposited by screen printing [197–202], spray pyrolysis [203–205] or drop-coating [165, 206]. Once deposited, these materials usually require an annealing at high temperatures (350 to 800°C) in an atmosphere with oxygen to modify the morphology (e.g. grain size) and microstructure (e.g. porosity, surface-to-volume ratio) [45, 163]. Thick films are favored since they exhibit a higher gas response due to a higher porosity of the layer as well as a higher stability [71, 165]. It led to the only viable device made of thick films in the case of gas sensors [186].

Packaging of the sensors is often necessary to prevent direct exposure of the metal-oxide

layer to the environment. However, encapsulation is often a cost issue [207]. It is usually performed using a metallic cap glued over the top of the sensing area [208, 209] to reduce the influence of the gas flow on the temperature of the sensor, which could lead to false measurements [209]. Methods at the chip scale have been shown, for example anodic bonding of a glass structure to protect the active area of the sensors [210] or the flip-chip assembly of a ceramic frame [211]. To reduce the price of the system and enable new production flows at the wafer level, Raible et al. [212] developed a technique of wafer level packaging (WLP) combining glass rims around the active area of the gas sensor with a gas permeable membrane glued on top.

Thermal simulations of micro-hotplates

Micro-heating devices have found interest in many applications such as gas sensors [44, 165, 210, 213–215], infrared sources [216–218] and flow/wind sensors [219–221]. Their thermal modeling has been performed for years [187, 194, 222–227].

A precise model to evaluate the power consumption and temperature uniformity over the heated area requires many empirical parameters to be measured, such as the thermal losses in the air. The thermal and electrical conductivity of the materials as a function of the temperature should also be identified. They are also often taken from previous work [187, 225], which may lead to erroneous results since the experimental conditions are rarely the same. As it will be demonstrated, this is especially the case when drastically decreasing the size of the heated area.

Metal-oxide gas sensor operation modes

Metal-oxide gas sensors can be operated in two modes: constant temperature (i.e. isothermal) or thermally-cycled temperature mode. In constant temperature mode, the selectivity can be enhanced by using an array of sensors covered with different materials or dopants [162, 228, 229] or operating at different temperatures [230, 231]. However, the use of several sensors drastically increases the complexity and the power consumption of the system. Additionally, a drawback with constant temperature operation is that a mixture of oxidizing and reducing gases can offset each other and no signal variation will be observed [71].

With the micromachining of the devices, their thermal response times were drastically reduced – in the millisecond range – and allowed their operation in a pulsed or cycled temperature mode to discriminate several gases with one single sensor. This measurement technique was first introduced by Sears [172, 232] and Nakata [233]. Each gas can be identified by a specific temporal response pattern, which depends on its chemical reaction with the gas sensitive material [172, 234]. The sensitivity can be further improved by taking advantage of the unsteady state of the number of oxygen species at the surface of the metal-oxide when its temperature is changing [235]. The transient response of thermally-cycled MOX sensors has also shown to decrease the sensor's response to humidity and the drift in the resistance of the gas sensitive layer [236]. Several options of temperature variations have been presented in the literature to

improve selectivity [234]. To attain the same objective, the influence of different waveforms at different frequencies have been applied to the heater of the gas sensor to thermally cycle its temperature [172, 232, 233, 237–242]. The sensor response can be then analyzed by signal processing, through FFT analysis [243] or an artificial neural network [236] for instance. However, they require complex and power consuming circuitries to generate and process the output signal of the devices, which might be a serious drawback for devices targeting applications in wireless systems. Pulsed temperature mode – heater only on and off – has also been presented [196, 244] and rely on a much simpler electronic driving circuit.

4.1.3 Progress beyond the state of the art

The devices presented in this chapter were fabricated on polyimide foil to make them compatible with an integration on an RFID tag. The vision here is to ultimately produce the sensor directly on the label to avoid any assembly. To this end, the size reduction of the drop-coated gas sensor to decrease their power consumption was studied. Fabrication on plastic foil is beneficial due to its low thermal conductivity compared to the silicon oxide or nitride membranes employed with Si-based devices. It can thus lead to a simplified fabrication process by avoiding bulk micromachining and high temperature process steps.

The impact of miniaturization and the use of plastic foil on the high temperature operation of the MOX gas sensor and gas sensing performances were investigated. To achieve these goals, the power consumption and the temperature uniformity of the transducers were first optimized using electrothermal finite element modeling. After the fabrication of the transducers, the thick film gas sensing material was deposited by drop-coating, which had to be adapted due to the reduced size of the sensor's active area. To protect the sensing layer from the environment, a foil level, polymer-compatible encapsulation method was developed.

We have shown the proper operation of these sensors with representative oxidizing and reducing gases. They exhibited responses comparable to silicon-based devices. The sensors were operated in both constant and pulsed temperature modes. By making use of a very small duty cycle, their power consumption was drastically decreased.

4.2 Experimental

The design of the metal-oxide gas sensors will first be introduced, followed by electrothermal simulations. Next, the fabrication of the transducers, the MOX layer coating and foil level packaging will be presented. Finally, the experimental characterization parameters will be provided.

4.2.1 Design of metal-oxide gas sensors on polyimide foil

The cross-sectional and top schematic views of the MOX gas sensors are illustrated in figure 4.3. They were made on a 50 µm thick polyimide foil, on which laid a double spiral heater with a square shape. It consisted in a 150 nm thick Pt-based layer lying on the PI foil. Five widths for the active areas were investigated for this study: 100 µm, 50 µm, 25 µm, 15 µm and 10 µm, the smallest size achievable with standard fabrication techniques. Their layout are presented in figure 4.4. The temperature uniformity of the heated area was improved by tuning the width of the conductive pathways of the Pt heater and the gap between them: the narrower the conductor, more heat is produced by Joule effect at a given current. By varying their widths along the electrical line of the heater, the higher thermal losses on the periphery of the heated area can be compensated.

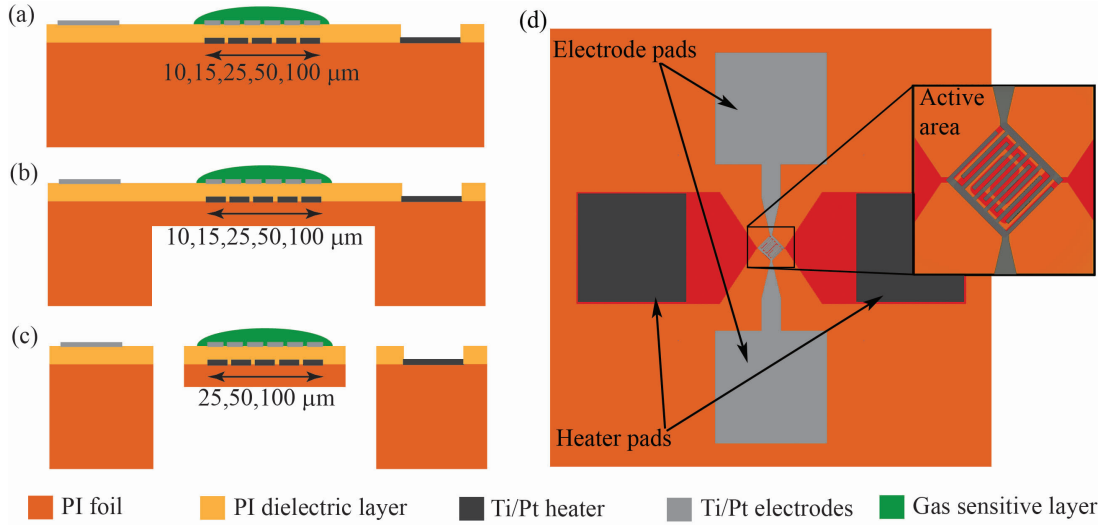

Figure 4.3: Schematic view of the metal-oxide gas sensor made of polyimide. Cross-sectional view of the (a) bulk, (b) closed membrane, (c) opened membrane structures. (d) Top view of the device without the gas sensitive layer.

To investigate the influence of a thinner membrane on the power consumption, three designs were evaluated referred to as bulk (fig. 4.3a), closed membrane (fig. 4.3b) and opened membrane (fig. 4.3c). Closed membranes were devices similar to the bulk hotplates but where the polyimide sheet was locally made thinner to 3 µm to thermally insulate the heated area to reduce the losses (section 4.2.2). The last design, opened membranes, was a membrane with openings to further insulate the heater. No devices with an active area of 10 and 15 µm in width were fabricated with opened membranes, due to the width of the heater and electrode interconnects, and because of the dimensions needed for the etching process.

The interdigitated electrodes used to measure the resistance of the gas sensing layer were patterned on top of the heater with a thin PI dielectric layer in between. They were of square shape covering the same area than the heater underneath. Their layouts depend on the properties of the gas sensitive material deposited on top. Their geometrical properties are given in table 4.1.

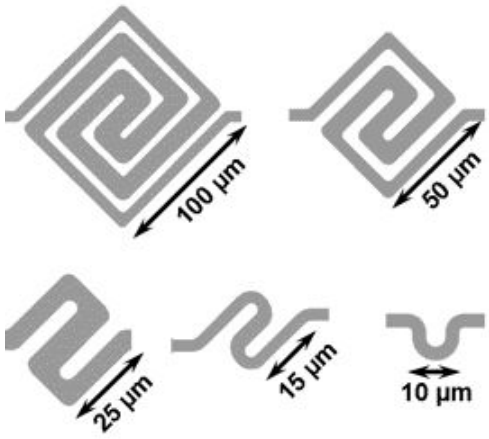

Figure 4.4: Layouts of the five investigated Pt heaters.

The gap width refers to the distance between two fingers of the interdigitated structure. The W/L value expresses the ratio of the path length between the fingers to the gap between them. That value decreased with the size of the active area due to processing limitations. Therefore, a decrease of the sensor response to the gases is expected while decreasing the size of the active area. The electrodes were covered with a thick film of SnO_2:3%Pd as sensing material.

A list of design parameters for the MOX sensors is summarized in table 4.2. The justification of the thicknesses of the membrane, its diameter and the PI dielectric layer will be given in section 4.2.2.

Table 4.1: Geometrical dimensions of the electrodes.

Electrode width (µm)	Gap width (µm)	Finger width (µm)	W/L (-)
10	3	-	3.3
15	3	3.0	6.3
25	3	3.0	10
50	4	3.5	47
100	5	4.5	164

4.2.2 Electrothermal finite element simulations of micro-hotplates

This section presents the electrothermal simulations of micro-hotplates (i.e. without the gas sensitive layer) made of polyimide. First, the design and the layout of the transducers are introduced before explaining the optimization methodology. The simulation parameters and boundary conditions are given before presenting the results. The comparison between the simulations and the experimental measurements are discussed in section 4.4.1.

Table 4.2: Summary of the design parameters of the MOX gas sensors on polyimide foil.

Element	Parameters
PI foil thickness	50 µm
Configuration	bulk, closed membrane, opened membrane
Membrane thickness	3 µm
Membrane diameter	200 µm
PI dielectric layer thickness	700 nm
Heater size	10, 15, 25, 50, 100 µm
Electrode width	10, 15, 25, 50, 100 µm

Thermal modeling of a micro-hotplate device

Figure 4.5 illustrates the heat losses that occurs in a micro-hotplate when operating. The thermal energy, Q, generated by Joule effect in the micro-heater is given by:

$$\Delta Q = R \cdot I^2 \cdot \Delta t \tag{4.1}$$

where I is the current flowing through the heater with a resistance R during Δt time. This heat is dissipated in the device and in the surrounding environment. They are of three types [245]:

- Conduction in the device;
- Convection in the surrounding media (typically air);
- Radiation.

Thus, the heat generated by the micro-heater is equal to the sum of the heat lost by conduction in the device, Q_{PI}, by convection in the air, Q_{conv}, and by radiation, Q_{rad}.

$$R \cdot I^2 \cdot \Delta t = \Delta Q_{PI} + \Delta Q_{conv} + \Delta Q_{rad} \tag{4.2}$$

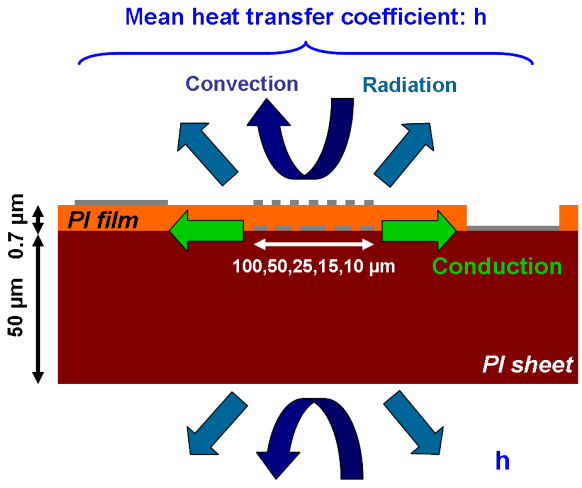

Figure 4.5: Heat losses in a micro-heating device. They are of three types: conduction, convection and radiation.

The power can be deduced from equation (4.2) by dividing it by the heating time:

$$R \cdot I^2 = \frac{\Delta Q_{PI}}{\Delta t} + \frac{\Delta Q_{conv}}{\Delta t} + \frac{\Delta Q_{rad}}{\Delta t} \tag{4.3}$$

where the power lost by conduction is given by:

$$\frac{\Delta Q_{PI}}{\Delta t} = \lambda_{PI} \cdot S_{PI} \cdot \frac{\Delta T}{\Delta x} \tag{4.4}$$

where λ_{PI} is the thermal conductivity in the polyimide substrate, S_{PI} the cross-sectional area of the surface of conduction of the substrate and $\Delta T/\Delta x$ the temperature gradient. To reduce these losses, the thermally conductive substrate should be as thin as possible, e.g. by integrating a membrane.

Second, the power lost by convection in the air is given by:

$$\frac{\Delta Q_{conv}}{\Delta t} = h_{conv} \cdot S_{conv} \cdot \Delta T \tag{4.5}$$

where h_{conv} is the mean heat transfer coefficient by convection, S_{conv} the area of the convection and ΔT the temperature difference between the heat source and the surrounding environment.

Third, the power lost by radiation is defined as:

$$\frac{\Delta Q_{rad}}{\Delta t} = \varepsilon \cdot \sigma \cdot S_{rad} \cdot \Delta T^4 \tag{4.6}$$

where ε is the emissivity of the material, σ the Stefan-Boltzmann constant, which is equal to $5.67 \times 10^{-8}\ Wm^{-2}K^{-4}$ and S_{rad} the surface of radiation. Therefore, the total power lost can be obtained by inserting equations (4.4) to (4.6) in equation (4.3):

$$R \cdot I^2 \cdot = \lambda_{PI} \cdot S_{PI} \cdot \frac{\Delta T}{\Delta x} + h_{conv} \cdot S_{conv} \cdot \Delta T + \varepsilon \cdot \sigma \cdot S_{rad} \cdot \Delta T^4 \tag{4.7}$$

The losses by radiation can by considered as negligible at the temperature range of interest for micro-hotplates [194, 215, 226, 246] and due to the very low emissivity of the materials involved [247]. Equation (4.7) can be further simplified by separating the power lost in the membrane (thermal conduction) and by combining the thermal losses in the surrounding media:

$$R \cdot I^2 = \lambda_{PI} \cdot S_{PI} \cdot \frac{\Delta T}{\Delta x} + h \cdot S \cdot \Delta T \tag{4.8}$$

where h is the mean heat transfer coefficient in the air and S the heated area of the device. Hence, one can conclude that the heat losses – and the power consumption of the device – can be best reduced by minimizing the heated area, choosing a material with a low thermal conductivity and by operating the device at low temperature to decrease the thermal gradient between the hot spot and the surrounding environment.

Methodology used for the electrothermal simulations

First, the mean heat transfer coefficients in air were extracted by fitting the power consumptions obtained from experimental measurements on a previous series of fabricated bulk heating structures when operating at 300°C. No hotplate with a membrane was processed at that time. These coefficients were an average value between the losses at the top and bottom sides of the hotplate.

The extracted mean heat transfer coefficients were applied to the design of new optimized micro-heater structures and their validity analyzed at the same time. A new series of hotplates – not only bulk, but also with a thin membrane – was subsequently optimized using the FE model to reduce their power consumption and improve the temperature uniformity over the heated area.

From the simulations, the influence of the thickness of the membrane and its diameter on the power consumption at 300°C was determined as well as the impact of the PI dielectric layer thickness in the case of the widest device. The effect of the layout of the electrical interconnections to the heater on the power consumption was evaluated on bulk devices and those with closed membranes. The temperature variation over the heated area and the temperature gradient between the buried heater and the surface of the device was also investigated. The temperature decrease through the bulk was carried out as well. A summary of the devices used for the performed simulations is given in table 4.3.

Table 4.3: Summary of the simulations performed on the PI micro-hotplates.

Factor investigated	Type of hotplate (HP) selected
Lowest power consumption	All HP
Membrane dimensions	100 μm wide HP with a closed membrane
PI dielectric layer thickness	100 μm wide HP with a closed membrane
Electrical connectors	Bulk HP and HP with a closed membrane
Temperature profiles	All HP

Simulation parameters and boundary conditions

The electrothermal simulations were performed using the *CoventorWare* software. A parabolic tetrahedron mesh with a maximum distance of 2 μm between the nodes was selected for the heater as shown in figure 4.6. The mesh was made coarser when moving away from the center of the device (where a high accuracy was not required) to save computation time.

The PI foil was 50 μm thick defined by the commercial substrate (*Upilex-50S* from *UBE Industries, Ltd.*) used for their fabrication. Its thermal conductivity was taken from the manufacturer's material datasheet and was set to 0.29 W/m·K. That of the PI dielectric layer (*PI-2737* from *HD Microsystems*) – 0.35 W/m·K – was experimentally determined in a previous

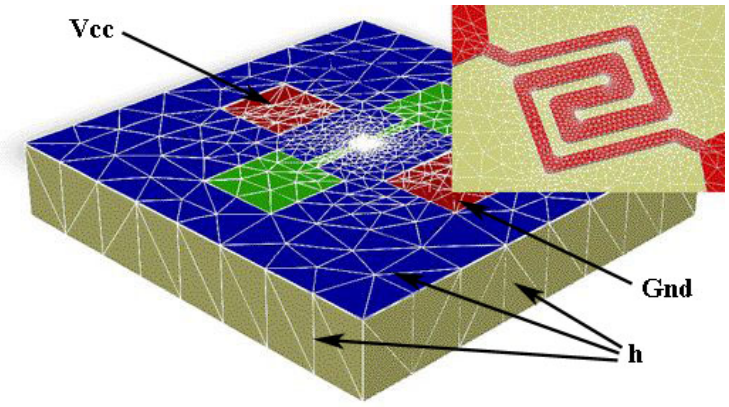

Figure 4.6: 3D structure of a 3×3 mm^2 chip with a 50 µm wide micro-hotplate meshed in *CoventorWare* simulation software (Z-scale×10). The supply voltage and the ground were applied to the connection pads of the heater and the mean heat transfer coefficient to all external surfaces of the device. Insert: mesh of the heater embedded in the device.

study by fitting experimental results to FE simulations to obtain a model as close as possible to the experimental measurements [50]. It was investigated for thicknesses from 5 µm down to 700 nm, respectively the thickest and the thinnest layers achievable with the material used for the fabrication of the devices (section 4.2.3). The thermal conductivity of Pt was taken as 70.6 W/m·K [248]. The resistance of the Pt layer was set as a function of the temperature. Its sheet resistance and its thermal coefficient of resistance (TCR) were experimentally determined to be of 1.3 Ω/□ at 20°C and 0.0017°C^{-1}, respectively.

The membrane thickness (i.e. the thickness of the thinned PI foil without the PI dielectric layer) was simulated for values ranging from 20 down to 3 µm, which was the thinnest reasonable thickness that could be processed in a repeatable manner. Moreover, the contribution of the membrane diameter on the thermal losses was investigated as well for values between 100 to 600 µm. The thickness and the diameter of the membrane were evaluated for 100 µm wide micro-hotplates with a closed membrane, since it will exhibit the highest influence of these geometrical factors. It had the widest heating area and it consequently needed the membrane with the largest diameter. This diameter was chosen for all the devices to ensure a good control on the uniformity of the membrane thickness all over the wafer (section 4.2.3).

The ambient temperature was set to 20°C. Figure 4.7 gives the mean heat transfer coefficients at 300°C, which were applied to all external surfaces of the device, independently of the temperature reached. As in [194, 215, 226, 246], no specific thermal losses by radiation were used as a parameter for the simulations considering the relatively low temperature of operation defined here (maximum of 300°C). They were however inherently embedded in the mean heat transfer coefficient in the air that was experimentally extracted and encompassed all the thermal losses in the surrounding media of the device. The supply voltage was applied to one contact pad of the heater to reach 300±0.5°C while the second one was grounded.

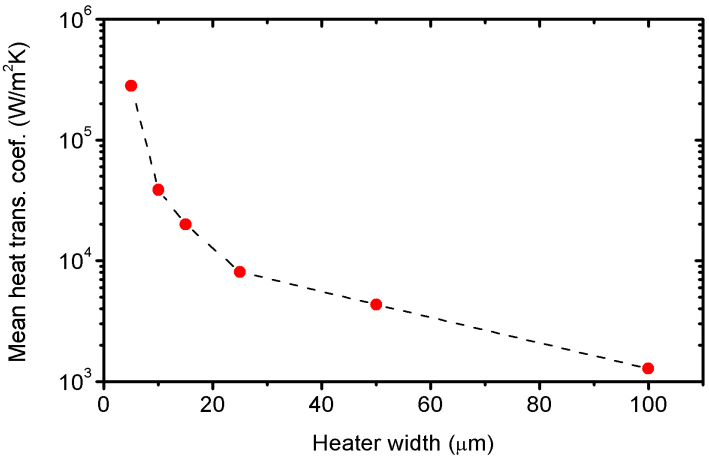

Figure 4.7: Mean heat transfer coefficients in air extracted from bulk polyimide-based micro-hotplates at 300°C.

Results of the electrothermal FEM simulations

The results of the finite element analysis will be first given for the optimum layouts obtained from the thermal simulations. Then, a more detailed analysis focused on several parameters that have an influence on the thermal behavior of the PI hotplates will be addressed. The impact of the membrane dimensions, the PI dielectric layer thickness as well as the geometry of the electrical connections to the heater will be discussed. Finally, the temperature profiles in the X-Y planes and in the Z direction through the substrate will be presented.

Properties of the optimum designs

Figure 4.8 presents a typical spatial temperature distribution obtained with the *CoventorWare* simulation software. The simulated power consumptions at 300°C of the different hotplates after minimization of their heat losses are given in table 4.4. As expected, the power consumption of the PI hotplates decreased significantly with their size and was further reduced with the incorporation of a membrane. However, a similar power consumption was found for the 15 and 10 μm wide layouts, which was due to higher thermal losses in the electrical pathways to the heater.

Table 4.4: Simulated power consumptions of the micro-hotplates when operating at 300°C.

	Power consumption (mW)				
Micro-hotplate type	100 μm	50 μm	25 μm	15 μm	10 μm
Bulk	26.9	19.0	14.0	10.2	10.2
Closed membrane	17.0	15.4	12.4	8.3	9.9
Opened membrane	12.6	14.7	12.5	-	-

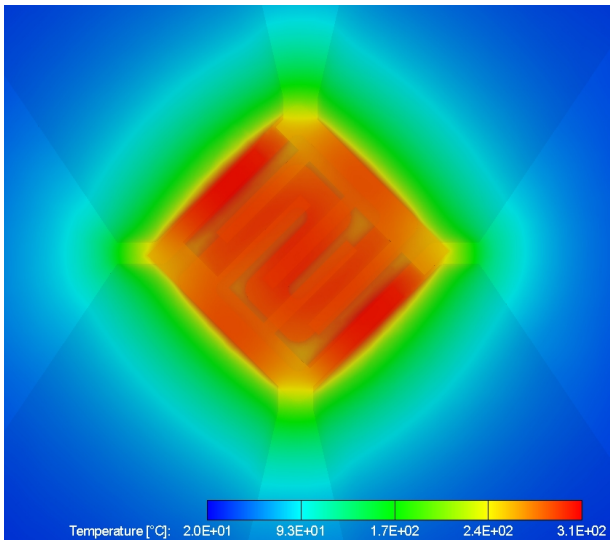

Figure 4.8: Electrothermal simulation at 300°C of a 50 µm wide hotplate with a closed membrane using *CoventorWare* software. The electrodes and dielectric film are made translucent to make the buried heater visible.

The total thickness of the membrane (thinned PI foil and PI dielectric layer) should be as thin as possible. A minimum value here of 3 µm for the PI foil resulted from the fabrication process. The thickness of the PI dielectric layer between the heater and the electrodes corresponded to 700 nm, the minimum achievable. To ensure a good thermal insulation of the heated area, a factor two between the diameter of the membrane and the width of the heater was selected. Considering the widest heated area, 100 µm, a membrane with a diameter of 200 µm was chosen for minimum heat losses by conduction. Only a factor two was required in these conditions to achieve a good thermal insulation, while a higher coefficient (2.6) is usually necessary for a membrane made of Si_3N_4 and/or SiO_2 [215].

In general, integrating holes in the membrane decreased slightly the power consumption. However, the simulation of a 25 µm wide hotplate with an opened membrane did not further reduce the power consumption compared to the same size with a closed membrane. For this particular geometry, the simulation model might be less accurate (section 4.3).

Dimensions of the membrane

The simulations of the power consumption for a 100 µm wide hotplate as a function of the thickness of the membrane are given in figure 4.9. The thinner the membrane, the lower was the power consumption. The membrane thickness was therefore limited only by the fabrication of the devices and its mechanical stability. The results presented in figure 4.9 are for a 100 µm wide hotplate for which there is high confidence level due the precision obtained in the measurements for this type of devices (section 4.3.1). However, as it will be discussed farther, for smaller dimensions, some imprecision were noticed when applying the bulk mean heat transfer coefficient to structures with a closed membrane. This would lead to uncertainties on the absolute value of the power consumed but still relative power variations when modifying the

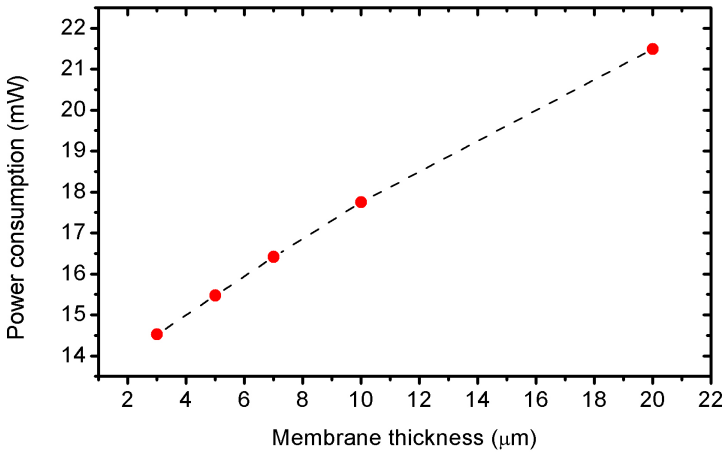

Figure 4.9: Power consumption of a 100 μm wide micro-hotplate (700 nm thick PI dielectric layer included) as a function of the membrane thickness when reaching 300°C.

membrane thickness could be extracted.

The optimum diameter of the membrane is correlated to the size of the heater area. For a 100 μm wide hotplate, a membrane with a diameter larger than 200 μm did not further improve the power savings as shown in figure 4.10. In this membrane configuration, a diameter twice larger than the heater for the membrane is sufficient to thermally insulate the heated area; a benefice provided by the low thermal conductivity of the PI.

Thickness of the dielectric layer

A nearly linear relation between the temperature and the power consumption was found when varying the thickness of the dielectric layer between the heater and the electrodes from 700 nm to 5 μm. The results obtained for a 100 μm wide micro-hotplate with a closed membrane are presented in figure 4.11. Decreasing the thickness of the dielectric layer reduces the power

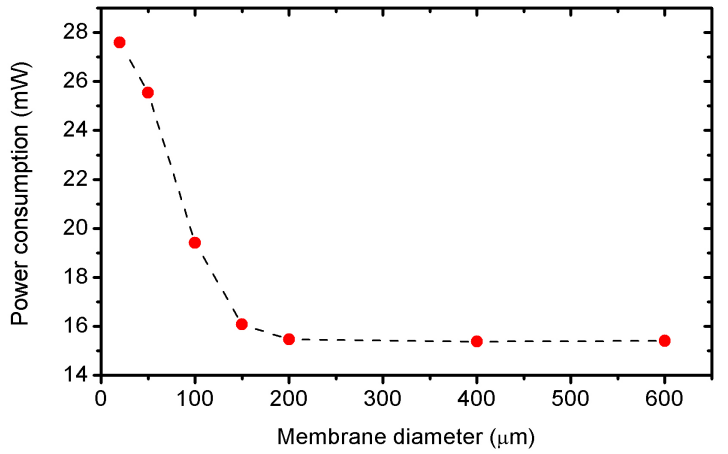

Figure 4.10: Power consumption of a 100 μm wide micro-hotplate with a closed membrane as a function of its diameter when reaching 300°C. The thickness of PI foil and the PI dielectric layer were respectively of 3 μm and 700 nm.

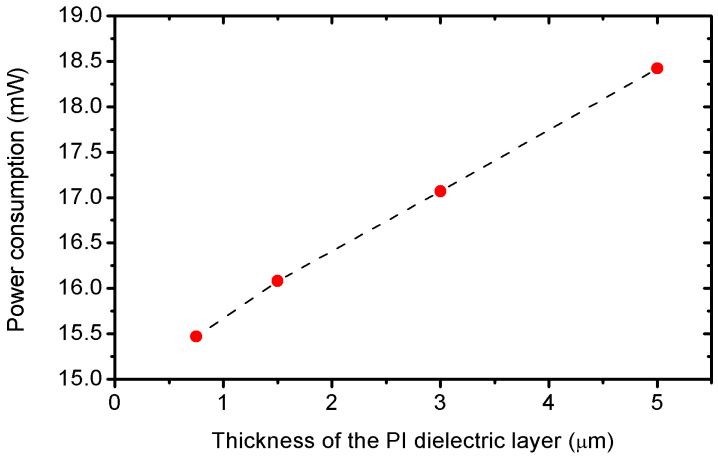

Figure 4.11: Power consumption of a 100 μm wide micro-hotplate with a closed membrane as a function of the thickness of the PI dielectric layer when reaching 300°C. The thickness of the thinned PI foil underneath was of 3 μm.

consumption by decreasing the heat losses by conduction in the membrane. The minimum power consumptions obtained with the technology we are using was reached for a 700 nm thick PI dielectric layer.

An increase in power consumption of 6.5% was for instance simulated when doubling the thickness of the PI dielectric layer to 1.4 μm for a 100 μm wide micro-hotplate with a closed membrane. For the same design, an increase of 19% was simulated with a 5 μm thick PI dielectric layer. However, due to the higher thermal mass in a bulk configuration, lower power increased occurred when changing the thickness of the PI dielectric layer. For a 100 μm wide micro-hotplate, a 1.4 μm and 5 μm thick layers led to an increase in consumption of respectively 1.5% and 8.9% compared to the initial thickness of 700 nm. Moreover, when going down in size of the active area, the variation in power consumption with the thickness of the PI dielectric layer increased.

Influence of the electrical connections to the heater

The total resistance of the heater and the ratio between the resistance of the active heating area and the whole Pt line (the active area plus the electrical interconnections) at room temperature and at 300°C are presented in table 4.5. The total resistance of the whole heater decreased with the hotplate size as well as the R_{heater}/R_{total} ratio at RT. At 300°C, the integration of the membrane slightly increased that ratio compared to the bulk devices.

The implication of this ratio on the power losses of the device is exhibited in figure 4.12. It shows the proportion of the power lost in the electrical pathways to the heater compared to the total power consumed by the hotplate to reach 300°C. These losses were almost negligible for the 100 μm wide hotplates – less than 6% of the total power consumption – but became significant for the smallest heating elements. Lower losses were obtained for the 15 μm than for the 25 μm wide heaters due to the lower ratio between the resistance of the active area and the electrical connections to the latter. Indeed, this demonstrates that the 25 μm wide layout

Table 4.5: Resistance of the heater at room temperature and ratio between the resistance of the active area and the whole heater of the hotplate at room temperature and at 300°C.

Micro-hotplate size	100 µm	50 µm	25 µm	15 µm	10 µm
Total resistance at RT (Ω)	134	79	31	45	26
R_{heater}/R_{total} at RT (-)	0.92	0.82	0.65	0.64	0.44
R_{heater}/R_{total}, bulk at 300°C (-)	0.94	0.85	0.64	0.77	0.32
R_{heater}/R_{total}, closed mem. at 300°C (-)	0.94	0.89	0.63	0.77	0.43
R_{heater}/R_{total}, opened mem. at 300°C (-)	0.94	0.88	0.67	-	-

was not optimum in terms of power efficiency. It exhibited a lower resistance than the 15 µm wide devices. This lower value arose from geometrical constraint – the space required by the electrical connectors to the active area – and from fabrication limitations. Therefore, only a heating element with relatively wide electrical lines in the active area, and consequently low resistance, could be designed (fig. 4.4). It resulted in a lower R_{heater}/R_{total} ratio obtained for this device, both at RT and when operating at 300°C.

These results show that the design of the interconnections is of prime importance at such small dimensions. The heater and its two connectors can be seen as three resistances in series. Since heat is generated by Joule effect, for a given current, the higher the resistance, the higher the thermal power dissipated and thus higher temperature. Hence, the resistance of the heated area has to be maximized while that of the connectors has to be minimized to reduce the thermal losses as much as possible.

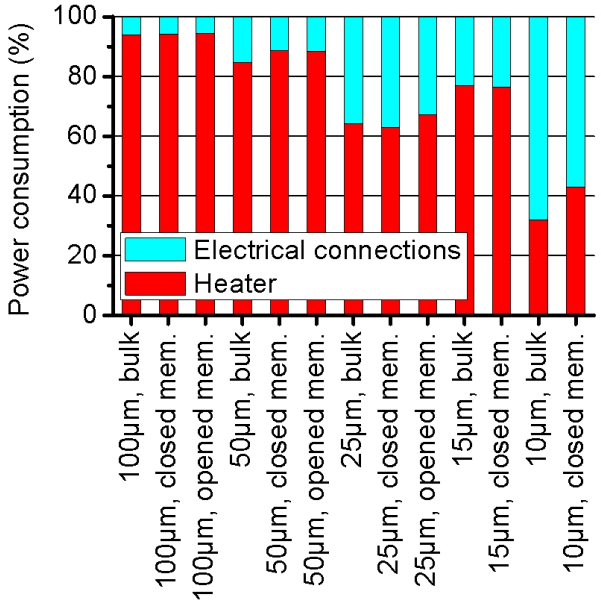

Figure 4.12: Proportion of the power consumed by the micro-hotplate in the heated area and in its connectors when at 300°C.

Besides decreasing the heated area and having a membrane, the power consumption of hotplates can be reduced by optimally designing the electrical interconnects as presented in figure 4.13. A wide interconnect would have a lower resistance and lower thermal losses. However, too large connectors (fig. 4.13a) may act as a thermal sink and increase the required power to reach the operating temperature of the device. The thermal simulations provided a nearly similar temperature distribution between hotplates with the wide and optimum connectors (fig. 4.13b) as shown in figure 4.13d and 4.13e, respectively. Narrower connectors (fig. 4.13c) have a lower thermal conductance, but their electrical resistance is higher, producing more heat. It can be observed in figure 4.13f where the temperature of the electrical connectors near the heater was higher than for the optimum layout (fig. 4.13e). A trade-off had to be found between low thermal conductance and low electrical resistance to reduce the heat losses, which are dependent on the heater size.

The "heat sink" effect – thermal conduction in the Pt electrical pathways and in the PI – was observed for the 25 and 50 µm wide devices and led to an increase of power consumption usually below 1 mW (fig. 4.14). The smallest devices were not affected by the "heat sink" effect due to their very localized heated area. An increase in thermal losses with narrow connectors was preponderant for the smallest devices, with a rise in power consumption up to 7 mW for a 10 µm wide bulk hotplate.

Only devices with optimized connectors were fabricated and one has to keep in mind that the thermal conductivity of Pt was taken from a handbook. The effect of its variation is discussed in section 4.4.1.

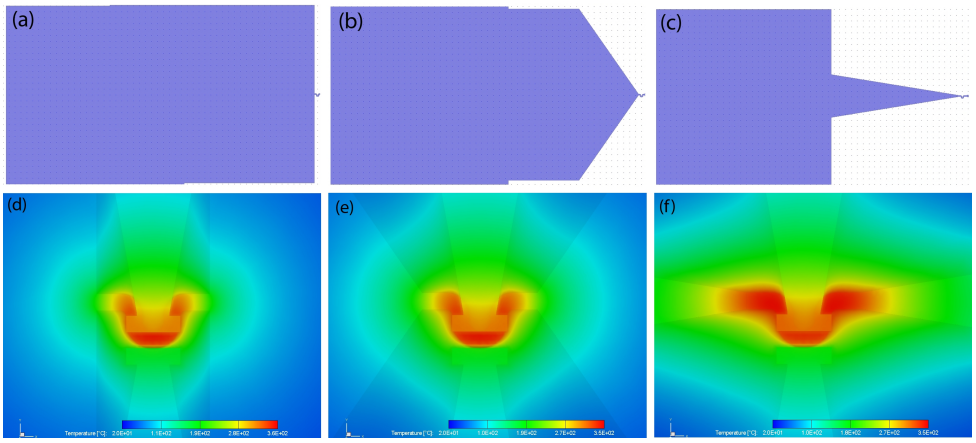

Figure 4.13: Electrical connections to the heater and their influence on the temperature distribution. (a) wide connector as heat sink; (b) optimum connector in term of power consumption; (c) narrow connector for the investigation of heat generation by Joule effect in the electrical pathways; temperature distribution as a function of a (d) wider connectors, (e) optimum connectors and (f) narrower connectors.

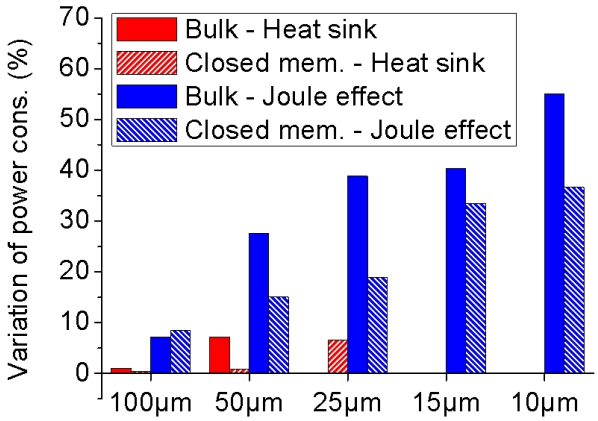

Figure 4.14: Variation of power consumption regarding to the optimum layout for the hotplate with a bulk design and a closed membrane when operating at 300°C.

Temperature gradient

The temperature gradients over the heated area and through the bulk PI were extracted from the simulations for the bulk hotplates and devices with a 3 µm membrane covered with a 700 nm PI dielectric layer. The temperature variations over the active area of the micro-hotplates are given in table 4.6. The temperature uniformity decreased when reducing the size of the heated area. When going down in size, the impact of the thermal losses by conduction through the Pt electrodes grew, increasing the thermal gradient over the active area. This effect was particularly observable for the 10 µm wide hotplate where the gradient along the electrode was very low (X direction) while it was much higher in the perpendicular direction (Y direction). A better temperature uniformity can be achieved by depositing a thicker dielectric layer between the heater and the electrodes at a cost of a higher power consumption.

Moreover, to achieve 300°C at the surface of the hotplate, the temperature of the buried heater had to be higher to compensate the thermal losses by conduction in the membrane. The temperature gradient between the heater and the electrodes increased with decreasing the size of the heated area of the hotplates. Due to the thickness of the PI dielectric layer and to the lower thermal conductivity of the PI than Si_3N_4, this thermal gradient was of few degrees for

Table 4.6: Temperature gradient over the active area of the micro-hotplates in X/Y direction when operating at 300°C.

	Temperature gradient in X/Y direction (°C)				
Micro-hotplate size	100 µm	50 µm	25 µm	15 µm	10 µm
Bulk	5/4	9/11	19/22	14/22	7/55
Closed membrane	4/3	9/15	12/21	13/25	5/32
Opened membrane	3/2	7/13	11/21	-	-

the widest hotplates but increased to some tens of degrees for the smallest layouts. The incorporation of the membrane decreased the temperature gradient by reducing the thermal losses by conduction in the substrate. Therefore, the PI dielectric layer should be kept as thin as possible to minimize the temperature difference between the heater and the surface of the hotplate. With a heater operating at a lower temperature, electromigration effects can be delayed, enhancing the life time of the device. On the other hand, a too thin PI dielectric layer would worsen the temperature uniformity over the heated area, increasing the presence of hotter spots.

The temperature profiles through the bulk micro-hotplates at their center were extracted and are presented figure 4.15. Despite the slimness of the polyimide sheet (50 µm), the backside of the device was kept almost at room temperature for the smallest hotplates, the 15 and 10 µm wide ones. This would be impossible with similar silicon-based devices due to its higher thermal conductivity.

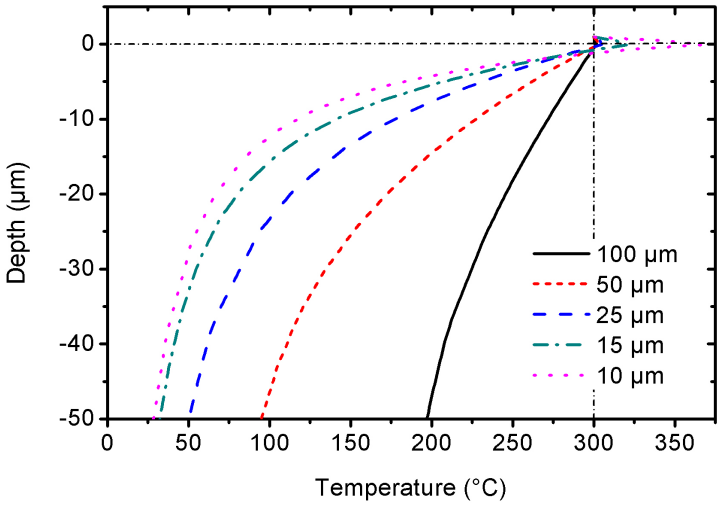

Figure 4.15: Temperature as a function of depth in the substrate for bulk micro-hotplates. The devices were at 300°C at the electrode level. A depth of 0 corresponds to the front side of the PI substrate, on which laid the heater, and -50 µm to the backside of the device. The electrodes were located at 0.9 µm (thickness of the heater plus the 700 nm thick PI dielectric layer).

Summary of the simulated parameters

Table 4.7 gives a summary of the geometrical properties for the design of micro-hotplates to minimize their power consumption.

Regarding to the thermal gradient over the heated area, it can be decreased by making the PI dielectric layer thicker at a cost of a higher power consumption. Such a thickness increase will also lead to a higher temperature variation between the heater and the surface of the electrodes.

Table 4.7: Influence of the geometrical parameters of a hotplate to decrease its power consumption.

Parameter	To reduce the power consumption
Size of the active area	As small as possible, limited by the fabrication
Thickness of the membrane and of the dielectric layer	As thin as possible, limited by the fabrication
Ratio membrane/active area diameter	At least a factor 2 for PI hotplates
Ratio R_{heater}/R_{total}	As high as possible
Geometry of the electrical pathways to the heater	Depends on the heater area, on the material and on the membrane thickness

4.2.3 Fabrication

Transducer on polyimide foil

Standard clean-room microfabrication equipments for the processing of rigid Si wafers were used for the fabrication of the devices. The plastic sheets were cut into circular 4" "wafers" for microfabrication. To handle the flexible polyimide substrates, custom-made adapters were fabricated and used as chucks compatible with the spinners and mask aligners. Depending on the fabrication step, the PI wafers were also temporarily fixed on a Si carrier wafer.

The process flow of the polyimide micro-hotplate is depicted in figure 4.16. It began with an Ar plasma surface activation of the 50 µm thick *Upilex-50S* polyimide foil from *UBE Industries, Ltd.* This material was chosen over the standardly used *Kapton* from *DuPont* because it can withstand higher temperatures. Their properties are compared in table 4.8. The surface activation was immediately followed by the deposition by DC sputtering and patterning by a lift-off technique of a 130 nm thick Pt heater with a 20 nm thick Ti adhesion layer (fig. 4.16a). Sputtering was chosen instead of evaporation because it improved the adhesion of these metal layers to the plastic foil (section 2.2). The resistance of the heater at room temperature varied from 130 down to 24 Ω depending on the hotplate size. A 700 nm thick photodefinable polyimide layer, *PI-2737* from *HD Microsystems*, used as an electrical insulator was then spin-coated and contacts were opened to allow the electrical connection to the heater (fig. 4.16b). The thermal curing of the insulating layer was performed at 375°C under N_2 atmosphere, allowing operation of the device up to 450°C [50]. During that step at high temperature, the polyimide foil shrank in-plane due to the stresses induced by the Pt heater leading to misalignment with the following photolithographic masks. This misalignment was compensated by redesigning the photolithographic masks accordingly.

A second layer of chemically inert Ti/Pt was deposited by sputtering and patterned by lift-off to obtain the electrodes and complete the process to produce bulk hotplates (fig. 4.16c). For

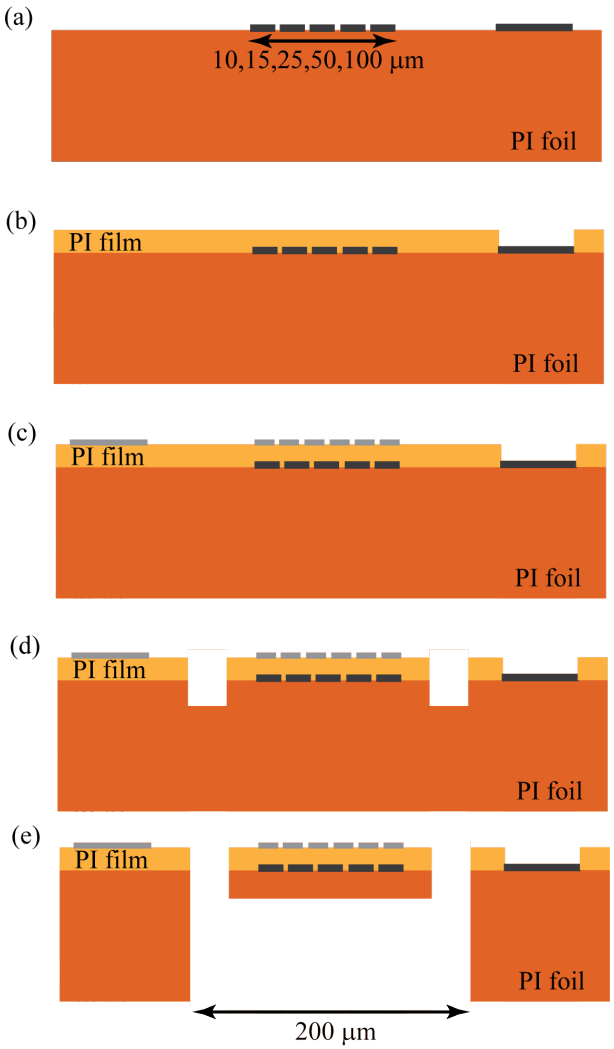

Figure 4.16: Process flow for the fabrication of micro-hotplates on polyimide foil: (a) DC sputtering and patterning by lift-off of the Pt heater, (b) Spin-coating and patterning of the PI dielectric layer, (c) DC sputtering and patterning by lift-off of the Pt electrodes, (d) Dry etching of the PI at the front side and (e) dry etching of the PI foil at the backside to obtain the membrane.

the thermal characterization of the devices, the Ti/Pt layer was replaced by a 100 nm thick Cr layer deposited by e-beam evaporation. The thickness of the Cr layer was adjusted to reach the same thermal conductivity than a Pt-based film [248]. That material was chosen for its high emissivity in the visible and near IR region for thermographic characterization of the devices (section 4.2.4) [249].

Closed membranes were obtained by RIE (reactive ion etching) of the polyimide foil from the backside and opened membrane with an additional etching step from the top side (fig. 4.16d and 4.16e). Aluminum masks were used for the dry etching of the PI in a mixture of SF_6 (16.7%) in O_2 to reduce the roughness of the membrane (section 2.3) and the mask underetch compared to the use of only O_2 [83]. By reducing the roughness, thinner membranes could be obtained, reducing the power consumption of the device. Since the etch rate of the polyimide

Table 4.8: Properties of the *Upilex* from *UBE Industries, Ltd.* and the *Kapton* from *DuPont* polyimide foils.

Properties	Upilex	Kapton
Tensile strength (MPa)	520	1231
Tensile modulus (GPa)	9.1	2.5
Density (kg/m^2)	1.47	1.42
Heat shrinkage (%)	0.1 (200°C)	0.17 (150°C)
Coef. of thermal expansion (ppm/°C)	12	20
Thermal conductivity (W/m·K)	0.29	0.12
Specific heat (J/g·K)	1.13	1.09
Degradation temperature (°C)	500	400
Dielectric constant (-)	3.5	3.4

foil depends on the area to be etched, all of the membranes were produced with a diameter of 200 µm, irrespective of the hotplate width. An etch rate of 1.2 µm/min was achieved, similar to values found in the literature [83]. A picture of a 50 µm wide micro-hotplate with an opened membrane is shown in figure 4.17.

Only devices with the thinnest membrane and PI dielectric layer were fabricated to achieve the lowest power consumption. Concerning the connectors, only the optimum designs derived from the simulations were produced. One has to keep in mind that the thermal conductivity of Pt was taken from a handbook but as discussed in section 4.4.1, a slight variation of it value has only a small influence on the results obtained. We are therefore confident that the designs presented are very close to the optimal layouts. Indeed, the experimental results obtained (power, voltage and current values) fit very well with the values predicted by the simulations.

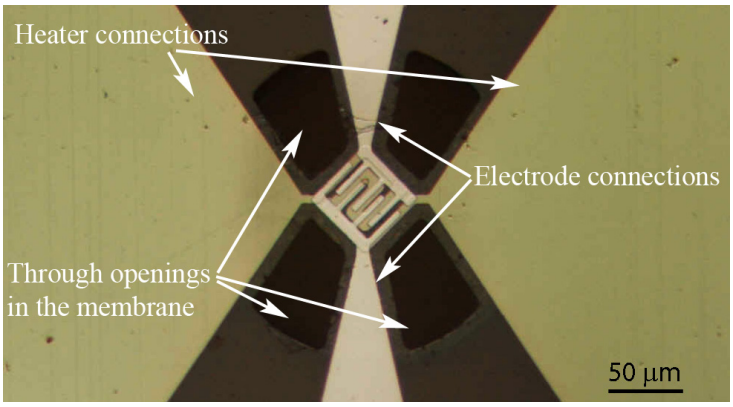

Figure 4.17: Optical picture of a 50 µm wide micro-hotplate fabricated on polyimide with an opened membrane.

Drop-coating of the metal-oxide gas sensitive layer

The method chosen for the deposition of the MOX layer was the drop-coating. This thick-film coating technique has proven to provide metal-oxide films with high gas sensitive performances [71] and was a key point for the successful development of commercially available micromachined MOX sensors [165, 186]. The scaling down of the MOX droplet was performed with glass capillaries (*GB150-8P* from *Science Products GmbH*), which showed to be compatible with the current industrial deposition machines. To achieve drops as small as 15 µm in diameter, the capillaries were elongated to reach a diameter at the apex between 10 and 100 µm, as the diameter of the droplet to be deposited. An optical picture of a micropipette is showed in figure 4.18.

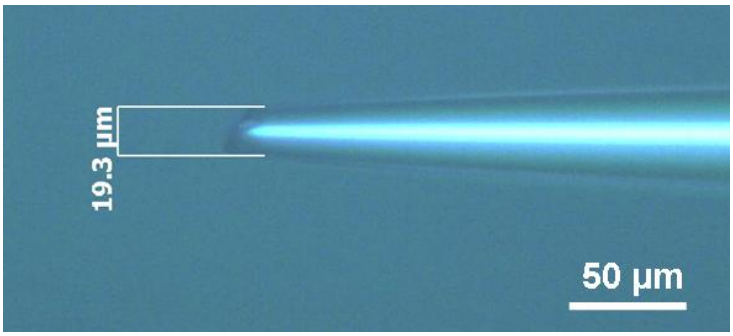

Figure 4.18: Optical picture of a micropipette used for the deposition of the metal-oxide paste.

The MOX material – SnO_2:3%Pd paste [250] – was pulled up into the glass tube by capillary forces before being deposited on the electrode area. Droplets as small as 15 µm in diameter and between 6 and 7 µm in height were successfully deposited on transducers of 15 µm in width as shown in figure 4.19. The drop however overflowed onto the electrodes by a few microns. The chips were annealed at 450°C for 10 min to sinter the MOX layer. The thicknesses of the metal-oxide layers were measured by white light interferometry (*Wyco NT1100* from *Veeco*)

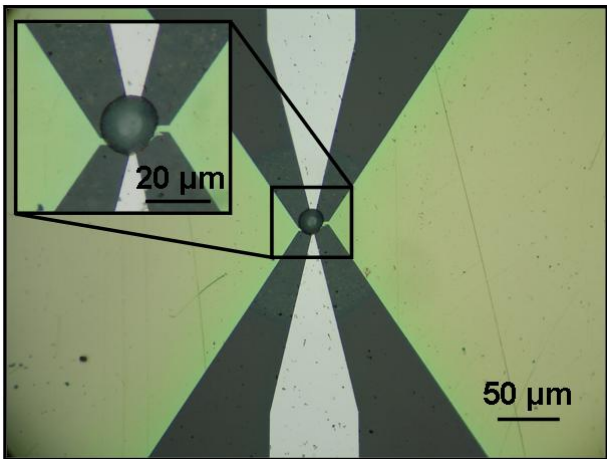

Figure 4.19: Optical picture of a 15 µm wide micro-hotplate coated with the MOX layer. The drop was about 20 µm in diameter.

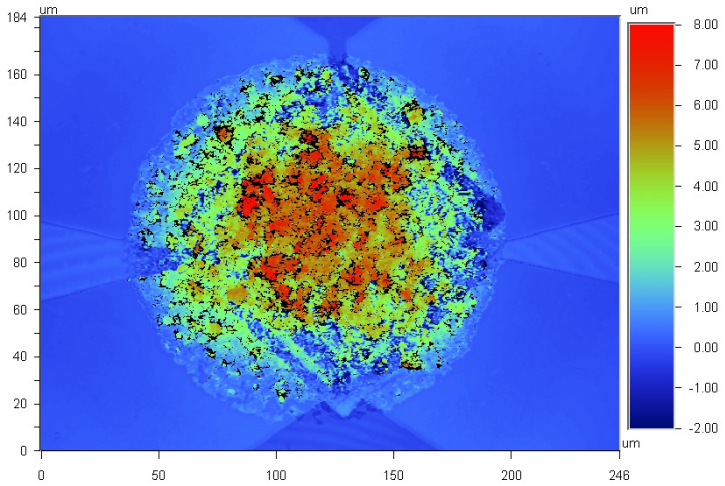

Figure 4.20: Topology of a 100 µm wide micro-hotplate coated with SnO_2 obtained by white light interferometry.

and were in the range of 5 to 8 µm, depending on its diameter. A thickness measurement of a drop-coated 100 µm wide hotplate is given in figure 4.20. The MOX layer exhibited an excellent adhesion to the transducer. No deterioration occurred to the gas sensitive layer after a scotch tape test (*3M Green*). The device was finally mounted and characterized on a TO-5 header, which was compatible with the gas measurement system at our disposal. A complete gas sensor is presented in figure 4.21.

Foil level packaging

Packaging of sensors is often necessary to prevent their sensing area to be directly exposed to the environment. The encapsulation concept consists in a cavity surrounding the active area of the sensor. In the case of gas sensor it has to be permeable to allow the gas mixture to interact with the functional material. A cross-sectional view of a packaged metal-oxide gas sensor is schematized in figure 4.22.

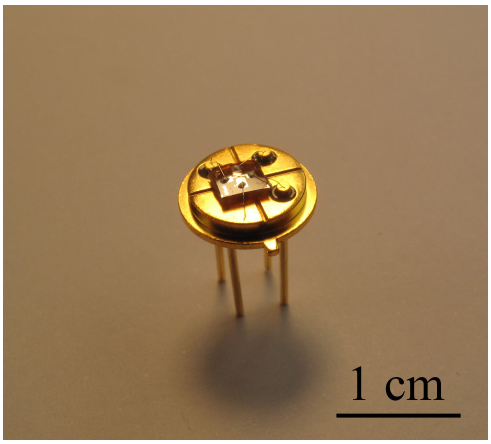

Figure 4.21: MOX gas sensor mounted on a TO-5 header for gas measurements.

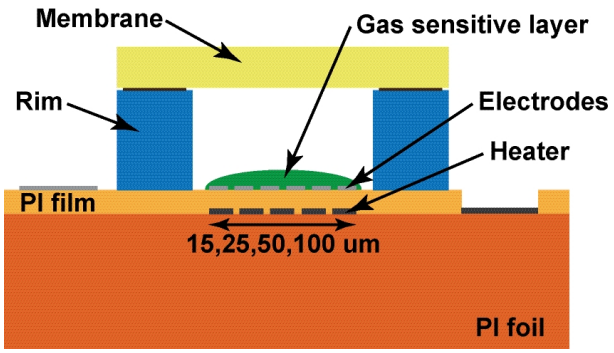

Figure 4.22: Cross-sectional schematic of the packaged gas sensor.

General concept and issues related to the packaging of chemical sensors

For the particular case of chemical sensors including a functional layer, several issues remain when post-processes are involved. In most cases, the chemical sensitive layer cannot be exposed to high temperatures or other chemicals. These back-end steps are therefore limited, for instance photolithography can be prohibited. In a foil level packaging method, the definition of a frame to encapsulate to the sensing area has to be carefully conceived. Once the functional layer was deposited, materials have to be deposited locally to prevent risks of contamination, namely subtracting processing methods involving for instance spin-coating (SU-8, polyimide,...) are not desired. Alternatively, one could deposit the functional layer after the integration of the frame on the substrate. However, a step at high temperature is sometimes required to functionalize the sensing layer (e.g. 450°C for MOX sensors), which would severely damage the polymeric encapsulation. Only polyimide could withstand such high temperatures but layers thick enough cannot be achieved with the commercial products available at the moment.

Considering these two possible limitations – no contamination and high temperature – the solution presented here consists in the deposition of pre-patterned structures around the active area already covered with the functional material. The use of solvents will be thus avoided as well as a post-processing step at a too high temperature. These pre-patterned structures are used as a frame around the chemical gas sensing devices on top of which a gas permeable membrane is bonded to seal the cavities.

Nevertheless, in some cases as for the local deposition (e.g. by drop coating or inkjet printing) of a gas sensitive layer (for instance polymeric) which required a low curing temperature, one can imagine to laminate the dry photopatternable foil before the gas sensitive coating.

Foil level packaging of chemoresistive gas sensor

The packaging of the sensors was performed at the foil level for cost effectiveness with a material compatible with roll-to-roll processing. The encapsulation of the metal-oxide gas sensors is illustrated in figure 4.23. The spacer between the sensor and the gas permeable membrane was made of dry photoresist (*PerMX3050* from *DuPont*). The processing to create these structures was presented in section 2.4. Once the rims were patterned and lying on their PE foil, they were assembled with the polyimide sheet embedding the MOX sensors (fig. 4.23a). They were

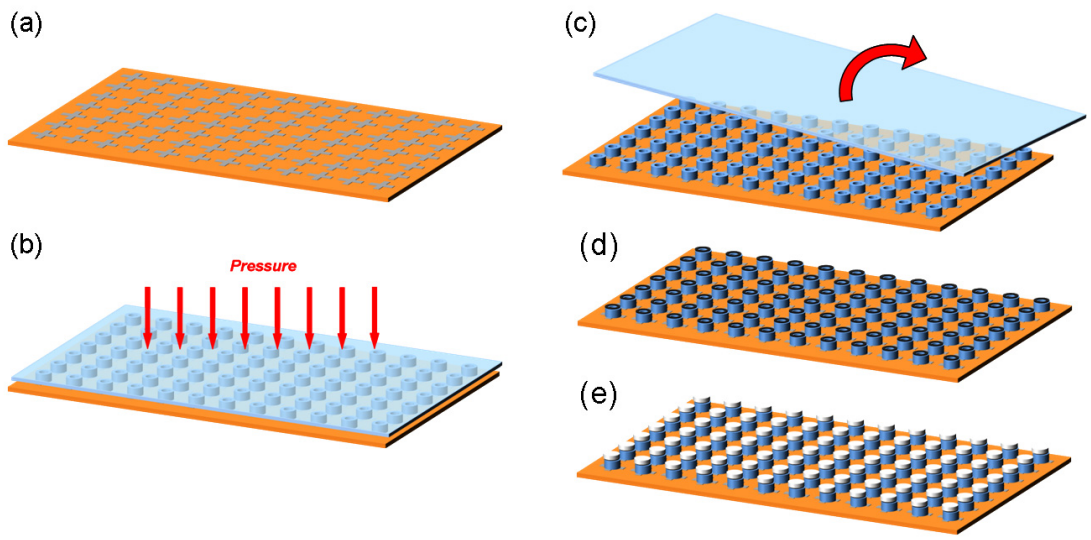

Figure 4.23: Process flow of the foil level packaging of the metal-oxide gas sensors. (a) Polyimide foil with gas sensing structures; (b) Alignment and lamination of the pre-patterned rims; (c) Removal of the handling film; (d) Glue dispensing on the rims; (e) Gas permeable membrane deposition.

then aligned and laminated at 75°C in a press for 3 min (fig. 4.23b). Prior to the lamination, an surface activation was performed with an O_2 plasma to enhance the adhesion. The PE handling film was next removed and the sensors with their surrounding rim were achieved at the foil level (fig. 4.23c). Since the polymeric materials involved can withstand fairly high temperatures, this step was followed by a hard-bake of 1 h at 150°C in an oven to further improve the adhesion of the frame to the substrate.

Figure 4.24 exhibits the metal-oxide-based gas sensors with the 50 µm thick rims acting as spacers. Their inner and outer diameters were respectively of 700 and 1200 µm. Adhesion tests

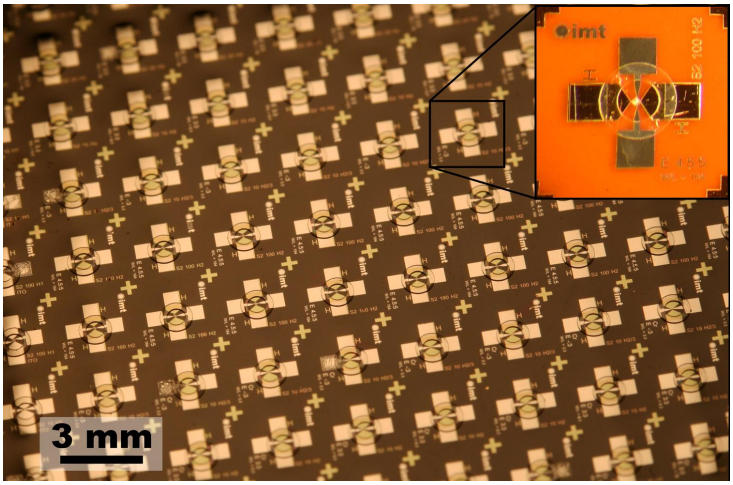

Figure 4.24: Gas sensors on polyimide foil with the laminated rims as spacers around the active area.

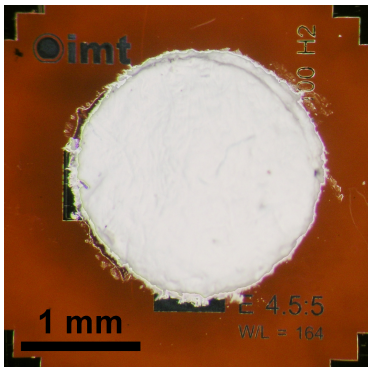

Figure 4.25: Fully packaged metal-oxide gas sensor on polyimide foil with the gas permeable membrane glued on the rim.

with the standard *3M Green Scotch* tape was performed and revealed a very good bonding of the rims to the polyimide substrate.

The final step was the dispensing of an epoxy glue (*Epotek H70E*) on the rims (fig. 4.23d) before the deposition of a Teflon-based gas permeable membrane (fig. 4.23e), which was carried out manually for this study. It is however foreseen to be performed with method compatible with mass production, such as gluing and laser ablation for patterning the membrane. The complete sensor is displayed in figure 4.25.

4.2.4 Thermal characterization

Thermal characterization was performed through thermographic measurements in the visible and NIR (near infrared) spectral range [249]. Measurements at such low wavelengths improve the spatial resolution and minimized the influence of the materials' emissivity on the temperature determination, unlike for standard IR cameras [227]. This non-contact method avoids any influence of the measurement system on the temperature of the microsystem as it would be the case with the use of a thermocouple for instance [251]. As a result, it provided a thermal image of the device with a theoretical resolution of about 450 nm and a very high precision on the temperature measured (error on temperature less than 2%, i.e. 6°C at 300°C) [247]. To thermally characterize the hotplates when operating at a temperature of 300°C, Cr was chosen as material for the electrodes because of its higher emissivity (0.7 [249]) than Pt (0.06 [247]), providing more precise measurements at such low light intensity for this measurement technique.

4.2.5 Reliability and robustness

To get an indication on the robustness of the devices, the maximum power they can withstand before breakdown occurred was identified. From these measurements, the maximum current density a micro-hotplate can withstand before its failure arose can be determined. Information can be extracted and compared to the powers and current densities required by the sensors to operate at a given temperature. Moreover, indications can be obtained on the breakdown

mechanisms, which could be used for future optimizations [193].

For these investigations, the voltage was ramped up from 0 to 10 V with steps of 50 mV every 500 ms until breakdown using a *Hewlett-Packard 4155A Semiconductor Parameter Analyzer*. This period of time between each step was longer than the time response of the hotplates (section 4.3.3) to ensure that they reached a steady state between each step. The experiment was performed on five bulk hotplates (without the gas sensitive layer) of each size because they dissipate the most power for a given temperature.

4.2.6 Gas measurements

To evaluate the gas sensing performances of these highly miniaturized drop-coated MOX gas sensors fabricated on polyimide foil, gas measurements were performed by *AppliedSensor GmbH*. They were carried out in synthetic air with 50% of relative humidity and with a flow of 200 sccm. Representative oxidizing and reducing gases were used at different concentrations: CO (10 to 100 ppm), NO_2 (0.5 to 2 ppm) and CH_4 (700 to 2500 ppm). The sensors were exposed to these gases between 15 and 30 min when operating at temperatures between 200 and 250°C. The latter correspond to the temperature at which sensitivity to these gases occurs, while the former aimed at determining the sensitivity of these sensors at a lower temperature and power consumption. Measurements at 300°C were not performed for fear that the devices would fail too quickly, particularly the smallest sensors. However, measurements at 300°C were carried out with the multisensor platform in chapter 6.

The devices operated in both constant and pulsed temperature modes using a standard test protocol from the industry. The use of a pulsed mode brings two advantages. It reduces the power consumption and improves the selectivity of the sensor. For instance, methane can no longer be detected. The pulse period was of 1 s, with the heater powered for 30 or 100 ms, which were longer than the thermal time response of the sensors. The resistance measurement of the gas sensing layer occurred 500 ms after switching off the heater. Commercial MEMS gas sensors from *AppliedSensor GmbH* were added for comparison. During these mesurements, the resistances of the gas sensing layers as well as the voltages applied to the heaters were monitored with a *Agilent 34970A Data Acquisition Switching unit*.

4.3 Results

This section first presents the electrical and thermal properties obtained with the micro-hotplates on polyimide. These results will be then compared to the electrothermal simulations performed in section 4.2.2. The response times and the maximum ratings these devices can withstand will be then given. Finally, the gas sensing performances in both constant and pulsed temperature modes of operation of the MOX sensors as well as their power consumptions will be shown and compared to a commercial silicon-based device.

4.3.1 Electrical and thermal properties of the transducers on polyimide

The resistance of the fabricated heater and the associated minimum width of the electrical pathways of the different hotplates are presented in table 4.9. Their values were between 30 and 125 Ω depending on the heater size. The power consumptions of the micro-hotplates when reaching a temperature of 300°C are given in figure 4.26 and summarized in table 4.10. These values were extracted from thermographic images as shown in figure 4.27 and corresponded to the behavior predicted by the simulations. Depending on the heater size, a decrease in power consumption between 40 and 60% was measured for devices with closed membranes compared to bulk ones. The processing of the devices with an opened membrane further reduced the power consumption of about 10%.

Table 4.9: Resistance at room temperature and minimum line width of the micro-hotplates.

Micro-hotplate size	100 µm	50 µm	25 µm	15 µm	10 µm
Heater resistance at RT (Ω)	125	75	32	41	30
Min. electric line width (µm)	6.5	5.0	2.5	2.7	3.0

A power consumption as low as 6 mW at 300°C was reached with a 15 µm wide hotplate with a membrane. Despite a thicker membrane, it makes the PI-based devices as low power as those fabricated on silicon due to the lower thermal conductivity of the PI compared to Si_3N_4 or SiO_2 [47, 194, 222]. A still very interesting power consumption of 10 mW was achieved with a 15 µm wide heater patterned on a bulk polyimide sheet. Such a low power consumption is not conceivable with silicon substrate due to its very high thermal conductivity. The current densities at 300°C are given in table 4.11. They were about of 10^6 A/cm^2 with lower values achieved with hotplates with a membrane due to their lower power consumption. A reduced

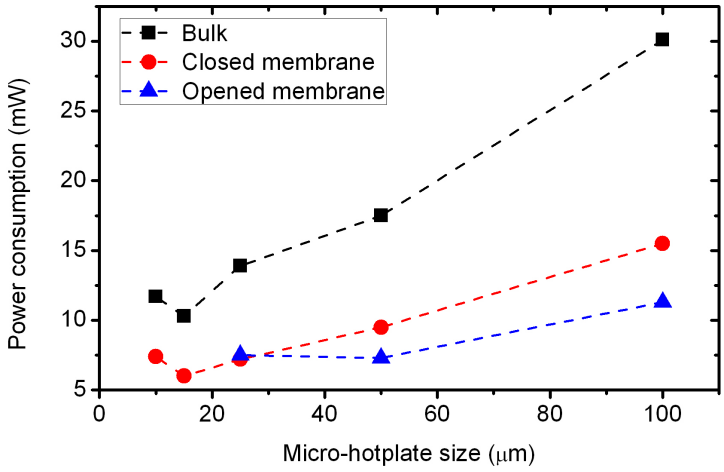

Figure 4.26: Power consumption of the micro-hotplates fabricated on polyimide when operating at 300°C.

Table 4.10: Measured power consumptions of the micro-hotplates operating at 300°C.

	Power consumption (mW)				
Micro-hotplate size	100 µm	50 µm	25 µm	15 µm	10 µm
Bulk	30.1	17.5	13.9	10.3	11.7
Closed membrane	15.5	9.5	7.2	6.0	7.4
Opened membrane	11.3	7.3	7.5	-	-

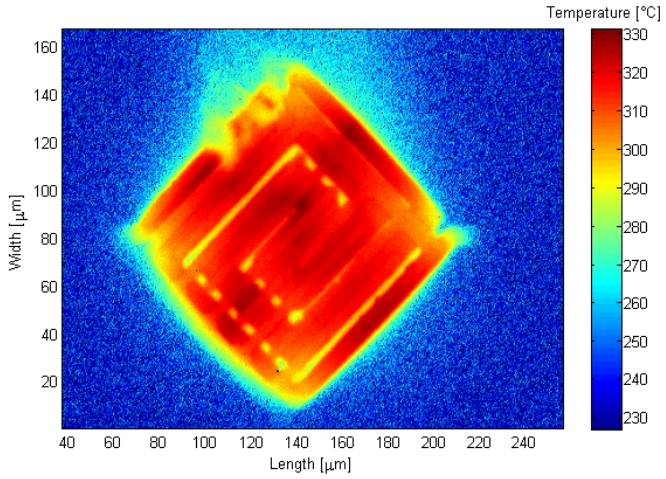

Figure 4.27: Thermographic image in the visible and NIR spectral range of a 100 µm wide hotplate with a closed membrane operating at 300°C.

current density may delay electromigration effects and hence improve the life time of the device [193].

For the smallest devices – 10 µm wide hotplates – the power consumptions to reach 300°C were higher than the values measured with the 15 µm wide heaters due to high power losses in the electrical pathways as indicated by the simulations.

Additionally, thermographic measurements allowed evaluating the temperature uniformity

Table 4.11: Measured current densities of the micro-hotplates when operating at 300°C.

	Current densities at 300°C (A/cm^2)				
Micro-hotplate size	100 µm	50 µm	25 µm	15 µm	10 µm
Bulk	$1.2{\cdot}10^6$	$1.6{\cdot}10^6$	$4.4{\cdot}10^6$	$2.9{\cdot}10^6$	$3.6{\cdot}10^6$
Closed membrane	$8.4{\cdot}10^5$	$1.1{\cdot}10^6$	$2.9{\cdot}10^6$	$2.2{\cdot}10^6$	$2.9{\cdot}10^6$
Opened membrane	$6.8{\cdot}10^5$	$9.5{\cdot}10^5$	$3.0{\cdot}10^6$	-	-

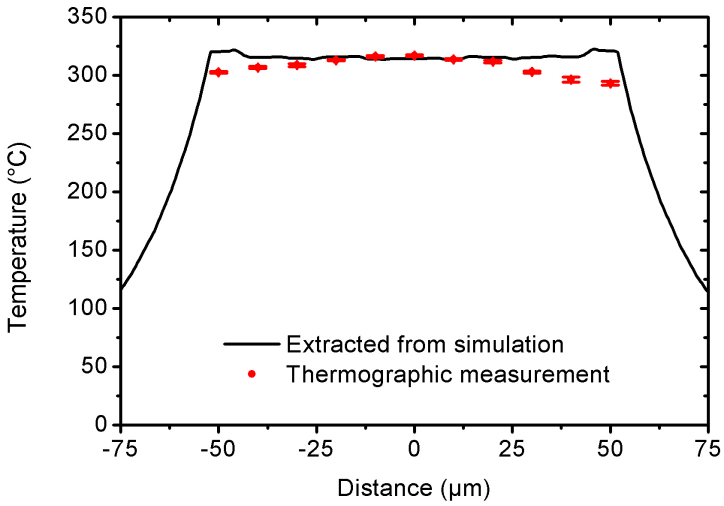

Figure 4.28: Simulated and measured (confidence interval of 95%) temperatures of a 100 µm wide hotplate with a closed membrane. The input power was of 15.5 mW to reach a temperature of 300°C.

over the heated area. Figure 4.28 presents the results obtained with a 100 µm wide hotplate. The temperature gradient between the center of the heater to its edge are given in table 4.12. Among all the investigated layouts, the higher temperature gradient was of 0.40°C/µm for a 10 µm wide heater. It corresponded to a gradient of 22°C between the center of the active area and its edge. The higher gradients were found for the devices with a closed membrane and tend to increased when reducing the size of the heated area. The temperature uniformity can be improved by having a thicker PI dielectric layer at a cost of a higher power consumption. The thermal gradient can be further decreased by the coating of the electrodes with the gas sensitive drop in a metal-oxide gas sensor configuration [252].

Due to the layout of the hotplates, several factors determined throughout the simulations could not be confirmed with the experimental investigations. The ratio of the resistance value between the heated area and the whole heater line could not be experimental extracted as well as the temperature gradient through the substrate in the case of bulk devices. The effect of

Table 4.12: Measured temperature gradient over the active area of the micro-hotplates in X/Y direction when operating at 300°C.

	Temperature gradient in X/Y direction (°C/µm)				
Micro-hotplate size	100 µm	50 µm	25 µm	15 µm	10 µm
Bulk	0.06/0.12	0.02/0.28	0.40/1.20	0.93/1.33	0.40/3.40
Closed membrane	0.22/0.34	0.80/0.80	0.56/1.6	1.33/1.87	0.20/4.40
Opened membrane	0.10/0.04	0.08/0.20	0.56/1.20	-	-

the thickness of the membrane and the PI dielectric layer on the power consumption was not experimentally determined since only devices with the thinnest layer were fabricated. However, due to the very good fitting of the simulations with the experimental results, the values obtained from the modeling and the out coming design guidelines drawn can be trusted with a high degree of confidence.

4.3.2 Comparison between the simulated and experimentally measured power consumptions and temperature uniformities

The power consumptions found for the bulk devices and for the 100 μm wide hotplates with a closed membrane were very accurate regarding to the simulations. The variation between the simulated and measured power consumptions of the hotplates are given in table 4.13. It validates thus the accuracy of the simulation parameters used and confirms the modelization performed on the widest layouts for investigating the effects of the membrane dimensions (section 4.2.2). However for devices with a membrane, lower power consumptions were obtained compared to the simulation values, especially for hotplates smaller than 100 μm, where variations up to 50% were observed. This variation demonstrated the mean heat transfer coefficient from the bulk hotplates resulted in a higher estimation of the power losses.

Table 4.13: Variation of the power consumption of the micro-heater between the simulations and the experimental results to reach an operating temperature of 300°C. A positive sign refer to a device with a lower measured power consumption than simulated.

	Variation of the power consumption (%)				
Micro-hotplate size	100 μm	50 μm	25 μm	15 μm	10 μm
Bulk	-11.9	7.9	0.4	-1.1	-15.6
Closed membrane	8.8	38.2	42.1	27.5	25.2
Opened membrane	10.4	50.3	40.0	-	-

The precise determination of the mean heat transfer coefficients is therefore of prime importance to obtain very accurate electrothermal simulations. This precision is even more critical for the smallest heaters. Its significance is shown in figure 4.7 where the mean heat transfer coefficient increases drastically when going down in heated area dimensions. As an example, to reach a temperature of 300°C, an undervaluation of the mean heat transfer coefficient of 50% led to lower power consumption between 9 and 16% for the bulk hotplates, depending on their size. A same variation of this coefficient for devices with a membrane decreased their power consumption of 13 to 40%. No significant differences were observed for devices with a closed or opened membrane.

Another factor to improve the accuracy of the simulations was the change in resistivity of

the platinum as a function of the temperature. Table 4.14 exhibits the variation of the voltage applied to the hotplates between the experimental results and the simulations when operating at 300°C. A maximum variation of 12.5% was obtained for the bulk designs. These excellent results confirmed the accurateness of the parameters and boundary conditions used for the simulations of these devices. Except for the 100 μm wide hotplates with a membrane, the smaller layouts exhibited a higher variation in applied voltage, which was due to the inadequate mean heat transfer coefficient used for those devices (section 4.4.1). Not only was the fitting of the power consumption with the temperature achieved throughout the simulations, but the matching of the applied voltage as well when the mean transfer coefficient was properly established. Consequently, the simulated results can give a very good confidence in term of current, current density and electrical resistance of the heating element when operating at 300°C.

Table 4.14: Variation of the applied voltage to the micro-heater between the simulations and the experimental results to reach an operating temperature of 300°C. A negative value refers to a higher voltage supplied to the fabricated device.

	Variation of the applied voltage (%)				
Micro-hotplate size	100 μm	50 μm	25 μm	15 μm	10 μm
Bulk	-2.5	0.0	-7.5	2.4	-12.5
Closed membrane	3.8	24.6	24.3	9.1	7.6
Opened membrane	5.3	32.3	23.9	-	-

4.3.3 Thermal response time

The response times of the sensors were measured with an oscilloscope by monitoring the voltage variation across a 47 Ω resistor connected in series with the heaters. The heaters were pulsed between 20°C and 300°C. The measured time response, $t_{90\%}$, of the micro-hotplates to reach their operating temperature are given in table 4.15. The response time decreased with the size of the heating element and with the presence of a membrane. A 100 μm wide bulk hotplate provided the longest response time, which was of 10 ms. Response times below 5 ms were achieved with the 15 and 10 μm wide devices fabricated on bulk substrates. 10 μm wide bulk hotplate however exhibited a longer response time than the 15 μm wide one. This result might be due to their higher power consumption and significant thermal losses in the electrical connections to the heater. Very fast switching hotplates can thus be produced at low-cost by avoiding of bulk micromachining of the polyimide.

Table 4.15: Response time, $t_{90\%}$, of the micro-hotplates to reach an operating temperature of 300°C.

	Response time (ms)				
Micro-hotplate size	100 µm	50 µm	25 µm	15 µm	10 µm
Bulk	10	8	5	2	3
Closed membrane	5	5	3	2	2
Opened membrane	5	4	3	-	-

4.3.4 Reliability and robustness

Since the thermal time constants of the devices were determined to be of a maximum of 10 ms, the time delay of 500 ms between each step of the applied voltage ramp ensured that the micro-heater reached their thermal equilibrium before increasing the voltage to its next level. The results of the maximum power test leading to the breakdown of the bulk micro-hotplates are given in figure 4.29 and summarized in table 4.16.

The maximum power reached before the breakdown of the device arose decreased with the size of the hotplate. The reproducibility of the measurement was very good regarding to the standard deviation of each type of heating element, especially for the 100 and 50 µm hotplates (below 2%). For the maximum current densities, the values obtained were about 20% higher than those measured when the device was operating at 300°C.

The breakdown of the micro-hotplates occurred either at the electrical connectors to the heated area or in the outer arm of the heating part. The failure is shown in figure 4.30 in the case of 50 µm wide hotplates where only the heater was patterned to better highlight the breakdown areas. These sections of the heater were under the highest current densities and thus the highest heat generated by Joule effect, leading to a faster collapsing. Therefore, to delay the

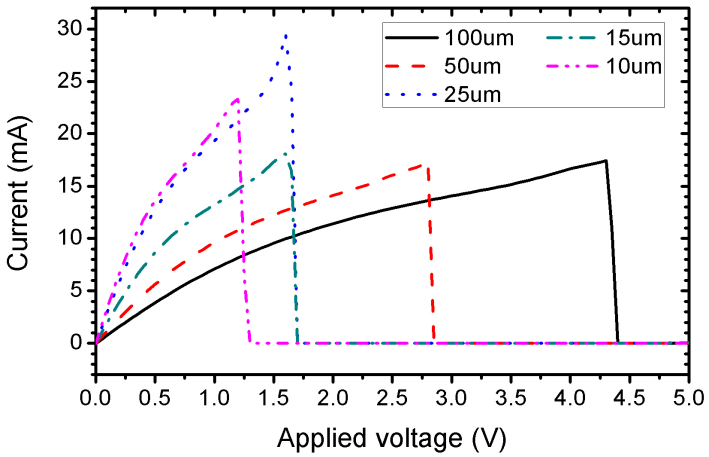

Figure 4.29: Maximum power before failure occurs.

failure of these devices, lower operation temperatures should be used, which will require lower current densities in the electrical pathways of the heater. Their operation in pulsed temperature mode can also bring some benefits since the device is not powered most of the time.

Table 4.16: Results of the maximum power test leading to the breakdown of the bulk micro-hotplates. The voltage was ramped up from 0 to 5 V with steps of 50 mV every 500 ms.

Micro-hotplate size	P_{max} (mW)	σ (%)	j_{max} (A/cm^2)
100 µm	73.0	1.5	1.54×10^6
50 µm	48.2	1.4	1.98×10^6
25 µm	36.8	8.3	5.72×10^6
15 µm	27.1	4.2	3.57×10^6
10 µm	27.0	3.0	4.28×10^6

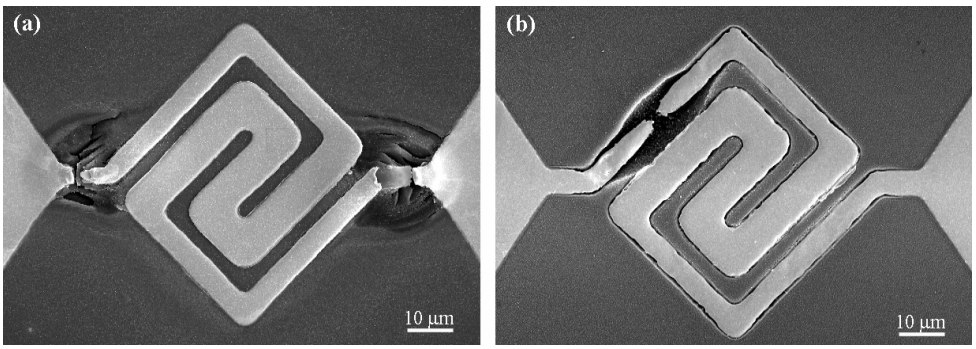

Figure 4.30: SEM pictures of 50 µm with only the heater patterned. The failure of the device occurred either in (a) the electrical interconnections or (b) in the outer part of the heated area.

4.3.5 Gas sensing performances of the sensors

Constant temperature mode of operation

Even if ultra-low power consumption is targeted, the operation of the MOX sensors in a isothermal mode was investigated to demonstrate their proper operation. Figure 4.31 presents the successful behavior of the polyimide-based gas sensors for the detection of CO, CH_4 and NO_2. They operated at 200°C to reduce their power consumption and avoid early damage. They all revealed a complete reversibility of the chemical reaction and a good logarithmic linearity, a typical response of metal-oxide gas sensors [215, 237].

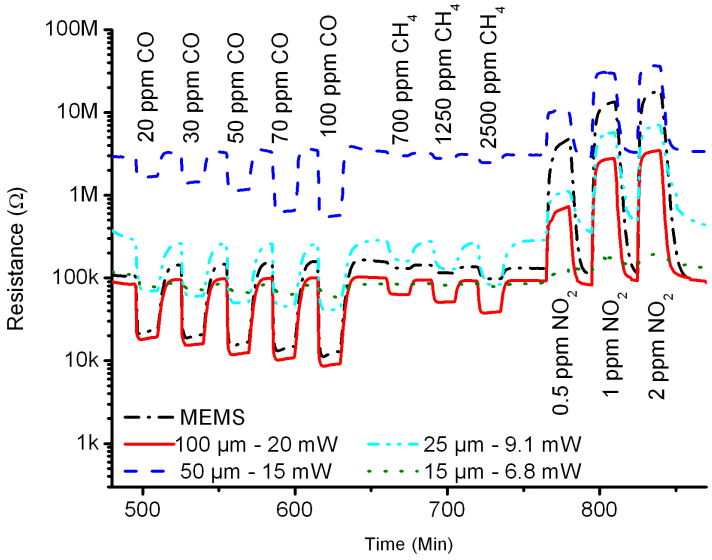

Figure 4.31: Responses of the bulk gas sensors when operating at 200°C in constant temperature mode to several gases.

Table 4.17: Chemoresistive response of SnO_2:3%Pd MOX gas sensors at 200°C in constant temperature mode when exposed to representative reducing and oxidizing gases.

	Chemoresistive response (-)				
	MEMS	100 µm	50 µm	25 µm	15 µm
CO: 20 ppm	5.44	4.79	1.79	4.09	1.10
CO: 100 ppm	10.03	10.07	5.34	6.89	2.17
CH_4: 700 ppm	1.00	1.46	1.01	1.79	1.02
CH_4: 2500 ppm	1.33	2.37	1.22	3.39	1.10
NO_2: 0.5 ppm	36.38	7.88	3.37	3.91	1.38
NO_2: 2 ppm	138.52	37.32	11.89	24.43	2.24

Chemoresistive responses[1] (CR) towards several concentrations of gases measured are given in table 4.17. As expected, the response to the gases decreased with the sensing area due to a reduction of the W/L of the electrodes. The PI sensors exhibited a good sensitivity to low concentrations of CO with CR close to the commercial MEMS device. In the case of CH_4, even slightly higher CR were reached with the polymeric sensors. However, the detection of NO_2 with the MEMS sensor revealed a much higher CR than polyimide-based device.

Table 4.18 presents the variation of the chemoresistive response of the SnO_2:3%Pd MOX gas sensors for an increase in temperature from 200°C to 250°C. The PI sensors exhibited a strong

[1]The chemoresistive response (CR) is the relation between the resistance of the gas sensitive layer when exposed to only synthetic air (baseline), R_0, and when exposed to the gas to be detected, R. It is defined as R/R_0 for oxidizing gases (e.g. NO_2) and R_0/R for reducing gases (e.g. CO, CH_4) so as to always obtain values equal or higher than 1.

Table 4.18: Variation of the chemoresistive response of SnO_2:3%Pd MOX gas sensors between 200°C and 250°C in constant temperature mode when exposed to CO.

	Variation of the chemoresistive response (%)				
	MEMS	100 μm	50 μm	25 μm	15 μm
CO: 20 ppm	15.9	12.8	42.8	13.8	30.4
CO: 30 ppm	3.3	19.1	49.4	16.6	32.9
CO: 50 ppm	-8.8	27.6	56.1	18.5	34.9
CO: 70 ppm	-13.3	34.8	62.9	24.6	40.0
CO: 100 ppm	-21.7	41.5	67.2	24.9	39.7

increase in the CR, while the opposite was obtained with the MEMS device. Several factors and their combination may be the cause of such a behavior, the use of smaller structures with the PI chips, the different nature of the substrate and the smaller W/L ratio for the PI devices. Further investigations should be undertaken to properly determine its origin. The highest CR variations were obtained for the 50 μm wide sensor with values between 43 and 67% corresponding to CO concentrations of 20 and 100 ppm. Despite their very small size, a still very good variation occurred with the smallest sensors with an increase in the CR between 30 and 40%.

The response time of the sensors were between 1 and 2 min depending on the gas to be detected and its concentration. The theoretical determination of the limit of detection with the 3σ rule (equation (1.3)) could not be computed because of the too low sampling rate of the acquisition system, which made the calculation of the background noise not possible. A strong drift of the baseline occurred during the first two hours of operation of the sensors. They exhibited then a high stability. However, long term operation should be undertaken to quantitatively determine their baseline drift over time.

Additional measurements with 100 μm wide MOX gas sensors were performed in chapter 6 with the multisensor platform. They were carried out at 300°C in an isothermal mode of operation. Their continuous operation was successfully monitored for a period of several weeks.

Influence of the packaging

A comparison of sensors' responses between unpackaged and packaged devices to several concentrations of CO is shown in figure 4.32. The temperature of the sensors was of 250°C since they showed a higher response at this temperature. The packaged sensors exhibited a lower response amplitude. The chemoresistive response of the packaged sensors was between 30 and 70% lower than the unpackaged devices. This could be due to a partial absorption of the gas species in the gas permeable membrane or in the rim. No correlation between the sensor size and the CO gas concentration were noticed for the CR variation. The response time ($t_{90\%}$) of the sensors to the gases when packaged was between 2 and 4 min depending on the device

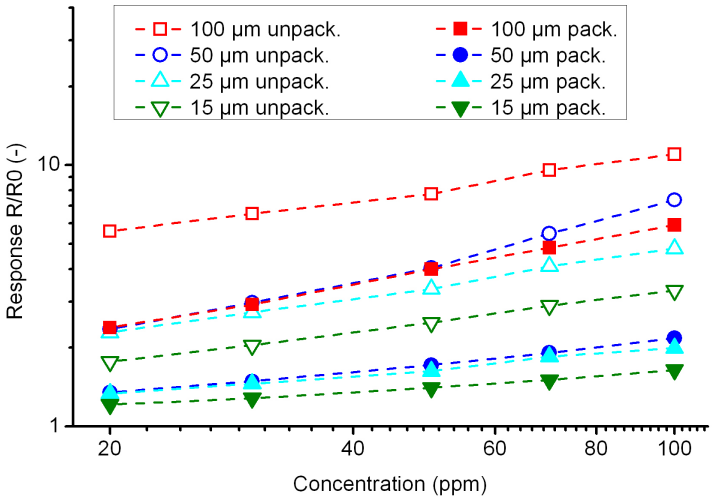

Figure 4.32: Response of the unpackaged and packaged bulk gas sensors when operating at 250°C to several concentrations of CO.

and the gas to be detected. It was increased by 50% compared to the unpackaged sensors.

Pulsed temperature mode of operation

The CO gas measurements when the sensors operated in a pulsed temperature mode are presented in figure 4.33. Only this gas was used because CH_4 cannot be detected in pulsed mode. The resistance of the MOX layer tends to increase compared to the isothermal mode at the same temperature. NO_2 being a oxidizing gas, it increases the resistance of the sensing layer, making it difficult to monitor. In addition, the sensing material used was not optimum for its detection. With the aim of reaching the lowest power consumption possible with an appropriate gas response, the operating temperature was of 200°C.

As for isothermal operation, the responses of the sensors decreased with reducing their active area. The optimized MEMS device gave a higher response than PI sensors for both duty cycles.

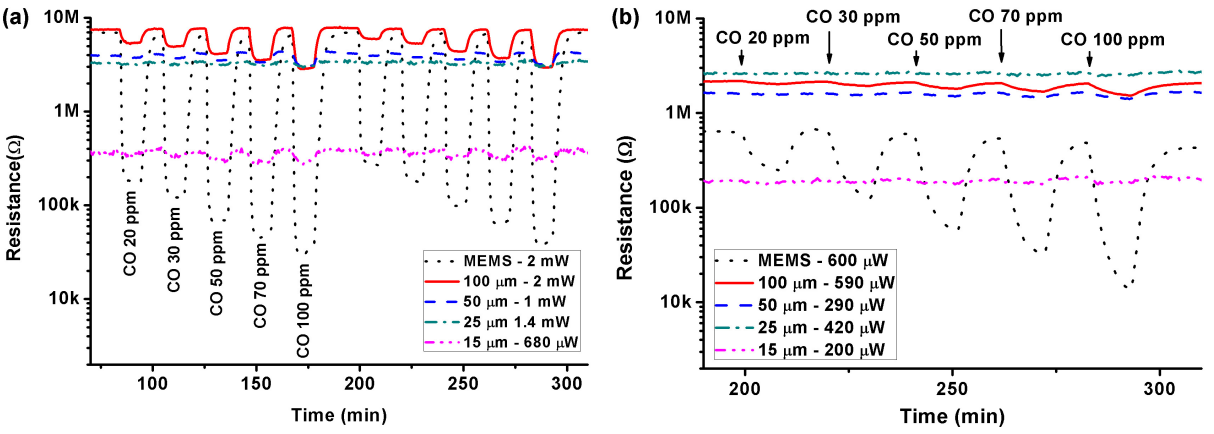

Figure 4.33: CO measurement in pulsed temperature mode (high temperature: 200°C) with a duty cycles of (a) 10% and (b) 3%.

By using a pulsed temperature mode of operation, the power consumption of the devices was drastically decreased. The 15 µm wide sensor reached the sub-milliwatt range in this operating mode with a duty cycle of 10%. By further reducing it to 3%, all devices reached the sub-milliwatt range. However, the gas response was considerably reduced by several tens of percent for the 100 µm wide sensors and this variation decreased with the size of the devices to a few percent for the 15 µm wide ones. The CR of the sensors when exposed to 20 ppm of CO are presented in table 4.19 for a duty cycle of 10% and 3%. The MOX sensors on polyimide exhibited a lower CR than the MEMS device. However, their variation of CR when reducing the duty cycle from 10 to 3% was lower. As before, it can be linked to the design of the transducer, its size, material and W/L ratio of the electrodes. The MEMS sensor lost 92% of its response while a maximum of only 15% was observed for the PI-based devices. Increasing the CO concentration increased the variation of CR between the two duty cycles used here. The reduction of the duty cycle had also an impact on the time response of the sensors as it can be easily observed in figure 4.33b.

Table 4.19: Chemoresisitive response of Pd-doped SnO_2 MOX gas sensors when exposed to 20 ppm of CO in pulsed mode of operation with duty cycle of 10% and 3%.

	MEMS	100 µm	50 µm	25 µm	15 µm
Duty cycle: 10%	26.57	1.30	1.05	1.02	1.12
Duty cycle: 3%	2.17	1.10	1.02	1.01	1.01
Varation (%)	92	15	3	1	10

Comparison between polyimide- and silicon-based sensors

This section aims at qualitatively summarizing the results obtained with the PI and MEMS devices in terms of gas response when operating at 200°C and 250°C. The response obtained with the PI sensors exhibited a lower amplitude than the commercial device as presented in figure 4.34. In general, the response of the Si-based sensor exhibited a response of one to two orders of magnitude higher than the PI sensors. The origin of this behavior may come from the smaller dimension of the active area of the PI devices and there lower W/L ratio. When operating in pulsed temperature mode, the response of the PI devices decreased whereas the signal from the MEMS sensor increased as observed in [235]. A significant increase in the response of the sensors to CO was observed by operating the transducers at 250°C (fig. 4.34d) instead of 200°C (fig. 4.34b).

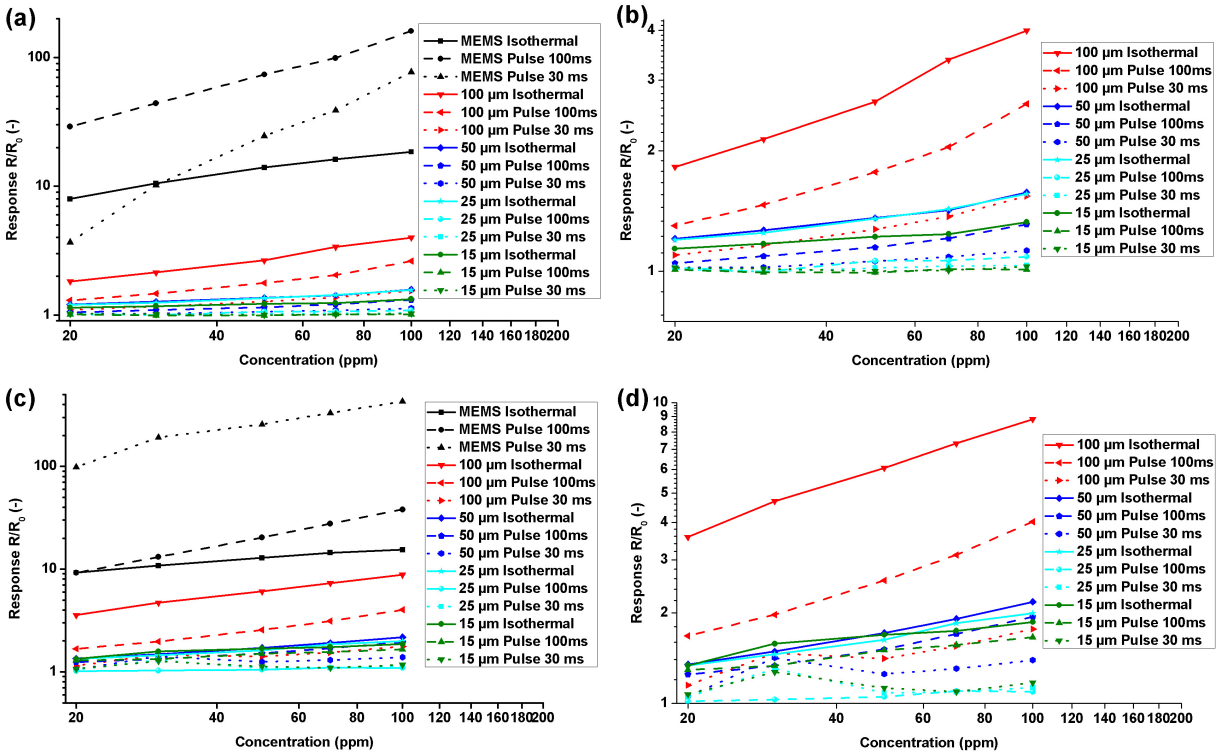

Figure 4.34: Response to CO (a) of the PI bulk sensors at 200°C compared to the MEMS device; (b) of only the PI sensors at 200°C; (c) of the PI sensors at 250°C compared to the MEMS device; (d) of only the PI sensors at 250°C.

4.4 Discussion

The fabrication of the smallest drop-coated metal-oxide gas sensors ever reported was presented. The investigation of their sensing capabilities with the miniaturization of the MOX sensors on polyimide foil was performed. Decreasing the size of these devices arose several observations on their power consumption, operation and sensing performances.

The detection of gases with MOX sensors rely on the change in resistance of a metal-oxide layer, which is known to exhibit a very high resistance. The drastic reduction of the electrode area went with a reduction of the W/L ratio, which increased the resistance and decreased the sensitivity. For the developed devices, the resistance stayed in a reasonable range that can be measured. However, it could become problematic with sensing materials with higher resistivities (e.g. WO_3). By using standard photolithography patterning for the electrodes, we have demonstrated that a sensor signal variation can be observed even with a very small W/L ratio combined with gas sensitive material from the industry.

This extreme miniaturization of the transducer would have been pointless without a suitable coating method to achieve the complete gas sensor. The technology developed here led to the drop-coating of MOX layers with as diameter as small as 20 µm, which has never been demonstrated so far. It was based on a technique compatible with those used by the industry and could be thus straightforwardly applied to the fabrication of greatly size-reduced MOX gas

sensors compared to what is found on the market. Smaller drops could certainly be achieved, but a modification of the metal-oxide paste should be undertaken, mainly to reduce its viscosity so it could fill narrower capillaries.

The next step here would be to investigate other fabrication techniques compatible with mass production to design the heater and the electrode layers. An issue remains with the minimum width of the heater lines. They need to be precisely defined to obtain a uniform temperature over the heated area, which is important for selectivity. The actual state-of-the-art in roll-to-roll processing does not reach the resolution that were required here.

4.4.1 Electrothermal modeling

The mean heat transfer coefficients were extracted from the thermal measurements and this for all the fabricated devices and are given in figure 4.35. With the extracted values, one notice the coefficient was very accurate for all the bulk devices, while it was overestimated for those with a membrane smaller than 100 µm. This study showed that the mean heat transfer coefficient in air has a clear dependence on the device geometry. It thus has to be properly determined. This is especially the case for the smallest heating areas where the mean heat transfer coefficient considerably increases (fig. 4.7). Therefore, coefficients directly taken from literature may lead to major imprecisions for designing a device. To improve the accuracy of the simulations, coefficients with different values should be used for the rim around the heated area, the top and the backside of the device to include the influence of the geometry of the membrane and of the packaging. Taking into account the variation of the mean heat transfer coefficient in air as a function of the temperature would further improve the accuracy of the simulation model. However, its experimental determination is highly challenging and is beyond the scope of this thesis. It involves fundamental work on the heat transfer at the micro-scale.

For a same power supplied to the hotplates to reach 300°C during the experimental charac-

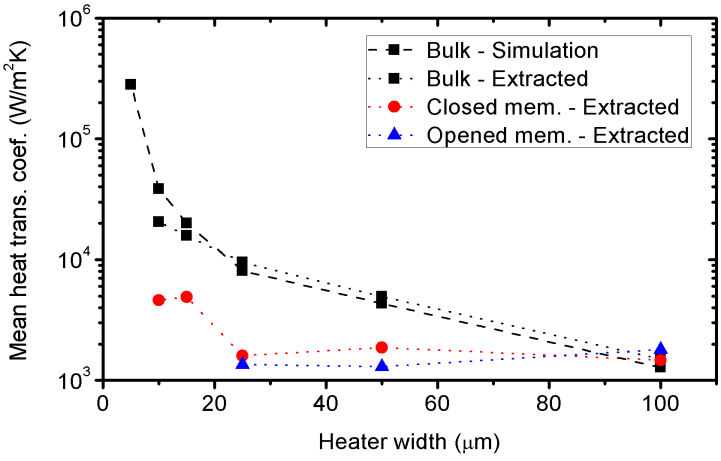

Figure 4.35: Mean heat transfer coefficients in air at 300°C extracted from polyimide-based micro-hotplates.

terization, the temperature variations between the experimental data and the simulations were of less than 12% for most of the bulk devices, except the 10 μm wide one (16%). These low variations were due to remaining inaccuracies in the electrothermal simulation. For instance, the same value of the mean transfer coefficient was applied to all the external surfaces of the chip and the thermal conduction of Pt was taken from a handbook, which were both not set as temperature dependant. Additionally, a slight change in the heater layout between the first and second series of bulk hotplates might also cause a small difference in the results obtained. Higher variations (up to 50%) were observed for the devices with a membrane. The fabricated devices exhibited lower power consumptions than the simulated ones due to a lower mean heat transfer coefficient when a membrane was integrated.

The temperature variation over the heated area between the experimental measurements and the simulations were generally lower than 10°C. It showed the high accuracy of the thermal parameter used. In general, smaller gradients were found for the measured hotplates compared to the simulations. It can be attributed to a change in thermal conduction with an increased temperature of the polyimide and the Pt, while those parameters were kept constant throughout the simulations with their values at room temperature. The 10 μm wide hotplates however exhibited a higher difference, which could be due to a combination of several reasons. Beside the thermal conductivities of the materials, a slight misalignment between the heater layer and the electrode layer may occur and lead to a significant difference of the temperature measured.

To further make the simulations more accurate, the thermal conductivity of the Pt and its variation with the temperature should be taken into account. Its precise determination was not essential for determining the power consumption of the largest device (100 μm wide with a closed membrane). A variation of 30% in the value used in this study – 70.6 W/m·K – led to an error on the power consumption of 3.5%. Therefore, values taken from handbooks should be avoided when designing very small devices. The error on the power consumption to achieve a specific temperature became significant when reducing the size of the heated area. Again, an imprecision of 30% in the Pt thermal conductivity altered the power consumption by 16.2% in the case of the 10 μm wide hotplate with a closed membrane when reaching 300°C. However, if looking at the power needed to operate the device at 300°C, these variations corresponds to an absolute error of about 1 mW.

4.4.2 Power consumption of the PI hotplates

The use of polyimide substrate offers some advantages over Si-based devices with a membrane made of Si_3N_4 and/or SiO_2 in term of mechanical stability and thermal insulation. According the *Upilex-50S* datasheet, its Young modulus was of 9.1 GPa, while those of silicon nitride and oxide are respectively of 310 and 151 GPa [253]. Devices made of polyimide would be thus more mechanically robust than devices made from Si substrates. Despite a thicker membrane, PI devices required only a membrane diameter twice wider than the heated area due to its lower thermal conductivity (0.29 W/m·K for the PI used here). Space can be thus saved

compared to Si-based transducers, where the use of Si_3N_4 and/or SiO_2 for the dielectric membrane (thermal conductivities respectively of 16 and 1.38 W/m·K, respectively [248]) involves a factor of 2.6 [215].

A closed membrane can reduce the power consumption compared to bulk devices (between 37 and 56% depending on the hotplate size), which can be further decreased by etching through holes to lower the thermal losses (up to 35% for the widest device here). However, for a 25 μm wide hotplate, and very likely smaller designs, an opened membrane only increased the complexity of the fabrication for an insignificant gain in power consumption. A smaller difference in power consumption between bulk devices and hotplates with a closed membrane was noticed when decreasing the size of the heated area.

Due to the very low thermal conductivity of the polyimide, power savings of only a few mW were achieved with the smallest hotplates with a membrane. By avoiding bulk micromachining of PI, the device is mechanically more stable. Its fabrication is simplified and potentially more cost effective by making it compatible with mass production processes. Furthermore, bulk devices could achieve a lower power consumption at no additional cost by fabricating them on thinner polyimide foils than the one used in this study (50 μm in thickness).

Regarding to the heater, the thermal losses could be further decreased by reducing the power lost in the electrical pathways. It could be achieved by fabricating a heated area with a higher resistance than the actual one. A material with a higher resistivity than Pt could be used while keeping its electrical connections with a material having a lower resistivity. By increasing the resistance in the heated area, the current would be reduced to reach the targeted power. With a reduced current, lower losses by Joule effect would therefore occur in the electrical connections. The current density would be decreased as well, delaying electromigration effects.

4.4.3 Gas sensing performances

The polyimide-based metal-oxide gas sensors exhibited a good sensitivity to representative oxidizing and reducing gases. Due to their smaller active areas and lower W/L ratio, their responses were lower than those of the commercial MEMS device (sensing area of 450 μm) used as a reference. Among the possible causes that can influence the response, the material used as substrate under the gas sensitive layer – polyimide and not silicon nitride as for the MEMS device – can also play a role in gas interactions [71].

Additional tests should be performed when operating the sensors in a pulsed temperature mode. This measurement method allows power savings that are highly desired for devices aiming at their integration in wireless systems. As observed, the response of the sensors decreased significantly when reducing the duty cycle. Experiments with both longer periods and heater on-time could be envisaged to keep small duty cycles – and low power consumption – and obtain a higher response to gases. In addition, experiments with other gases and coating materials could be foreseen to determine their impacts on the selectivity that can be achieved with such devices when operating them in both isothermal and pulsed temperature modes. By using

different modes of operation and sensing materials, the gas species can be identified [162, 172].

By comparing the sensor signals when operating in constant and both pulsed temperature modes, the response of the PI sensors decreased with the duty cycle, while the MEMS devices gave a higher response when the temperature was cycled as found in literature [235]. The MEMS device was optimized to operate in such conditions and had a wider sensing area with a higher W/L ratio than the PI devices. These factors were not investigated here and therefore not optimized.

Finally, experiments should be undertaken on the long-term stability of these gas sensors. Preliminary results are given in chapter 6 with their continuous operation at 300°C for about two months. The possible applications of these devices could be defined depending on their life time.

4.5 Conclusion

The miniaturization of drop-coated metal-oxide gas sensors on plastic foil was carried out to investigate its impact on their sensing performances with low power consumption. The fabrication of MOX gas sensors and their complete integration on plastic foil targeting wireless applications was demonstrated. Their transducers were optimized in term of power consumption by using electrothermal simulations. Several aspects were pointed out to design ultra-low power hotplates, such as the influence of a membrane, and the resistivity and geometry of the electrical pathways to the heaters. The simulation results were in very good agreement to the experimental measurements. The devices were fabricated on polyimide foil with standard microfabrication equipments. The deposition of the gas sensitive layer was performed by drop-coating with custom-made micropipettes to achieve the smallest thick-film MOX gas sensor ever published. The smallest droplet had a minimum diameter of about 20 µm and was lying on a 15 µm wide transducer. An original method was proposed for their packaging at the foil level with a dry technique based on the lamination of pre-patterned structures and finally covered with a gas permeable membrane.

By deceasing the size of the heated area of the transducer and by incorporating a membrane, consumptions in the low-milliwatt range were achieved. A power consumption as low as 6 mW was required to reach 300°C with a 15 µm wide heater with a closed membrane in a continuous operating mode. With a simplified fabrication process avoiding the bulk micromachining of the polyimide foil, only 10 mW was necessary with the same heater size. Furthermore, lower power consumptions could be reached with bulk devices by using a thinner polyimide foil as substrate.

Successful gas measurements of CO, CH_4 and NO_2 in both continuous and pulsed temperature modes proved the proper operation of the sensors with power consumptions as low as 200 µW. Lower powers might be reached by further reducing the duty cycle of the heating element. The PI sensors however exhibited a lower chemoresistive response than MEMS sensors, mainly because of the reduced size of the electrodes, which decreased the sensitivity of the

devices.

Other investigations should be performed on the further decrease of their power consumption by benefiting of the advantages that can bring a pulsed mode of operation. Additional tests should be carried out to investigate the sensitivity of these devices with longer periods between two successive measurements. Devices with a very low power consumption could be thus foreseen for their integration in wireless systems. Future developments should include their improved compatibility with production techniques compatible with large scale manufacturing. The use of additive processes for the fabrication of the heater and the electrodes would bring some advantages, mainly in cost-efficiency.

Chapter 5

Capacitive gas sensors on plastic foil

5.1 Introduction

After the selective detection of ammonia in chapter 3 and oxidizing/reducing gases in chapter 4, this chapter deals with the development of a VOCs (Volatile Organic Compounds) and humidity sensor fabricated on a polyimide foil. We have investigated in particular how the affinity of the polyimide substrate could be exploited in gas sensing through a capacitive detection. It resulted in some benefits for the discrimination between humidity and measurements of gases.

The concept presented in this chapter involves a very easy fabrication with only one metalization layer and no alignment requirement. It consisted in only the patterning of electrodes on a foil used as sensitive dielectric. Such a structure is possible due to the inherent nature of the substrate to response to the environment (mainly humidity). To further improve the functionality of the device, another capacitive structure was coated with a polymeric material sensitive to VOCs. These gases are widely encountered in the environment and are found in paints, coatings, fuels and refrigerants, just to name a few. They are present in buildings and an important source is in the agriculture field.

By operating the two capacitors in a differential mode, several parameters can be deduced. The influence of the substrate can be canceled to obtain only the response to gases of the sensing film deposited on the second capacitive structure. Moreover, parasitic effects can also be suppressed. The sensing performances of these highly simplified devices were investigated to determine their ability of being used as gas sensors with high sensitivity. By combining them with the state-of-the-art of commercial capacitive readout, humidity, temperature and low levels of VOCs were detected on the same platform with the use of a common plastic foil. Such development can lead to the fabrication of low-cost sensors fabricated on substrates compatible with large scale fabrication to reduce their manufacturing cost.

The design of the sensing platform presented in this chapter rely only on one fabrication step on a plastic substrate to obtain electrodes as a capacitive structure, making the device simpler than the optical sensor presented in chapter 3 or the chemoresistive device in chapter 4, which

required a more complex processing. By using capacitive transduction, the consumption of the device becomes negligible and the main part of the power needed to operate it is for its electronic readout, making it very attractive for wireless systems.

5.1.1 Operating principle of a capacitive gas sensor

A capacitor is composed of two electrodes separated by a dielectric material as illustrated in figure 5.1. The capacitance value , C, of the capacitor is defined as:

$$C = \frac{\varepsilon_0 \cdot \varepsilon \cdot A}{d} \tag{5.1}$$

where ε_0 and ε are respectively the permittivity of the free space (8.85×10^{-12} F/m) and the dielectric constant of the material between the two electrodes. A is the area of the electrodes and d the distance between them.

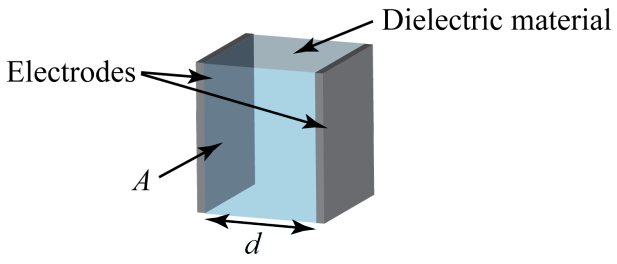

Figure 5.1: Schematic three-dimensional view of a capacitor. Two electrodes of area A are separated by a dielectric material of thickness d.

For the sensor developed in this study and schematized in figure 5.2, the system had interdigitated electrodes to increase the A/d ratio – thus the capacitance – and keep a planar structure with small dimensions. Since the substrate and the top layer of the device are made of different materials, their dielectric constants differed. The sensors can thus be seen as two capacitors in parallel, one related to the substrate, C_{sub}, and the other to the top layer (air or sensing material), $C_{top\ layer}$:

$$C = C_{sub} + C_{top\ layer} \tag{5.2}$$

For both C_{sub} and $C_{top\ layer}$, the only difference are their dielectric constants. All the other parameters are either dimensional factors or constants and stay the same. Hence, equation (5.1) can be rewritten as:

$$C = \frac{\varepsilon_0 \cdot \left(\varepsilon_{sub} + \varepsilon_{top\ layer}\right) \cdot A}{d} \tag{5.3}$$

The capacitive detection of chemical species thus rely on the change of these dielectric constants and/or on the effective thickness of the dielectric layer due to swelling [254]. For most of polymeric substrates, the analyte will diffuse in it, modifying its dielectric properties. The

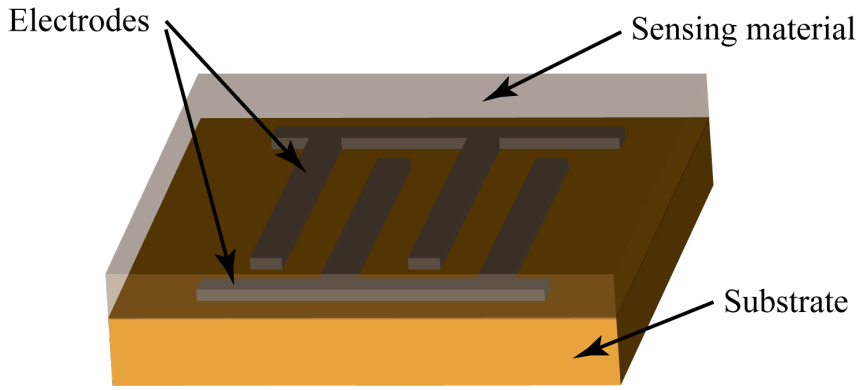

Figure 5.2: Schematic three-dimensional view of a capacitive sensor. Interdigitated electrodes are lying on a substrate and can be covered with a sensing material.

polymers usually used – PI, PEN, PET – have low dielectric constants, between 3 and 6, while that of water for instance is about 80 at room atmosphere [255]. When increasing the relative humidity in the environment, the dielectric constant of the polymer will increase due to the absorption of water. The same behavior occurs with gases and their ability to be capacitively sensed depends on their dielectric constants and the swelling of the film. The simplest device that can be thus fabricated out of polymeric material consist in only depositing a conductive material used as electrodes on the substrate. In this configuration, the top layer is the surrounding media, typically air. The device can be further functionalized by coating the capacitor with a material with specific sensing properties. Each polymer/analyte combination has a particular partition coefficient, K, which is the ratio of the concentration of an analyte in the gas phase to the concentration in the solid material. This coefficient varies exponentially with the temperature in thermal equilibrium ($\Delta G = 0$):

$$K = exp\left(-\frac{\Delta G^0}{R \cdot T}\right) \tag{5.4}$$

where ΔG^0 is the variation of standard free Gibbs energy, R, the ideal gas constant equal to 8.3145 J/mol·K and T the absolute temperature. The more negative ΔG^0, the larger K is, the larger is the reaction extent and the more spontaneous the latter will occur. The sensitivity and selectivity of the sensor can thus be enhanced by choosing the adequate sensing material as a function of the analyte to be detected. As a result, when exposed to a gas in this arrangement, both dielectric constants of the substrate and the functional material will vary according to its concentration in the surrounding atmosphere and the affinity of the film towards specific analytes.

5.1.2 State of the art

Ceramics [256, 257] or polymers [254, 258] have been proposed for the capacitive detection of humidity by exploiting the variation of their dielectric properties. Two interfacing methods

have been investigated, through resistive [51] and capacitive [254, 256] measurements. The capacitive detection presents several advantages over the resistive one. It exhibits a better linear response [78, 258], needs a less complex electronics, can operate over a wider range of relative humidities [259]. In addition, its operation requires almost no power, but that of the readout electronics [260]. To reduce the sensor drift and improve the response to specific analytes, the differential measurement of two capacitors was proposed on Si substrate [261]. In this configuration, one capacitor was coated with the sensing material, while the second was passivated as a reference.

Due to the low capacitance of capacitive sensors (pF range), the readout circuitry was often devised directly with the sensing device. Such systems were based on a CMOS electronic circuitry with a set of detecting electrodes on top of the chip [257]. Further developments led to the fabrication of "3D" structures by using a second metal layer of the CMOS process to enhance the humidity sensitivity of the sensor [261]. As sensing material, polyimide has been widely studied on such systems due to its CMOS compatibility and high humidity absorption [77–81]. Moreover, by selecting adequate sensing polymers, the detection of gases was also performed [257]. To improve the selectivity of capacitive structures as gas sensors, several studies were reported on the evaluation of different polymers employed as sensing films [254, 258, 262]. Polymers with different partition coefficients towards defined gases can be used to improve the selectivity of the sensor. The influence of the polymer thickness to discriminate VOCs with water was also reported [263]. In these studies, the gas concentrations detected were usually much higher than the TWA (Time Weighted Average[1]) exposure doses [264–266], limiting the applications of the sensors developed.

With the increasing demand for low-cost and high throughput device fabrication, such as for wireless systems, their is a growing interest in structures fabricated from inexpensive plastic foils. They were mainly fabricated on PEN (polyethylene naphthalate), PES (polyethersulfone) or PI (polyimide) for the detection of humidity [49, 259, 267]. These polymeric substrates are primarily used for industrial fabrication of flexible printed circuit boards (flexPCB) and flexible displays.

5.1.3 Progress beyond the state of the art

The device presented in this chapter was based on PI to take advantage of its high response to humidity compared to PET or PEN. This material as well as the platinum for the electrodes were also selected with the aim of combining the capacitive structures developed in this chapter with the metal-oxide sensors in chapter 4 to implement a multisensor platform with advanced sensing capabilities presented in chapter 6.

Compared to previous studies based on polyimide as substrate [49], the metallic electrodes were made of platinum, which is commonly used in chemical sensors due to its chemical inert-

[1]The average exposure to a contaminant to which workers may be exposed without adverse effect over a period such as in an 8-hour day or 40-hour week.

ness and high stability over time. The benefit of the presence of a second capacitor coated with a polymer will be exploited to achieve higher functionalities and improve the sensing abilities of the platform towards volatile gaseous compounds. Unlike Si-based devices, one can take advantage of the substrate's response to the environment and combine it with the signal measured from the coated capacitor. By doing so, new sensing and discrimination abilities are offered. With a simple architecture, the detection of VOCs, humidity and temperature was demonstrated.

The measurement methodology employed here was based on a differential measurement of the two capacitors to remove the parasitic effects of the polyimide substrate from the sensing film coated capacitive structure. However, the signal from the substrate response to humidity can also be exploited to improve the discrimination between humidity and VOCs. By subtracting the signal from the two capacitors, the background influence of water was removed to enhance the sensitivity towards VOCs. Moreover, contrary to what is commonly found in the literature, the devices developed here were exposed to concentrations of gas species in the TWA range, widening their field of use for human comfort or safety applications. To achieve theses goals, the readout of the sensor was ensured by a commercially available IC (Integrated Circuit), instead of a dedicated CMOS circuit or laboratory equipment.

5.2 Experimental

5.2.1 Design and fabrication of the capacitive sensing platform

The device was fabricated on polyimide foil due to its high sensitivity to humidity and to make it compatible with the metal-oxide gas sensors presented in chapter 4. Their combination will lead to the design of a multisensor platform (chapter 6), in which the MOX structures require a high temperature to operate. The sensing device designed in this chapter embedded two capacitive structures – as chemical sensors – and a resistance thermometer integrated on the same substrate. The chip was designed in order to interface it directly with a commercial capacitance-to-digital converter from the latest generation of low-power IC.

Figure 5.3 shows the fabricated device. The gas sensing function was provided by a polymer layer deposited over one of the planar capacitors. They had a 30 µm electrode width and gap

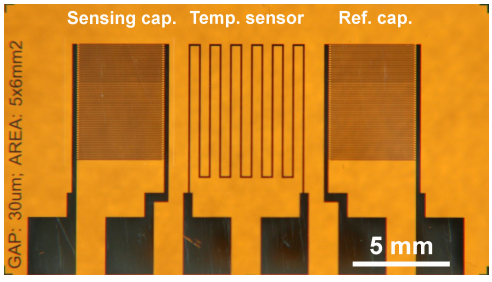

Figure 5.3: Capacitive (left and right) and resistive (center) structures fabricated on a polyimide foil. The electrode width and spacing were of 30 µm. The size of the chip was of 14×25 mm^2.

spacing, which corresponded to the thickness of the polymeric film deposited on the sensing capacitor. The electrodes covered an area of 5×6 mm^2 to achieve a nominal capacitance 10 pF that was required by the IC used for its readout. A resistance of 1 kΩ for the RTD was targeted to ensure a good temperature sensitivity. The whole chip area was of 14×25 mm^2. Its size was defined by the electrical connectors of the readout.

The devices were manufactured on a 4" wafer of 50 μm thick commercial polyimide. Our choice was the *Upilex-50S* from *UBE Industries, Ltd* to use the same substrate than the MOX sensor developed in chapter 4. Deposition by sputtering and a lift-off technique were used to fabricate and pattern the electrical elements, based on a 130 nm thick, 1.06 $\Omega/\square$ platinum film deposited above a 20 nm titanium adhesion layer. Therefore, only one technological step was required to obtain the capacitive devices, making it a very simple structure. In the last technological step, commercial PEUT or PDMS (*Fluka*) test sensing layers were deposited by drop, spray or spin coating onto the sensing capacitor of the platform substrate. These polymers were selected because of their known sensitivity towards VOCs. The thickness of the sensing layers were between 10 and 30 μm, which corresponded to the inter-electrode spacing. The deposition of the functional layers was carried out at the *Institute of Physical Chemistry* (*IPC*) of the *University of Tuebingen*, Germany. The remaining capacitive transducer was left uncoated. It was used as reference during the measurements, but also to benefit from the sensing ability of the substrate towards gaseous compounds. The platform layout allows the coating with a wide range of sensitive materials, depending on the analytes to be detected. The choice of polymers employed here was not made for any specific application but to demonstrate the high sensing potential of this device architecture.

5.2.2 Electronic readout

The sensing device was designed for low-power readout electronics, which was designed and realized at *IPC*. For these experiments, a dual differential $\Sigma\Delta$ capacitance-to-digital converter was employed. The model chosen was the *AD7746* from *Analog Devices*. This IC has a very high resolution of 4 aF (4 pF over 24 bits) and it can be brought to a very low power dissipation level when operating at a reduced acquisition rate. Its sleep mode power consumption is of 10 μW. Additionally, the IC includes a voltage/resistance input that was used for the interfacing of the temperature sensor.

The acquired data delivered on an I^{2}C bus of the *AD7746* were recorded on a computer through a I^{2}C-to-USB converter developed by *JLM-Innovation GmbH* [268]. The sensing device interfaced to the IC is presented in figure 5.4. The data treatment was performed with standard softwares, but it could be done using a microcontroller if the device was embedded in complete system. In most of the measurements, the electronic circuitry was kept at the same temperature than the sensing platform to simulate real working conditions. Compared to acquisition at room temperature, no difference occurred.

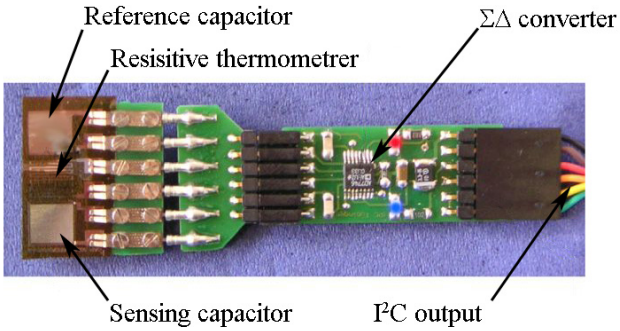

Figure 5.4: Photograph of the sensor platform connected to the readout electronics based on a capacitance-to-digital converter.

5.2.3 Gas measurements

To evaluated their gas sensing performances, the capacitive sensors were exposed to several VOCs and humidity levels. The gas measurements were performed at *IPC*. The gas mixtures were prepared by a computer driven gas mixing system. Depending on the availabilities of the gas mixing stations, the different sensors were not exposed to exactly the same gaseous species. Figure 5.5 shows a typical gas sequence used to appraise the sensing abilities of the platforms. The four chosen gas concentrations usually started with values close to the TWA threshold. They are given in table 5.1. The platform was first exposed to the gases in a dry atmosphere before adding a background of 50% relative humidity (RH). In the last step, the response of the chip was measured under several humidity levels. The n-hexane exposure however did not fulfill this criterion because of some functional limitation on the allocated channel in the gas mixing system. Beside to the Pt thermometer embedded in the sensing platform, the temperature in the measurement chamber was independently monitored with a Pt thermometer (Pt 1000, *UST GmbH* [269]) and took as a reference.

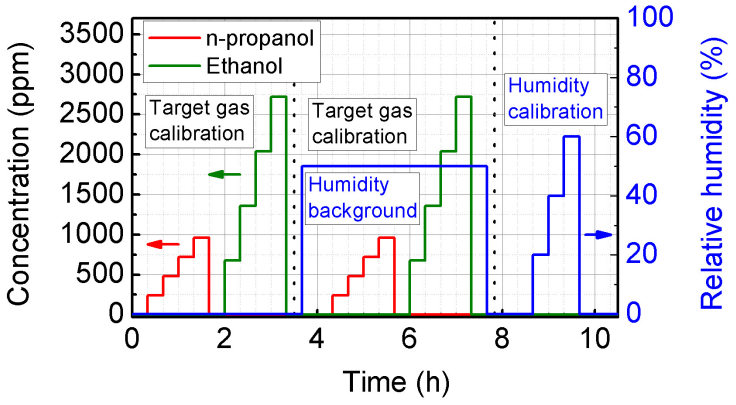

Figure 5.5: Typical gas sequence used to characterize the sensors. The sensing platform was first exposed to the targeted gases in a dry atmosphere, followed by a background humidity of 50% RH. The response of the device to different humidity level was carried out at the end of the sequence.

Table 5.1: Selected gases, their concentrations used in these experiments and their dielectric constants at a given temperature[a]. The TWA were taken from the Swiss Accident Insurance Fund (Suva) [270].

	Exposure step (ppm)				ε	TWA
Gas	1	2	3	4	(-)	(ppm)
Dimethyl pentane (ppm)	500	1000	1500	2000	1.91 (-7°C)	-
n-Hexane (ppm)	1500	3000	7500	15000	2.02 (-90°C)	50
Toluene (ppm)	50	100	150	200	2.4 (20°C)	50
Ammonia (ppm)	5	10	25	-	16.5 (21°C)	20
n-Propanol (ppm)	240	480	720	960	20.1 (81°C)	200
Acetone (ppm)	500	1000	1500	2000	20.7 (25°C)	500
Ethanol (ppm)	780	1360	2140	2720	24.3 (25°C)	500
Humidity (ppm)	5000	10000	15000	20000	80.4 (20°C)	-
Humidity (%)	20	40	60	80	80.4 (20°C)	-

[a] The dielectric constant decreases with the temperature.

5.3 Results

The results obtained with the sensing platform made of polyimide are presented in this section. First, the raw responses acquired by the readout will be presented. The combination of the information provided by the two capacitors will be combined to separate the signals due to humidity and to VOCs. In a second phase, calibration curves will be presented to give the influence of VOCs and humidity for both the investigated sensing films. Their performances could be thus compared and discussed.

5.3.1 Raw signals and benefits from the differential mode of measurement

The raw signals acquired through the capacitance-to-digital converter with the sensing capacitor coated with PDMS and the uncoated one are shown in figure 5.6. The device was exposed to VOCs and humidity. When exposed to the analytes, the capacitance shift increased due to the higher dielectric constants of the absorbed analytes as compared to the polymer films used as substrate and sensing layer. Note the strong sensitivity to humidity of both channels as well as the very long time constant required to stabilize the sensor response. One observes the uncoated capacitor did not exhibit any response to the targeted gases. To circumvent the parasitic influences of the substrate, a differential operation mode was used. The signal from the reference channel was subtracted from the sensing channel during post-processing of the data. In figure 5.6, it corresponded to subtract the “Upilex-50S” signal from the “PDMS/Upilex-50S” measurement. The differential response is displayed in figure 5.7.

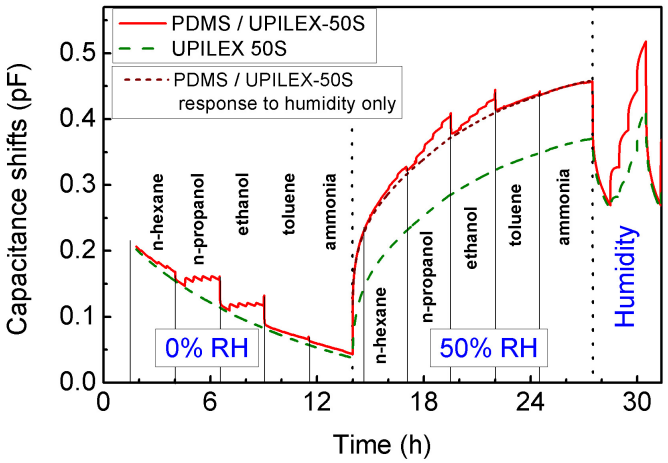

Figure 5.6: Raw signal from a 30 µm sensor with spin-coated PDMS when exposed to n-hexane, n-propanol, ethanol, toluene and ammonia. The response of the substrate is also included.

The large drifts and the long response times encountered with the raw signals (fig. 5.6) were almost completely removed by operating the two capacitors differentially as it can easily be observed in figure 5.7. By doing so, the response of the sensing layer to very low capacitance shifts could still be observed. The response of the film to VOCs was still high – with a capacitance shift in the fF range – but even very lower shift of few hundreds of aF were still detectable, as for ammonia. The latter was also detectable in the presence of 50% of RH, despite a capacitance shift of 85 fF due to humidity absorption in the substrate.

The differential response of the platform actually represents the signal obtained only by the

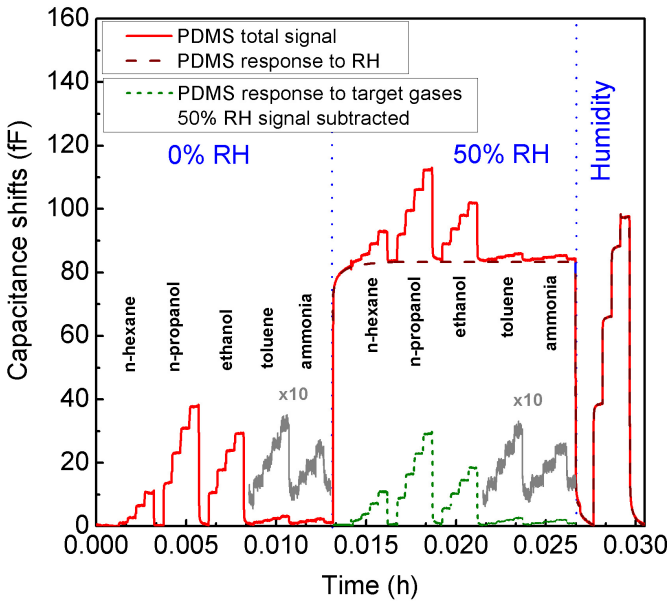

Figure 5.7: Processed signal from a 30 µm sensor with spin-coated PDMS when exposed to n-hexane, n-propanol, ethanol, toluene and ammonia. The response of the substrate is also included.

sensing layer alone to the ambient atmosphere, without the contribution of the substrate. The intrinsic sensitivity to humidity is however still enclosed in this signal. It is possible to remove its influence from the targeted gases by a second numerical subtraction as illustrated in figure 5.7. It was performed by removing the response of the PDMS film when only exposed to humidity from the signal when this layer was exposed to the targeted gaseous species in the presence of humidity. The humidity background can thus be canceled and only the response of the PDMS to the gases in the atmosphere can be obtained. The signal however still slightly differed from the one obtained without the presence of humidity, very likely due to cross-sensitivities of the gases and humidity.

5.3.2 Response of the substrate to humidity and temperature

The intrinsic sensitivity of the substrate could be seen first as a drawback for such application, but it is not necessarily the case. The uncoated capacitor can be used as a humidity sensor for specific applications where the humidity level is expected to vary slowly. The response of only the substrate towards humidity at different temperatures is presented in figure 5.8 together with the calibration of the temperature sensor embedded on the same chip. Noticeable capacitance shifts were measured, confirming that only the substrate covered with appropriate electrodes can lead to a humidity sensor.

Polyimide is known for its permeability to water [79]. While increasing the temperature, the graph in figure 5.8 shows the capacitance shift went up as well. It can be explained as follow. To keep the relative humidity constant when increasing the temperature, the absolute humidity has to be increased as well, leading to a higher concentration of water molecules in the atmosphere. With an increased concentration of water, the change of capacitance will be higher. Both the isothermal response to humidity and temperature influence at constant relative humidity levels led to non linear capacitance shifts.

Regarding to the temperature sensor, it showed a very high linearity. It had a resistance of

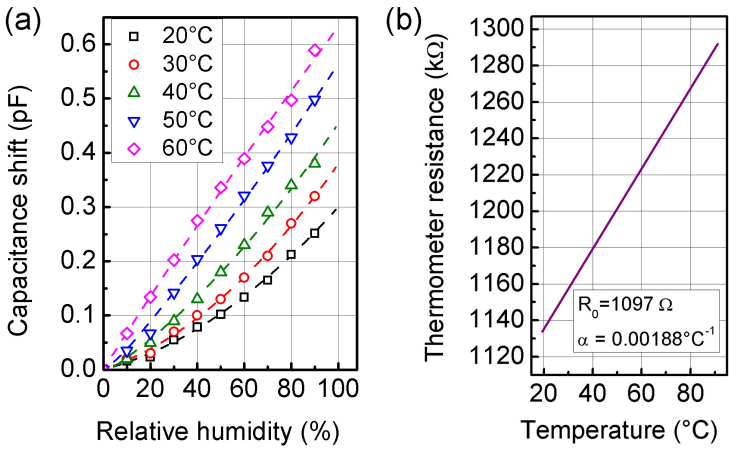

Figure 5.8: (a) Calibration curves of the *Upilex-50S* foil towards humidity and (b) calibration curve of the Pt thermometer.

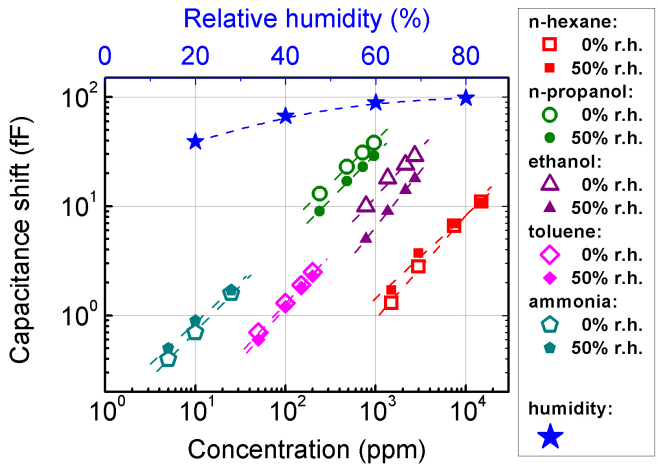

Figure 5.9: Calibration curves of the 30 µm sensor with spin-coated PDMS for the selected targeted gases. For the gas signal, the response from the substrate was subtracted as well as the response of the sensing film to humidity.

1097 Ω at 0°C and a TCR (Thermal Coefficient of Resistance) of 0.00188°C^{-1}. The latter was measured in an computer-controlled oven.

5.3.3 Response of the PDMS to humidity and VOCs

From the gas measurements, the calibration curves were derived for the gas sensing films. They were extracted from the differential measurement and the subtracted response obtained. The calibration curves for the PDMS-coated capacitor are given in figure 5.9. The response to the five targeted gases gave a linear response in dry air. In the contrary, when humidity is present in the atmosphere, the film had a non-linear behavior with water vapor concentrations. The gas concentration could however be retrieved by using a second humidity sensor, such as the uncoated capacitor in this case. The linear response of the capacitance shift to gases could thus be recovered once the influence of RH was removed from the signal. The sensitivities of the PDMS coated sensor towards the five investigated gases are given in table 5.2. The highest sensitivity (67 aF/ppm) was reached with ammonia, while the lowest one was obtained with n-hexane was of 0.82 aF/ppm. Toluene showed the best linearity with the highest coefficient of determination in dry air and a very high value with a background of humidity. It also exhibited the lowest variation of sensitivity between 0% and 50% of RH with a variation of only 8%.

5.3.4 Response of the PEUT to humidity, VOCs and temperature

Similar responses were obtained with the PEUT coating and are displayed in figure 5.10. As for the PDMS coating, the differential response of the sensor to the five targeted gases showed linear responses in both dry atmosphere and in air with a 50% humidity background once the influence of the latter was removed from the signal.

Table 5.2: Sensitivities obtained with the 30 µm sensor coated with PDMS. The film showed a good linearity to all gaseous species.

	0% RH		50% RH	
Gas	Sensitivity (aF/ppm)	Coef. of determination (-)	Sensitivity (aF/ppm)	Coef. of determination (-)
n-hexane	0.82	0.9889	0.92	0.9674
n-propanol	39.58	0.9840	30.21	0.9908
ethanol	10.73	0.9842	6.65	0.9998
toluene	12.50	0.9990	11.50	0.9988
ammonia	66.67	0.9767	77.78	0.9967

The sensitivities and coefficients of determination of a linear regression of the response of PEUT to the analytes are given in table 5.3. The highest sensitivity was obtained when the film was exposed to n-propanol. It was of 73.50 aF/ppm in dry air and increased to 114.25 aF/ppm with humidity. Similar responses were achieved with the other compounds, except for toluene. Therefore, the presence of water molecules seemed to enhance the VOC absorption in the film. As for PDMS coating, the smallest difference between dry and wet air arose with toluene with a difference of 7.6%. The PEUT exhibited a high linear response to all the gaseous species. They were higher when VOCs were in dry air than with a 50% humidity background. Additional measurements were performed with the PEUT coated on the multisensor platform. They are presented in chapter 6.

Figure 5.11 presents the calibration curves of the PEUT-coated capacitor when exposed to

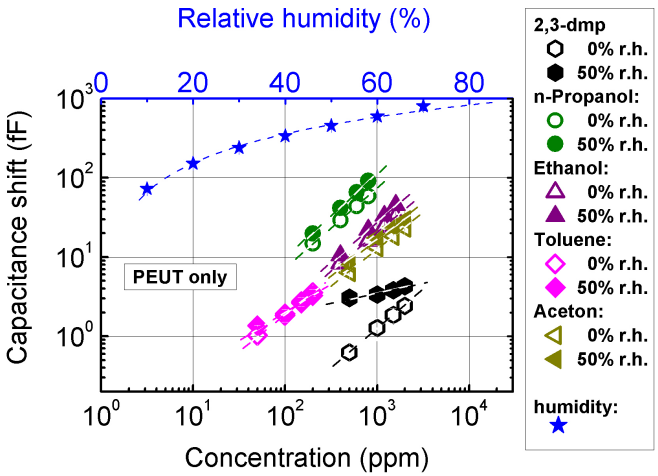

Figure 5.10: Calibration curves of the 30 µm sensor with spray-coated PEUT for the selected targeted gases. For the gas signal, the response from the substrate was subtracted as well as the response of the sensing film to humidity.

Table 5.3: Sensitivities obtained with the 30 µm sensor coated with PEUT. The film showed a good linearity to all gaseous species.

	0% RH		50% RH	
Gas	Sensitivity (aF/ppm)	Coef. of determination (-)	Sensitivity (aF/ppm)	Coef. of determination (-)
dimethylpentane	1.22	0.9989	2.15	0.9929
n-propanol	73.50	0.9999	114.25	0.9988
ethanol	20.13	0.9995	28.38	1.0000
toluene	17.75	0.9997	16.40	0.9979
acetone	11.65	0.9925	14.65	0.9837

n-propanol and to ethanol. The sensing platform was at different temperatures and the influence of humidity is also shown. Again, a higher linearity was obtained for sensor exposed in dry atmosphere than when exposed to 50% RH. In both cases, without or with humidity, the

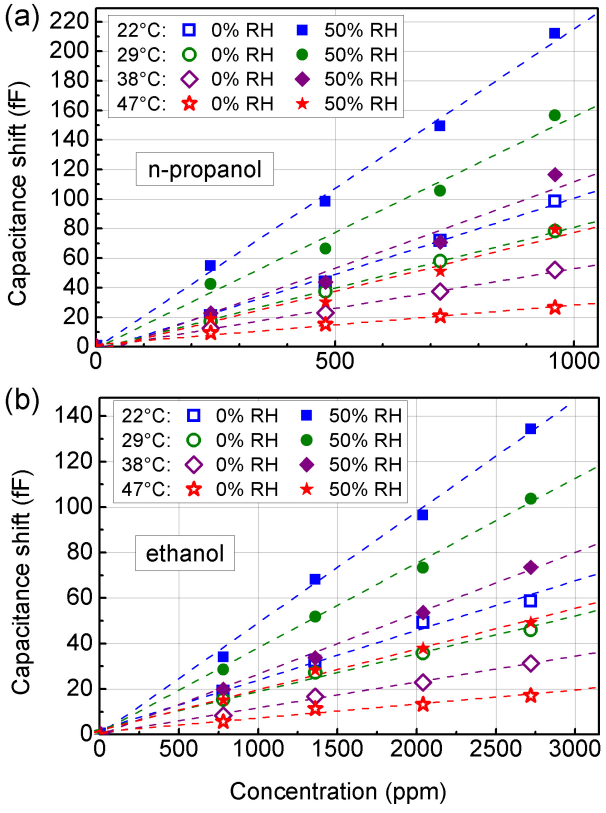

Figure 5.11: Calibration curves of the 30 µm sensor with PEUT coating for (a) n-propanol and (b) ethanol at different temperatures measured with the embedded Pt thermometer.

sensitivity to the target analyte decreased with the temperature. In the case of n-propanol, the sensitivity was of 0.10 fF/ppm at 22°C and was reduced to 0.03 fF/ppm at 47°C in dry air. Such a behavior is well known [271], since the partition coefficient exponentially decay with the temperature as expressed in equation (5.4). The absorption of the gas in the sensing film strongly decreases with the temperature, reducing thus the capacitance shift. In this temperature range, the sensitivity increased by a factor two to three when measured in air with 50% RH, i.e. in standard measurement conditions met in most applications. Similar results were obtained with the detection of ethanol with the PEUT. The sensitivity was of 22 aF/ppm at 22°C and decreased to 6 aF/ppm at 47°C in dry atmosphere. As for n-propanol, the sensitivity to ethanol increased when the capacitance of the film was measured in wet atmosphere. For 50% of RH, the sensitivity to EtOH at 22 and 47°C were respectively of 50 and 18 aF/ppm, namely an increase in sensitivity by a factor between 2.3 and 2.9 compared to a measurement in dry air. The sensing film showed a lower sensitivity to ethanol compared to n-propanol despite a higher dielectric constant ($\varepsilon_{EtOH} = 24.1$ against $\varepsilon_{n-prop} = 20.1$). This was due to the lower coefficient of partition of ethanol in PEUT than for n-propanol.

5.3.5 Comparison between PDMS and PEUT for VOCs detection

Based on the sensitivities measured with PDMS and PEUT coating and the resolution of the readout circuitry given in its datasheet, 4 aF, the smallest measurable step of concentration of each analyte was computed. The results are given in table 5.4. At a first glance, the system is capable of discriminating sub-ppm variation of VOCs with the exception of n-hexane and dimethylpentane. For the common gas species measured with both films, one noticed the PEUT coating had a higher sensitivity than PDMS by exhibiting the lowest concentration steps that can be measured. The highest variations of sensitivities between the sensing layers were ob-

Table 5.4: Resolution in terms of gas concentrations with the PDMS and PEUT coating combined with the readout electronics.

	Resolution (ppm)			
	0% RH		50% RH	
Gas	PDMS	PEUT	PDMS	PEUT
n-propanol	0.10	0.05	0.13	0.04
ethanol	0.37	0.20	0.60	0.14
toluene	0.32	0.23	0.35	0.24
n-hexane	4.85	-	4.34	-
ammonia	0.06	-	0.05	-
dimethylpentane	-	3.29	-	1.86
acetone	-	0.34	-	0.27

tained with n-propanol and ethanol. In the case of PEUT, the resolution was enhanced with the presence of humidity, while in general, the opposite was observed with PDMS.

5.4 Discussion

The capacitive sensor developed herein took advantage of combining the substrate signal with the one taken out of the sensing layer when exposed to gaseous compounds. By combining these two responses, additional information could be extracted compared to devices fabricated on silicon. The sensing platform developed here offered further functionalities. It was possible to discriminate humidity from very low concentrations of VOCs in the TWA range by using the two capacitors in differential mode and by subtracting the effect of humidity on the sensing film. These operations can easily be handled by a embedded microcontroller in a system and do not need advanced signal processing. However, by using two capacitors, only a total VOCs content in the atmosphere can be detected. This concept of differential measurement could be easily extended to arrays of sensors to increase the selectivity by coating them with different functional materials.

The capacitive platform combined with its commercially available electronic readout presents several advantages. By operating the two capacitors differentially, the electrical parasitic noise is canceled out, while the remaining noise was drastically reduced by the capacitance-to-digital converter used here with its embedded noise reduction system. It offered thus a very low capacitance resolution of about 4 aF and allowed the detection of very low concentrations of gases. As an example with PEUT coating, the lowest signal obtained was for 50 ppm of toluene, which corresponded to a capacitance shift of about 1 fF, which was easily detected. In the case of n-propanol, a theoretical resolution of about 40 ppb could be achieved with this system.

The readout circuitry used here made the whole device compatible with wireless systems due to its very low power consumption. Nonetheless, another IC is now on the market (*AD7150* from *Analog Devices*). It exhibits a lower power consumption but was not yet commercially available at the time of these developments.

Due to the flexible nature of the substrate, the capacitance of the sensors can be modified only by bending the foil. By operating these sensors differentially, the mechanical distortion of the substrate can be completely eliminated as long as both capacitors are equally affected. These layers are usually porous and present a relatively low deformation modulus, but additional investigations should be carried out to determine quantitatively the effect of the bending of these structures on their gas measurement abilities.

Further developments can be foreseen to first reduce the size of the capacitive sensors. A vertical configuration with the sensing layer sandwiched between the electrodes could be envisaged to minimize the gap. The use of more economical substrates such as PEN or PET should be evaluated in terms of sensing abilities with this differential measurement concept.

5.5 Conclusion

The capacitive sensor developed here was based on a commercial polyimide foil. The fabrication of the device could not be further simplified since only one metalization layer was necessary and no alignment was required to obtain a capacitive structure and a resistive element. To functionalize the sensing platform for VOC detection, a second step was necessary to coat the sensing capacitor with an appropriate polymer – PDMS or PEUT in this study – and to allow the operation of the device in a differential mode. Such mode of operation combined with a polymeric substrate brought some advantages compared to silicon-based devices. Since the substrate reacts to the gaseous environment, its signal can be exploited to improve the functionality of the sensing platform and led to the discrimination of VOCs from humidity.

The readout circuitry was based on the latest generation of commercially available capacitance-to-digital converter, which offered a high resolution combined with a low noise and power consumption. This chip additionally interfaced the resistive temperature sensor, leading to only one IC to read out the whole sensing platform.

Under differential operation, the sensor revealed the detection of the targeted gases at concentrations as low as the TWA levels, which is the current state of the art for Si-based sensors driven by dedicated ASICs. These measurements were performed in a normal humidity atmosphere and by using common polymers without any specific sensing features. In this configuration, the PEUT layer revealed a sensitivity to the targeted analytes about twice higher than the PDMS coating.

The selected transducing principle of the sensor combined with its low-power electronics, make this type of device very attractive for mobile and autonomous systems, such as RFID tags. Due to the configuration of the platform, it can still evolve towards a full plastic implementation, appropriate for large scale and very low cost production. Additional sensing capabilities can be straightforwardly envisaged by increasing the number of capacitors and coating them with different functional materials. It would further improve the sensitivity and selective of the capacitive sensing platform, making it even more attractive.

Chapter 6

Towards smart environmental sensing systems

6.1 Introduction

The development of autonomous sensing systems has gained a significant interest in the last years due to the decrease in power consumption of the electronic components and the spread of wireless communications. These devices continually integrate more features to make them "*smarter*". Monitoring environmental parameters is one of them. By adding gas sensors on the same substrate combined with data processing/storage and communication capabilities leads to the development of so-called smart sensing systems. They may find relevance in several domains, such as human comfort or health, pollution and perishable good monitoring. This chapter presents the first steps towards the design of a smart sensing system on polymeric substrates.

Among smart sensing systems, one found wireless sensor networks (WSN) for instance. They are based on a distribution of "nodes", which are battery-powered autonomous systems. Information is relayed through the network of nodes to a base station. A second architecture of smart sensing systems relies on the radio frequency identification (RFID) of a label, or RFID tag. In this case, the label can only communicate with a reader and no inter-tag transmission is possible. Depending on the application, different tag configurations are found, from the active labels (entirely powered by a battery), to the passive ones, which are only powered by the inductive or electromagnetic field emitted by the reader. In between, there are semi-active tags in which the sensing part is supplied by a battery, while communication is powered by the reader.

The goal here is not only to integrate sensing features on a wireless device, but to make a first step towards their integration at reduced cost. This could be achieved by designing all the devices – sensors, microcontroller, passive electronic components, antenna – directly on the same substrate. For gas sensing, the integration of components with different transducing principles may result in some benefits for the discrimination between different gaseous species, improve the sensitivity over a wider range of gas concentrations and correct the sensor responses by

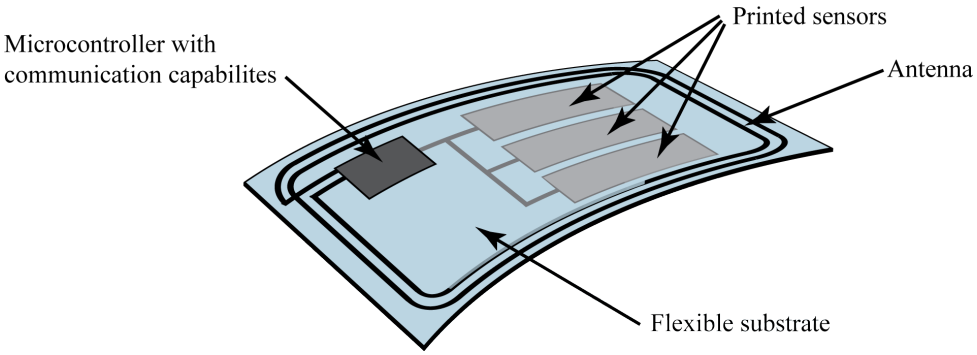

Figure 6.1: Schematic view of a smart sensing system, more specifically an RFID tag. It combines a microcontroller with communication capabilities, an antenna and sensors.

cross-calibration of the embedded devices. By combining several sensors on a single substrate, the need of an assembly step can be avoided. Further cost reduction can be obtained by using only additive fabrication techniques, such as printing. It this way, the precise deposition of materials can be performed at large scale with limited waste. A concept of printed RFID tag with sensing functionalities is illustrated in figure 6.1.

To achieve a first step towards these goals, sensors devised on plastic foils were presented in the previous chapters and their gas sensing performances were evaluated. They were designed to minimize their power consumption as much as possible to make them attractive for wireless systems. In this chapter, developments towards the design of smart environmental sensing systems are presented. First, the benefits brought by the combination of different transducing principle on a same substrate were investigated to determine the advantages of such a configuration in terms of sensing capabilities. Second, solutions for interfacing the sensors at low-power on smart sensing systems will be proposed.

6.1.1 State of the art

Measurement of several parameters – e.g. temperature, relative humidity, gases or pressure – on the same platform has already been demonstrated on silicon substrates [260, 266, 272, 273]. Li et al. [274] presented different types of transducing principles – calorimetric, capacitive, mass, chemoresistive – for gas sensing. Interesting performances were obtained with this most integrated version of smart sensing systems. However, they did not embed any communication capabilities. To our knowledge the only project that addressed the realization of a smart gas sensing RFID label was the European FP6 Integrated Project “Goodfood”. It aimed at integrating Si-based MOX gas sensors on a RFID tag for the ethylene detection [26]. A German project “TREK” targeted the integration of humidity sensors on plastic sheets used for RFID tags [49], but gas sensors were not addressed in this study.

From a commercial point of view, several RFID tags with sensing capabilities based on silicon sensors are already available on the market, mainly for temperature [29–33], shocks [32] or humidity [32, 33] measurements. No commercial product is available yet with gas sensing

functions.

Regarding to the interfacing of sensors, their electronic readout should be designed to minimize the power consumption to allow the highest autonomy possible in a wireless configuration. Several groups have worked on the reduction of the consumption for the measurement of resistive sensors. A major issue with MOX devices is the variation of resistance of the sensing layer over several decades. The majority of readout circuitry to measure it is based on active components, such as operational amplifiers or multiplexers [275–279], which are expensive and power hungry. Power consumptions in the miliwatt range were reached [276, 279–282], which are still too high for wireless applications. To avoid the use of active components and make the readout simpler, a time-to-digital conversion was implemented [283, 284]. It based on the time required to discharge a capacitor through a resistor. Such systems were designed for metal-oxide gas sensors, but to our knowledge, no validation through gas measurement was published to date. The lowest power consumption found in the literature for the driving and readout circuitry of a MOX sensors was of 366 μW with a dedicated ASIC [284].

6.1.2 Progress beyond the state of the art

The integration of different transducing principles was carried out here by combining the metal-oxide (MOX) gas sensors with capacitive structures on a single polymeric substrate. Compared to the implementations reported before with metal-oxide gas sensors in chapter 4 and capacitive sensors in chapter 5, the multisensor platform presented in this chapter shows significant advantages with a higher degree of integration. Bringing together, on the same flexible plastic substrate, gas sensors with different working principles, and providing temperature and humidity corrected responses, the same sensing potential as Si-based platforms/substrates can be reached [272]. Furthermore, devices with different transducing operations permit their cross-calibration to remove the influence of interfering parameters on all sensor responses. Thus, the detection of the reducing/oxidizing gases in low concentration ranges was ensured by two dedicated MOX sensors, while for the humidity and VOCs measurements, two capacitive interdigitated structures, with almost no power consumption, were preferred. The platform could be extended to include additional interdigitated capacitors for the detection of other analytes. The accurate temperature values required for the data processing are delivered by the Pt thermometer of the device.

In smart sensing systems, a major constraint is the power available for the sensing and the communication. Very low power driving and readout circuitries were already presented for the optical colorimetric sensor in chapter 3 and the interface of the capacitive sensors presented in chapter 5 was based on commercial low-power capacitance-to-digital converter. However, the interface of the MOX sensor was not yet addressed in this study. To deal with the large resistance variation of the gas sensitive layer, a readout based only on passive components for a time-to-digital conversion was developed.

A communication capability was implemented to design a complete smart sensing system

with the developed sensors. The communication technique employed here was the RFID with the development of a passive tag. A main challenge was to devise a system with a power consumption low enough to ensure the operation of all the electronic components on the tag as well as the sensors. It allowed the instantaneous measurement of the humidity level with possible extension towards the data-logging of humidity, temperature and VOCs concentrations.

6.2 Multisensor platform on polyimide foil

This multisensor platform aimed at combining several transducing principles and investigate the benefits brought for gas detection. With several detection methods, different gas species can be detected. Moreover, cross-calibration can be performed between the different sensors to remove some parasitic effect from the raw signal, such as humidity. For the actual device, the MOX gas sensors presented in chapter 4 were combined with the capacitive devices developed in chapter 5. By doing so, a larger spectrum of gases could be detected with a wider concentration range. The oxidizing/reducing gases were measured with the MOX sensors, while the VOCs and humidity had a stronger affinity with the capacitive structures.

6.2.1 Design

The configuration of the hybrid multisensor platform (6×6 mm^2) is presented in figure 6.2. It combined three different transducers on the same polymeric substrate: two metal-oxide and two capacitive gas sensors, and a resistive temperature sensor. Based on the results obtained in chapter 4, 100 µm wide MOX gas sensors with a closed membrane were selected for the multisensor platform. Despite their higher power consumption than the smaller devices, they exhibited the highest gas responses and were thus suitable for the proof of concept presented in this chapter. Second, two capacitive sensors were included with the same configuration as those presented in chapter 5. One was left uncoated as a reference, while the second one was covered with a humidity/VOC gas sensitive polymer. Their size was however considerably decreased

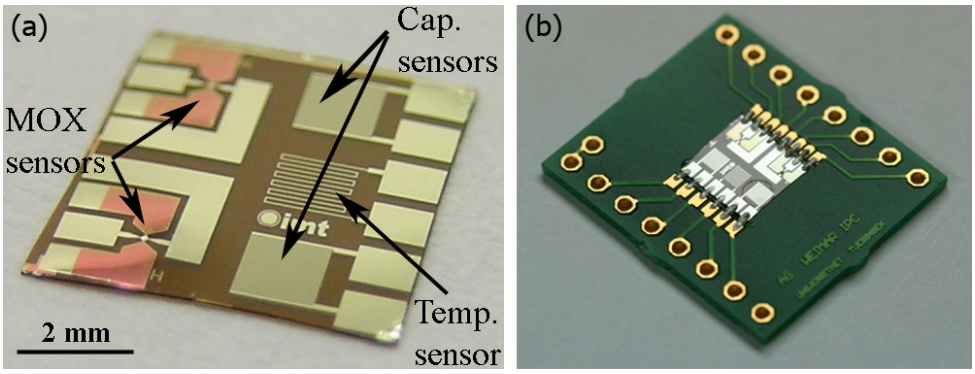

Figure 6.2: Optical picture of (a) the fabricated multisensor platform on polyimide and (b) the device packaged on a PCB for its characterization.

compared to the devices presented in chapter 5. For the multisensor platform, each capacitor covered an area of 1.4×1.4 mm^2 and had 10 µm electrode width and spacing to fit in the defined area of 6×6 mm^2. As in chapter 5, a nominal capacitance of about 10 pF was targeted to allow the direct readout of the humidity/VOCs induced responses with a commercial capacitance-to-digital converter. The last transducer was a resistive temperature sensor. Its size was scaled down as well, but kept at a nominal resistance of 1 kΩ.

The 100 µm wide heaters of the MOX gas sensors were patterned with the first Pt layer, while their electrodes, those of the capacitive sensors and the resistance thermometer were produced with the second Pt layer. The metal-oxide gas sensors were coated with different gas sensing materials – SnO_2:0.2%Pd [250] and WO_3 – to improve their selectivity towards reducing and oxidizing gases. The functionalized capacitor was either coated with cellulose acetate butyrate (CAB) for humidity measurement or polyetherurethane (PEUT) for VOCs detection. PEUT was chosen instead of PDMS because of its higher sensitivity to these gases (chap. 5).

6.2.2 Fabrication

The device was realized on a 50 µm thick polyimide (PI) wafer (*Upilex-50S* from *Ube Industries, Ltd*) making use of a minimal number of conventional technological steps. Its cross-section is sketched in figure 6.3. The conducting elements of the sensors (thermoresistor, heaters, electrodes and pads) required only two levels of platinum (130 nm) with an adhesion layer of titanium (20 nm) deposited by DC sputtering and patterned by the lift-off technique described in section 2.2. The electrical insulation from the top electrodes is made by a 700 nm thick polyimide film (*PI-2737* from *HD Microsystems*). The fabrication process used was the same as the one developed for the metal-oxide gas sensor, which is fully described in section 4.2.3. An optical picture of the fabricated device is presented in figure 6.2a.

Once the transducers were designed, the last step to be performed was the deposition by drop-coating of the functional materials for gas sensing. It was carried out at the *Institute of Physical Chemistry* (*IPC*) of the *University of Tuebingen*, Germany. A strategy had to be defined because of the very different nature of each component and to avoid contamination. First the metal-oxide

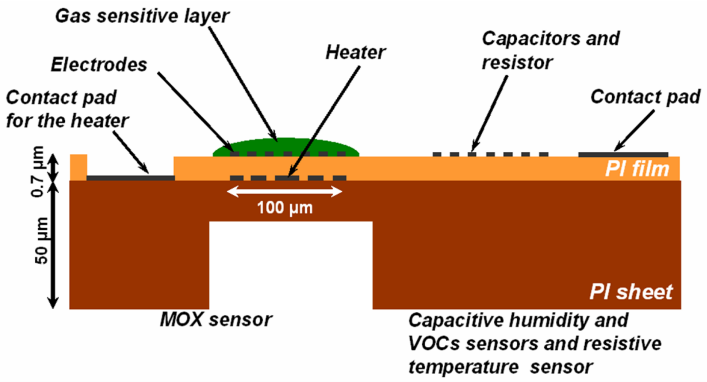

Figure 6.3: Cross-sectional schematic of the multisensor platform.

layers were deposited followed by an annealing at 400°C to sinter them. In a second phase, the coating of the capacitor with polymers was carried out and left to dry at room temperature. In that order, the polymers were not degraded by the high temperature annealing step. The multisensor platform was packaged on a PCB for its characterization (fig. 6.2b) and electrical contacts were ensured by a conductive epoxy glue (*Epotek H20E*).

6.2.3 Gas measurement protocol and sensor response monitoring

The platforms, packaged on printed circuit boards (PCB) and placed in a teflon-based gas chamber, were tested at *IPC* and characterized with a computer controlled gas-mixing and measuring system to different humidity levels and gas concentrations with values in the TWA (time weighted average) range or below. The carrier gas was synthetic air and the flow rate was of 200 sccm. The multisensor platforms were exposed to different concentration of CO (20-80 ppm), NO_2 (0.1-1 ppm), EtOH (2-20 or 300-3000 ppm) and humidity (0-70%). These gas measurements were performed at the *Institute of Physical Chemistry* of the *University of Tuebingen*, Germany.

The voltage applied to the heater of the MOX sensors and the resistance of their gas sensitive layers were monitored using a standard laboratory multichannel multimeter. The readout of the capacitive humidity and gas sensor was ensured with a capacitance-to-digital converter *AD7746* from *Analog Devices, Inc*. This IC has a very low resolution of 4 aF at a fairly low power consumption at low acquisition rate. The additional voltage/resistance input of the converter was used to monitor the resistance of the temperature sensor. The digital data were delivered to a PC through a I^2C-to-USB converter developed by *JLM-Innovation GmbH* [268].

6.2.4 Electrical characteristics of the multisensor platform

The heaters of the metal-oxide gas sensors had a nominal resistance of 150 Ω at 0°C and, as for the same MOX sensor described in chapter 4, needed 15.5 mW to reach an operation temperature of 300°C in a continuous heating mode of operation. The resistance of the MOX layer was in the MΩ range when not heated. The resistive thermometer had a resistance of 1.16 kΩ at room temperature. Its response showed a high degree of linearity with the temperature. Its thermal coefficient of resistance (TCR) was experimentally measured in an oven and was 0.002 $°C^{-1}$. The capacitive transducers had a capactitance of 2 pF at 40%RH.

6.2.5 Gas sensing performances of the multisensor platform

The polymeric multisensor platform was exposed to several humidity levels and different gas concentrations to compare its performances in gas discrimination over devices produced by conventional technologies on standard substrates, such as ceramic or silicon.

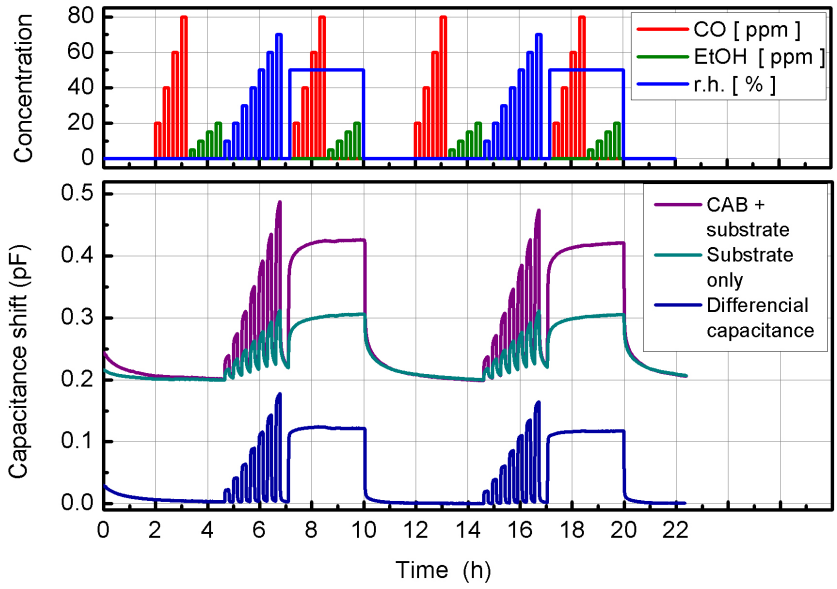

Figure 6.4: Gas response of the CAB-coated capacitive sensor to carbon monoxide, ethanol and relative humidity. The raw measurements of the two capacitors are shown as well as their differential signal. The sensor responded only to humidity.

Differential capacitive measurements of humidity

Figure 6.4 shows the raw results obtained with the uncoated and CAB-coated capacitors on the platform for humidity measurements. The sensors were exposed to humidity (0-70%) and to potential interfering gases, CO (20-80 ppm) and ethanol (2-20 ppm). The subtraction of the two curves is plotted as well. It shows the positive effect of operating the two sensors in a differential mode. It improved both the linearity of the response and the response time as we have reported for these devices in chapter 5. The film was only sensitive to humidity. No response was obtained for exposure to CO and low concentrations of ethanol.

Table 6.1 presents the response and recovery times of the substrate and the coated capacitor. The use of the differential measurement decreased the response time by a factor six between 0 and 50% RH, while the recovery time was reduced twenty-four times compared to using only

Table 6.1: Response and recovery time ($t_{90\%}$) of the capacitive sensors between 0 and 50% of relative humidity.

	$t_{res,90\%}$ (min)	$t_{rec,90\%}$ (min)
Reference capacitor	29.3	113.0
Sensing capacitor	24.7	104.8
Differential measurement	3.8	4.3

the coated capacitor. Similar values were found in the literature [267]. To further reduce the response time, thinner plastic foils could be used as suggested in [259].

The reproducibility of the capacitive sensor response was tested together with the sensor reliability during a few weeks of uninterrupted operation. The results are presented in figure 6.5. No depreciation occurred for the capacitive sensors. Over a twenty-day period, the highest decrease in sensitivity observed was of 0.2%/day in the case of 70% of relative humidity.

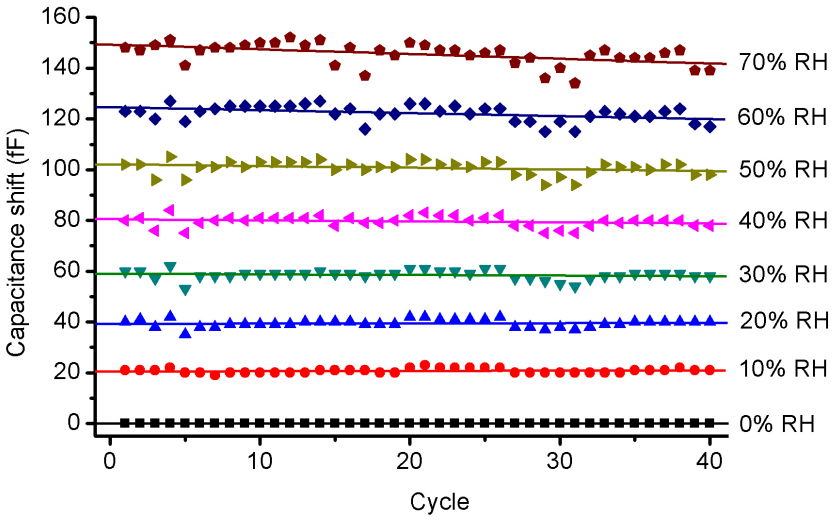

Figure 6.5: Stability of the capacitive humidity sensor over a period of 20 days. One cycle of the differential measurement lasted 12 h. The periodic instabilities were due to the switching off of the air conditioning system in the laboratory during the weekends.

Responses of the multisensor platform to gases and humidity

Gas measurements performed with all the chemical sensors embedded in the multisensor platform are presented in figure 6.6. All sensors operated properly. The positive effect of the differential measurement of the capacitive sensor is again demonstrated here (fig. 6.6b). The sensor immunity to the substrate cross-sensitivity towards the detected analytes was clearly improved compared to the raw signals. The capacitive sensor was based on PEUT as sensing element. That material revealed a sensitivity to humidity ten fold lower than CAB (fig. 6.4), but was suitable for VOC detection (chap. 5). However, its sensitivity was not high enough to detect ethanol in the exposure range used here, 2 to 20 ppm.

As expected, the WO_3 sensor is more sensitive to NO_2 [285]. One observes its sensitivity was not affected by the humidity level. Same responses were obtained when exposed to dry synthetic air or with 50% of relative humidity. A lower sensitivity to EtOH than NO_2 was measured in dry atmosphere. However, under the presence of humidity, the sensitivity of EtOH with the WO_3 sensor is almost quenched. The selectivity towards NO_2 was thus improved in normal exposure conditions where humidity is present.

The same process than for WO_3 occurred when SnO_2:0.2%Pd sensing material was exposed to ethanol. In both dry and humid air, the sensor exhibited a higher sensitivity to EtOH than

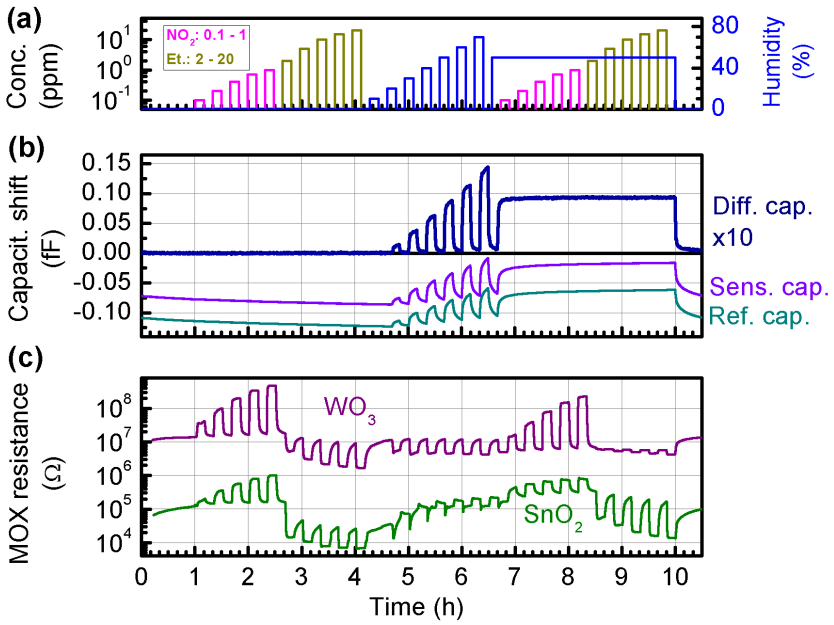

Figure 6.6: Gas response of the capacitive and chemoresistive gas sensors to nitrogen dioxide (0.1-1 ppm), ethanol (2-20 ppm) and relative humidity (0-70%). (a) Gas protocol; (b) Differential response of the capacitive sensors with PEUT coating; (c) Gas response of the MOX sensors coated with SnO_2:0.2%Pd and WO_3.

for NO_2. Again, with humidity, the response to NO_2 was reduced, improving the selectivity towards EtOH.

To emphasize the detection of EtOH with the PEUT-coated capacitive sensor, the same gas sequence was used again but with concentrations of ethanol in the range of 300 to 3000 ppm. The results are shown in figure 6.7. With higher EtOH concentrations, a clear response was measured with the differential capacitive sensor, in both dry and humid air. The sensor response was higher to humidity than to ethanol since 50% RH corresponds to an absolute humidity of roughly 23000 ppm at 20°C. Additionally, similar sensitivities were observed in both dry and wet air. The responses to humidity and ethanol thus seemed to be additive. Regarding to the MOX sensors, a similar behavior than the previous measurements (fig. 6.6) was observed.

Response of the MOX sensors to humidity

The humidity response of the SnO_2:0.2%Pd MOX gas sensor is presented in figure 6.8. The humidity effect on the MOX sensors was high for the 0 - 10% RH interval with a factor of 2.5. A plateau was obtained for relative humidity level between 10 and 30% with a variation of the response of 5%. If a wider range of measurement is desired as it would be the case for most applications, a variation of only 20% was measured between 10 to 70% of relative humidity.

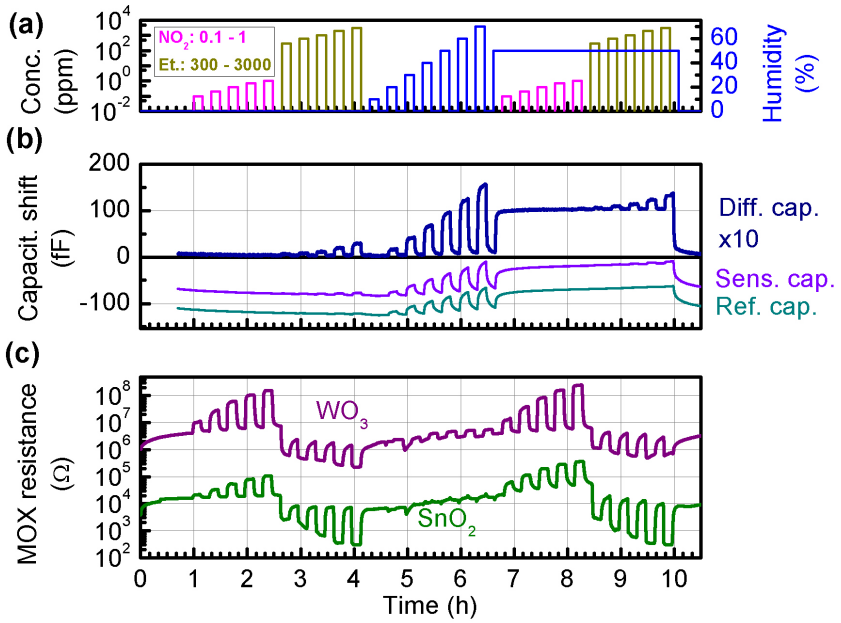

Figure 6.7: Gas response of the capacitive and chemoresistive gas sensors to nitrogen dioxide (0.1-1 ppm), ethanol (300-3000 ppm) and relative humidity (0-70%). (a) Gas protocol; (b) Differential response of the capacitive sensors with PEUT coating; (c) Gas response of the MOX sensors coated with SnO_2:0.2%Pd and WO_3.

Stability of the MOX sensors

The resistance variation of the MOX sensors when operating at 300°C over a period of 68 days is presented in figure 6.9. The voltage applied to the heaters was modified during the 14 first days to investigate the behavior of the devices. After, the high stability of the sensors with time can be noticed. the resistance variation of the WO_3 and SnO_2:0.2%Pd coated sensors were respectively of 0.17 Ω and 0.14 Ω in the last 44 days.

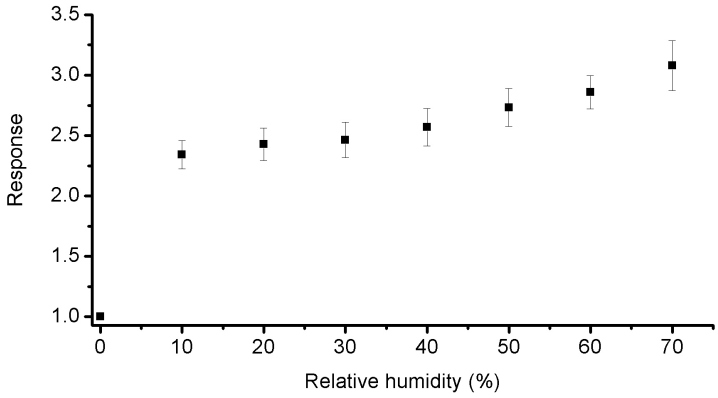

Figure 6.8: Response (R/R_0) of the SnO_2:0.2%Pd MOX gas sensor to humidity when operating at 300°C. Eight measurements were performed with the same device. The confidence interval was of 95%.

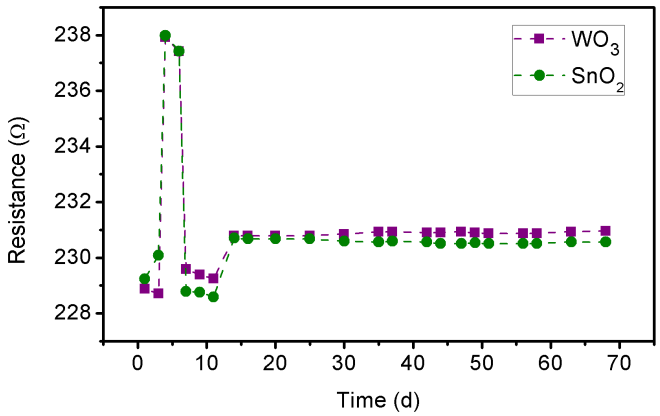

Figure 6.9: Resistance of the MOX sensor heaters on the multisensor platform. They showed a high stability. The power supplied to the sensors was modified at the beginning of the experiment.

Calibration curves

The main advantage of combining several sensors with different transducing principles on the same substrate is the possibility of correcting their response throughout calibration curves. From the capacitive measurements performed in figures 6.6 and 6.7, a calibration curve can be deduced and is given in figure 6.10. The differential capacitive measurement showed an excellent linearity with the relative humidity with a good sensitivity of 2.45 fF/%RH. With eight successive measurements carried out, the sensor showed a very good reproducibility. The largest variation of the results recorded was of 3 fF with a confidence interval of 95%, leading to an error of about 1% RH.

The response of the MOX sensors can be compensated by using the response of the capacitive humidity sensor, which would lead to a more accurate determination and discrimination of the gas concentrations detected by the metal-oxide sensors. Figure 6.11 shows the calibra-

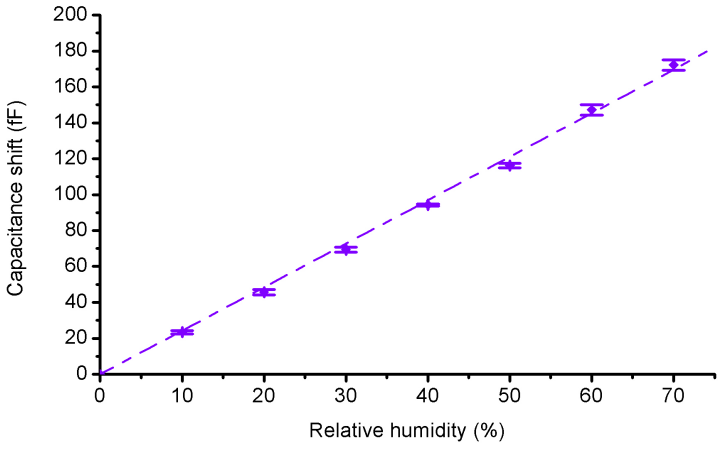

Figure 6.10: Differential output response of the capacitive humidity sensor. Eight measurements performed with the same device, confidence interval of 95%.

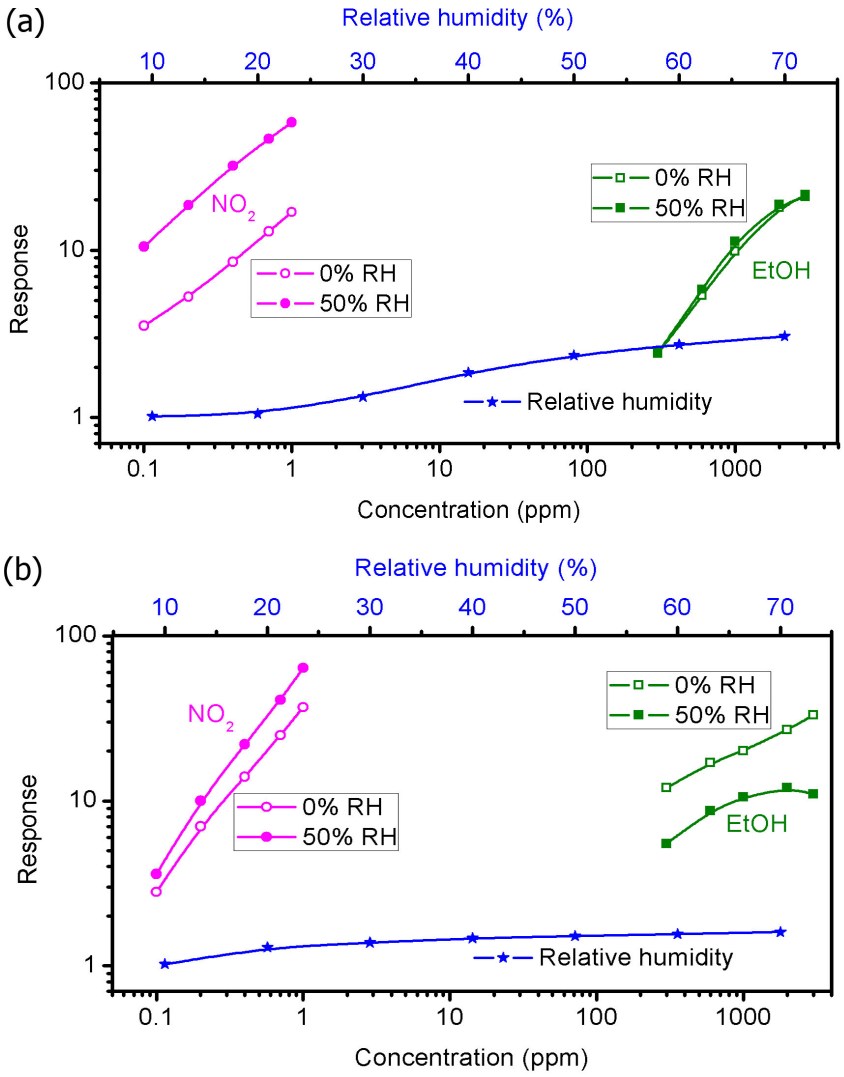

Figure 6.11: Calibration for the gas sensors based on (a) SnO_2:0.2%Pd and (b) WO_3 MOX layers.

tion curves obtained for the metal-oxide gas sensors based on SnO_2:0.2%Pd and WO_3 sensing materials. The former presented a higher sensitivity to humidity with a factor 3 over the 10 to 70% RH range versus a factor of 1.7 for WO_3 over the same interval. The response of the SnO_2:0.2%Pd based sensor to ethanol was found to be virtually independent of the humidity level. The largest measured discrepancy between dry air and 70%RH was of 12% when exposed to 1000 ppm of EtOH. Humidity level however played a significant role upon the response to NO_2 with a maximum variation of about 70% between the response in dry air and an atmosphere with 50%RH. The opposite was obtained with the WO_3-based sensor. The interference due to humidity influencing the response to NO_2 was of maximum 40%, while its was more marked for EtOH with a variation up to 67% between dry and wet synthetic air. The use of two different gas sensitive layers combined with an intelligent readout circuitry and light signal processing would allow abstracting the influence of humidity on the gas response of these two sensors.

6.2.6 Discussion on the multisensor platform

The simultaneous measurement of reducing/oxidizing gases and VOCs can be problematic under given circumstances. Increases in ethanol concentrations – but still in the TWA range ($\sim$500 ppm) – can saturate the MOX channels [286] of the platform, while it remained well detectable by the differential capacitive measurement. This issue is not specific to integrated sensors, being encountered for all type of MOX sensors with high sensitivity. The multisensor platform, however, has an important advantage here. A smart driving electronic can switch off the MOX heaters and validate only the capacitive outputs, preventing inaccurate records. By intelligently switching off the heaters of the MOX sensors depending on the gas species in presence and their concentrations, the power consumption can be decreased, enhancing the device life time if embedded in a wireless system.

Moreover, the use of an integrated circuit – the *AD7150* – could be avoided by reading all the sensors with a time-to-digital conversion. This method was used for the resistance measurement of the MOX sensor (section 6.3), but it could be extended to the measurement of capacitive sensors [287]. However, an evaluation on both solutions – with the IC or through passive components – has to be performed in terms of resolution, power consumption as well as manufacturing cost.

6.3 Electronic interface for MOX gas sensors

To further integrate the transducers towards a smart and low-power environmental sensing system, the gas sensors need to be properly interfaced with an appropriate electronic circuitry. To design cost-effective systems by minimizing the number of electronics components, an analog time-to-digital conversion was selected. It simplifies the system architecture to the sensor, microcontroller and a few passive components.

Since energy is very limited in wireless systems, the readout of the sensors has to be designed with care. The electronic circuitry of the optical and capacitive sensors were already presented in chapter 3 and 5, respectively. Here, the driving and readout of a metal-oxide gas sensor based on low-power components will be addressed. The interface of the sensor was developed around an ultra-low power microcontroller, which should be in its idle mode most of time to reduce the power consumed by the computational time. The measurement should thus be fast in order to minimize the duty cycle of the microcontroller. The microcontroller was operated at a fairly low frequency (low MHz range) since the power consumption of a processor rapidly increases with the frequency. Moreover, to design cost-effective systems, the number of electronic components should be as small as possible with a preference for cheap passive elements, e.g. resistors, capacitors, instead of expensive and power consuming active ICs (operational amplifiers, multiplexers,...).

6.3.1 Operation principle

To reduce the power consumption of the gas sensing system, the ultra-low power MOX sensors on plastic foil were combined with low-power electronic components. The circuitry illustrated in figure 6.12 was controlled by an ultra-low power *MSP430* microcontroller from *Texas Instruments*, which ensured the driving and the readout of the sensors. The driving circuitry (on the left in the figure) was composed of a MOS transistor used as a switch to operate the heater of the sensor in either continuous or pulsed mode. The proper voltage across the heater, R_{heater}, was tuned with a load resistor, R_{load}, to achieve the desired temperature over the active area of the device. To reduce the power consumption, the heater was used in pulsed temperature mode. The cycle period was of 1 s with a duty cycles of 10%.

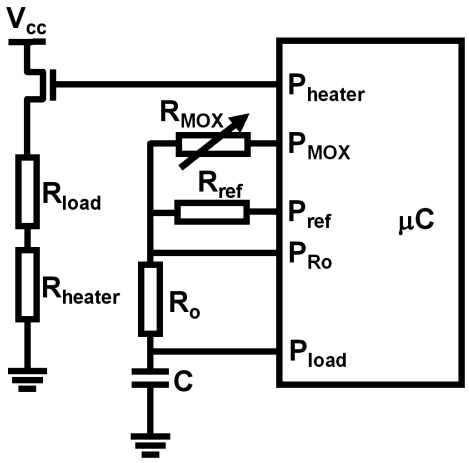

Figure 6.12: Low power driving and readout circuitry based on time-to-digital conversion for the measurement of the MOX layer.

The readout system was based on time-to-digital conversion as illustrated in figure 6.13 [288]. It was used to determine the resistance of the gas sensitive layer of the metal-oxide gas sensor (chap. 4). The time-to-digital conversion measured the time required to discharge a capacitor through a resistor. If the resistor changes its value over a time period as it is the case for a resistive sensor, the output signal of the sensor can be extracted.

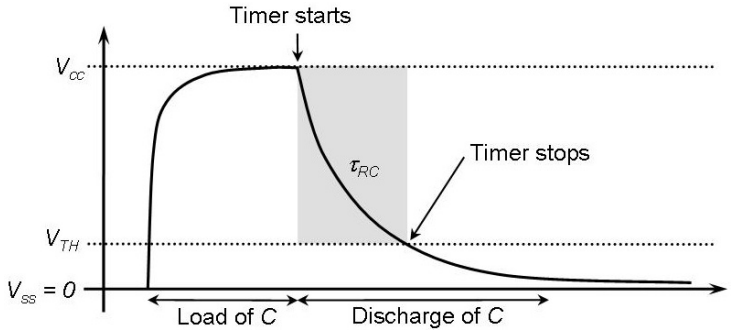

Figure 6.13: Principle of the time-to-digital conversion with the voltage across the capacitor.

As shown in figure 6.13, the measurement cycle of the readout began with the load of the capacitor, C, to the supply voltage of the system, V_{cc}, and then successively discharged through the gas sensitive layer resistor, R_{MOX}, the reference resistor, R_{ref}, and R_o, which limited the current sunk by a pin of the microcontroller to prevent its damage. The sequence of logic levels of each microcontroller pin, P, involved for the measurements of R_{MOX} are given in table 6.2. For example, to measure R_{MOX}, first P_{load} was set to logic 1 to load C, while keeping the other pins at high impedance. The timer then started and all the pins were set to high impedance, but P_{MOX}, which was set to logic 0 to allow the discharge of the capacitor through R_{MOX} and R_o. When the decreasing voltage across C reached V_{TH} – a threshold value between logic one and logic zero in the microcontroller –, an interrupt was generated and stopped the timer yielding τ_{MOX}. This procedure was repeated twice more to evaluate τ_{ref} and τ_o. The time constants of each discharge time are given in equations (6.1), (6.2) and (6.3).

Table 6.2: Successive logic states of the microcontroller pins to measure the resistances by time-to-digital conversion.

	Step 1	Step 2	Step 3	Step 4	Step 5	Step 6
P_{load}	1	Hi-Z	1	Hi-Z	1	Hi-Z
P_{Ro}	Hi-Z	Hi-Z	Hi-Z	Hi-Z	Hi-Z	0
P_{ref}	Hi-Z	Hi-Z	Hi-Z	0	Hi-Z	Hi-Z
P_{MOX}	Hi-Z	0	Hi-Z	Hi-Z	Hi-Z	Hi-Z

$$\tau_{MOX} = (R_{MOX} + R_o)C \cdot ln\left(\frac{V_{cc} - V_{ss}}{V_{TH} - V_{ss}}\right) \tag{6.1}$$

$$\tau_{ref} = (R_{ref} + R_o)C \cdot ln\left(\frac{V_{cc} - V_{ss}}{V_{TH} - V_{ss}}\right) \tag{6.2}$$

$$\tau_o = (R_o)C \cdot ln\left(\frac{V_{cc} - V_{ss}}{V_{TH} - V_{ss}}\right) \tag{6.3}$$

where V_{ss} is the ground reference. By combining the above equations, the value of the MOX resistor can be computed:

$$R_{MOX} = R_{ref} \cdot \frac{\tau_{MOX} - \tau_o}{\tau_{ref} - \tau_o} \tag{6.4}$$

R_{MOX} was converted into an analog output voltage through a DAC (Digital-to-Analog Converter) of the microcontroller and was then monitored with an *Agilent 34970A* data acquisition/switching unit. An example of the measurement signal is illustrated in figure 6.14. To prove the principle of operation of the circuit, the sensor was replaced here by a potentiometer. The first peak in voltage corresponds to load of the capacitor and its discharge through

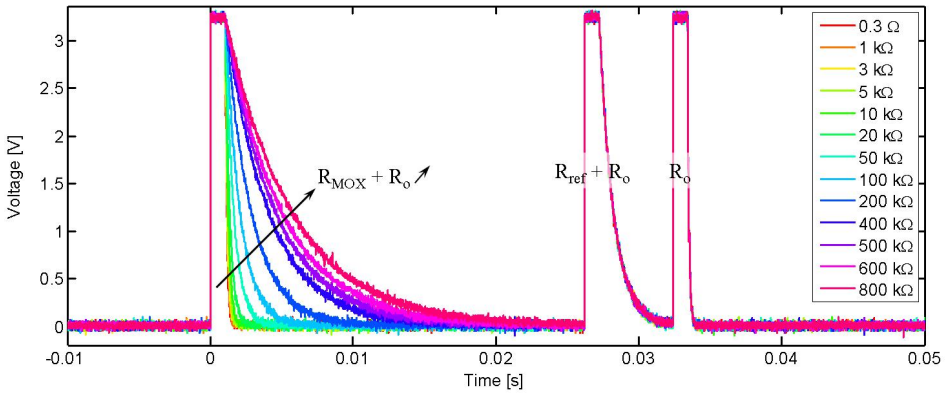

Figure 6.14: Operation of the electronic readout with the time-to-digital conversion simulated with a potentiometer. The first peak corresponds to the sensor signal, the second to the reference and the last one to the current limitation.

$R_{pot} + R_o$. The discharge time increased with the resistance of the potentiometer, while the two other peaks – the reference and the current limitation – stayed identical over the successive measurements, showing the proper operation of the readout. The circuitry used for the actual gas measurement had a reference resistor of 100 kΩ, a current limitation resistor of 10 kΩ and a capacitor of 10 pF. It allowed the measurement of the gas sensing layer over a range from 10 kΩ to 21 MΩ with a resolution of about 100 Ω.

The MOX resistance was measured 500 ms after switching off the heater to improve the sensitivity to specific gases such as CO [235]. The microcontroller was in sleep mode when no calculation was required (heater and/or MOX measurement) to further reduce the power consumption. The gas measurements carried out with this interface and its power consumption of are presented in section 6.3.2.

6.3.2 Performances of the MOX sensor interface

Gas response through time-to-digital conversion

The proper operation of the circuitry is shown in figure 6.15 with the measurement of different concentrations of CO with the MOX gas sensors drop-coated with SnO_2:3%Pd paste from *AppliedSensor GmbH*. They were operating at 200°C in a pulsed mode (period of 1 s, duty cycle of 10%). The supply voltage of the circuitry was of 1.8 V. The output signal of the device was converted back in resistance values to make the comparison with the previous measurements (fig. 4.33a) easier. The chemoresistive responses of the sensors are presented in table 6.3. Similar results were obtained with the custom-made circuitry as with the laboratory equipment (chap. 4). The CR response decreased with the sensor size. The readout became out of range for the MEMS device for concentration of CO of 70 and 100 ppm, because its resistance decreased below 10 kΩ. The range of the measured resistance was defined for the measurement of the polyimide-based sensor, which exhibit higher values than the MEMS device. The measurement

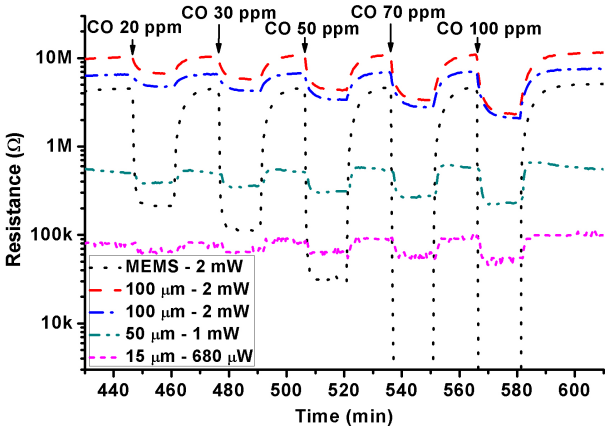

Figure 6.15: Response of bulk PI MOX sensors drop-coated with SnO_2:3%Pd paste from *AppliedSensor GmbH* to different CO concentrations with the time-to-digital conversion circuitry (period of 1 s and duty cycle of 10%).

range can be modified by changing the reference resistor in the readout circuitry.

Power consumption

The power consumption of the electronic circuitry based on an *MSP430* from *Texas Instruments* was measured as well. It was of 130 µW when operating with a duty cycle of 10% for the operation of the sensor and 72 µW when only in sleep mode. These results were obtained based on a commercial microcontroller with no specific function for such sensor readout. In comparison, the lowest power consumption found in the literature was of 366 µW with a dedicated ASIC [284].

The total power consumption of the system (electronics plus the sensor) was however of 1.9 mW when monitoring a 15 µm wide bulk MOX gas sensor. A majority of the power was dissipated in the load resistor (about 1.1 mW) while the sensor itself consumed only 680 µW. Since the applied voltage is constrained by the electronics and the current required to reach the desired temperature was in the same range (12-15 mA) for all sensors independently of their size, the total power consumption of the system was similar for all devices: decreasing the power consumption of the sensor only served to increase the power dissipated in the load resistor. Therefore, in order to reduce the consumption of the system, one must decrease the

Table 6.3: Chemoresistive responses of the metal-oxide gas sensor when interfaced with the time-to-digital converter.

	MEMS	100 µm	100 µm	15 µm	15 µm
CO: 20 ppm	21.31	1.54	1.37	1.28	1.27
CO: 100 ppm	-	2.90	2.29	1.70	1.17

current flowing through the heater. This can be achieved by fabricating the heater with a material that has a higher resistivity than the Pt used here.

6.3.3 Discussion on the MOX interface

The proper operation of the electronic driving and readout circuitry for the MOX sensors was proven throughout gas measurements. It allowed the measurement of resistance values over several decades, from 10 kΩ to about 21 MΩ. The circuitry was based on inexpensive and low-power electronic components making it conceivable for low-cost wireless systems. Moreover, the system was developed here for the measurement of only one sensor, but it can very easily extended for the monitoring of several devices successively at almost no additional cost. An array of chemoresistive – or resistive – sensors could thus be straightforwardly interfaced.

In the previous sections, it was pointed out that the majority of the power losses occurred in the load resistor used to tune the temperature of the sensor heater. The first solution to reduce these losses would consist in operating the circuitry at a lower supply voltage. However, 1.8 V is at the moment the lowest one to operate electronic devices available on the market. A second option to avoid the use of a load resistor could be envisaged. It would consist in applying a pulsed width modulation (PWM) signal to the heater. No resistive divider would be needed since only the duty cycle of the PWM signal would regulate the temperature. Depending on the resistance of the heater, a relatively high current could flow in the Pt heater at each pulsed, which could rapidly lead the device to failure due to electromigration. Moreover, such a method might decrease the temperature stability over a measurement depending on the response time of the sensor. Slight temperature fluctuations could occur, decreasing its selectivity. Here again, the best solution would consist in using a material with a higher resistivity than Pt for the heated area of the device. A higher voltage could be applied to dissipate the same thermal power, while a lower current would flow in the electrical conductor, decreasing the consumption and thus the life time of a battery in the case of a wireless system.

6.4 RFID tag interfaced with capacitive sensors

Figure 6.1 at the beginning of this chapter illustrated a schematic view of a smart RFID tag. To go one step further towards the development of a smart sensing system, the combination of the sensors with a wireless communication system was addressed. As before, a special attention was given to minimize the power consumption of the system. The principle of operation was validated here with the instantaneous mode of operation for which no power supply on the tag is required (passive tag). The tag shown here however allows its future development towards the data-logging of information. In that case, a battery will power the system when no RF field is present (semi-active tag).

To demonstrate the implementation of a smart sensing system, the capacitive sensors presented in chapter 5 was chosen for its interfacing with the passive RFID tag due to its lower

power consumption compared to the colorimetric sensor (chapter 3) or the MOX sensor (section 6.3.2). The tag operated at a frequency of 13.56 MHz according to the standardized protocol ISO 15693. This choice of frequency represents a compromise between transfer data rate, reading distance and insensitivity to obstacles.

6.4.1 Design of the RFID system

RFID reader

The RFID reader was developed at the *HES-SO Valais* in Sion, Switzerland [289]. The block diagram for the RFID reader is presented in figure 6.16. The chip used for the communication was the model *IDS-R13MP* from *IDS Microchip*, which encompasses the communication at 13.56 MHz according to the ISO 15693 protocol. An ultra low-power *MSP430* microcontroller from *Texas Instruments* was used to operate the reader. It controlled the RF chip to transmit and received the data to and from the tag. The communication between the microcontroller and the RFIC was performed through a parallel interface. A 256 kB EEPROM allowed the storage of the data measured by the sensors. The USB interface has two functions, charging the lithium-ion battery of the reader and to communicate with an external computer. It enabled data transmission to a PC for further processing. As direct interface to the user, a LCD screen and buttons were added to configure the tag and read the instantaneous measurement values.

Figure 6.17 shows an optical picture of the RFID reader. Its dimensions were of 70×90 mm^2. It was of a particularly small size, making it compact and thus hand-held. Its fabrication combined SMD (Surface Mount Device) and through hole devices mounted on a standard FR4 PCB substrate.

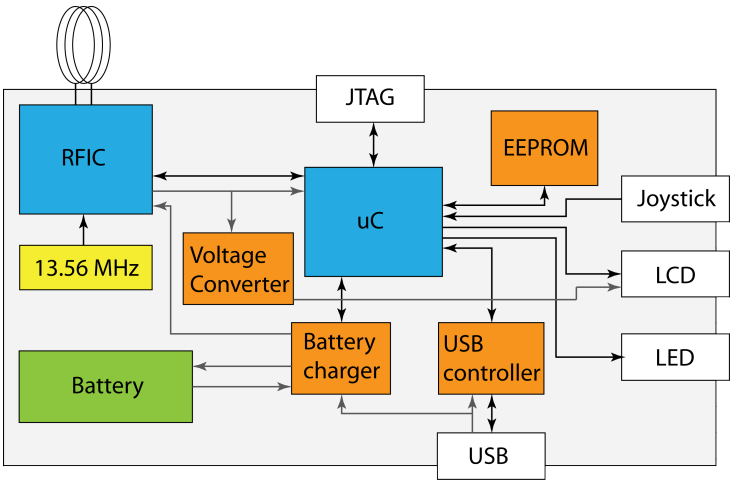

Figure 6.16: Block diagram of the RFID reader. It was developed around an RFID chip and microcontroller, which treated the data and controlled the user interface. Arrows in black and gray are respectively the data path and the power supply.

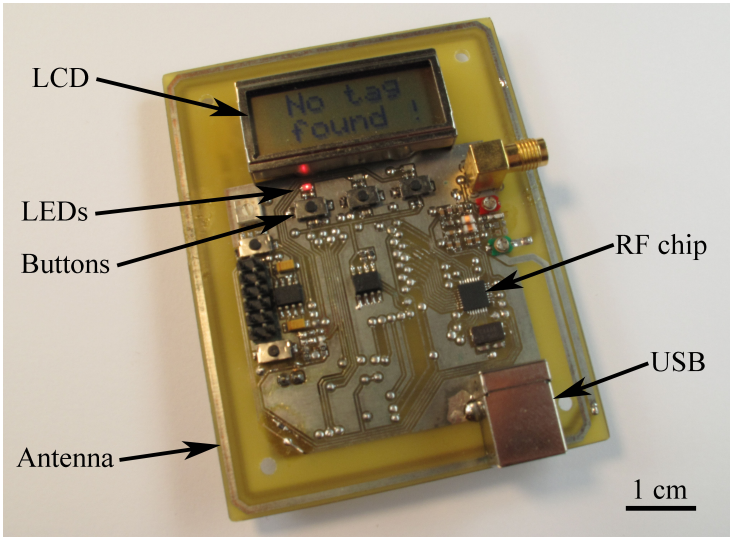

Figure 6.17: Optical picture of the RFID reader based on SMD and through hole electronic devices on an FR4 substrate.

RFID tag

The RFID tag was developed in collaboration with the *HES-SO Valais*. The basic components of a passive RFID tags are a silicon-based chip with communication capabilities combined to an antenna for the wireless transmission of data. In the case of smart sensing system based on the RFID technology, chemical and physical sensors together with a microcontroller for data processing are also included. An optional memory chip can be incorporated to store the sensor's calibration curves or measured data.

The block diagram of a passive RFID tag with sensing components presented in chapter 5 is illustrated in figure 6.18. As for the RFID reader, the tag was built around an *MSP430* microcontroller from *Texas Instruments* to interface the IC to read the capacitive sensor. The RFID communication was ensured by an RFIC (*IDS-SL13A* from *IDS Microchip*), embedding the communication protocol defined by the standard ISO 15693. The communication between

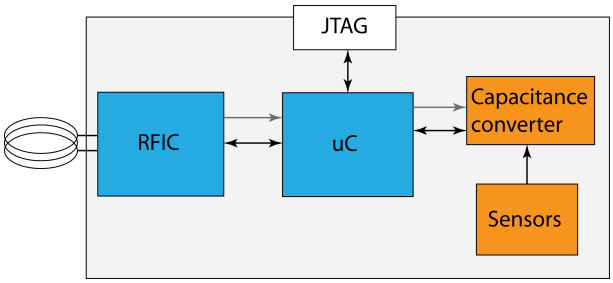

Figure 6.18: Block diagram of the RFID tag. The capacitance of the sensors was converted in a digital signal before being processed by the microcontroller. The RFID chip ensured the wireless communication. Arrows in black and gray are respectively the data path and the power supply.

the RFIC and the microcontroller was performed through a SPI interface. The solution of two ICs was chosen because the RFIC could not directly interface the sensors.

The capacitance measurement obtained from the sensors was converted to a 12 bit digital signal with a two channel capacitance-to-digital converter (*AD7150* from *Analog Devices*). Its very low power consumption of only 430 µW in operation (16.5 µW in sleep mode) makes it particularly attractive for wireless systems. It possesses a measurement range of 0 to 4 pF, with a sensitivity of 1 fF. By adding an internal offset, higher capacitance values up to 13 pF can be measured. The capacitance-to-digital converter communicated through the I^2C protocol with the microcontroller.

As a proof of concept and to avoid as many electronic components as possible, the Pt resistive temperature sensor of the sensing platform (not shown in figure 6.18) was directly interfaced with the ADC (Analog-to-Digital) converter of the microcontroller through a voltage divider. The ADC had a resolution of 10 bits, which led to a resolution in temperature of 0.5°C. Higher resolution could be achieved with a Wheatstone bridge or the time-to-digital conversion depicted in section 6.3 for instance.

The antenna was designed at the *HES-SO* with the *SonnetLite* software package. The dimensions of the tag antenna were about 30% smaller than the one of the reader. Its outer dimensions were 52×40 cm^2. The spiral had five turns and exhibited a quality factor of 154.

An optical picture of the fabricated RFID tag is presented in figure 6.19. Its dimensions were 115×45 mm^2. For the proof of concept, it was fabricated with a standard FR4 PCB substrate. Only the sensing chip was made of flexible polyimide foil. All the electronic components were SMD, which made the whole tag compatible with flexible PCB technology. In addition, a battery was included on the tag to eventually enable data-logging functionalities. However, this semi-active mode was not implemented in this work.

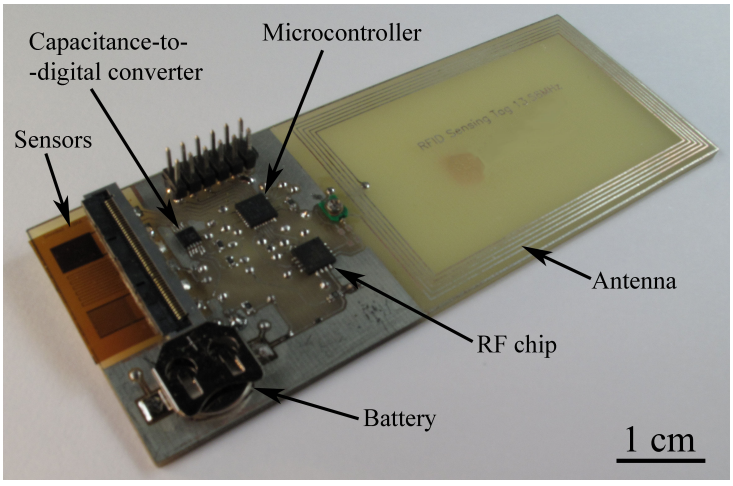

Figure 6.19: Optical picture of the RFID tag. For the demonstration, it was based on a rigid FR4 substrate.

6.4.2 Operation of the RFID tag

The last step to achieve a smart environmental sensing system is the integration of the capacitive sensor and its readout circuitry in a wireless system. The operation of the RFID system in instantaneous measurement mode is shown in figure 6.20. The maximum reading distance of the tag was of about 5 cm and corresponded to similar values found in the literature when operating at this frequency [260]. This distance depended on the tag antenna design and the operational power requirement of the RF chip.

For measurements with the smart sensing system, the capacitive humidity sensor and the Pt resistive temperature sensor were previously calibrated in a climatic chamber. The resulting curves, similar to the capacitive response to humidity given in figure 6.10, were stored in the memory of the microcontroller embedded in the tag. The good result obtained with the tag was confirmed with a commercially available humidity/temperature sensor from *Sensirion AG*, Switzerland.

However, there remain a number of reliability issues. First, the value acquired and displayed by the RFID tag reader depended on the distance between the tag and the reader. This was due to the variation of the tag's supply voltage generated by the RF field from the reader and used to operate the sensors. Second, the on-tag implementation of the humidity/capacitance shift calibration curve turned out to be unexpectedly complicated. The capacitance-to-digital converter only measures capacitance shifts – with the first values measured as reference – and not absolute capacitances. Therefore it was not possible to directly link the capacitance shift measured to a calibration since the first value was usually unknown. Additional improvements have thus to be performed to reliably link the measured capacitance shift to the calibrated relative humidity level.

The main concern for wireless systems is their power consumption, which has to be as low as possible to ensure an operation without an external power supply. The regulator of the RF chip supplied the tag at 3.4 V with a maximum current of 5 mA that can be delivered. Consequently,

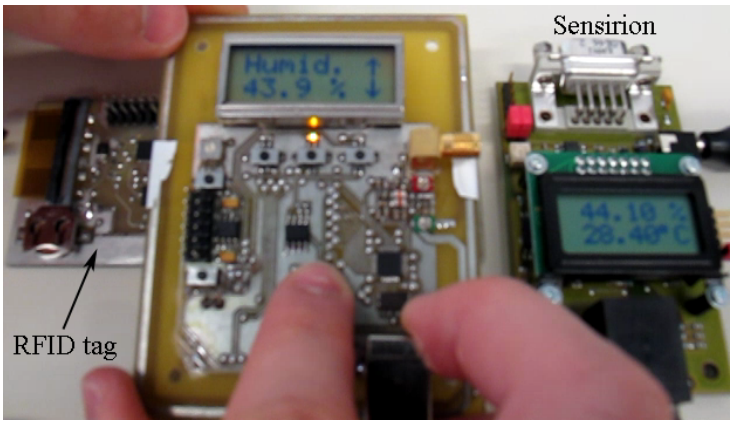

Figure 6.20: Instantaneous measurement of relative humidity with the RFID tag. The result is compared with a commercial humidity sensor (Model *SHT75* from *Sensirion AG*, Switerland).

the optical sensor presented in chapter 3 or the metal-oxide sensor from chapter 4 could not be interfaced on a passive tag due to their excessive current consumption of their LED and heater, respectively. An on-tag battery would be thus required to operate these transducers.

The microcontroller provided the minimum 2.7 V to operate the capacitance-to-digital converter, which was powered only when a measurement was performed. It was idled the rest of the time to reduce overall power consumption. During operation, the constant consumption of the RF chip was measured to be of 415 μA. The microcontroller required 300 μA to operate at 1.2 MHz. That current was required for only few milliseconds to read the sensors, process the acquired data and send them to the RF chip for wireless transmission. This operating frequency was chosen since it allowed a fast reading of the sensors at a suitable power consumption. A lower frequency could be used, but several seconds were then required before the user could read the measured data on the LCD. When no operation was performed (i.e. the microcontroller in sleep mode), its consumption was reduced to the sub-microampere range. For the capacitance-to-digital converter, its consumption was of 100 μA, as given in its datasheet. Therefore, the minimum (i.e. microcontroller and capacitance converter in sleep mode) and maximum (all ICs switched on) current (and power) required were respectively of 415 μA (1.41 mW) and 815 μA (2.77 mW), which were within the capacities of the RFIC.

6.4.3 Discussion on the capacitive sensors interfaced with an RFID tag

The concept of gas sensing on an RFID tag was demonstrated with the integration of the humidity and temperature sensors made on a polyimide foil developed in this work. The system operated as expected for instantaneous measurements, when the tag was only supplied by the power transmitted by RF field from the reader. However, stability issues remained. The values from the sensors sent to the reader were indeed slightly dependent of the distance between the reader and the tag, which modified the supply voltage in the latter, leading to variations of the capacitance and resistance measurements of the humidity and temperature sensors. To counteract this drawback a constant voltage source should be integrated in a future implementation of the RFID tag to ensure a constant and stable voltage, independently of the reading distance.

The interface of the temperature sensor could also be improved. With the voltage divider and the ADC of the microcontroller, only a resolution of 0.5°C was achieved, which is similar to commercial products [33]. To improve the resolution, another interface should be envisaged to measure the temperature. It could be carried out with a Wheatstone bridge or a time-to-digital conversion as developed for the resistance measurement of the metal-oxide gas sensor. The preference would go to the latter since the power consumption of a Wheatstone bridge can be relatively high depending on the values of the resistances of the bridge.

In addition, the capacitance-to-digital converter outputs a capacitance shift and not the absolute capacitance value of the humidity sensor. Improvements are needed to obtain the absolute value of the capacitance to then convert it in a humidity level according to a defined calibration curve. As mentioned above, another option to extract the capacitive sensor would be to use a

circuit based only on passive components and on a time-to-digital conversion. However, using such a method, capacitances of more than 10 pF are required. To obtain a large enough time resolution to ensure good precision in the humidity measurements, a very high resistance would be needed. This will increase the risk of leakage current in the pins of the microcontroller, even when in a high impedance mode. To remedy to this problem, a larger sensing capacitor can be design to reduce the value of the resistor in series. By avoiding the use of an active device, the total power consumption and the cost might be reduced as well.

To reach a higher degree of tag integration, one could make use of a microcontroller that directly embeds RFID communication capabilities. The circuitry would be simplified and the power consumption would very likely decrease. However, such electronic components are not yet available on the market.

A possible extension in tag functionalities would be the data-logging of environmental parameters. Instantaneous measurement of humidity using the tag was only possible when it was powered by the RF field of the RFID reader. Therefore, no autonomous measurements with a passive tag are possible. Data-logging with a semi-active tag would allow sensor measurements without the presence of the RF field. The wireless device would be able to perform measurements at given time intervals (from seconds to hours) as defined by the user, who would configure the tag with the reader. The RFID reader would then be used to download the stored results in the microcontroller of the tag.

6.5 Conclusion

In this chapter, the initial steps were presented towards the realization of a smart environmental sensing system. Such device combines sensors, their interface with data processing/storage and communications capabilities. The concept was demonstrated here with the wireless measurement of humidity and temperature with an RFID tag operating at 13.56 MHz according to the standard ISO 15693. However, the tag still requires some improvements, mainly to remove the influence of the reading distance, which distorted the sensor measurements. In a second step, the data-logging of the environmental parameters could be implemented. The tag developed here was already designed to perform such a task, with the presence of a battery to supply the device when no RF field is present and with enough memory in the microcontroller to store the acquired data.

However, a smart environmental sensing system cannot be limited to the transmission of only one or two parameters. For that purpose, the integration of different transducing principles on a same substrate was also performed. By design such a platform on plastic foil, drawbacks that can be obtained with such substrate revealed to be an advantage here by operating the sensors in a *smart* way. By integrating together on the same plastic foil capacitive and metal-oxide devices, the detection of a wider range of gases was achieved. The capacitive structures monitored the humidity and VOCs, while the metal-oxide gas sensors responded to oxidizing and reducing gases. They showed some benefits in terms of sensitivity, selectivity and cross-

calibration. Moreover, the continuous operation of the MOX sensors during a period of more than two months revealed a very high stability when operating at 300°C, making them attractive for logistic applications. The first generation of devices was devised to prove the sensor concept and can evolve towards hybrid sensor arrays with an increased number of elements to further improve the sensitivity and selectivity towards other analytes.

A significant point that also has to be addressed for a smart sensing system is the interface of the sensors with the electronic circuitry. Due to the limited energy available in a wireless system, it has to be designed accordingly. To reach the low power consumption and the inexpensiveness required by an RFID tags, active components should be avoided. A direct time-to-digital conversion was implemented for the MOX gas sensors and low concentrations of CO (20 ppm) were successfully measured. The total power consumption of the system was of 1.9 mW when operating in pulsed temperature mode with a duty cycle of 10%. The origin of the highest losses was identified and came from the load resistor to tune the temperature of the sensor heater. These losses could be as high as half the total power consumption of the whole system. They could be reduced by fabricating the heated area of the sensors with a material having a higher resistivity than the Pt used for the electrical connections.

The measurement method based on a time-to-voltage conversion with only passive components can be easily extended to other resistive sensors (e.g. for temperature measurement) or modified to monitor capacitive sensors (e.g. humidity sensor). This technique can provide the interface for a wide range of resistive and capacitive sensors, but not only for chemical sensing devices. Physical sensors (acceleration, shock, light, pressure,...) could be envisage as long as they do not required a very short measurement time since this method needs a few milliseconds to perform a measurement.

Finally, once a fully operating RFID system will be reached, its further integration will be performed to evolve towards a System-in-Foil (SiF) concept with the integration of gas sensors with different transducing principles and their respective electronic circuities on a flexible tag. This could be achieved at first with standard manufacturing techniques for flexible PCBs. However, to reduce the fabrication cost and meet the application requirements, techniques employed for large scale fabrication such as roll-to-roll processing, inkjet printing, should be foreseen as well. It would also consist in fabricating the RFID tag entirely on flexible substrates, i.e. the sensors as well as the electronic components and the antenna.

Chapter 7

General discussion

7.1 Gas sensors fabricated on plastic foil

The substrate for the design of transducers on plastic foil has to be chosen according to its compatibility with the sensors. Polyimide was selected for the metal-oxide gas sensors because of its high temperature performances and its low thermal conductivity. It allowed conceiving MOX devices with a simpler architecture and processing than those made from silicon by reaching a low power consumption without bulk micromachining of the substrate. They revealed same gas sensing performances than a commercial Si-based device when operating in isothermal mode. However, further developments should be carried out for their operation in pulsed-temperature modes to enhance their sensitivity. It can be achieved with an optimization of the pulsing cycle as well as with the design of the electrodes.

The capacitive sensor took the advantage of the water absorption of the polyimide to achieve a very simple layout based on only one fabrication step. By operating differentially an uncoated and a functionalized capacitor, the discrimination of VOCs in the TWA range from humidity became possible. The use of less expensive substrates such as PEN or PET should be investigated to evaluate their gas sensing performances in this configuration. However, due to the lower absorptivity of these substrates, coatings on both capacitors might be required.

PET and PEN substrates were selected for the colorimetric gas sensor to to benefit from their good optical transparency. The foil was thus directly used as an optical waveguide. It led to a very simple architecture with a minimum of fabrication steps potentially compatible with roll-to-roll processing. With its planar configuration, the detection of ammonia concentrations in the sub-ppm range was achieved with a power consumption in the sub-milliwatt. A further increase in sensitivity for a same consumption could be achieved by optimizing the pulsed-mode with a longer period between two measurements and a longer regulation time of the light source.

For all three sensors, further investigations should be carried out to evaluate their stability on a long term period. For the specific field of logistics, a reliable operation of the sensors over a period of about two months, which corresponds to the duration of a shipment by sea, would be required. In their actual configuration, the assets and drawbacks of each sensor are summarized

Table 7.1: Comparison between the sensors fabricated on plastic foils.

Sensor	Advantages	Disadvantages
Colorimetric gas sensor	Simple fabrication based on additive processes High selectivity High sensitivity	Power consumption of the LED Strong influence of humidity Long response time
Metal-oxide gas sensor	Based on commercial devices High sensitivity Limited influence of humidity Simple electronics	More complex architecture Platinum as conductor Low selectivity High power losses in the driving circuitry
Differential capacitive gas sensor	Simple processing Low-power Discrimination between H_2O and VOCs Short response time Improved response linearity	Platinum as conductor Low selectivity Strong influence of temperature

in table 7.1.

7.2 Power consumption and potential integration on RFID tags

The power consumption of the investigated sensors presented in the previous chapters with their associated electronics are summarized in table 7.2 when operating in pulsed mode with a period of 1 s. The lower consumption was achieved with the differential capacitive sensor, which was interfaced with a low-power capacitance-to-digital converter. This IC could be avoided by implementing a time-to-digital conversion based on the readout of the MOX sensor. This concept has already been demonstrated for interfacing commercial humidity sensors [287]. For its implementation with the actual sensors, it has first to be evaluated in terms of compatibility with the designed capacitors, power consumption and price.

Beside its lower power required, the capacitive sensor needed only a very low current to operate its readout. Hence, it was possible to directly integrate it on a passive RFID tag since the maximum current that can be delivered by the RF chip was of 5 mA. Due to their very low-power consumptions, additional capacitive sensors could be easily embedded in the system. By coating the capacitors with different functional materials, a higher selectivity might be achieved

Table 7.2: Comparison of the power consumption of the gas sensors and their interfaces when used in pulsed mode.

Sensor	Power consumption. (μW)
Colorimetric gas sensor	947
Metal-oxide gas sensor	1900
Differential capacitive gas sensor	170*

*: Estimation with an *MSP430* microcontroller and a *AD7150* C-V converter supplied at 3 V with duty cycles of 2 and 1%, respectively.

on a passive RFID label.

In the contrary, the two other sensors involved higher peaks of current. The LED of the colorimetric gas sensor required several milliamperes to be lit, while currents between 12 and 15 mA were necessary to operate the heaters of the metal-oxide gas sensing devices. They were therefore not suitable for their integration on the passive RFID tag implemented in this study.

The addition of a battery on the label would however deliver enough current to operate the MOX or the colorimetric sensor. It would lead to the implementation of a semi-active tag, which can operate when no RF field is present. In this configuration, more than one sensor could be integrated. Their number would only be limited by the expected operation time of the smart sensing system, the period between two measurements and the amount of energy stored in the battery. Such a configuration brings some advantages over a passive tag. It could be used for the data-logging of environmental parameters, which is of high interest in the supply chain management.

7.3 Towards fully printed devices

The metal-oxide and capacitive gas sensors were fabricated with processing derived from the silicon industry. Their main drawback is the use of platinum as conductive layer. They are consequently not compatible with large scale manufacturing techniques. Pt is expensive and should be avoided to produce cost-effective sensors. It was deposited by sputtering and patterned by a lift-off technique, a subtractive method. To reduce the price of the device and make them attractive for large scale deployment, a cheaper conductive material should be selected and deposited with an additive method such as printing.

Beside its price, the choice of the electrically conductive material should also be driven by its chemical inertness. This factor is of prime importance for chemical sensors where stability is the cornerstone to achieve a reliable device. Materials that easily oxidize have to be avoided or

at least covered by protective coating. A cost reduction could also be achieved by using a PEN substrate instead of PI. A main challenge resides here in the operation temperature of the MOX sensor. A strong effort should be dedicated to the development of highly sensitive materials for low temperature (100-150°C) measurement. The use of metal-oxide nanotubes might fulfill this requirement [179, 180], but a robust integration method still need to be developed.

Another drawback of the capacitive and metal-oxide gas sensors is the dimensions of the patterned structures. Conductive pathways with widths of a few micrometers were fabricated to reduce the size of these transducers. This was especially the case for the metal-oxide gas sensor where precise and narrow lines were needed to reach a good temperature uniformity. Their compatibility with large scale fabrication has still to be demonstrated since the actual state-of-the-art in roll-to-roll manufacturing is higher than 5 μm for the line widths and 10 μm for alignment tolerances.

A major achievement was reached with the design of the colorimetric gas sensor for compatibility with large scale manufacturing. The sensing film was deposited by inkjet printing, while the fabrication of the mirrors was performed by the dispensing and patterning of a UV-glue. This step could very likely be achieved at large scale, but more straightforward methods should be envisaged. For example, hot embossing – a roll-to-roll compatible process – of the mirrors in the foil would simplify their fabrication. The printing of OLED and PPD would make the sensing device all polymeric and compatible with printed electronics processes.

Chapter 8

Conclusion and outlook

The gas sensing capabilities of low-power sensors designed on plastic foils for wireless applications were investigated. Three types of transducing principles were addressed for their implementation on polymeric substrates. A selective ammonia sensor was based on colorimetric detection, a metal-oxide gas sensor was dedicated to the measurement of oxidizing and reducing gases and capacitive structures were selected for the detection of volatile organic compounds and humidity.

By designing them on plastic foil, the fabrication techniques derived from the silicon micromachining were adapted to be compatible with the processing on foil. Methods compatible with roll-to-roll manufacturing for the fabrication of sensors were also developed. A major achievement towards the production of gas sensors compatible with large scale processing was realized with the colorimetric gas sensor. It was designed with a planar configuration and only additive deposition methods. The sensing film was inkjet printed and the resist to make the mirrors dispensed. Due to the nature of the substrate, an innovative method of foil level packaging for chemical sensors was developed.

Despite their fabrication on plastic foil, very good performances and gas sensing properties were achieved with all devices. The selective colorimetric ammonia gas sensor had a sensitivity of 12.1 mV/ppm and a theoretical limit of detection of 800 ppb when operating in pulsed mode. The metal-oxide gas sensor detected oxidizing and reducing gases with similar chemoresistive responses than commercial silicon-based devices when operating in continuous mode. In pulsed mode, lower values were obtained compared to the MEMS device. It consequently should be further optimized, mainly the layout of the electrodes. The capacitive gas sensor allowed the discrimination between volatile organic compounds and humidity by taking advantage of a differential mode of measurement. Even though the device was exposed to high humidity level, concentrations of gases in the TWA range were detected with this technique.

The realization of a multisensor platform was achieved by combining together two capacitive elements and a temperature sensor with two metal-oxide gas sensing devices, enhanced gas sensing capabilities were obtained for the discrimination of VOCs, oxidizing and reducing gas. Their cross-calibration allowed the correction of their responses to achieve more accurate

information on the gaseous environment.

In this thesis, not only efforts were dedicated to the realization of sensors on plastic foil, but also at looking at the system aspect. A key point to integrate them in a wireless system is their power consumption. All sensors functioned with in a sub-milliwatt range to make them compatible with the targeted application. A large part of the power was dissipated by the electronic driving circuitry, while the readout of the devices operated with a very low consumption. With the interfacing of a humidity sensor to a passive RFID tag, a first step was achieved towards the design of a smart sensing system with sensors devised on plastic foil. The device was able to transmit the sensor information by wireless communication to a reader. Even if calibration issues remained, it foresees to the development of autonomous RFID tag for environmental parameters monitoring. The next step would be to print the sensors directly on the flexible RFID label.

To evaluate the performances of these sensors over time, long-term measurements tests are necessary. The stability of these sensors could be defined and their suitability for reliable gas detection could be determined. These experiments would assess the potential of these devices for their integration on smart RFID labels for environmental monitoring.

Future progresses should be dedicated to the direct implementation of these sensors by methods fully compatible with roll-to-roll processing to make them more cost-effective. The first issue that has to be addressed is the replacement of the platinum by a low-cost conductive material that can be printed. By using additive techniques, fully printed devices on foil could be realized. They would not be limited to the fabrication of the sensors, but should be extend to the design of the whole tag, including the antenna and the electrical connections for the embedded electronic components. It would lead to cost-effective smart sensing systems with the potential of being widely deployed in logistics.

References

[1] B. J. de Gans, P. C. Duineveld, and U. S. Schubert, "Inkjet printing of polymers: State of the art and future developments," *Advanced Materials*, vol. 16, no. 3, pp. 203–213, 2004.

[2] S. E. Shaheen, R. Radspinner, N. Peyghambarian, and G. E. Jabbour, "Fabrication of bulk heterojunction plastic solar cells by screen printing," *Applied Physics Letters*, vol. 79, no. 18, pp. 2996–2998, 2001.

[3] F. C. Krebs, H. Spanggard, T. Kjaer, M. Biancardo, and J. Alstrup, "Large area plastic solar cell modules," *Materials Science and Engineering, B: Solid State Materials for Advanced Technology*, vol. 138, no. 2, pp. 106–111, 2007.

[4] S. H. Eom, S. Senthilarasu, P. Uthirakumar, S. C. Yoon, J. Lim, C. Lee, H. S. Lim, J. Lee, and S. H. Lee, "Polymer solar cells based on inkjet-printed PEDOT:PSS layer," *Organic Electronics*, vol. 10, no. 3, pp. 536–542, 2009.

[5] S. C. Chang, J. Bharathan, Y. Yang, R. Helgeson, F. Wudl, M. B. Ramey, and J. R. Reynolds, "Dual-color polymer light-emitting pixels processed by hybrid inkjet printing," *Applied Physics Letters*, vol. 73, no. 18, pp. 2561–2563, 1998.

[6] F. Villani, P. Vacca, G. Nenna, O. Valentino, G. Burrasca, T. Fasolino, C. Minarini, and D. Della Sala, "Inkjet printed polymer layer on flexible substrate for OLED applications," *Journal of Physical Chemistry C*, vol. 113, no. 30, pp. 13398–13402, 2009.

[7] G. H. Gelinck, H. E. A. Huitema, E. Van Veenendaal, E. Cantatore, L. Schrijnemakers, J. B. P. H. Van der Putten, T. C. T. Geuns, M. Beenhakkers, J. B. Giesbers, B. H. Huisman, E. J. Meijer, E. M. Benito, F. J. Touwslager, A. W. Marsman, B. J. E. Van Rens, and D. M. De Leeuw, "Flexible active-matrix displays and shift registers based on solution-processed organic transistors," *Nature Materials*, vol. 3, no. 2, pp. 106–110, 2004.

[8] F. Garnier, R. Hajlaoui, A. Yassar, and P. Srivastava, "All-polymer field-effect transistor realized by printing techniques," *Science*, vol. 265, no. 5179, pp. 1684–1686, 1994.

[9] B. A. Ridley, B. Nivi, and J. M. Jacobson, "All-inorganic field effect transistors fabricated by printing," *Science*, vol. 286, no. 5440, pp. 746–749, 1999.

[10] S. R. Forrest, "The path to ubiquitous and low-cost organic electronic appliances on plastic," *Nature*, vol. 428, no. 6986, pp. 911–918, 2004.

[11] D. Marculescu, R. Marculescu, N. H. Zamora, P. Stanley-Marbell, P. K. Khosla, S. Park, S. Jayaraman, S. Jung, C. Lauterbach, W. Weber, T. Kirstein, D. Cottet, J. Grzyb, G. Troster, M. Jones, T. Martin, and Z. Nakad, "Electronic textiles: A platform for pervasive computing," *Proceedings of the IEEE*, vol. 91, no. 12, pp. 1995–2018, 2003.

[12] A. Bonfiglio, D. De Rossi, T. Kirstein, I. R. Locher, F. Mameli, R. Paradiso, and G. Vozzi, "Organic field effect transistors for textile applications," *IEEE Transactions on Information Technology in Biomedicine*, vol. 9, no. 3, pp. 319–324, 2005.

[13] K. U. Roscher, W. J. Fischer, J. Landgraf, G. Pfeifer, and E. Starke, "Sensor networks for integration into textile-reinforced composites," in *Transducers '07 and Eurosensors XXI*, vol. 1-2, (Lyon, France), pp. U803–U804 2616, 2007.

[14] Y. Hasegawa, M. Shikida, D. Ogura, and K. Sato, "Glove type of wearable tactile sensor produced by artificial hollow fiber," in *Transducers '07 and Eurosensors XXI*, vol. 1-2, (Lyon, France), pp. U735–U736 2616, 2007.

[15] T. Kinkeldei, C. Zysset, K. Cherenack, and G. Troester, "Development and evaluation of temperature sensors for textile integration," in *IEEE Sensors 2009*, (Christchurch, New Zealand), pp. 1580–1583, 2009.

[16] J.-H. Moon, D. Baek, Y. Choi, K. Lee, H. Kim, and S.-H. Lee, "Wearable polyimide-PDMS electrodes for intrabody communication," *Journal of Micromechanics and Microengineering*, vol. 20, no. 2, p. 025032, 2010.

[17] R. Angeles, "RFID technologies: Supply-chain applications and implementation issues," *Information Systems Management*, vol. 22, no. 1, pp. 51–65, 2005.

[18] http://www.polyapply.org/, PolyApply, 2010.

[19] http://www.polyic.com/en/index.php, PolyIC, 2010.

[20] C. Turcu, *Development and Implementation of RFID Technology*. IN-TECH, 2009.

[21] Y. Arthus-Bertrand, "Home," 2009.

[22] T. Paarup, J. A. Sanchez, A. Moral, H. Christensen, M. Bisgaard, and L. Gram, "Sensory, chemical and bacteriological changes during storage of iced squid (todaropsis eblanae)," *Journal of Applied Microbiology*, vol. 92, no. 5, pp. 941–950, 2002.

[23] A. Pacquit, K. T. Lau, and D. Diamond, "Development of a colorimetric sensor for monitoring of fish spoilage amines in packaging headspace," *Proceedings of IEEE Sensors 2004*, vol. 1, pp. 365–367, 2004.

[24] L. Palou, C. H. Crisosto, D. Garner, and L. M. Basinal, "Effect of continuous exposure to exogenous ethylene during cold storage on postharvest decay development and quality attributes of stone fruits and table grapes," *Postharvest Biology and Technology*, vol. 27, no. 3, pp. 243–254, 2003.

[25] R. Jedermann, C. Behrens, D. Westphal, and W. Lang, "Applying autonomous sensor systems in logistics - combining sensor networks, RFIDs and software agents," *Sensors and Actuators, A: Physical*, vol. 132, no. 1, pp. 370–375, 2006.

[26] E. Abad, S. Zampolli, S. Marco, A. Scorzoni, B. Mazzolai, A. Juarros, D. Gomez, I. Elmi, G. C. Cardinali, J. M. Gomez, F. Palacio, M. Cicioni, A. Mondini, T. Becker, and I. Sayhan, "Flexible tag microlab development: Gas sensors integration in RFID flexible tags for food logistic," *Sensors and Actuators, B: Chemical*, vol. 127, no. 1, pp. 2–7, 2007.

[27] R. Jedermann, L. Ruiz-Garcia, and W. Lang, "Spatial temperature profiling by semi-passive RFID loggers for perishable food transportation," *Computers and Electronics in Agriculture*, vol. 65, no. 2, pp. 145–154, 2009.

[28] C. Amador, J. P. Emond, and M. C. N. Nunes, "Application of RFID technologies in the temperature mapping of the pineapple supply chain," *Sensing and Instrumentation for Food Quality and Safety*, vol. 3, no. 1, pp. 26–33, 2009.

[29] http://www.ksw microtec.de/, KSW Microtec AG, 2010.

[30] http://www.schreiner logidata.com/, Schreiner Logidata, 2010.

[31] http://www.scemtec.com/, Scemtec GmbH, 2010.

[32] http://www.montalbanotechnology.com/, Montalbano Technologies, 2010.

[33] http://www.omega.com/, Omega engineering, Inc., 2010.

[34] P. Pursula, J. Marjonen, H. Ronkainen, and K. Jaakkola, "Wirelessly powered sensor transponder for UHF RFID," in *Transducers '07 and Eurosensors XXI*, pp. U40–U41 2616, 2007.

[35] http://www.vtt.fi/, VTT 2010.

[36] W. Goepel, T. Jones, M. Kleitz, J. Lundstrom, and T. Seiyama, *Chemical and Biochemical Sensors Part I*. Sensors: A comprehensive Survey, Weinheim, Switzerland: VCH, 1991.

[37] J. W. Gardner, H. V. Shurmer, and T. T. Tan, "Application of an electronic nose to the discrimination of coffees," *Sensors and Actuators, B: Chemical*, vol. 6, no. 1-3, pp. 71–75, 1992.

[38] T. Eklov, P. Martensson, and I. Lundstrom, "Selection of variables for interpreting multivariate gas sensor data," *Analytica Chimica Acta*, vol. 381, no. 2-3, pp. 221–232, 1999.

[39] L. Torsi, M. C. Tanese, N. Cioffi, M. C. Gallazzi, L. Sabbatini, P. G. Zambonin, G. Raos, S. V. Meille, and M. M. Giangregorio, "Side-chain role in chemically sensing conducting polymer field-effect transistors," *Journal of Physical Chemistry B*, vol. 107, no. 31, pp. 7589–7594, 2003.

[40] L. Torsi and A. Dodabalapur, "Organic thin-film transistors as plastic analytical sensors.," *Analytical Chemistry*, vol. 77, no. 19, pp. 380a–387a, 2005.

[41] J. B. Chang, V. Liu, V. Subramanian, K. Sivula, C. Luscombe, A. Murphy, J. S. Liu, and J. M. J. Frechet, "Printable polythiophene gas sensor array for low-cost electronic noses," *Journal of Applied Physics*, vol. 100, no. 1, pp. –, 2006. 063YS Times Cited:16 Cited References Count:26.

[42] R. A. Potyrailo, C. Surman, W. G. Morris, and S. Go, "Selective detection of chemical species in liquids and gases using radio-frequency identification (RFID) sensors," in *Transducers 2009*, (Denver, CO, USA), pp. 1650–1653, 2009.

[43] R. A. Potyrailo and W. G. Morris, "Multianalyte chemical identification and quantitation using a single radio frequency identification sensor," *Analytical Chemistry*, vol. 79, no. 1, pp. 45–51, 2007.

[44] H. Meixner, J. Gerblinger, U. Lampe, and M. Fleischer, "Thin-film gas sensors based on semiconducting metal-oxides," *Sensors and Actuators, B: Chemical*, vol. 23, no. 2-3, pp. 119–125, 1995.

[45] M. Ferroni, V. Guidi, G. Martinelli, G. Faglia, P. Nelli, and G. Sberveglieri, "Characterization of a nanosized TiO2 gas sensor," *Nanostructured Materials*, vol. 7, no. 7, pp. 709–718, 1996.

[46] M. Blaschke, T. Tille, P. Robertson, S. Mair, U. Weimar, and H. Ulmer, "MEMS gas-sensor array for monitoring the perceived car-cabin air quality," *IEEE Sensors Journal*, vol. 6, no. 5, pp. 1298–1308, 2006.

[47] I. Elmi, S. Zampolli, E. Cozzani, F. Mancarella, and G. C. Cardinali, "Development of ultra-low-power consumption MOX sensors with ppb-level VOC detection capabilities for emerging applications," *Sensors and Actuators, B: Chemical*, vol. 135, no. 1, pp. 342–351, 2008.

[48] E. Espinosa, R. Ionescu, S. Zampolli, I. Elmi, G. C. Cardinali, E. Abad, R. Leghrib, J. L. Ramírez, X. Vilanova, and E. Llobet, "Drop-coated sensing layers on ultra low power hotplates for an RFID flexible tag microlab," *Sensors and Actuators, B: Chemical*, vol. 144, no. 2, pp. 462–466, 2010.

[49] A. Oprea, N. Barsan, U. Weimar, M. L. Bauersfeld, D. Ebling, and J. Wollenstein, "Capacitive humidity sensors on flexible RFID labels," *Sensors and Actuators, B: Chemical*, vol. 132, no. 2, pp. 404–410, 2008.

[50] D. Briand, S. Colin, A. Gangadharaiah, E. Vela, P. Dubois, L. Thiery, and N. F. de Rooij, "Micro-hotplates on polyimide for sensors and actuators," *Sensors and Actuators, A: Physical*, vol. 132, no. 1, pp. 317–324, 2006.

[51] P. G. Su and C. S. Wang, "Novel flexible resistive-type humidity sensor," *Sensors and Actuators, B: Chemical*, vol. 123, no. 2, pp. 1071–1076, 2007.

[52] K. Parikh, K. Cattanach, R. Rao, D. S. Suh, A. M. Wu, and S. K. Manohar, "Flexible vapour sensors using single walled carbon nanotubes," *Sensors and Actuators, B: Chemical*, vol. 113, no. 1, pp. 55–63, 2006.

[53] P. G. Su, C. T. Lee, C. Y. Chou, K. H. Cheng, and Y. S. Chuang, "Fabrication of flexible NO2 sensors by layer-by-layer self-assembly of multi-walled carbon nanotubes and their gas sensing properties," *Sensors and Actuators, B: Chemical*, vol. 139, no. 2, pp. 488–493, 2009.

[54] K. Cattanach, R. D. Kulkarni, M. Kozlov, and S. K. Manohar, "Flexible carbon nanotube sensors for nerve agent simulants," *Nanotechnology*, vol. 17, no. 16, pp. 4123–4128, 2006.

[55] T. Wakamatsu and K. Aizawa, "Penetration-depth characteristics of evanescent fields at metal attenuated total reflection," *Japanese Journal of Applied Physics, Part 1: Regular Papers and Short Notes and Review Papers*, vol. 44, no. 6 A, pp. 4272–4274, 2005.

[56] S. Harlepp, J. Robert, N. C. Darnton, and D. Chatenay, "Subnanometric measurements of evanescent wave penetration depth using total internal reflection microscopy combined with fluorescent correlation spectroscopy," *Applied Physics Letters*, vol. 85, no. 17, pp. 3917–3919, 2004.

[57] M. Madou, *Fundamentals of microfabrication*. Boca Raton, USA: CRC Press, 2001.

[58] S. I. Park, J. H. Ahn, X. Feng, S. D. Wang, Y. G. Huang, and J. A. Rogers, "Theoretical and experimental studies of bending of inorganic electronic materials on plastic substrates," *Advanced Functional Materials*, vol. 18, no. 18, pp. 2673–2684, 2008.

[59] S. Grego, J. Lewis, E. Vick, and D. Temple, "Development and evaluation of bend-testing techniques for flexible-display applications," *Journal of the Society for Information Display*, vol. 13, no. 7, pp. 575–581, 2005.

[60] S. Grego, J. Lewis, E. Vick, and D. Temple, "A method to evaluate mechanical performance of thin transparent films for flexible displays," *Thin Solid Films*, vol. 515, no. 11, pp. 4745–4752, 2007.

[61] J. van den Brand, J. de Baets, T. van Mol, and A. Dietzel, "Systems-in-foil - devices, fabrication processes and reliability issues," *Microelectronics Reliability*, vol. 48, no. 8-9, pp. 1123–1128, 2008.

[62] Y. Leterrier, L. Medico, F. Demarco, J. A. E. Manson, U. Betz, M. F. Escola, M. K. Olsson, and F. Atamny, "Mechanical integrity of transparent conductive oxide films for flexible polymer-based displays," *Thin Solid Films*, vol. 460, no. 1-2, pp. 156–166, 2004.

[63] D. R. Cairns and G. P. Crawford, "Electromechanical properties of transparent conducting substrates for flexible electronic displays," *Proceedings of the IEEE*, vol. 93, no. 8, pp. 1451–1458, 2005.

[64] J. Lewis, "Material challenge for flexible organic devices," *Materials Today*, vol. 9, no. 4, pp. 38–45, 2006.

[65] M. Boehme and C. Charton, "Properties of ITO on PET film in dependence on the coating conditions and thermal processing," *Surface and Coatings Technology*, vol. 200, no. 1-4, pp. 932–935, 2005.

[66] C. N. de Carvalho, A. Luis, O. Conde, E. Fortunato, G. Lavareda, and A. Amaral, "Effect of rf power on the properties of ITO thin films deposited by plasma enhanced reactive thermal evaporation on unheated polymer substrates," *Journal of Non-Crystalline Solids*, vol. 299, pp. 1208–1212, 2002.

[67] H. Tetsuka, T. Ebina, T. Tsunoda, H. Nanjo, and F. Mizukami, "Fabrication and characterization of ITO thin films on heat-resistant transparent flexible clay films," *Surface and Coatings Technology*, vol. 202, no. 13, pp. 2955–2959, 2008.

[68] K. Sidler, O. Vazquez-Mena, V. Savu, G. Villanueva, M. A. F. van den Boogaart, and J. Brugger, "Resistivity measurements of gold wires fabricated by stencil lithography on flexible polymer substrates," *Microelectronic Engineering*, vol. 85, no. 5-6, pp. 1108–1111, 2008.

[69] D. J. Lichtenwalner, A. E. Hydrick, and A. I. Kingon, "Flexible thin film temperature and strain sensor array utilizing a novel sensing concept," *Sensors and Actuators; A: Physical*, vol. 135, no. 2, pp. 593–597, 2007.

[70] D. Briand, S. Colin, J. Courbat, S. Raible, J. Kappler, and N. F. de Rooij, "Integration of MOX gas sensors on polyimide hotplates," *Sensors and Actuators, B: Chemical*, vol. 130, no. 1, pp. 430–435, 2008.

[71] N. Barsan, M. Schweizer-Berberich, and W. Gopel, "Fundamental and practical aspects in the design of nanoscaled SnO2 gas sensors: a status report," *Fresenius Journal of Analytical Chemistry*, vol. 365, no. 4, pp. 287–304, 1999.

[72] U. Buder, R. Petz, M. Kittel, W. Nitsche, and E. Obermeier, "Aeromems polyimide based wall double hot-wire sensors for flow separation detection," *Sensors and Actuators, A: Physical*, vol. 142, no. 1, pp. 130–137, 2008.

[73] A. Mahmood, D. P. Butler, and Z. Celik-Butler, "Micromachined bolometers on polyimide," *Sensors and Actuators, A: Physical*, vol. 132, no. 2, pp. 452–459, 2006.

[74] C. Y. Lee, S. J. Lee, and G. W. Wu, "Fabrication of micro temperature sensor on the flexible substrate," in *7th IEEE Conference on Nanotechnology*, vol. 1-3, (Hong Kong, China), pp. 1054–1057 1353, 2007.

[75] R. Matsuzaki and A. Todoroki, "Wireless flexible capacitive sensor based on ultra-flexible epoxy resin for strain measurement of automobile tires," *Sensors and Actuators, A: Physical*, vol. 140, no. 1, pp. 32–42, 2007.

[76] http://www.microchem.com/products/pmgi.htm, MicroChem, PMGI and LOR resists 2010.

[77] T. Boltshauser, C. A. Leme, and H. Baltes, "High-sensitivity CMOS humidity sensors with on-chip absolute capacitance measurement system," *Sensors and Actuators, B: Chemical*, vol. 15, no. 1-3, pp. 75–80, 1993.

[78] P. R. Story, D. W. Galipeau, and R. D. Mileham, "A study of low-cost sensors for measuring low relative-humidity," *Sensors and Actuators, B: Chemical*, vol. 25, no. 1-3, pp. 681–685, 1995.

[79] J. Laconte, V. Wilmart, D. Flandre, and J. P. Raskin, "High-sensitivity capacitive humidity sensor using 3-layer patterned polyimide sensing film," in *Proceedings of the IEEE Sensors 2003*, vol. 1-2, pp. 372–377 1367, 2003.

[80] L. Gu, Q. A. Huang, and M. Qin, "A novel capacitive-type humidity sensor using CMOS fabrication technology," *Sensors and Actuators, B: Chemical*, vol. 99, no. 2-3, pp. 491–498, 2004.

[81] N. Lazarus, S. Bedair, C.-C. Lo, and G. Fedder, "CMOS-MEMS capacitive humidity sensor," *Journal of Microelectromechanical Systems*, vol. 19, no. 1, pp. 183–191, 2010.

[82] G. Turban and M. Rapeaux, "Dry etching of polyimide in O2-CF4 and O2-SF6 plasmas," *Journal of the Electrochemical Society*, vol. 130, no. 11, pp. 2231–2236, 1983.

[83] U. Buder, J. P. von Klitzing, and E. Obermeier, "Reactive ion etching for bulk structuring of polyimide," *Sensors and Actuators, A: Physical*, vol. 132, no. 1, pp. 393–399, 2006.

[84] J. Celeste, "Process for making photoresists," 30.09.1969 1969.

[85] http://www2.dupont.com/, DuPont, Riston 2010.

[86] http://www.elgaeurope.it/, Elga, Ordyl 2010.

[87] http://www.eternal group.com/, Eternal, Etertec 2010.

[88] http://www.asahi-kasei.co.jp/ake mate/dfr/en/index.htm, Asahi Kasei 2010.

[89] H. Lorenz, L. Paratte, R. Luthier, N. F. deRooij, and P. Renaud, "Low-cost technology for multilayer electroplated parts using laminated dry film resist," *Sensors and Actuators, A: Physical*, vol. 53, no. 1-3, pp. 364–368, 1996.

[90] E. Kukharenka, M. M. Farooqui, L. Grigore, M. Kraft, and N. Hollinshead, "Electroplating moulds using dry film thick negative photoresist," *Journal of Micromechanics and Microengineering*, vol. 13, no. 4, pp. S67–S74, 2003.

[91] R. Guijt, E. Candish, and M. Breadmore, "Dry film microchips for miniaturised separations," *Electrophoresis*, vol. 30, no. 24, pp. 4219–4224, 2009.

[92] P. Vulto, N. Glade, L. Altomare, J. Bablet, L. Del Tin, G. Medoro, I. Chartier, N. Manaresi, M. Tartagni, and R. Guerrieri, "Microfluidic channel fabrication in dry film resist for production and prototyping of hybrid chips," *Lab on a Chip*, vol. 5, no. 2, pp. 158–162, 2005.

[93] P. Vulto, T. Huesgen, B. Albrecht, and G. A. Urban, "A full-wafer fabrication process for glass microfluidic chips with integrated electroplated electrodes by direct bonding of dry film resist," *Journal of Micromechanics and Microengineering*, vol. 19, no. 7, pp. –, 2009.

[94] P. W. Leech, N. Wu, and Y. Zhu, "Application of dry film resist in the fabrication of microfluidic chips for droplet generation," *Journal of Micromechanics and Microengineering*, vol. 19, no. 6, p. 065019, 2009.

[95] A. D. Radadia, L. Cao, H. K. Jeong, M. A. Shannon, and R. I. Masell, "A 3d micromixer fabricated with dry film resist," *Proceedings of the IEEE 20th Annual International Conference on Micro Electro Mechanical Systems (MEMS)*, pp. 602–605 897, 2007.

[96] M. Y. Jung, W. I. Jang, C. A. Choi, M. R. Lee, C. H. Jun, and Y. T. Kim, "Novel lithography process for extreme deep trench by using laminated negative dry film resist," *Technical Digest of the 17th IEEE International Conference on Micro Electro Mechanical Systems (MEMS)*, pp. 685–688 868, 2004.

[97] L. T. Jiang, T. C. Huang, C. Y. Chang, J. R. Ciou, S. Y. Yang, and P. H. Huang, "Direct fabrication of rigid microstructures on a metallic roller using a dry film resist," *Journal of Micromechanics and Microengineering*, vol. 18, no. 1, p. 015004, 2008.

[98] M. Bale, J. C. Carter, C. Creigton, H. Gregory, P. H. Lyon, P. Ng, L. Webb, and A. Wehrum, "Ink jet printing: The route to production of full color p-OLED displays," *Proceedings of the Twenty-Fifth International Display Research Conference - Eurodisplay 2005*, pp. 480–483 590, 2005.

[99] R. Bennett and D. Albertalli, "Use of industrial inkjet printing in flat panel displays," *IDMC 05: Proceedings of the International Display Manufacturing Conference 2005*, pp. 631–634 852, 2005.

[100] S. H. Lee, J. Y. Hwang, K. Kang, and H. Kang, "Fabrication of organic light emitting display using inkjet printing technology," in *ISOT 2009 - International Symposium on Optomechatronic Technologies*, ISOT 2009 - International Symposium on Optomechatronic Technologies, (Istanbul), pp. 71–76, 2009.

[101] D. Soltman and V. Subramanian, "Inkjet-printed line morphologies and temperature control of the coffee ring effect," *Langmuir*, vol. 24, no. 5, pp. 2224–2231, 2008.

[102] K. Crowley, A. Morrin, A. Hernandez, E. O'Malley, P. G. Whitten, G. G. Wallace, M. R. Smyth, and A. J. Killard, "Fabrication of an ammonia gas sensor using inkjet-printed polyaniline nanoparticles," *Talanta*, vol. 77, no. 2, pp. 710–717, 2008.

[103] F. Loffredo, A. D. Del Mauro, G. Burrasca, V. La Ferrara, L. Quercia, E. Massera, G. Di Francia, and D. D. Sala, "Ink-jet printing technique in polymer/carbon black sensing device fabrication," *Sensors and Actuators, B: Chemical*, vol. 143, no. 1, pp. 421–429, 2009.

[104] A. Liberski, R. Zhang, and M. Bradley, "Inkjet fabrication of polymer microarrays and grids-solving the evaporation problem," *Chemical Communications*, no. 3, pp. 334–336, 2009.

[105] K. Murata, J. Matsumoto, A. Tezuka, Y. Matsuba, and H. Yokoyama, "Super-fine ink-jet printing: toward the minimal manufacturing system," *Microsystem Technologies-Micro-and Nanosystems-Information Storage and Processing Systems*, vol. 12, no. 1-2, pp. 2–7, 2005.

[106] S. Gamerith, A. Klug, H. Scheiber, U. Scherf, E. Moderegger, and E. J. W. List, "Direct ink-jet printing of Ag-Cu nanoparticle and Ag-precursor based electrodes for OFET applications," *Advanced Functional Materials*, vol. 17, no. 16, pp. 3111–3118, 2007.

[107] S. H. Lee, K. Y. Shin, J. Y. Hwang, K. T. Kang, and H. S. Kang, "Silver inkjet printing with control of surface energy and substrate temperature," *Journal of Micromechanics and Microengineering*, vol. 18, no. 7, pp. –, 2008.

[108] B. Y. Ahn, E. B. Duoss, M. J. Motala, X. Y. Guo, S. I. Park, Y. J. Xiong, J. Yoon, R. G. Nuzzo, J. A. Rogers, and J. A. Lewis, "Omnidirectional printing of flexible, stretchable, and spanning silver microelectrodes," *Science*, vol. 323, no. 5921, pp. 1590–1593, 2009.

[109] D. Huang, F. Liao, S. Molesa, D. Redinger, and V. Subramanian, "Plastic-compatible low resistance printable gold nanoparticle conductors for flexible electronics," *Journal of the Electrochemical Society*, vol. 150, no. 7, pp. G412–G417, 2003.

[110] S. H. Ko, J. Chung, H. Pan, C. P. Grigoropoulos, and D. Poulikakos, "Fabrication of multilayer passive and active electric components on polymer using inkjet printing and low temperature laser processing," *Sensors and Actuators, A: Physical*, vol. 134, no. 1, pp. 161–168, 2007.

[111] S. H. Ko, H. Pan, C. P. Grigoropoulos, C. K. Luscombe, J. M. J. Frechet, and D. Poulikakos, "Air stable high resolution organic transistors by selective laser sintering of ink-jet printed metal nanoparticles," *Applied Physics Letters*, vol. 90, no. 14, pp. –, 2007.

[112] C. P. R. Dockendorf, M. Steinlin, D. Poulikakos, and T. Y. Choi, "Individual carbon nanotube soldering with gold nanoink deposition," *Applied Physics Letters*, vol. 90, no. 19, pp. –, 2007.

[113] J. Siden, B. Lee, and J. Ganjei, "On the efficiency of RFID tag antennas produced by copper plating catalytic ink traces," 2008.

[114] S. J. Hong, Y. H. Kim, and J. I. Han, "Development of ultrafine indium tin oxide (ITO) nanoparticle for ink-jet printing by low-temperature synthetic method," *IEEE Transactions on Nanotechnology*, vol. 7, no. 2, pp. 172–176, 2008.

[115] H. Sirringhaus, T. Kawase, R. H. Friend, T. Shimoda, M. Inbasekaran, W. Wu, and E. P. Woo, "High-resolution inkjet printing of all-polymer transistor circuits," *Science*, vol. 290, no. 5499, pp. 2123–2126, 2000.

[116] K. E. Paul, W. S. Wong, S. E. Ready, and R. A. Street, "Additive jet printing of polymer thin-film transistors," *Applied Physics Letters*, vol. 83, no. 10, pp. 2070–2072, 2003.

[117] T. Kawase, T. Shimoda, C. Newsome, H. Sirringhaus, and R. H. Friend, "Inkjet printing of polymer thin film transistors," *Thin Solid Films*, vol. 438, pp. 279–287, 2003.

[118] T. Kawase, S. Moriya, C. J. Newsome, and T. Shimoda, "Inkjet printing of polymeric field-effect transistors and its applications," *Japanese Journal of Applied Physics*, vol. 44, no. 6A, pp. 3649–3658, 2005.

[119] Y. Noguchi, T. Sekitani, and T. Someya, "Organic-transistor-based flexible pressure sensors using ink-jet-printed electrodes and gate dielectric layers," *Applied Physics Letters*, vol. 89, no. 25, pp. –, 2006.

[120] M. Barret, S. Sanaur, and P. Collot, "Inkjet-printed polymer thin-film transistors: Enhancing performances by contact resistances engineering," *Organic Electronics*, vol. 9, no. 6, pp. 1093–1100, 2008.

[121] H. Al-Chami and E. Cretu, "Inkjet printing of microsensors," in *IEEE 15th International Mixed-Signals, Sensors, and Systems Test Workshop, IMS3TW '09*, 2009 IEEE 15th International Mixed-Signals, Sensors, and Systems Test Workshop, IMS3TW '09, (Scottsdale, AZ), 2009.

[122] Y. Liu, T. H. Cui, and K. Varahramyan, "All-polymer capacitor fabricated with inkjet printing technique," *Solid-State Electronics*, vol. 47, no. 9, pp. 1543–1548, 2003.

[123] M. F. Mabrook, C. Pearson, and M. C. Petty, "Inkjet-printed polypyrrole thin films for vapour sensing," *Sensors and Actuators, B: Chemical*, vol. 115, no. 1, pp. 547–551, 2006.

[124] M. O'Toole, R. Shepherd, G. G. Wallace, and D. Diamond, "Inkjet printed LED based pH chemical sensor for gas sensing," *Analytica Chimica Acta*, vol. 652, no. 1-2, pp. 308–314, 2009.

[125] J. Miettinen, V. Pekkanen, K. Kaija, P. Mansikkamaki, J. Mantysalo, M. Mantysalo, J. Niittynen, J. Pekkanen, T. Saviauk, and R. Ronkka, "Inkjet printed system-in-package design and manufacturing," *Microelectronics Journal*, vol. 39, no. 12, pp. 1740–1750, 2008.

[126] V. Subramanian, P. C. Chang, J. B. Lee, S. E. Molesa, and S. K. Volkman, "Printed organic transistors for ultra-low-cost RFID applications," *IEEE Transactions on Components and Packaging Technologies*, vol. 28, no. 4, pp. 742–747, 2005.

[127] R. D. Deegan, O. Bakajin, T. F. Dupont, G. Huber, S. R. Nagel, and T. A. Witten, "Capillary flow as the cause of ring stains from dried liquid drops," *Nature*, vol. 389, no. 6653, pp. 827–829, 1997.

[128] R. D. Deegan, O. Bakajin, T. F. Dupont, G. Huber, S. R. Nagel, and T. A. Witten, "Contact line deposits in an evaporating drop," *Physical Review E*, vol. 62, no. 1, pp. 756–765, 2000.

[129] R. D. Deegan, "Pattern formation in drying drops," *Physical Review E*, vol. 61, no. 1, pp. 475–485, 2000.

[130] M. A. Sutton, J. W. Erisman, F. Dentener, and D. Moeller, "Ammonia in the environment: From ancient times to the present," *Environmental Pollution*, vol. 156, no. 3, pp. 583–604, 2008.

[131] W. Cao and Y. Duan, "Optical fiber-based evanescent ammonia sensor," *Sensors and Actuators, B: Chemical*, vol. 110, no. 2, pp. 252–259, 2005.

[132] http://www.draeger.com/, Draeger, 2010.

[133] R. L. Shepherd, W. S. Yerazunis, K. T. Lau, and D. Diamond, "Low-cost surface-mount LED gas sensor," *IEEE Sensors Journal*, vol. 6, no. 4, pp. 861–865, 2006.

[134] A. Morales-Bahnik, R. Czolk, and H. J. Ache, "An optochemical ammonia sensor based on immobilized metalloporpyrins," *Sensors and Actuators: B. Chemical*, vol. 19, no. 1-3, pp. 493–496, 1994.

[135] A. A. Vaughan, M. G. Baron, and R. Narayanaswamy, "Optical ammonia sensing films based on an immobilized metalloporphyrin," *Analytical Communications*, vol. 33, no. 11, pp. 393–396, 1996.

[136] A. Mills, L. Wild, and Q. Chang, "Plastic colorimetric film sensors for gaseous ammonia," *Mikrochimica Acta*, vol. 121, no. 1-4, pp. 225–236, 1995.

[137] T. Werner, I. Klimant, and O. S. Wolfbeis, "Ammonia-sensitive polymer matrix employing immobilized indicator ion pairs," *The Analyst*, vol. 120, no. 6, pp. 1627–1631, 1995.

[138] G. Gauglitz and G. Kraus, "A reflectometric sensor for ammonia and hydrocarbons," *Fresenius' Journal of Analytical Chemistry*, vol. 346, no. 6-9, pp. 572–576, 1993.

[139] Z. Opilski, R. Rogozinski, P. Karasinski, and A. Opilski, "Spectral properties of bromophenol blue used as sensor layer of ammonia vapours," *Proceedings of SPIE - The International Society for Optical Engineering*, vol. 3731, pp. 172–178, 1999.

[140] N. A. Rakow and K. S. Suslick, "A colorimetric sensor array for odour visualization," *Nature*, vol. 406, no. 6797, pp. 710–713, 2000.

[141] K. S. Suslick, N. A. Rakow, and A. Sen, "Colorimetric sensor arrays for molecular recognition," *Tetrahedron*, vol. 60, no. 49, pp. 11133–11138, 2004.

[142] R. Klein and E. Voges, "Integrated-optic ammonia sensor," *Sensors and Actuators, B: Chemical*, vol. 11, no. 1-3, pp. 221–225, 1993.

[143] S. Tao, L. Xu, and J. C. Fanguy, "Optical fiber ammonia sensing probes using reagent immobilized porous silica coating as transducers," *Sensors and Actuators, B: Chemical*, vol. 115, no. 1, pp. 158–163, 2006.

[144] V. Anisimov, A. Borisov, O. Ivanova, and S. Krutovertsev, "Environment factors effect on characteristics of optical NH3 sensor," *Proceeding of the Eurosensors 2006 Conference*, 2006.

[145] Y. Cao, P. Smith, and A. J. Heeger, "Counter-ion induced processibility of conducting polyaniline and of conducting polyblends of polyaniline in bulk polymers," *Synthetic Metals*, vol. 48, no. 1, pp. 91–97, 1992.

[146] G. J. Mohr, N. Tirelli, C. Lohse, and U. E. Spichiger-Keller, "Development of chromogenic copolymers for optical detection of amines," *Advanced Materials*, vol. 10, no. 16, pp. 1353–1357, 1998.

[147] S. S. Sarkisov, M. J. Curley, C. Boykin, D. E. Diggs, J. Grote, and F. Hopkins, "Planar optical waveguide sensor of ammonia," *Proceedings of SPIE - The International Society for Optical Engineering*, vol. 5586, pp. 33–44, 2004.

[148] T. Grady, T. Butler, B. D. MacCraith, D. Diamond, and M. A. McKervey, "Optical sensor for gaseous ammonia with tuneable sensitivity," *The Analyst*, vol. 122, no. 8, pp. 803–806, 1997.

[149] H. Guo and S. Tao, "Silver nanoparticles doped silica nanocomposites coated on an optical fiber for ammonia sensing," *Sensors and Actuators, B: Chemical*, vol. 123, no. 1, pp. 578–582, 2007.

[150] H. P. Ninh, Y. Tanaka, T. Nakamoto, and K. Hamada, "A bad-smell sensing network using gas detector tubes and mobile phone cameras," *Sensors and Actuators, B: Chemical*, vol. 125, no. 1, pp. 138–143, 2007.

[151] K. Crowley, A. Pacquit, J. Hayes, K. T. Lau, and D. Diamond, "A gas-phase colorimetric sensor for the detection of amine spoilage products in packaged fish," *Proceedings of IEEE Sensors*, vol. 2005, pp. 754–757, 2005.

[152] T. Nakamoto, M. Yosihioka, Y. Tanaka, K. Kobayashi, T. Moriizumi, S. Ueyama, and W. S. Yerazunis, "Colorimetric method for odor discrimination using dye-coated plate and multiLED sensor," *Sensors and Actuators, B: Chemical*, vol. 116, no. 1-2, pp. 202–206, 2006.

[153] B. D. Gupta, H. Dodeja, and A. K. Tomar, "Fibre-optic evanescent field absorption sensor based on a U-shaped probe," *Optical and Quantum Electronics*, vol. 28, no. 11, pp. 1629–1639, 1996.

[154] T. Mayr, B. Enko, T. Abel, S. Koestler, C. Konrad, and I. Klimant, "A novel sensor concept paving the way for the integration of OLEDs and organic photodiodes," in *Eurosensors XXII*, (Dresden, Germany), pp. 1300–1303, 2008.

[155] S. Vallon, B. Drevillon, and F. Poncin-Epaillard, "In situ spectroellipsometry study of the crosslinking of polypropylene by an argon plasma," *Applied Surface Science*, vol. 108, no. 1, pp. 177–185, 1997.

[156] M. Losurdo, M. M. Giangregorio, P. Capezzuto, G. Bruno, F. Babudri, D. Colangiuli, G. M. Farinola, and F. Naso, "Spectroscopic ellipsometry for characterization of organic semiconductor polymeric thin films," *Synthetic Metals*, vol. 138, no. 1-2, pp. 49–53, 2003.

[157] E. Wagner, R. Daendliker, and K. Spenner, *Optical Sensors*, vol. 6 of *Sensors: A Comprehensive Survey*. Weinheim, Germany: Wiley-VCH Verlag, 1999.

[158] G. J. Mohr, N. Tirelli, and U. E. Spichiger-Keller, "Plasticizer-free optode membranes for dissolved amines based on copolymers from alkyl methacrylates and the fluoro reactand eth(t) 4014," *Analytical Chemistry*, vol. 71, no. 8, pp. 1534–1539, 1999.

[159] http://europe.dupontteijinfilms.com/marketspaces/electricalcomponents/flexibleelectronics.aspx, DuPont Teijin Films 2010.

[160] D. Montgomery, *Design and analysis of experiments*. New York, USA: John Wiley and Sons, Inc., 5th edition ed., 2001.

[161] N. Barsan and U. Weimar, "Understanding the fundamental principles of metal oxide based gas sensors; the example of CO sensing with SnO2 sensors in the presence of humidity," *Journal of Physics-Condensed Matter*, vol. 15, no. 20, pp. R813–R839, 2003.

[162] J. Woellenstein, J. A. Plaza, C. Cane, Y. Min, H. Bottner, and H. L. Tuller, "A novel single chip thin film metal oxide array," *Sensors and Actuators, B: Chemical*, vol. 93, no. 1-3, pp. 350–355, 2003.

[163] A. Stankova, X. Vilanova, E. Llobet, J. Calderer, C. Bittencourt, J. J. Pireaux, and X. Coffeig, "Influence of the annealing and operating temperatures on the gas-sensing properties of RF sputtered WO3 thin-film sensors," *Sensors and Actuators, B: Chemical*, vol. 105, no. 2, pp. 271–277, 2005.

[164] V. D. Kapse, S. A. Ghosh, G. N. Chaudhari, and F. C. Raghuwanshi, "Nanocrystalline In2O3-based H2S sensors operable at low temperatures," *Talanta*, vol. 76, no. 3, pp. 610–616, 2008.

[165] D. Briand, A. Krauss, B. van der Schoot, U. Weimar, N. Barsan, W. Gopel, and N. F. de Rooij, "Design and fabrication of high-temperature micro-hotplates for drop-coated gas sensors," *Sensors and Actuators, B: Chemical*, vol. 68, no. 1-3, pp. 223–233, 2000.

[166] N. Yamazoe, J. Fuchigami, M. Kishikawa, and T. Seiyama, "Interactions of tin oxide surface with O2, H2O and H2," *Surface Science*, vol. 86, no. Jul, pp. 335–344, 1979.

[167] G. Sberveglieri, "Recent developments in semiconducting thin-film gas sensors," *Sensors and Actuators, B: Chemical*, vol. 23, no. 2-3, pp. 103–109, 1995.

[168] G. G. Mandayo, E. Castano, F. J. Gracia, A. Cirera, A. Cornet, and J. R. Morante, "Strategies to enhance the carbon monoxide sensitivity of tin oxide thin films," *Sensors and Actuators, B: Chemical*, vol. 95, no. 1-3, pp. 90–96, 2003.

[169] T. Seiyama, A. Kato, K. Fujiishi, and M. Nagatani, "A new detector for gaseous components using semiconductive thin films," *Analytical Chemistry*, vol. 34, no. 11, pp. 1502–1503, 1962.

[170] http://www.figarosensor.com/, Figaro Engineering Inc., Japan 2010.

[171] S. R. Morrison, "Mechanism of semiconductor gas sensor operation," *Sensors and Actuators*, vol. 11, no. 3, pp. 283–287, 1987.

[172] W. M. Sears, K. Colbow, and F. Consadori, "Algorithms to improve the selectivity of thermally-cycled tin oxide gas sensors," *Sensors and Actuators*, vol. 19, no. 4, pp. 333–349, 1989.

[173] N. Yamazoe, Y. Kurokawa, and T. Seiyama, "Effects of additives on semiconductor gas sensors," *Sensors and Actuators*, vol. 4, no. 2, pp. 283–289, 1983.

[174] H. Meixner and U. Lampe, "Metal oxide sensors," *Sensors and Actuators, B: Chemical*, vol. 33, no. 1-3, pp. 198–202, 1996.

[175] E. Comini, G. Faglia, G. Sberveglieri, Z. W. Pan, and Z. L. Wang, "Stable and highly sensitive gas sensors based on semiconducting oxide nanobelts," *Applied Physics Letters*, vol. 81, no. 10, pp. 1869–1871, 2002.

[176] E. Comini, G. Faglia, G. Sberveglieri, D. Calestani, L. Zanotti, and M. Zha, "Tin oxide nanobelts electrical and sensing properties," *Sensors and Actuators, B: Chemical*, vol. 111, pp. 2–6, 2005.

[177] G. Sberveglieri, C. Baratto, E. Comini, G. Faglia, A. Ferroni, A. Ponzoni, and A. Vomiero, "Synthesis and characterization of semiconducting nanowires for gas sensing," *Sensors and Actuators, B: Chemical*, vol. 121, no. 1, pp. 208–213, 2007.

[178] J. S. Wright, W. Lim, D. P. Norton, S. J. Pearton, F. Ren, J. L. Johnson, and A. Ural, "Nitride and oxide semiconductor nanostructured hydrogen gas sensors," *Semiconductor Science and Technology*, vol. 25, no. 2, pp. –, 2010.

[179] E. Comini, G. Faglia, and G. Sberveglieri, "UV light activation of tin oxide thin films for NO2 sensing at low temperatures," *Sensors and Actuators, B: Chemical*, vol. 78, no. 1-3, pp. 73–77, 2001.

[180] E. H. Espinosa, R. Ionescu, B. Chambon, G. Bedis, E. Sotter, C. Bittencourt, A. Felten, J. J. Pireaux, X. Correig, and E. Llobet, "Hybrid metal oxide and multiwall carbon nanotube films for low temperature gas sensing," *Sensors and Actuators, B: Chemical*, vol. 127, no. 1, pp. 137–142, 2007.

[181] R. E. Cavicchi, J. S. Suehle, K. G. Kreider, B. L. Shomaker, J. A. Small, M. Gaitan, and P. Chaparala, "Growth of SnO2 films on micromachined hotplates," *Applied Physics Letters*, vol. 66, no. 7, pp. 812–814, 1995.

[182] B. Panchapakesan, D. L. DeVoe, M. R. Widmaier, R. Cavicchi, and S. Semancik, "Nanoparticle engineering and control of tin oxide microstructures for chemical microsensor applications," *Nanotechnology*, vol. 12, no. 3, pp. 336–349, 2001.

[183] J. S. Suehle, R. E. Cavicchi, M. Gaitan, and S. Semancik, "Tin oxide gas sensor fabricated using CMOS micro-hotplates and insitu processing," *IEEE Electron Device Letters*, vol. 14, no. 3, pp. 118–120, 1993.

[184] S. Semancik, R. E. Cavicchi, M. C. Wheeler, J. E. Tiffany, G. E. Poirier, R. M. Walton, J. S. Suehle, B. Panchapakesan, and D. L. DeVoe, "Microhotplate platforms for chemical sensor research," *Sensors and Actuators, B: Chemical*, vol. 77, no. 1-2, pp. 579–591, 2001.

[185] http://www.e2v.com/products-and-services/Sensors/gas sensors/, MiCS 2010.

[186] http://www.appliedsensor.com/, AppliedSensor GmbH, 2010.

[187] F. Udrea, J. W. Gardner, D. Setiadi, J. A. Covington, T. Dogaru, C. C. Lu, and W. I. Milne, "Design and simulations of SOI CMOS micro-hotplate gas sensors," *Sensors and Actuators, B: Chemical*, vol. 78, no. 1-3, pp. 180–190, 2001.

[188] J. A. Covington, F. Udrea, and J. W. Gardner, "Resistive gas sensor with integrated MOSFET micro hotplate based on an analogue SOI CMOS process," in *IEEE Sensors 2002*, vol. 1 of *First IEEE International Conference on Sensors - IEEE Sensors 2002*, (Orlando, FL), pp. 1389–1394, 2002.

[189] M. Graf, S. K. Müller, D. Barrettino, and A. Hierlemann, "Transistor heater for microhotplate-based metal-oxide microsensors," *IEEE Electron Device Letters*, vol. 26, no. 5, pp. 295–297, 2005.

[190] P. K. Guha, S. Z. Ali, C. C. C. Lee, F. Udrea, W. I. Milne, T. Iwaki, J. A. Covington, and J. W. Gardner, "Novel design and characterisation of SOI CMOS micro-hotplates for high temperature gas sensors," *Sensors and Actuators, B: Chemical*, vol. 127, no. 1, pp. 260–266, 2007.

[191] M. Graf, D. Barrettino, M. Zimmermann, A. Hierlemann, H. Baltes, S. Hahn, N. Barsan, and U. Weimar, "CMOS monolithic metal-oxide sensor system comprising a microhotplate and associated circuitry," *IEEE Sensors Journal*, vol. 4, no. 1, pp. 9–16, 2004.

[192] P. Ivanov, M. Stankova, E. Llobet, X. Vilanova, J. Brezmes, I. Gracia, C. Cane, J. Calderer, and X. Correig, "Nanoparticle metal-oxide films for micro-hotplate-based gas sensor systems," *Ieee Sensors Journal*, vol. 5, no. 5, pp. 798–809, 2005.

[193] J. Courbat, D. Briand, and N. F. de Rooij, "Reliability improvement of suspended platinum-based micro-heating elements," *Sensors and Actuators, A: Physical*, vol. 142, no. 1, pp. 284–291, 2008.

[194] S. Z. Ali, F. Udrea, W. I. Milne, and J. W. Gardner, "Tungsten-based SOI microhotplates for smart gas sensors," *Journal of Microelectromechanical Systems*, vol. 17, no. 6, pp. 1408–1417, 2008.

[195] I. Elmi, S. Zampolli, and G. C. Cardinali, "Optimization of a wafer-level process for the fabrication of highly reproducible thin-film MOX sensors," *Sensors and Actuators, B: Chemical*, vol. 131, no. 2, pp. 548–555, 2008.

[196] G. Faglia, E. Comini, A. Cristalli, G. Sberveglieri, and L. Dori, "Very low power consumption micromachined CO sensors," *Sensors and Actuators, B: Chemical*, vol. 55, no. 2-3, pp. 140–146, 1999.

[197] T. Oyabu, T. Osawa, and T. Kurobe, "Sensing characteristics of tin oxide thick-film gas sensor," *Journal of Applied Physics*, vol. 53, no. 11, pp. 7125–7130, 1982.

[198] G. Sberveglieri, S. Groppelli, P. Nelli, V. Lantto, H. Torvela, P. Romppainen, and S. Leppavuori, "Response to nitric-oxide of thin and thick SnO2 films containing trivalent additives," *Sensors and Actuators, B: Chemical*, vol. 1, no. 1-6, pp. 79–82, 1990.

[199] W. Y. Chung, D. D. Lee, and B. K. Sohn, "Effects of added TiO2 on the characteristics of SnO2-based thick-film gas sensors," *Thin Solid Films*, vol. 221, no. 1-2, pp. 304–310, 1992.

[200] S. G. Ansari, P. Boroojerdian, S. R. Sainkar, R. N. Karekar, R. C. Aiyer, and S. K. Kulkarni, "Grain size effects on H2 gas sensitivity of thick film resistor using SnO2 nanoparticles," *Thin Solid Films*, vol. 295, no. 1-2, pp. 271–276, 1997.

[201] E. Traversa, Y. Sadaoka, M. C. Carotta, and G. Martinelli, "Environmental monitoring field tests using screen-printed thick-film sensors based on semiconducting oxides," *Sensors and Actuators B-Chemical*, vol. 65, no. 1-3, pp. 181–185, 2000.

[202] B. Riviere, J. P. Viricelle, and C. Pijolat, "Development of tin oxide material by screen-printing technology for micro-machined gas sensors," *Sensors and Actuators, B: Chemical*, vol. 93, no. 1-3, pp. 531–537, 2003.

[203] W. M. Sears and M. A. Gee, "Mechanics of film formation during the spray pyrolysis of tin oxide," *Thin Solid Films*, vol. 165, no. 1, pp. 265–277, 1988.

[204] T. Sahm, L. Madler, A. Gurlo, N. Barsan, S. E. Pratsinis, and U. Weimar, "Flame spray synthesis of tin dioxide nanoparticles for gas sensing," *Sensors and Actuators, B: Chemical*, vol. 98, no. 2-3, pp. 148–153, 2004.

[205] S. Kuehne, M. Graf, A. Tricoli, F. Mayer, S. E. Pratsinis, and A. Hierlemann, "Wafer-level flame-spray-pyrolysis deposition of gas-sensitive layers on microsensors," *Journal of Micromechanics and Microengineering*, vol. 18, no. 3, pp. –, 2008.

[206] M. Epifani, E. Comini, R. Diaz, J. Arbiol, P. Siciliano, G. Sberveglieri, and J. R. Morante, "Oxide nanopowders from the low-temperature processing of metal oxide sols and their application as gas-sensing materials," *Sensors and Actuators, B: Chemical*, vol. 118, no. 1-2, pp. 105–109, 2006.

[207] R. A. Lawes, "Manufacturing costs for microsystems/MEMS using high aspect ratio microfabrication techniques," *Microsystem Technologies-Micro-and Nanosystems-Information Storage and Processing Systems*, vol. 13, no. 1, pp. 85–95, 2007.

[208] M. Graf, U. Frey, S. Taschini, and A. Hierlemann, "Micro hot plate-based sensor array system for the detection of environmentally relevant gases," *Analytical Chemistry*, vol. 78, no. 19, pp. 6801–6808, 2006.

[209] J. Figaro Engineering Inc., "General information for TGS sensors," 2005.

[210] A. Gotz, I. Gracia, J. A. Plaza, C. Cane, P. Roetsch, H. Bottner, and K. Seibert, "A novel methodology for the manufacturability of robust CMOS semiconductor gas sensor arrays," *Sensors and Actuators, B: Chemical*, vol. 77, no. 1-2, pp. 395–400, 2001.

[211] H. Baltes, O. Brand, and M. Waelti, "Packaging of CMOS MEMS," *Microelectronics Reliability*, vol. 40, no. 8-10, pp. 1255–1262, 2000.

[212] S. Raible, D. Briand, J. Kappler, and N. F. de Rooij, "Wafer level packaging of micromachined gas sensors," *IEEE Sensors Journal*, vol. 6, no. 5, pp. 1232–1235, 2006.

[213] V. Demarne and A. Grisel, "An integrated low-power thin-film CO gas sensor on silicon," *Sensors and Actuators*, vol. 13, no. 4, pp. 301–313, 1988.

[214] J. W. Gardner, A. Pike, N. F. Derooij, M. Koudelkahep, P. A. Clerc, A. Hierlemann, and W. Gopel, "Integrated array sensor for detecting organic-solvents," *Sensors and Actuators, B: Chemical*, vol. 26, no. 1-3, pp. 135–139, 1995.

[215] T. Simon, N. Barsan, M. Bauer, and U. Weimar, "Micromachined metal oxide gas sensors: opportunities to improve sensor performance," *Sensors and Actuators, B: Chemical*, vol. 73, no. 1, pp. 1–26, 2001.

[216] D. Bauer, M. Heeger, M. Gebhard, and W. Benecke, "Design and fabrication of a thermal infrared emitter," *Sensors and Actuators, A: Physical*, vol. 55, no. 1, pp. 57–63, 1996.

[217] M. N. Weber, P. Lerch, and P. Renaud, "Improved design for fast modulating IR sources," *Journal of Micromechanics and Microengineering*, vol. 7, no. 3, pp. 210–213, 1997.

[218] G. De Graaf, W. der Vlist, and R. R. Wolffenbuttel, "Design and fabrication steps for a MEMS-based infrared spectrometer using evanescent wave sensing," *Sensors and Actuators, A: Physical*, vol. 142, no. 1, pp. 211–216, 2008.

[219] J. Robadey, O. Paul, and H. Baltes, "2-dimensional integrated gas-flow sensors by CMOS IC technology," *Journal of Micromechanics and Microengineering*, vol. 5, no. 3, pp. 243–250, 1995.

[220] D. N. Pagonis, G. Kaltsas, and A. G. Nassiopoulou, "Fabrication and testing of an integrated thermal flow sensor employing thermal isolation by a porous silicon membrane over an air cavity," *Journal of Micromechanics and Microengineering*, vol. 14, no. 6, pp. 793–797, 2004.

[221] R. J. Adamec, D. V. Thiel, and P. Tanner, "MEMS wind direction detection: From design to operation," *Proceedings of the IEEE Sensors 2003*, vol. 1-2, pp. 340–343 1367, 2003.

[222] E. Cozzani, A. Roncaglia, S. Zampolli, I. Elmi, F. Mancarella, F. Tamarri, and G. C. Cardinali, "Material properties measurement and numerical simulation for characterization of ultra-low-power consumption hotplates," *Transducers '07 and Eurosensors XXI, Digest of Technical Papers*, vol. 1-2, pp. U839–U840 2616, 2007.

[223] M. Messina, F. Franze, N. Speciale, E. Cozzani, and A. Roncaglia, "3D simulation of conjugate heat transfer of ULP hotplates for a MOX gas sensing device," *2007 IEEE Sensors*, vol. 1-3, pp. 95–98 1483, 2007.

[224] T. Bechtold, J. Hildenbrand, J. Wollenstein, and J. G. Korvink, "Model order reduction of 3d electro-thermal model for a novel micromachined hotplate gas sensor," *Thermal and Mechanical Simulation and Experiments in Microelectronics and Microsystems*, pp. 263–267 627, 2004.

[225] T. Li, L. Wu, Y. X. Liu, L. C. Wang, Y. Wang, and Y. L. Wang, "Micro-heater on membrane with large uniform-temperature area," *2006 IEEE Sensors*, vol. 1-3, pp. 571–575 1522, 2006.

[226] A. Pike and J. W. Gardner, "Thermal modelling and characterisation of micropower chemoresistive silicon sensors," *Sensors and Actuators, B: Chemical*, vol. 45, no. 1, pp. 19–26, 1997.

[227] S. Astie, A. M. Gue, E. Scheid, L. Lescouzeres, and A. Cassagnes, "Optimization of an integrated SnO2 gas sensor using a fem simulator," *Sensors and Actuators, A: Physical*, vol. 69, no. 3, pp. 205–211, 1998.

[228] T. Maekawa, K. Suzuki, T. Takada, T. Kobayashi, and M. Egashira, "Odor identification using a SnO2-based sensor array," *Sensors and Actuators, B: Chemical*, vol. 80, no. 1, pp. 51–58, 2001.

[229] B. Panchapakesan, R. Cavicchi, S. Semancik, and D. L. DeVoe, "Sensitivity, selectivity and stability of tin oxide nanostructures on large area arrays of microhotplates," *Nanotechnology*, vol. 17, no. 2, pp. 415–425, 2006.

[230] R. E. Cavicchi, J. S. Suehle, K. G. Kreider, M. Gaitan, and P. Chaparala, "Fast temperature-programmed sensing for micro-hotplate gas sensors," *IEEE Electron Device Letters*, vol. 16, no. 6, pp. 286–288, 1995.

[231] R. E. Cavicchi, J. S. Suehle, K. G. Kreider, M. Gaitan, and P. Chaparala, "Optimized temperature-pulse sequences for the enhancement of chemically specific response patterns from micro-hotplate gas sensors," *Sensors and Actuators, B: Chemical*, vol. 33, no. 1-3, pp. 142–146, 1996.

[232] W. M. Sears, K. Colbow, and F. Consadori, "General-characteristics of thermally cycled tin oxide gas sensors," *Semiconductor Science and Technology*, vol. 4, no. 5, pp. 351–359, 1989.

[233] S. Nakata, H. Nakamura, and K. Yoshikawa, "New strategy for the development of a gas sensor based on the dynamic characteristics - principle and preliminary experiment," *Sensors and Actuators, B: Chemical*, vol. 8, no. 2, pp. 187–189, 1992.

[234] A. P. Lee and B. J. Reedy, "Temperature modulation in semiconductor gas sensing," *Sensors and Actuators, B: Chemical*, vol. 60, no. 1, pp. 35–42, 1999.

[235] A. Heilig, N. Barsan, U. Weimar, M. Schweizer-Berberich, J. W. Gardner, and W. Gopel, "Gas identification by modulating temperatures of SnO2-based thick film sensors," *Sensors and Actuators, B: Chemical*, vol. 43, no. 1-3, pp. 45–51, 1997.

[236] E. Llobet, J. Brezmes, R. Ionescu, X. Vilanova, S. Al-Khalifa, J. W. Gardner, N. Barsan, and X. Correig, "Wavelet transform and fuzzy ARTMAP-based pattern recognition for fast gas identification using a micro-hotplate gas sensor," *Sensors and Actuators, B: Chemical*, vol. 83, no. 1-3, pp. 238–244, 2002.

[237] S. Wlodek, K. Colbow, and F. Consadori, "Signal-shape analysis of a thermally cycled tin-oxide gas sensor," *Sensors and Actuators, B: Chemical*, vol. 3, no. 1, pp. 63–68, 1991.

[238] T. A. Kunt, T. J. McAvoy, R. E. Cavicchi, and S. Semancik, "Optimization of temperature programmed sensing for gas identification using micro-hotplate sensors," *Sensors and Actuators, B: Chemical*, vol. 53, no. 1-2, pp. 24–43, 1998.

[239] M. Schweizer-Berberich, S. Strathman, U. Weimar, R. Sharma, A. Seube, A. Peyre-Lavigne, and W. Gopel, "Strategies to avoid VOC cross-sensitivity of SnO2-based CO sensors," *Sensors and Actuators, B: Chemical*, vol. 58, no. 1-3, pp. 318–324, 1999.

[240] X. J. Huang, F. L. Meng, Z. X. Pi, W. H. Xu, and J. H. Liu, "Gas sensing behavior of a single tin dioxide sensor under dynamic temperature modulation," *Sensors and Actuators, B: Chemical*, vol. 99, no. 2-3, pp. 444–450, 2004.

[241] A. Vergara, E. Llobet, J. Brezmes, P. Ivanov, X. Vilanova, I. Gracia, C. Cane, and X. Correig, "Optimised temperature modulation of metal oxide micro-hotplate gas sensors through multilevel pseudo random sequences," *Sensors and Actuators, B: Chemical*, vol. 111, pp. 271–280, 2005.

[242] K. Frank, H. Kohler, and U. Guth, "Influence of the measurement conditions on the sensitivity of SnO2 gas sensors operated thermo-cyclically," *Sensors and Actuators, B: Chemical*, vol. 141, no. 2, pp. 361–369, 2009.

[243] S. Nakata and N. Ojima, "Detection of a sample gas in the presence of an interferent gas based on a nonlinear dynamic response," *Sensors and Actuators, B: Chemical*, vol. 56, no. 1-2, pp. 79–84, 1999.

[244] T. Amamoto, T. Yamaguch, Y. Matsuura, and Y. Kajiyama, "Development of pulse-drive semiconductor gas sensor," *Sensors and Actuators, B: Chemical*, vol. 14, no. 1-3, pp. 587–588, 1993.

[245] F. Kreith and M. Bohmn, *Principle of heat transfer*. Pacific Grove, USA: Brooks/Cole, 2001.

[246] J. Puigcorbe, D. Vogel, B. Michel, A. Vila, I. Gracia, C. Cane, and J. R. Morante, "Thermal and mechanical analysis of micromachined gas sensors," *Journal of Micromechanics and Microengineering*, vol. 13, no. 5, pp. 548–556, 2003.

[247] D. Teyssieux, D. Briand, J. Charnay, N. F. de Rooij, and B. Cretin, "Dynamic and static thermal study of micromachined heaters: the advantages of visible and near-infrared thermography compared to classical methods," *Journal of Micromechanics and Microengineering*, vol. 18, no. 6, pp. –, 2008.

[248] G. Kovacs, *Micromachined transducers sourcebook*. New-York, USA: McGraw-Hill, 1998.

[249] D. Teyssieux, L. Thiery, and B. Cretin, "Near-infrared thermography using a charge-coupled device camera: Application to microsystems," *Review of Scientific Instruments*, vol. 78, no. 3, pp. –, 2007.

[250] J. Kappler, N. Barsan, U. Weimar, A. Dieguez, J. L. Alay, A. Romano-Rodriguez, J. R. Morante, and W. Gopel, "Correlation between XPS, Raman and TEM measurements and the gas sensitivity of Pt and Pd doped SnO2 based gas sensors," *Fresenius Journal of Analytical Chemistry*, vol. 361, no. 2, pp. 110–114, 1998.

[251] D. Briand, D. Teyssieux, J. Courbat, L. Thiery, B. Cretin, and N. F. de Rooij, "On the thermal simulation and characterization of microsystems: Progress and status," in *Eurosensors XXII*, (Dresden, Germany), pp. 133–136, 2008.

[252] J. Puigcorbe, A. Vila, J. Cerda, A. Cirera, I. Gracia, C. Cane, and J. R. Morante, "Thermomechanical analysis of micro-drop coated gas sensors," *Sensors and Actuators, A: Physical*, vol. 97-8, pp. 379–385, 2002.

[253] M. Ohring, *The materials science of thin films*. London, UK: Academic Press, 1992.

[254] C. Cornila, A. Hierlemann, R. Lenggenhager, P. Malcovati, H. Baltes, G. Noetzel, U. Weimar, and W. Gopel, "Capacitive sensors in CMOS technology with polymer coating," *Sensors and Actuators, B: Chemical*, vol. 25, no. 1-3, pp. 357–361, 1995.

[255] N. Yamazoe and Y. Shimizu, "Humidity sensors - principles and applications," *Sensors and Actuators*, vol. 10, no. 3-4, pp. 379–398, 1986.

[256] M. Parameswaran, H. P. Baltes, M. J. Brett, D. E. Fraser, and A. M. Robinson, "A capacitive humidity sensor based on CMOS technology with adsorbing film," *Sensors and Actuators*, vol. 15, no. 4, pp. 325–335, 1988.

[257] T. Ishihara and S. Matsubara, "Capacitive type gas sensors," *Journal of Electroceramics*, vol. 2, no. 4, pp. 215–228, 1998.

[258] M. Matsuguchi, S. Umeda, Y. Sadaoka, and Y. Sakai, "Characterization of polymers for a capacitive-type humidity sensor based on water sorption behavior," *Sensors and Actuators, B: Chemical*, vol. 49, no. 3, pp. 179–185, 1998.

[259] P. M. Harrey, B. J. Ramsey, P. S. A. Evans, and D. J. Harrison, "Capacitive-type humidity sensors fabricated using the offset lithographic printing process," *Sensors and Actuators, B: Chemical*, vol. 87, no. 2, pp. 226–232, 2002.

[260] A. D. DeHennis and K. D. Wise, "A wireless microsystem for the remote sensing of pressure, temperature, and relative humidity," *Journal of Microelectromechanical Systems*, vol. 14, no. 1, pp. 12–22, 2005.

[261] C. Hagleitner, A. Hierlemann, D. Lange, A. Kummer, N. Kerness, O. Brand, and H. Baltes, "Smart single-chip gas sensor microsystem," *Nature*, vol. 414, no. 6861, pp. 293–296, 2001.

[262] P. Kurzawski, C. Hagleitner, and A. Hierlemann, "Detection and discrimination capabilities of a multitransducer single-chip gas sensor system," *Analytical Chemistry*, vol. 78, no. 19, pp. 6910–6920, 2006.

[263] A. M. Kummer, A. Hierlemann, and H. Baltes, "Tuning sensitivity and selectivity of complementary metal oxide semiconductor-based capacitive chemical microsensors," *Analytical Chemistry*, vol. 76, no. 9, pp. 2470–2477, 2004.

[264] R. Igreja and C. J. Dias, "Dielectric response of interdigital chemocapacitors: The role of the sensitive layer thickness," *Sensors and Actuators, B: Chemical*, vol. 115, no. 1, pp. 69–78, 2006.

[265] M. Kitsara, D. Goustouridis, S. Chatzandroulis, M. Chatzichristidi, I. Raptis, T. Ganetsos, R. Igreja, and C. J. Dias, "Single chip interdigitated electrode capacitive chemical sensor arrays," *Sensors and Actuators, B: Chemical*, vol. 127, no. 1, pp. 186–192, 2007.

[266] C. Hagleitner, D. Lange, A. Hierlemann, O. Brand, and H. Baltes, "Cmos single-chip gas detection system comprising capacitive, calorimetric and mass-sensitive microsensors," *IEEE Journal of Solid-State Circuits*, vol. 37, no. 12, pp. 1867–1878, 2002.

[267] E. Zampetti, S. Pantalei, A. Pecora, A. Valletta, L. Maiolo, A. Minotti, A. Macagnano, G. Fortunato, and A. Bearzotti, "Design and optimization of an ultra thin flexible capacitive humidity sensor," *Sensors and Actuators, B: Chemical*, vol. 143, no. 1, pp. 302–307, 2009.

[268] http://www.jlm innovation.de/, JLM Innovation GmbH, 2010.

[269] http://www.umweltsensortechnik.de/index3.htm, UST GmbH, 2010.

[270] "Valeurs limites d'exposition aux postes de travail 2009 vme/vle, vbt valeurs admissibles pour agents physiques," tech. rep., Swiss Accident Insurance Fund (Suva), 2009. Doc. Number 1903.F.

[271] J. W. Grate and M. H. Abraham, "Solubility interactions and the design of chemically selective sorbent coatings for chemical sensors and arrays," *Sensors and Actuators, B: Chemical*, vol. 3, no. 2, pp. 85–111, 1991.

[272] M. Hautefeuille, C. O'Mahony, B. O'Flynn, K. Khalfi, and F. Peters, "A MEMS-based wireless multisensor module for environmental monitoring," *Microelectronics Reliability*, vol. 48, no. 6, pp. 906–910, 2008.

[273] J. Hayes, S. Beirne, K. T. Lau, and D. Diamond, "Evaluation of a low cost wireless chemical sensor network for environmental monitoring," in *Proceedings of the IEEE Sensors 2008 Conference*, pp. 530–533, 2008.

[274] Y. Li, C. Vancura, D. Barrettino, M. Graf, C. Hagleitner, A. Kummer, M. Zimmermann, K. U. Kirstein, and A. Hierlemann, "Monolithic CMOS multi-transducer gas sensor microsystem for organic and inorganic analytes," *Sensors and Actuators, B: Chemical*, vol. 126, no. 2, pp. 431–440, 2007.

[275] H. Shurmer and J. Gardner, "Odour discrimination with an electronic nose," *Sensors and Actuators, B: Chemical*, vol. 8, no. 1, pp. 1–11, 1992.

[276] A. Flammini, D. Marioli, and A. Taroni, "A low-cost interface to high-value resistive sensors varying over a wide range," *IEEE Transactions on Instrumentation and Measurement*, vol. 53, no. 4, pp. 1052–1056, 2004.

[277] T. Conrad, P. Hiry, and A. Schutze, "Pumah - a temperature control and resistance read-out system for microstructured gas sensors based on PWM signals," in *2005 IEEE Sensors*, (Irvine, USA), pp. 377–384 1413, 2005.

[278] M. Grassi, P. Malcovati, L. Francioso, P. Siciliano, and A. Baschirotto, "Integrated interface circuit with multiplexed input and digital output for a 5 x 5 SnO2 thick film gas-sensor matrix," *Sensors and Actuators, B: Chemical*, vol. 132, no. 2, pp. 568–575, 2008.

[279] G. Ferri, C. Di Carlo, V. Stornelli, A. De Marcellis, A. Flammini, A. Depari, and N. Jand, "A single-chip integrated interfacing circuit for wide-range resistive gas sensor arrays," *Sensors and Actuators, B: Chemical*, vol. 143, no. 1, pp. 218–225, 2009.

[280] M. Grassi, P. Malcovati, and A. Baschirotto, "A high-precision wide-range front-end for resistive gas sensors arrays," *Sensors and Actuators, B: Chemical*, vol. 111, pp. 281–285, 2005.

[281] M. Grassi, P. Malcovati, and A. Baschirotto, "A 141-dB dynamic range CMOS gas-sensor interface circuit without calibration with 16-bit digital output word," *IEEE Journal of Solid-State Circuits*, vol. 42, no. 7, pp. 1543–1554, 2007.

[282] A. Lombardi, M. Grassi, P. Malcovati, S. Capone, L. Francioso, P. Siciliano, and A. Baschirotto, "A CMOS integrated interface circuit for metal-oxide gas sensors," *Sensors and Actuators, B: Chemical*, vol. 142, no. 1, pp. 82–89, 2009.

[283] M. Malfatti, M. Perenzoni, N. Viarani, A. Simoni, L. Lorenzelli, and A. Baschirotto, "A complete front-end system read-out and temperature control for resistive gas sensor array," *Proceedings of the 2005 European Conference on Circuit Theory and Design*, vol. 3, pp. 31–34 474, 2005.

[284] B. Jayaraman and N. Bhat, "High precision 16-bit readout gas sensor interface in 0.13 um CMOS," in *IEEE International Symposium on Circuits and Systems*, vol. 1-11, pp. 3071–3074 4023, 2007.

[285] D.-D. Lee and D.-S. Lee, "Environmental gas sensors," *IEEE Sensors Journal*, vol. 1, no. 3, pp. 214–224, 2001.

[286] A. Fort, M. Gregorkiewitz, N. Machetti, S. Rocchi, B. Serrano, L. Tondi, N. Ulivieri, V. Vignoli, G. Faglia, and E. Comini, "Selectivity enhancement of SnO2 sensors by means of operating temperature modulation," *Thin Solid Films*, vol. 418, no. 1, pp. 2–8, 2002.

[287] F. Reverter and O. Casas, "Direct interface circuit for capacitive humidity sensors," *Sensors and Actuators, A: Physical*, vol. 143, no. 2, pp. 315–322, 2008.

[288] F. Reverter, J. Jordana, M. Gasulla, and R. Pallas-Areny, "Accuracy and resolution of direct resistive sensor-to-microcontroller interfaces," *Sensors and Actuators, A: Physical*, vol. 121, no. 1, pp. 78–87, 2005.

[289] D. Petrovic, "RFID interface for environment sensors," Bachelor thesis, HES-SO Valais, 2008.

Acknowledgements

A thesis is an important team effort and mine is no exception. Without the help and support of my family, friends, colleagues, to whom I wish to extend my gratitude, this work would not have been possible.

I first thank my supervisor, Danick Briand, for his support, encouragement and guidance during this adventure. His advice were a key ingredient to the success of this thesis. I am grateful Prof. Nico de Rooij, who gave me the opportunity to do this work in his laboratory. I would like to thank all my colleagues for their support, fruitful discussions, the very good atmosphere in the lab. In particular Alexandra Homsy, Vincent Linder, Peter van der Wal, Wilfried Noell, Milena Koudelka-Hep, for all their good advice. A special thank goes to the first coffee break team I knew (nine o'clock sharp): Olivier Frey, Michael Zickar, Nicolas Golay, Luca Berdondini, Silvia Generelli and, last but not least, Renato Krpoun for their inspiring discussions. I wish to thank all the member of the EnviroMEMS group for their help and the nice time we spend together: Rahel Strässle, Don Isarakorn, Rokhaya Gueye, Pattanaphong Janphuang, Francisco Molina Lopez and in particular David de Koninck, who partly reviewed this thesis. I cannot forget all my former and actual colleagues, who made these last four years particularly pleasant at SAMLAB: Muhamed Niklaus, Philippe Dubois, Daniel Parrat, Kaspar Suter, Raphaël Imer, Yves Pétremand, Samuel Rosset, Severin Waldis, Dara Bayat, Roland Bitterli, Terunobu Akyiama, Sebastian Gautsch, Patrick Carazzetti, Friedjof Heuck, Caglar Ataman, Fabio Jutzi, Sébastien Lani, Jonathan Masson, Luca Ribetto, Sara Talei, Stefan Weber, Philip Wägli, Frédéric Loizeau and Yexian Wu.

Most of the microfabrication was performed in the cleanroom of the *COMLAB* (now at *CSEM*). I am grateful to Sylvain Jeanneret and his team for their support: Edith Millotte, Sylviane Pochon, Laurent Guillot, Eduardo Santoli, Pierre-André Clerc, Giovanno Bergonzi, Rémy Fournier, Stéphane Ischer, Sabina Jenny and José Vaquera. Without their help, the fabrication of the devices would not have been possible. I also would like to thank Philippe Flückiger and his team at the *CMI* in Lausanne for granting me access to their cleanroom and their wonderful tools with my plastic substrates. Many thanks to Massoud Dadras and Mireille Leboeuf for their assistance with the microscope tools and for always reminding me to put a scalebar in figures. I thank Claudio Novelli and Karine Frossard, who were always there for me.

A significant part of this work was performed at the *Fraunhofer Institute for Physical Measurement Techniques* (*IPM*), in Freiburg im Breisgau. I show my gratitude to Prof. Jürgen Wöllenstein, whom welcomed my in his research group and made me feel like at home. A spe-

cial thanks goes to his team and more particularly to Emmanuel Moretton, Jürgen Hildenbrand, and Marie-Luise Bauersfeld for their help.

The success of this work would not have been possible without collaborations. I thank Stefan Raible and Liu Yue from *AppliedSensor GmbH* for the numerous gas measurements with the MOX sensors, Alexandru Oprea from *IPC* in Tuebingen for the gas measurements with the capacitive sensors and the multisensor platforms, Damien Teyssieux from *FEMTO-ST* in Besançon for his help with the thermal measurements of the micro-hotplates, Riad Kanan and Darko Petrovic from the *HES-SO Valais* in Sion for the realization of the RFID reader and tag. I am thankful to Jérôme Damon-Lacoste of the PV-lab of the EPFL for his help with the ellipsometric measurements and to Toralf Scharf of the Optics lab of the EPFL for the fruitful discussions on the design of optical waveguides.

I am also grateful to all the students, who took part to this work through master thesis, semester projects, diploma works and traineeships: Michael Canonica, Michael Linder, Michela Barbieri, Jules Neabo, Blaise Guélat, Chakravarty Devulapalli, Alexandre Haemmerli, Nicolas Ferrier, Damien Wittwer, Ruben de Araujo, Alexis Weinstein, Maxime Dottori and Gaël Rossier. They have greatly contributed to the success of this thesis.

I thank the GOSPEL European Network of Excellence on Artificial Olfaction and Advanced Gas Sensing Technologies for the partial funding of this project.

Finally, I would like to thank all my family for their love, patient and everlasting support all along this journey.

Thank you all!

Appendix: Results of the analysis of variance

The results of the analysis of variance performed in chapter 3 are given below. Before presenting them, a short explanation is given concerning the signification of each parameter.

The *sum of squares* is a measurement of the dispersion of a set of data. It is given by:

$$SSTR = \sum_{n_i} \left(\overline{Y}_{i.} - \overline{Y}_{..}\right)^2 \tag{1}$$

where $\overline{Y}_{..}$ is the overall mean of the n samples. $\overline{Y}_{i.}$ is the sum of all the data point for a given parameter i:

$$\overline{Y}_{i.} = \sum_{j=1}^{n_i} \overline{Y}_{ij} \tag{2}$$

The *error sum of square* is a measure of the random variation of the samples around their respective parameter mean ($\overline{Y}_{i.}$):

$$SSE = \sum\sum \left(Y_{ij} - \overline{Y}_{i.}\right)^2 \tag{3}$$

The less variation among the data points for each parameter mean, the smaller the SSE. The *sum of square* and the *error sum of square* increase with the number of data in the collection. To compare between several data sets with different amounts of data, it is divided by the *degree of freedom*. The result obtained is the *mean square* and *mean square error* defined by:

$$MSTR = \frac{SSTR}{r-1} \tag{4}$$

$$MSE = \frac{SSE}{n_T - r} \tag{5}$$

where r is the number of data points per parameter and n_T the total number of sample across all different parameters. It corresponds to an adjusted – independent of the number of data points – measurement of the dispersion of the data around a mean value. The *Mean square error* express the dispersion of the data from their estimation.

The *Test statistic*, F, is the ratio between the explained and unexplained variances, namely the *Mean square* and *Mean square error*:

$$F = \frac{MSTR}{MSE} \tag{6}$$

The higher F, the more significant is the parameter compared to the others. In this thesis, a high significance corresponds to results in a confidence interval of 99%, while a significant value relates to an interval to 95%. Insignificant means out of these intervals. Additional information on the statistics used can be found in:

- M. Kuttner, C.J. Nachtsheim, W. Li, *Applied linear statistical models*. Boston, USA: McGraw-Hill, 2005.

Table 1 presents the results obtained with the ANOVA performed on the optical losses of the plastic waveguides presented in chapter 3. The analysis of variance for the gas response are given in table 2.

Table 1: ANOVA table for the optical losses in the waveguide.

Source	Sum of squares	Degree of freedom	Variance	Test statistic (F)	Prob>F
Substrate	19.80	1	19.80	96.68	0
Thickness	12.67	1	12.67	61.87	0
Length	23.64	1	23.64	115.43	0
Coating	88.88	1	88.88	433.90	0
Interaction (Substrate, Thickness)	0.16	1	0.16	0.76	0.3867
Interaction (Substrate, Length)	3.30	1	3.30	16.13	0.0002
Interaction (Substrate, Coating)	5.72	1	5.72	27.94	0
Interaction (Thickness, Length)	0.01	1	0.01	0.05	0.8303
Interaction (Thickness, Coating)	3.30	1	3.30	16.13	0.0002
Interaction (Length, Coating)	0.25	1	0.25	1.22	0.2743
Error	10.86	53	0.2048		
Total	168.60	63			

Table 2: ANOVA table for the sensor response when exposed to 5 ppm of NH_3 for different waveguide configurations.

Source	Sum of squares	Degree of freedom	Mean square	Test statistic (F)	Prob>F
Substrate	$1.15 \cdot 10^{-3}$	1	$1.15 \cdot 10^{-3}$	$19.97 \cdot 10^{3}$	$6.99 \cdot 10^{-15}$
Thickness	$0.94 \cdot 10^{-3}$	1	$0.94 \cdot 10^{-3}$	$16.24 \cdot 10^{3}$	$1.61 \cdot 10^{-14}$
Length	$1.94 \cdot 10^{-3}$	1	$1.94 \cdot 10^{-3}$	$33.62 \cdot 10^{3}$	$8.88 \cdot 10^{-16}$
Coating	$0.97 \cdot 10^{-3}$	1	$0.97 \cdot 10^{-3}$	$16.82 \cdot 10^{3}$	$1.40 \cdot 10^{-14}$
Error	0	8	0		
Total	$7.87 \cdot 10^{-3}$	15			

Biography

Jérôme Courbat was born in 1981 in Porrentruy, Switzerland. He received his M.Sc. degree in microtechnology from the Ecole Polytechnique de Lausanne (EPFL) in 2005. He performed his master thesis on the "Development of capacitive MEMS for vibration energy scavenging" at the Philips Research Laboratories in Eindhoven, The Netherlands.

In September 2005, he joined the Sensors, Actuators and Microsystems Laboratory (SAMLAB) of Prof. Nico de Rooij (University of Neuchâtel, since 2009 at EPF Lausanne). His research activities in the EnviroMEMS group of Dr. Danick Briand are focused on the development and integration of low-power and low-cost sensors on plastic foils for wireless applications.

Publication list

Journal papers

1. J. Courbat, M. Canonica, D. Teyssieux, D. Briand, B. Cretin, and N.F. de Rooij, "Design and fabrication of micro-hotplates made on polyimide foil: Electrothermal simulation and characterization to achieve power consumptions in the low mW range", Submitted.

2. J. Courbat, D. Briand, and N.F de Rooij, "Foil level packaging of chemical gas sensor", *Journal of Micromechanics and Microengineering*, Vol. 20, pp. 055026, 2010.

3. J. Courbat, D. Briand, J. Damon-Lacoste, J. Wöllenstein, and N.F. de Rooij, "Evaluation of pH indicator-based colorimetric films for ammonia detection using optical waveguides", *Sensors and Actuators, B: Chemical*, Vol. 143, pp. 62-70, 2009.

4. D. Briand, S. Colin, J. Courbat, S. Raible, J. Kappler, and N. F. de Rooij, "Integration of MOX gas sensors on polyimide hotplates", *Sensors and Actuators, A: Physical*, Vol. 130, pp. 430-435, 2007.

5. A. Oprea, J. Courbat, N. Bârsan, D. Briand, N.F. de Rooij, and U Weimar, "Temperature, humidity and gas sensors integrated on plastic foil for low power applications", *Sensors and Actuators, B: Chemical*, Vol. 140, pp. 227-232, 2009.

Conference contributions

Oral presentations

6. (Invited) J. Courbat, D. Briand, and N.F. de Rooij, "Ink-jet printed colorimetric gas sensors on plastic foil", *SPIE Photonic Devices + Applications Conference*, 2010.

7. (Invited) D. Briand, J. Courbat and N. F. de Rooij, "Towards gas sensors on plastic foil", *The 13th International Meeting on Chemical Sensors (IMCS13)*, 2010.

8. (Accepted) J. Courbat, D. Briand, R. De Araujo, M. Barbieri, N.F. de Rooij, "Mechanical and electrical characterization of Platinum lines used in sensing devices on polyimide foil", *LOPE-C*, 2010.

9. D. Briand, J. Courbat, N.F. de Rooij, "Smart sensing systems integration: from silicon to plastic foil", *Proc. the Smart Sensing Integration Conference*, Paper n°19, 2010.

10. J. Courbat, D. Briand, J. Wöllenstein, and N.F. de Rooij, "Colorimetric gas sensors based on optical waveguides made on plastic foil", *Proc. of the Eurosensors XXIII Conference*, Procedia Chemistry, Vol.1, No. 1, pp. 576-579, 2009.

11. J. Courbat, D. Briand, A. Oprea, N. Bârsan, U. Weimar, and N.F. de Rooij, "Multi sensor platform on plastic foil for environmental monitoring", *Proc. of the Eurosensors XXIII Conference*, Procedia Chemistry, Vol.1, No. 1, pp. 597-600, 2009.

12. J. Courbat, D. Briand, L. Yue, S. Raible, and N.F. de Rooij, "Ultra-low power metal oxide gas sensor on plastic foil", *Proc. of the Transducers 2009 Conference*, Vol. 1, pp. 584-587, 2009.

13. D. Briand, J. Courbat, and N.F. de Rooij, "Autonomous sensors on flexible foils powered by RFID and energy scavenging for environmental and goody monitoring", *Proc. of the PowerMEMS 2008 Conference*, pp. 173-176, 2008.

14. A. Oprea, U. Altenberend, J. Courbat, D. Briand, N. Barsan, U. Weimar, and N. F. de Rooij, "Capacitive gas sensor arrays on plastic substrates for low power and mobiles applications", *Proc. of the Eurosensors XXII Conference*, Vol. 1, pp. 1431-1434, 2008.

15. A. Oprea, J. Courbat, N. Barsan, D. Briand, U. Weimar, and N. F. de Rooij, "Integrated temperature, humidity and gas sensors on plastic substrates for RFID and low-power applications", Presented in *GOSPEL Workshop on Plastic Chemical Sensors*, 2008.

16. J. Courbat, M. D. Canonica, D. Teyssieux, L. Thiery, D. Briand, B. Cretin, and N. F. de Rooij, "Thermal simulation and characterization for the design of ultra-low power micro-hotplates on flexible substrate", *Proc. of IEEE Sensors 2008 Conference*, pp. 74-77, 2008.

17. J. Courbat, D. Briand, J. Wöllenstein, and N. F. de Rooij, "Evaluation of spin-coatable colorimetric films for ammonia detection using optical waveguides", Presented at *The 12th International Meeting on Chemical Sensors (IMCS12)*, 2008.

18. D. Briand, S. Colin, J. Courbat, S. Raible, J. Kappler, and N. F. de Rooij, "Metal oxide gas sensors on polyimide micro-hotplates", Presented at *The 11th International Meeting on Chemical Sensors (IMCS11)*, 2006.

Poster presentations

19. J. Courbat, M. Linder, M. Dottori, D. Briand, J. Woellenstein, and N.F. de Rooij, "Inkjet printed colorimetric ammonia sensor on plastic foil for low-cost and low-power devices", *Proc. of the MEMS2010 Conference*, pp. 883-886, 2010.

20. D. Briand, D. Teyssieux, J. Courbat, L. Thiery, B. Cretin, and N. F. de Rooij, "On the thermal simulation and characterisation of microsystems: progress and status", *Proc. of the Eurosensors XXII Conference*, Vol. 1, pp. 133-136, 2008.

21. J. Courbat, D. Briand, N. Wyrsch, C. Ballif, and N. F. de Rooij, "Hybrid organic/inorganic sensing platforms on flexible plastic substrates", Presented at the *GOSPEL Workshop on Plastic Chemical Sensors*, 2008.

22. A. Oprea, J. Courbat, N. Barsan, D. Briand, U. Weimar, and N. F. de Rooij, "Integrated temperature, humidity and gas sensors on flexible substrates for low-power applications", *Proc. of the IEEE Sensors 2007 Conference*, pp. 158-161, 2007.

23. D. Briand, J. Courbat, J. Wöllenstein, and N. F. de Rooij, "Micro gas sensing components on flexible substrates", Presented at the *2nd International Workshop on Smart Gas Sensors Technology and Application*, 2007.

Scientific contributions not related to this thesis

24. J. Courbat, D. Briand, and N. F. de Rooij, "Reliability improvement of suspended platinum-based micro-heating elements", *Sensors and Actuators, A: Physical*, Vol. 142, pp. 284-291, 2007.

25. D. Beckel, D. Briand, A. Bieberle-Hütter, J. Courbat, N. F. de Rooij, and L. J. Gauckler, "Micro-hotplates – A platform for micro-solid oxide fuel cells", *Journal of Power Sources*, Vol. 166, No. 1, pp. 143-148, 2007.

26. C. Pijolat, M. Camara, J. Courbat, J.-P. Viricelle, D. Briand, and N. F. de Rooij, "Application of carbon nano-powders for a gas micro-preconcentrator", *Sensors and Actuators, B: Chemical*, Vol. 127, pp. 179-185, 2007.

27. D. Briand, D. Beckel, J. Courbat, L. Castens, L. J. Gauckler, and N. F. de Rooij, "Micromachined platforms on silicon for micro-SOFC", *Proc. of the PowerMEMS 2007 Conference*, pp. 157-160, 2007.

28. D. Beckel, D. Briand, J. Courbat, A. Bieberle-Hütter, N. F. de Rooij, and L. J. Gauckler, "Micro-hotplate devices for micro-SOFC", *Proc. of the 10th International Symposium on Solid-Oxide Fuel Cells (SOFC-X)*, Vol. 7, pp. 421-427, 2007.

29. J. Courbat, D. Briand, and N. F. de Rooij, "Optimization of the material composition of platinum micro-heating elements", Presented at the *Eurosensors XX Conference*, pp. W1B-P1, 2006.

30. C. Pijolat, M. Camara, J. Courbat, J.-P. Viricelle, D. Briand, and N. F. de Rooij, "Application of carbon "nano"powders and porous silicon for gas preconcentration", *Proc. of the Eurosensors XX Conference*, pp. W1A-P11, 2006.

31. D. Beckel, D. Briand, A. Bieberle-Hütter, J. Courbat, N. F. de Rooij, and L. J. Gauckler, "Electrical conductivity of LSCF thin films for SOFC on micro hotplates", Presented at the *Fuell Cell Forum 2006*, 2006.

32. D. Briand, F. Beaudoin, J. Courbat, N. F. de Rooij, R. Desplats, and P. Perdu, "Failure analysis of micro-heating elements suspended on thin membranes", *Microelectronics Reliability*, Vol. 45, No. 9-11, pp. 1786-1789, 2005.

33. F. Beaudoin, D. Briand, J. Courbat, N. F. de Rooij, R. Desplats, and P. Perdu, "Failure analysis of micro-heating elements suspended on thin membranes, Presented at the 16^{th} *European Symposium on Reliability of Electron Devices, Failure Physics and Analysis*, 2005.

34. D. Briand, J. Courbat, P. Q. Pham, and N. F. de Rooij, "Micro-Heat Generation for Chemical Reactions", Presented at the 207^{th} *Meeting of the Electrochemical Society, ECS*, 2005.